3D Biofabrication of Constructs Targeting Orthopaedic Tissue Regeneration and Clinical Biofilm Study

Gareth Stephen Turnbull MBChB MRCSEd PgDipClinEd MSc

Department of Biomedical Engineering

University of Strathclyde

This thesis is submitted in partial fulfilment of the requirements of the degree of
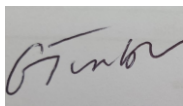
Doctor of Philosophy

2022

Signed: Date: October 2022

Words: 77 627 (53 612 excluding references).

Acknowledgements

There are many individuals who have made a significant contribution in some way to the completion of this thesis, and I have little doubt that it would not have been possible without their involvement and support.

To begin with, I would like to acknowledge my sincere thanks to my primary supervisor Professor Will Shu. Without his guidance, support, high level of patience (as clinical work slowed progress) and dynamic enthusiasm for research, this thesis would undoubtedly not have been possible. His efforts in arranging opportunities for me, including a visit to a collaborating laboratory in China, opened my eyes to the huge benefits of developing collaborations and the strength and opportunities in international research.

I am also hugely indebted to my clinical supervisors, Mr Jon Clarke and Professor Picard, for taking an initial chance by granting me a Clinical Research Fellowship at The Golden Jubilee Hospital. During the course of this Fellowship they both provided me with ongoing encouragement, intellectual support, guidance and inspiration to pursue what remains a novel area of research whilst providing clinical opportunities. With their help and support, added to that of Professor Shu and Dr Philip Riches, I have been able to achieve a coveted registrar training in post in Scotland, whilst our research won national orthopaedic research prizes. I look forward to hopefully maintaining close links with all of them in future.

I would like to thank all my laboratory colleagues including significant mention to Dirk-Jan, Alan, Jack, Ross and Catherine for their support and borrowed expertise as I moved from the

clinical environment to negotiating cell culture and bioprinting! I am also especially grateful to have worked with collaborators including Evita Ning and Professor Faulds, who allowed their research expertise to be combined with our own to develop a stronger overall piece of work.

Finally, and perhaps most importantly, I would like to thank my wife Sadaf and daughters Sara and Isla for their patience, help and understanding as numerous evenings, weekends and annual leave days were sacrificed to complete this thesis. I dedicate this thesis to them for pushing me on to complete this work.

Abstract

The rising prevalence of arthritis and osteochondral defects (OCDs) has led to growing worldwide demand for joint replacement surgery. Meanwhile, the prevalence of antimicrobial resistance (AMR) and prosthetic joint infections (PJIs) in clinical orthopaedics is growing at alarming pace. A novel approach to help tackle AC defects and AMR alike is offered by 3D biofabrication, as a technology with the capacity to deposit cells, bacteria and biomaterials in user-defined patterns to build 3D constructs from the "bottom-up."

Initially composite AlgMA/Col and AlgMA/GelMA bioinks were developed and combined with a novel triple-crosslinking approach (double ionic and UV) following extrusion FRESH (freeform reversible embedding of suspended hydrogels) bioprinting to allow creation of 1mm thick constructs. Constructs maintained shape in culture over 28 days, whilst stability was improved with addition of AlgMA ($p<0.05$). High chondrocyte and MSC viability was achieved following bioprinting (>95%) with accelerated cell growth demonstrated with inclusion of cell spheroids ($p<0.05$). The prolonged stability and cell viability seen outperformed many commercially available bioinks. The composite bioinks were also successfully injected into *in vitro* OCDs and crosslinked in situ, with cell viability and 3D integrity of OCD patches maintained over 14-days. Focussing on AMR, a biocompatible ionically cross-linked bacterial bioink was also developed that allowed precise 3D bioprinting of bacterial structures that developed clinically relevant, mature 3D biofilms during culture. Further analysis of 3D biofilms allowed antimicrobial penetration and the biofilm lifecycle to be observed in 3D. The 3D biofilms were also utilised to allow development of a novel Raman spectroscopy technique, that allowed detection of bacterial biofilms within a joint infection model.

In summary, we hope that our findings show potential for a new approach to the regeneration of AC defects, progress the investigation of 3D biofilm formation and AMR, and finally show a new approach to diagnosis of joint infection.

Contents

List of Figures

List of Tables

List of Abbreviations

2D	Two-Dimensional
3D	Three-Dimensional
A. xylinum	*Acetobacter Xylinium*
ABS	Acrylonitrile Butadiene Styrene
AC	Articular Cartilage
ACI	Autologous Chondrocyte Implantation
ACPCs	Articular Cartilage-Resident Chondroprogenitor Cells
AD-MSCs	Adipose Derived MSCs
ADSCs	Adipose-Derived Stem Cells
AG	Agarose
AL , Alg	Alginate
AlgMA	Alginate Methacrylate
ALP	Alkaline Phosphatase
AMR	Antimicrobial Resistance
ANOVA	Analysis of Variance
AST	Antimicrobial Sensitivity Testing
AuNPs	Gold Nanoparticles
$BaCl_2$	Barium Chloride
BHI	Brain Heart Infusion
BMMSCs	Bone Marrow Derived MSCs
BMPs	Bone Morphogenic Proteins
$CaCl_2$	Calcium Chloride

CAD	Computer-Aided Design
CAM	Computer-Aided Manufacture
CF	Cystic Fibrosis
CFU	Colony Forming Units
CLSM	Confocal Laser-Scanning Microscope
Col	Collagen
CRP	C-Reactive Protein
CS	Chondroitin Sulphate
CSMA	Chondroitin Sulphate-Methacrylate
CT	Computed Tomography
Ct	Chitosan
ddH$_2$O	Deionized Distilled Water
dECM	Decellularized Extracellular Matrix
DI	Deionised
DLS	Dynamic Light Scattering
DMEM	Dulbecco's Modified Eagle Medium
DMSO	Dimethyl Sulphoxide
DNA	Deoxyribonucleic Acid
E.coli	*Escherichia coli*
EB	Embryoid Body
ECM	Extracellular Matrix
EDTA	Ethylenediaminetetraacetic acid
EPS	Extracellular Polymeric Substance
ESCs	Embryonic Stem Cells

ESR	Erythrocyte Sedimentation Rate
F-127	Pluronic F-127
FBS	Foetal Bovine Serum
FBS	Fetal Bovine Serum
FDA	Fluorescein Diacetate
US FDA	US Food and Drug Administration
FDM	Fused Deposition Modelling
FGF	Fibroblast Growth Factor
Fmoc-F2	Fluorenyl-9-Methoxycarbonyl-Diphenylalanine
Fmoc-S	Surfactant-Like Fmoc-Serine
FRESH	Freeform Reversible Embedding of Suspended Hydrogels
GAG	Glycosaminoglycan
GelMA	Gelatin Methacryloyl/Methacrylate
HA	Hydroxyapatite
HAMA	Hyaluronic Acid Methacrylate
HBSS	Hank's Balanced Salt Solution
HCs	Human Chondrocytes
HEPA	High Efficiency Particulate Air
HLA	Hyaluronic Acid
hMSCs	Human MSCs
hBMMSCs	Human Bone Marrow Derived MSCs
HPLC	High-Performance Liquid Chromatography
HUVECs	Human Umbilical Vein Endothelial Cells
ICRS	International Cartilage Repair Society

IGF-1	Insulin-Like Growth Factor-1
IL-1	Interleukin-1
iPSCs	Induced Pluripotent Stem Cells
IR	Infrared
dECM	Decellularized Extracellular Matrix
Irgacure®2959	1-[4-(2-Hydroxyethoxy)Phenyl]-2-Hydroxy-2-Methyl-1-Propan-1-One
LAB	Laser Assisted Bioprinting
LAP	Lithium Phenyl-2,4,6-Trimethylbenzoylphosphinate
LIFT	Laser-Induced Forward Transfer
MA	Methacrylic Anhydride
MACI	Matrix-Induced Autologous Chondrocyte Implantation
MBEC	Minimal Biofilm Eradicating Concentration
MC3T3-E1	Mouse Embryonic Osteoblast Precursor Cells
MEM α	Alpha Minimum Essential Medium
MF	Microfracture
MG	Matrigel™
MIC	Minimum Inhibitory Concentration
MMPs	Matrix Metalloproteinases
MRI	Magnetic Resonance Imaging
MRSA	Methicillin-Resistant *Staphylococcus aureus*
MS	Microsoft
MSCs	Mesenchymal Stem Cells
MSSA	Methicillin-Sensitive *Staphylococcus aureus*

NaOH	Sodium Hydroxide
NC	Numerical Control
NFC	Nanofibrillated Cellulose
NIR	Near-Infrared
NM	Nuclear Medicine
OA	Osteoarthritis
OALT	Osteochondral Allograft Transfer
OAT	Osteochondral Autograft Transfer
OCD	Osteochondral Defect
OCL	Osteochondral Lesion
OD	Optical Density
OTE	Orthopaedic Tissue Engineering
P. aeruginosa	*Pseudomonas aeruginosa*
PBS	Phosphate-Buffered Solution
PCL	Polycaprolactone
PCR	Polymerase Chain Reaction
PCT	Procalcitonin
PDGF	Platelet-Derived Growth Factor
PDMS	Polydimethylsiloxane
PEG	Polyethylene Glycol
PEO	Polyethylene Oxide
PET	Positron Emission Tomography
PGA	Polyglycolic Acid

pH	Potential Of Hydrogen - Negative 10-Base Log (Power) Of The Positive Hydrogen Ion Concentration; Measure Of Acidity
PI	Propidium Iodide
PJI	Prosthetic Joint Infection
PLA	Polylactic Acid
PLGA	Poly(lactic-co-glycolic acid)
PLLA	Poly(L-lactic) Acid
POE	Polyoxyethylene
PVA, PVOH, PVA1	Polyvinyl Alcohol
QS	Quorum Sensing
RCT	Randomised Control Trial
RGD	Arginylglycylaspartic Acid
RT	Room Temperature
SA	Sodium Alginate
SEM	Scanning Electron Microscopy
SERS	Surface Enhanced Raman Spectroscopy
SESORS	Surface Enhanced Spatially Offset Raman Spectroscopy
SESORRS	Surface Enhanced Spatially Offset Resonance Raman Spectroscopy
SLA	Stereolithography
SLS	Selective Laser Sintering
SORS	Spatially Offset Raman Spectroscopy
STL	Standard Tessellation Language
TG	Transglutaminase
TGF-β	Transforming growth factor-β

THR / THA	Total Hip Replacement/ Arthroplasty
TKR / TKA	Total Knee Replacement/ Arthroplasty
TNF-α	Tumour necrosis factor -α
UK	United Kingdom
USB	Universal Serial Bus
UV	Ultraviolet
VBL	Visible Blue Light
VEGF	Vascular Endothelial Growth Factor
WCA	Water Contact Angle
WBC	White Blood Cell Count
WHO	World Health Organisation
XYZ	Three-Dimensional Datum Axes

Publications, presentations, and prizes arising from this thesis

Peer reviewed publications from this thesis

1. 3D Biofabrication for Cartilage and Soft Tissue Engineering.

   Turnbull G, Clarke J, Picard F, Riches P, Zhang W, Li B, Shu W.

   Medical Engineering and Physics, July 2020; 82:13-39.

2. 3D bioactive composite scaffolds for bone tissue engineering.

   Turnbull G, Clarke J, Picard F, Riches P, Jia L, Han F, Li B, Shu W.

   Bioactive Materials. 2017 Dec 1;3(3):278-314.

3. 3D bioprinting of mature bacterial biofilms for antimicrobial resistance drug testing.

   Turnbull G, Ning E, Clarke J, Picard F, Vendrell M, Riches P, Grahame D, Wark A,

   Faulds K, Shu W. Biofabrication. 2019 Sep 13;11(4):045018.

4. Carbon quantum dots derived from lysine and arginine simultaneously scavenge

   bacteria and promote tissue repair. Li P, Han F, Cao W, Zhang G, Li J, Zhou J, Gong

   X, Turnbull G, Shu W, Xia L, Fang B, Xing X, Li B.

   Applied Materials Today. 2020 June; 19: 100601

5. Microfluidic Fabrication of 3D Biomimetic Helical Microfibers for Vessel-on-a-chip

   Jia L, Han F, Yang H, Wang J, Guo M, Turnbull G, Shu W, Clarke J and Li B.

   Advanced Functional Materials. 2019 Jul;8(13):e1900435

6. Microfluidics-Based Fabrication of Cell-Laden Hydrogel Microfibers for Potential

   Applications in Tissue Engineering. Wang G, Jia L, Han F, Wang J, Yu L, Yu Y,

   Turnbull G, Guo M, Shu W, Li B. Molecules. 2019 Apr 25;24(8):1633. doi:

   10.3390/molecules24081633.

Peer reviewed published abstracts

1. 3D bioprinted bacterial biofilms: a novel, 3D method for studying orthopaedic infection.

   G.S. Turnbull, E.Ning, K. Faulds, P. Riches, W. Shu, F. Picard and J.V. Clarke

   Orthopaedic Proceedings. The Bone and Joint Journal, May 2019.

2. 3D biofabrication of constructs for osteochondral regeneration.

   G.S. Turnbull, P. Riches, W. Shu, F. Picard and J.V. Clarke.

   Orthopaedic Proceedings. The Bone and Joint Journal. 2018 100-B:SUPP 18, 1-1.

3. Development of composite bioinks that can be injected or 3D bioprinted to aid osteochondral defect repair.

   G.S. Turnbull, W. Shu, F. Picard and J.V. Clarke.

   Orthopaedic Proceedings. The Bone and Joint Journal. 2022 104-B:SUPP 6.

Presentations

1. 3D biofabrication of constructs for osteochondral regeneration.

   G Turnbull, W Shu, P Riches, F Picard and J Clarke.

   EFORT 2018 Annual Congress, Barcelona.

2. 3D bioprinting the future of orthopaedics.

   G Turnbull, W Shu, J Clarke, F Picard.

   International Society for Biofabrication World Congress 2017, Beijing, China.

3. 3D bioprinted bacterial biofilms: a novel, 3D method for studying orthopaedic infection. G.S. Turnbull, E.Ning, K. Faulds, P. Riches, W. Shu, F. Picard and J.V. Clarke. 2019 Scottish Orthopaedic Meeting, Crieff Hydro.

4. 3D bioprinted bacterial biofilms: a novel, 3D method for studying orthopaedic infection. G.S. Turnbull, E.Ning, K. Faulds, P. Riches, W. Shu, F. Picard and J.V. Clarke. 2019 BOA Annual Meeting, Liverpool.

5. 3D biofabrication of constructs for osteochondral regeneration. G Turnbull, W Shu, P Riches, F Picard and J Clarke. 2018 Scottish Orthopaedic Meeting, Crieff Hydro.

6. Surface Enhanced Spatially Offset Resonance Raman Spectroscopy (SESORRS) and 3D Biofilms: A Novel Method for Identifying Orthopaedic Joint Infection. G Turnbull, JV Clarke, P Riches, W Shu. South East Scotland Orthopaedic Registrars Research Day, May 2021; Glasgow Meeting of Orthopaedic Research (GlaMOR) Meeting 2018.

7. 3D bioprinting for Orthopaedic Tissue Regeneration and Infection Models. G Turnbull, JV Clarke, P Riches, W Shu. Golden Jubilee Hospital Research Symposium, 2018.

8. 3D bioprinting for Orthopaedic Tissue Regeneration and Infection Models. G Turnbull, JV Clarke, P Riches, W Shu. Invited Lecture, MSc Student Curriculum 2018 and 2019.

9. 3D Bioprinting for Orthopaedic Tissue Regeneration and Infection Models. G Turnbull, JV Clarke, P Riches, W Shu. University of Strathclyde Research Symposium, 2018.

10. Development of Composite Bioinks That Can Be Injected or 3D Bioprinted to Aid Osteochondral Defect Repair. G.S. Turnbull, W. Shu, F. Picard and J.V. Clarke. 2022 Scottish Orthopaedic Meeting.

11. Composite Bioinks That Can Be Injected or 3D Bioprinted to Aid Osteochondral Defect Repair. G.S. Turnbull, W. Shu, F. Picard and J.V. Clarke.

2022 British Orthopaedic Annual Congress, Birmingham.

12. Composite Bioinks That Can Be Injected or 3D Bioprinted to Aid Osteochondral Defect Repair. G.S. Turnbull, W. Shu, F. Picard and J.V. Clarke.
2022 International Combined Orthopaedic Research Societies (ICORS) World Congress, Edinburgh and 2022 BOA Annual Meeting, Birmingham.

Prizes

1. Research Oral Presentation Prize (1st Place), Scottish Committee for Orthopaedics and Trauma Meeting 2022.

2. Oral Presentation Prize (1st Place), South-East Scotland Orthopaedic Research Day - Out of Programme Research 2021.

3. Research Oral Presentation Prize (1st Place), Scottish Committee for Orthopaedics and Trauma Meeting 2019.

4. Research Oral Presentation Prize (2nd Place), Glasgow Meeting of Orthopaedic Research (GlaMOR) Meeting 2019.

5. Research Oral Presentation Prize (3rd Place), Scottish Committee for Orthopaedics and Trauma Meeting 2018.

1   Introduction

1.1 Background and motivation

By the age of 65, one in four people is symptomatic from osteoarthritis (OA) and 80% have radiological evidence of OA [1, 2]. Central to the pathogenesis of OA is the irreversible damage and degeneration of articular cartilage (AC), a highly specialised connective tissue found within articulating joints. It principally acts to facilitate the smooth movement of opposing joint surfaces, providing a lubricated surface with a low frictional coefficient. Despite being only 2 to 4mm thick, viscoelastic properties and a deceptively intricate structure also allow AC to shield underlying bone from some of the mechanical stresses generated during locomotion [3, 4]. Structurally, AC can be divided into four zones extending from superficial to deep zones based on the orientation of type II collagen fibres and proteoglycan content. Throughout the structural zones, AC is devoid of blood vessels, nerves or lymphatics and has limited cellular content resulting in a poor intrinsic capacity for healing and repair [5]. Despite possessing a highly developed structure, AC is frequently irreversibly damaged by acute trauma, chronic repetitive overloading and degenerative processes, with 5-10% of people over 40 having high grade AC lesions [6, 7]. Symptoms of pain, instability and mechanical locking can develop, leading to arthroscopic surgery being performed in over 150 000 patients annually in the UK [108].

Several techniques can be deployed to treat cartilage defects surgically. Unfortunately, current arthroscopic repair techniques (Fig. 2.3) have critical limitations including a tendency to result in mechanically inferior fibrocartilage formation, ongoing pain and morbidity, and an inability to treat globalised AC destruction [115]. Over 180 000 patients therefore require total joint replacement surgery in the UK annually, a major operation which can result in incomplete satisfaction and residual symptoms, particularly in younger patients [116-119]. A rising number

of patients also face the prospect of requiring revision joint replacement, a technically more complex and costly procedure with generally inferior clinical results [120-123].

A significant limitation of joint replacement surgery for patients is the risk of developing periprosthetic joint infection (PJI). The inert bearing surfaces of artificial joint replacements lack an inherent blood supply and compared to native tissue can therefore develop infection after exposure to a relatively low bacterial inoculum [8, 9]. PJI represents a leading cause of joint replacement failure, accounting for over 15% of American revision total knee replacements (TKRs) and total hip replacements (THRs) and a similar proportion of revisions in the UK and Australia [10, 11]. Although the incidence of PJI following THR and TKR remains steady at 1–2%, the increasing numbers of hip and knee arthroplasties being performed worldwide means that the number of revisions for infection is increasing [9]. Central to the pathogenies of PJI is the formation by bacteria of a protective membrane termed a "biofilm." Biofilms can be defined as structured three-dimensional (3D) communities of bacterial cells enclosed in a self-produced polymeric matrix, attached to a solid surface such as a joint replacement [12] . Within the protective environment of a biofilm, bacteria increase their resistance to host immune defences and tolerance of antibiotics up to 1000%, whilst their ability to exchange genetic information is also greatly increased [13, 14]. Eradication of PJI once biofilm formation has occurred on a joint implant is therefore hugely challenging, and in patients often leads to chronic infection, surgical removal of implants and prolonged antibiotic therapy [15].

Cartilage defects, osteoarthritis and periprosthetic joint infection continue to affect a significant number of patients within clinical orthopaedics. In patients unfortunate enough to develop osteoarthritis and then PJI following joint replacement treatment, the burden of experiencing degenerative joint pathology is compounded by serious infection, leading to significant

morbidity and even risk of mortality [9]. There is therefore significant clinical demand for novel and alternative treatment strategies to regenerate damaged joint surfaces and aid the treatment of PJI.

As a developing technology, 3D biofabrication offers a novel approach to help ease the treatment burden of cartilage defects and to help investigate the role of bacterial biofilms in PJI. Biofabrication involves combining biological constituents such as cells, growth factors and biomaterials with precise biomanufacturing techniques such as 3D cell printing, known as "bioprinting" [16, 17]. Complex tissue constructs can therefore be created, or biofabricated, "from the bottom up." Through the incorporation of clinical imaging and autologous cells into the biofabrication process, regeneration of cartilage and other bodily tissues could even feasibly be performed in a patient specific manner, adding a significant and novel option to the armamentarium of reconstructive orthopaedic surgeons. The potential to biofabricate 3D bacterial constructs could also have great clinical significance at a time when antimicrobial resistance (AMR) is rising to dangerously high levels worldwide. According to the World Health Organization (WHO), urgent action is required to avoid a "post-antibiotic era", in which common infections and minor injuries can once again kill [18]. Future strategies to overcome AMR are likely to target the bacterial process of biofilm formation, a key survival mechanism against antibiotics. Whilst traditional biofilm laboratory models are often based on 2D cultures, biofabricated 3D biofilms potentially mirror *in vivo* bacterial growth and behaviour environment more closely, given that it normally occurs in a 3D biological environment [19-21].

1.2 **Aims**

The overall aim of this thesis is to utilise a 3D biofabrication approach to study two pressing and interrelated areas within clinical orthopaedics; the regeneration and reconstruction of osteochondral tissue, and the study and treatment of bacterial biofilms that cause infection of joint replacements and native joint destruction. To develop a successful methodology, different biofabrication techniques, biomaterials and cell culture techniques will be utilised. Biofabricated constructs must support cell growth after production, maintain structure during culture conditions and allow for further investigation to be performed. Accordingly, the main objectives of this thesis can be summarised as:

- To biofabricate 3D constructs capable of supporting osteochondral tissue regeneration.
- To biofabricate clinically relevant 3D bacterial biofilms that facilitate further investigation of biofilm growth, antimicrobial treatment, and detection of joint infection.

1.3 **Structure of Thesis**

- Chapter 1 presents the background of the thesis and details the main aims and objectives of the research.
- Chapter 2 provides a literature review beginning with the clinical impact of cartilage defects and currently available treatment options. 3D biofabrication is then introduced with reference to how it has already been applied to regenerate orthopaedic tissues elsewhere in the literature. An overview of the impact of infection within orthopaedics and currently available methods of studying and detecting clinical biofilms is then provided.

- Chapter 3 describes the methodology and experimental details for the projects in the following chapters. This will include aspects of design, calibration, and initial testing phases.

- Chapter 4 describes initial development of 3D biofabrication approaches for osteochondral regeneration.

- Chapter 5 describes development of composite bioinks for osteochondral regeneration.

- Chapter 6 describes the first example of successful biofabrication of mature, 3D bacterial biofilms together with an analysis of biofilm response to antimicrobial treatment.

- Chapter 7 describes the use of 3D biofilms to test novel Raman technology aimed at detecting bacterial biofilm infections within a joint infection model.

- Chapter 8 concludes this thesis and provides recommendations for future work.

- Chapter 9 lists all references for previous chapters.

2   Cartilage Defects, Joint Infection, Currently Available Treatment Options in Clinical Orthopaedics and the Future Role for Biofabrication

2.1 The Clinical Burden of Articular Cartilage Lesions

Despite possessing a highly developed structure, articular cartilage (AC) is commonly damaged by aetiologies including acute trauma, chronic repetitive overloading, degenerative or osteoarthritic processes and developmental issues such as osteochondritis dissecans [1]. The limited cellular content within AC and lack of inherent blood vessels, nerves or lymphatics results in a poor intrinsic capacity for healing and repair [2]. Once articular cartilage sustains damage full recovery of structure and function is therefore unlikely, and significant alteration of native biomechanics can occur [3]. As more and more lesions are accumulated throughout life, patients become increasingly predisposed towards development of symptomatic osteoarthritis [4]. Although the true prevalence of AC lesions is difficult to estimate, many of the patients who suffer from cartilage defects are relatively young with 5-10% of people over 40 thought to have high grade AC lesions. Furthermore, nearly 70% of patients undergoing knee arthroscopy have been found to have articular defects [5]. Symptoms of pain, instability and mechanical locking can develop in patients, with initial treatment usually involving conservative measures such as analgesia, physiotherapy and even intra-articular injections [3].

When conservative treatment fails to ameliorate symptoms, a range of surgical techniques can be deployed to treat cartilage defects. Arthroscopic (keyhole) surgery is currently performed on over 150 000 patients annually in the UK on major joints including the shoulders, knees and ankles [6]. However, arthroscopic repair techniques have limitations and can only treat discrete cartilage lesions. As a result, over 180 000 patients require total joint replacement surgery in

the UK annually, a major operation that can result in incomplete satisfaction and residual symptoms, particularly in younger patients [7-10]. As patients outlive the life span of their first joint replacement, a rising number also face the prospect of requiring revision joint replacement, a technically more complex and costly procedure with generally inferior clinical results [11-16]. Extensive efforts have therefore been made to search for novel and alternative strategies to aid and promote cartilage repair. In the following sections, the structure and function of cartilage will be introduced alongside current treatment options for cartilage lesions. Recent use of biofabrication strategies including 3D bioprinting to promote cartilage repair will subsequently be covered.

2.1.1 Cartilage Function, Composition and Structure

2.1.1.1 Cartilage Function

AC is a highly specialised connective tissue found within articulating joints. It principally acts to facilitate the smooth movement of opposing joint surfaces, providing a lubricated surface that allows the transmission of loads with a low frictional coefficient [2]. Despite common perception otherwise, the thin articular cartilage surface has limited capacity to act as a "shock absorber" [17]. Instead, it provides a large friction-reducing, weight-bearing surface area within joints, allowing articulating surfaces to move relative to one another with minimal wear occurring. AC is typically 2 to 4mm thick and unlike most bodily tissues is devoid of blood vessels, nerves or lymphatics. When combined with a low cellular content, these features result in cartilage having a very poor regenerative capacity. Around 60-80% of the total weight of articular cartilage is fluid, with the remaining content made up from chondrocytes and solid extra-cellular matrix (ECM).

2.1.1.2 **Composition**

Collagens and proteoglycans account for the bulk of cartilage dry weight, with a small number of other molecules also present including lipids, phospholipids, glycoproteins and non-collagenous proteins. However, the most abundant component of articular cartilage is water, contributing up to 80% of net weight. Movement of water through cartilage helps to deliver nutrients to chondrocytes, with the relative water content decreasing from around 80% at the superficial zone to 65% in the deep zone (Fig. 2.1). Water also contributes to the ability of cartilage to withstand mechanical loads; as the ECM provides resistance to flow of water, mechanical loading of water-laden ECM results in the generation of hydrostatic pressure, which dissipates when mechanical loads are released [18].

Collagen is the most abundant macromolecule with the ECM, providing tensile strength and a structural framework accounting for 15 to 20% % of cartilage net weight. Of the collagen content, 90% to 95% is composed of Type II collagen fibrils and fibres which are intertwined with proteoglycan aggregates. A minor faction of collagen types I, IV, V, VI, IX, and XI are also present within the ECM, helping to form and stabilize the type II collagen fibril network. The triple helix structure of collagen also helps to stabilise the matrix and adds to the shear and tensile properties of cartilage [2].

Proteoglycans are heavily glycosylated proteins and represent the second-largest group of macromolecules within the ECM, accounting for 10 to 15% of cartilage net weight. Synthesised by chondrocytes, proteoglycans consist of a core protein and covalently attached glycosaminoglycan (GAG) chains, including chondroitin sulphate and keratin sulphate. Proteoglycans are highly hydrophilic and negatively charged, with each GAG sugar subunit having one or two negative charges that repel one another, leading the molecule to extend

outwards towards positively charged collagen molecules to form a matrix. The negative charges also attract cations, including sodium ions, which in turn draw copious water into the matrix. The most abundant proteoglycan is aggrecan, which consists of more than 100 keratin sulphate and chondroitin sulphate chains. Aggrecan interacts with hyaluronic acid via link proteins to form large proteoglycan aggregates which occupy the interfibrillar space within the cartilage ECM. The osmotic potential provided by these aggregates and other proteoglycans help with retention of water within the ECM, thereby providing resistance to compressive loads [19]. Further non-aggregating proteoglycans are also present within the ECM including decorin, biglycan, and fibromodulin. These proteoglycans have differing glycosaminoglycan content, with biglycan thought to interact with collage VI, whilst decorin and fibromodulin interact with collagen II fibrils and contribute to fibrillogenesis and interfibril interactions [20, 21].

Chondrocytes are the only cell type present within articular cartilage and account for around 2% of the total volume of articular cartilage [22]. Chondrocytes originate from mesenchymal stem cells (MSCs) and play an active role in the development, maintenance, and repair of their surrounding ECM. Whilst the material properties of articular cartilage depend on its ECM, the existence and maintenance of the ECM depends on chondrocytes. The ECM microenvironment essentially traps the chondrocyte within its own matrix and thereby prevents any cell migration to adjacent areas. As a result, chondrocytes rarely form cell-to-cell contacts for direct signal transduction and communication between cells. Chondrocytes also vary in shape and number depending on anatomical zones of articular cartilage. In the absence of a neurovascular supply, chondrocytes respond to a variety of stimuli, including mechanical loads, piezoelectric forces and hydrostatic pressures. Unfortunately, the limited potential of chondrocytes to self-replicate contributes to the restricted intrinsic healing capacity of cartilage [22, 23].

2.1.1.3 **Articular Cartilage Structure**

Articular cartilage has a deceptively intricate structure and can be divided into four zones based on the orientation of type II collagen fibres and proteoglycan content (Fig. 2.1).

The superficial zone makes up 10% to 20% of articular cartilage thickness and is responsible for most of the tensile properties of cartilage. Providing protection to deeper layers, the collagen fibres of this zone are tightly packed and orientated parallel to the joint surface. A relatively high number of flattened chondrocytes are also present, with sparse proteoglycan content found. The superficial layer is the only zone where articular cartilage progenitor cells have been found [24].

The intermediate or transitional zone represents 40% to 60% of cartilage volume and provides resistance to compressive forces. Thick collagen fibrils are orientated in an oblique or random fashion, with spherical chondrocytes present at low density alongside abundant proteoglycans [2].

The deep zone provides the greatest resistance to compressive forces, with large diameter collagen fibrils arranged perpendicular to the articular surface. This layer also contains the highest proteoglycan content, with round chondrocytes typically orientated in a columnar distribution, perpendicular to the joint surface [22].

Below the deep layer a tidemark interface marks the transition between noncalcified articular cartilage and deeper calcified cartilage. The deep calcified layer below the tidemark plays an integral role in securing cartilage to bone, by anchoring collagen fibrils to subchondral bone. Within this zone few inert and hypertrophic chondrocytes are present, embedded within a calcified ECM. The tidemark is found only in joints and is a remnant of the cartilage anlage

which participated in endochondral ossification during longitudinal growth in childhood. It is the only zone having collagen type X, which helps cartilage mineralization and provides structure integrity [25].
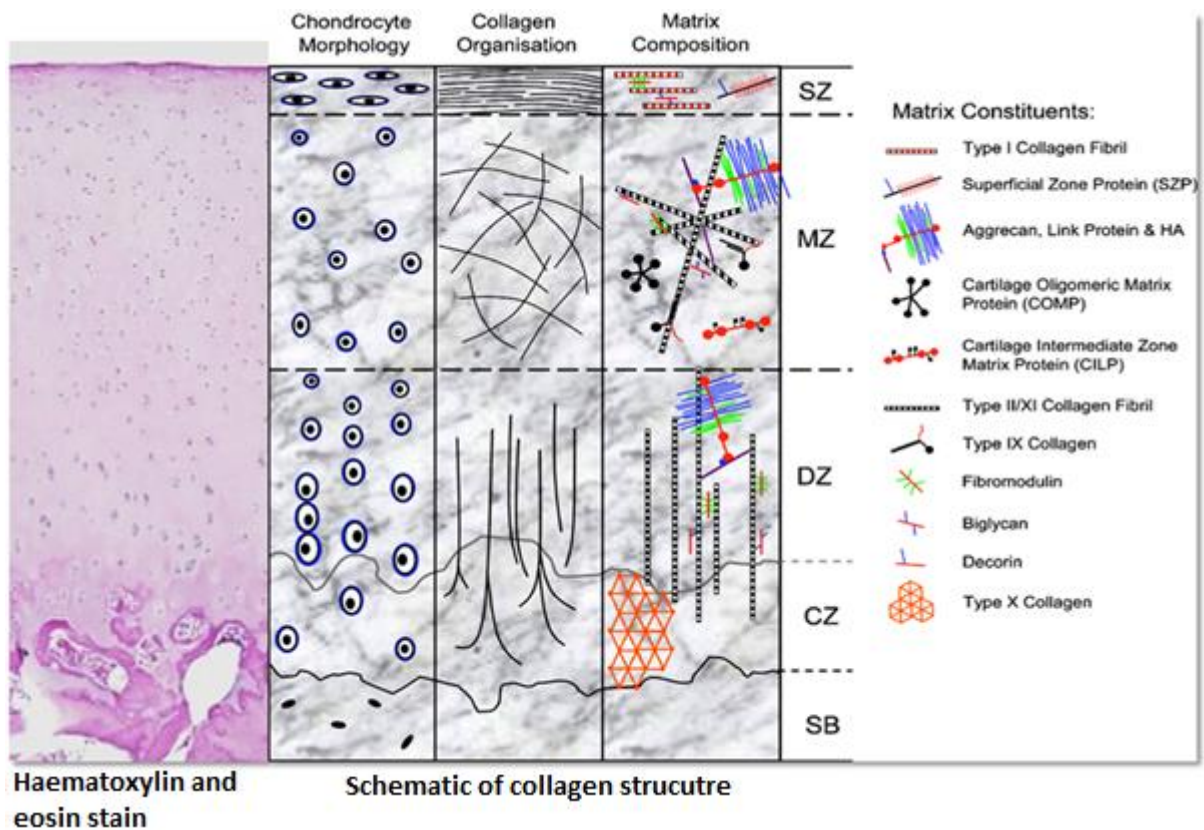
Figure 2.1   Hyaline cartilage haematoxylin and eosin stain, morphology and structure. SZ, superficial zone; MZ, middle zone; DZ, deep zone; CZ, calcified zone; SB, subchondral bone. Adapted from Di Bella *et al.* [26].

2.2 **Current Management of Symptomatic Articular Cartilage Lesions**

2.2.1   **Initial Evaluation and Treatment Planning**

Initial management of cartilage lesions begins with a clinical history and examination. The knee joint is classically split into medial tibiofemoral, lateral tibiofemoral, and anterior patellofemoral compartments. Symptomatic cartilage lesions can initially present as localised

knee pain affecting a single compartment, or as more globalised pain affecting the whole knee. The location of pathology can sometimes be correlated with symptoms. For instance, patellofemoral lesions often give rise to anterior knee pain that is exacerbated by descending stairs, arising from a chair, or squatting. Tibiofemoral lesions are often exacerbated by weight bearing and give rise to pain located either medial or lateral to the midline, along the tibiofemoral joint line. Recurrent mechanical symptoms such as catching, swelling or locking may be suggestive of meniscal tears or focal chondral defects.

Initial imaging of the affected joint may be performed through standard weight-bearing radiographs. Although radiographs do not directly demonstrate cartilage damage, evidence of joint space narrowing, osteophytes and joint malalignment may be seen. Such features are important to detect as concurrent osteoarthritis is considered a contraindication for performing cartilage restoration techniques. Magnetic resonance imaging (MRI) is often requested, allowing extremely detailed imaging of articular joints and their respective soft tissues to be performed. As the current gold standard investigation, MRI has been shown to be as reliable as arthroscopy for investigating most osteochondral lesions [27, 28]. For example, in the knee pathology of the cruciate ligaments and menisci can be identified at the same time as investigation for osteochondral lesions (OCLs); if an anterior cruciate ligament, collateral ligament or meniscal injury is detected, all of which can accompany an OCL, more significant surgery may be required [29]. OCLs are usually graded in terms of their severity and size to allow a surgical plan to be developed. The International Cartilage Repair Society (ICRS) grading system is commonly used to describe OCLs and is based on two main factors: the depth of the OCL and the degree to which subchondral bone is involved [30].

Grade	Appearance	Extent of Injury	Morphology
0	Normal		
1	Nearly normal	Superficial lesion with softening, indentation or fissuring.	
2	Abnormal	Lesion extending <50% of cartilage depth	
3	Severely abnormal	Lesion extending > 50% of cartilage depth but not though to subchondral bone	
4	Full thickness injury	Full thickness defect with subchondral involvement	

Figure 2.2 The International Cartilage Repair Society (ICRS) grading system is commonly used to describe cartilage lesions and reflects the depth of cartilage damage down to subchondral bone [30].

Definitive surgical management is planned after consideration of patient factors (such as patient level of mobility, desire to have surgery and presence of comorbidities) and surgical factors (such as the number and severity of OCLs detected, concurrent lesions needing treatment and locally available treatment options). Reconstructive surgery is usually performed via an arthroscopic or "key-hole approach." In some cases, a small incision or arthrotomy may be performed to aid repair of larger lesions or to facilitate harvest of autograft tissue. Arthroscopy may even be performed as an initial procedure to treat major problems such as cruciate ligament damage before later cartilage reconstruction is attempted. A range of reconstructive techniques that are available to surgeons will now be reviewed.

2.2.2 Articular Cartilage Repair Techniques and Joint Reconstruction

2.2.2.1 Microfracture

Microfracture (MF) is a frequently performed technique used to stimulate the repair of articular cartilage lesions. MF involves making multiple holes, or "microfractures," in the subchondral bone underlying full-thickness chondral defects (Fig. 2.3 A). The holes are made as close together as necessary, but not so close that one breaks into another, thus damaging the subchondral plate between them. The released bone marrow that oozes from the holes forms a "super clot" that engulfs the cartilage defect, providing an enriched environment for tissue regeneration [31]. Whilst this technique supports cartilage regeneration, it most often results in the production of biomechanically inferior fibrocartilage which typically deteriorates within 24 months as it is exposed to mechanical joint forces [32, 33]. Treatment of lesions in the patellofemoral joint and large defects with microfracture is particularly associated with risk of cartilage deterioration; more than 5 years after surgery, treatment failure can be expected in many patients regardless of the size of the lesion [34]. Nevertheless, many clinicians still consider microfracture to be the gold standard for cartilage repair, depending on the size, depth and location of the lesion [31].

2.2.2.2 Osteochondral Autograft/Allograft Transfer (Mosaicplasty)

Osteochondral autograft transfer (OAT) or mosaicplasty is performed by transferring one or more cylindrical grafts of hyaline cartilage and underlying subchondral bone from a low weight-bearing area of the knee towards a defective site, usually the femoral condyle (Fig. 2.3 B). Grafts are harvested arthroscopically or mini-arthrotomy most often from the medial or lateral trochlea, and then press-fit, flush with the cartilage, into recipient sockets of the same

depth drilled into areas of defective cartilage. OAT therefore has the benefit of being a one-stage, low-cost procedure. However, this can be a difficult procedure with limitations including management of joint congruency, problems with osteointegration and difficulty in treating large lesions [35, 36]. Usually, the topography of the donor site is different from the recipient site, and it is therefore difficult to fully recreate natural biomechanics. Mosaicplasty is generally restricted to young patients (under 50), with symptomatic chondral or osteochondral defects of less than 3 cm in the weight-bearing part of the femoral condyle [37].Good results have been demonstrated up to 9 years following OAT surgery, although a deterioration in results was observed from 12 months postoperatively onwards in one study [38]. Furthermore, randomised control trail (RCT) evidence has shown inferior results when OAT was compared to patients treated with ACI [39].

Osteochondral allograft transfer (OALT) uses the same basic technique as OAT, substituting autografts for grafts taken from cadaveric donors. This allows defects to be repaired with like-for-like tissue taken from corresponding areas of articular surface in cadaveric donors; potentially this allows closer replication of natural biomechanics and topography. Larger defects can also be repaired due to the greater potential to harvest donor tissue from cadaveric sources. However, allograft usage does have limitations including risk of viral disease transmission, tissue rejection and limited availability of suitable tissue. Studies of OALT have reported good outcomes in up to 80% of patients [40].

2.2.2.3 **Autologous Chondrocyte Implantation (ACI) and Matrix-induced Autologous Chondrocyte Implantation (MACI)**

Due to the shortcomings of microfracture and mosaicplasty in treating larger defects, other techniques have been developed including ACI and MACI. ACI involves two procedures; in

the first, a cartilage biopsy is harvested from a low-weight-bearing region of the joint to provide a chondrocyte population that is then expanded *in vitro*, yielding up to 50 million chondrocytes [41]. During a second procedure via an open incision, the cartilage defect is debrided down to subchondral bone. The cells expanded *in vitro* are then injected into the defect site beneath a periosteal flap (Fig. 2.3 C). ACI has the benefit of using a patient's own cells, as well as minimising the size of initial biopsy taken, compared to techniques such as mosaicplasty (Fig. 4B). Drawbacks to ACI include the need for two operations, cost and the prolonged recovery time required to ensure neotissue regeneration [41-43]. Positive clinical and functional outcomes of ACI have been confirmed by clinical trials with long-term case series with >10 years demonstrating ACI to be an effective and durable treatment for large (>4 cm^2) knee cartilage lesions [42-45]. However, further work is required to achieve faster neotissue maturation and integration with native tissue [17]. Survival analysis suggests that long-term results are better with ACI than with MF, although research is needed into long-term results of new forms of ACI [46].

Matrix-induced autologous chondrocyte implantation (MACI) is an advancement of the ACI technique and begins with arthroscopic cartilage biopsy, allowing isolation of autologous chondrocytes. Expanded populations of autologous chondrocytes are then incubated on absorbable porcine-derived type I and III collagen matrices before implantation; these matrices help to direct and stimulate autologous chondrocyte growth before implantation, whilst maintaining cell phenotype and viability. The resulting chondrocyte laden membrane can be glued or sutured onto a cartilage defect in a secondary procedure (Fig. 2.3 C). MACI circumvents the need for the watertight sutures required with ACI and reduces the chances of chondrocyte leakage inside of the joint post-implantation. Overall, MACI achieves similar, if not superior, functional outcomes to either ACI or microfracture in follow-up studies ≥2 years

[47]. Recent RCT evidence reported that symptomatic cartilage knee defects 3 cm^2 or larger treated with MACI were clinically and statistically significantly improved at 5 years compared with microfracture treatment [48].

Hyaluronic-acid-based scaffolds have also been used in place of the collagen matrices used in MACI. Some promising results have been demonstrated, with hyaline cartilage shown to develop following scaffold implantation and improved clinical outcome scores reported when compared to treatment with microfracture [49, 50].

2.2.2.4 **Joint Replacement**

As patients accumulate more and more OCLs throughout life, they become increasingly predisposed to developing OA or degenerative joint disease. Even a single OCL can lead to degradative changes in surrounding cartilage and altered joint biomechanics [4, 51]. By the age of 65, one in four people is symptomatic from OA and 80% have some radiological evidence of OA. Medical management of arthritis is directed at relieving symptoms, and common treatment options include analgesics and anti-inflammatory medications [52, 53]. When patients are unable to obtain adequate pain relief and functional improvement from conservative treatment, joint replacement or arthroplasty surgery is considered (Fig. 2.3 D).

Total joint replacement involves the surgical replacement of both articulating surfaces of a joint. In 1961 Sir John Charnley first described his pioneering total hip arthroplasty (THA), articulating a metal ball with a polyethylene (plastic) socket [54]. A short time later after Charnley's THA the first total knee arthroplasty (TKA) was performed in 1968 [55]. Today arthroplasty surgery is increasingly common with over 75 000 TKAs and over 80 000 THAs performed each year in the UK alone [10]. Ceramic, plastic and metallic components can be

found in modern joint replacements, whilst the range of joints that can be replaced has expanded to include shoulders, elbows, ankles and even the small joints of the mandible, hands and feet [56, 57]. With high levels of long-term implant survivorship (time from implant insertion to surgical removal and replacement) demonstrated in primary THA and TKA, the indications for both operations have expanded to include younger, more active and indeed older patients [9, 15, 16, 58, 59]. Over the past decade the incidence of total joint replacement has increased not only in older (> 65 years) but also in younger patients (< 65 years) [10, 60]. Recent projections suggest that more than 50% of both procedures will soon be performed on patients under 65. Increasing demand is expected to continue, with exponential growth of up to 637% predicted for primary procedures by 2030 [61]. However, due to complications including infection, peri-prosthetic fracture, implant loosening and mechanical wear, total joint replacements can fail and have a finite life expectancy [62, 63]. Large increases in the number of revision THA and TKA procedures are therefore expected in the future as younger patients outlive the natural longevity of their original arthroplasty[11-14]. Unfortunately, revision arthroplasty is a technically more complex and costly procedure, with generally inferior clinical results [13, 62, 64-67].
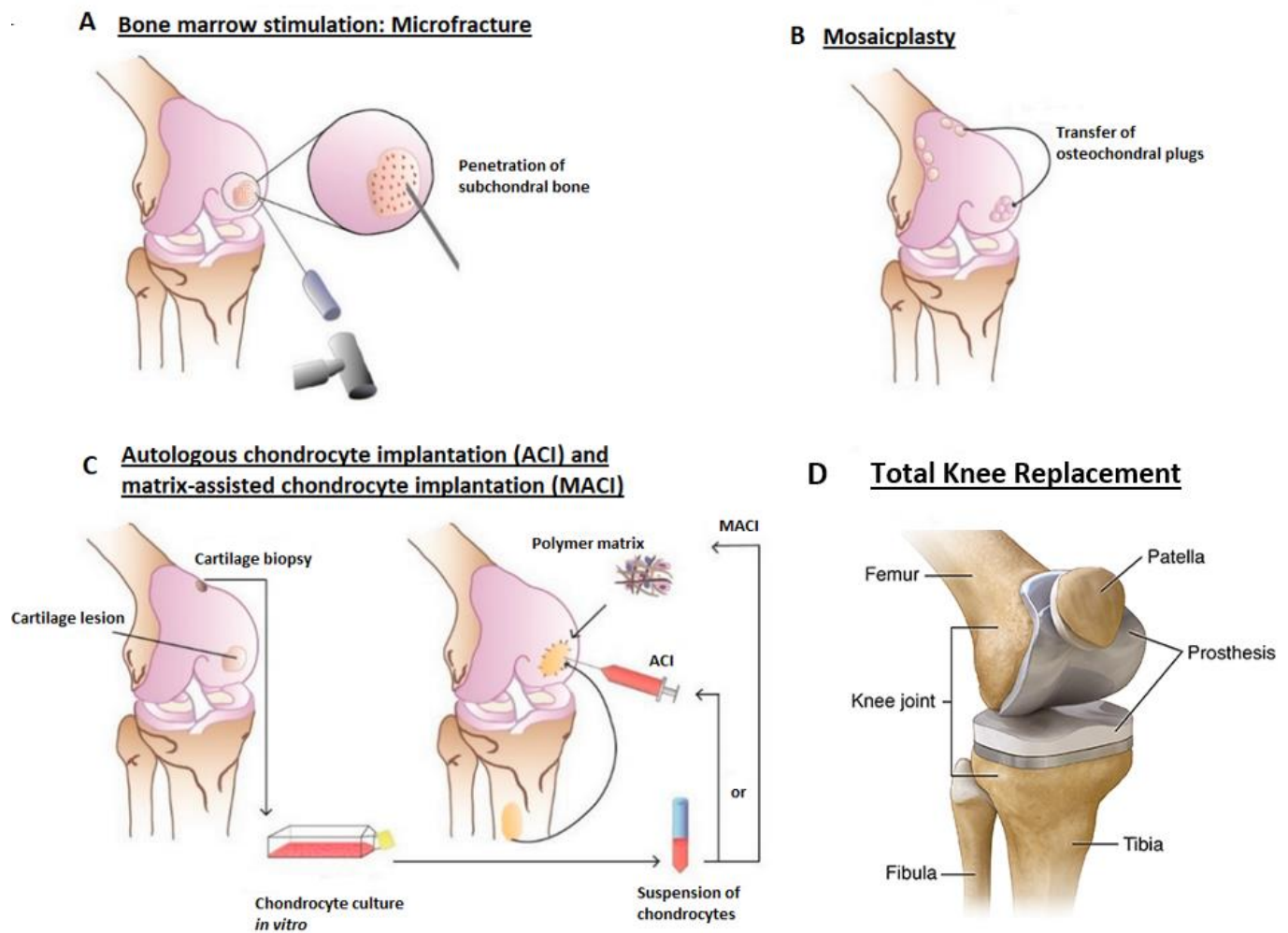
Figure 2.3 Schematic representation of current regenerative cartilage repair and reconstruction techniques: **(A)** Microfracture (MF) involves making multiple holes, or "microfractures," in the subchondral bone underlying full-thickness chondral defects. Released bone marrow forms a "super clot" that provides an enriched environment for tissue regeneration [31]. **(B)** Mosaicplasty is performed by transferring one or more cylindrical osteochondral autografts from a low weight-bearing area of the knee towards a defective site, usually the femoral condyle. **(C)** Autologous chondrocyte implantation involves a periosteal flap or collagen membrane being sewn over the defect, under which a suspension of autologous, cultured chondrocytes is injected (ACI). Matrix-assisted chondrocyte implantation (MACI) advances

ACI by incorporating chondrocyte cells into a type-I/III collagen scaffold during the culturing process. **(D)** Total knee replacement or arthroplasty involves replacing the worn native joint surface with prosthetic implants typically composed of metallic, plastic, or ceramic materials [68].

2.2.2.5 **Limitations of Current Treatment Options**

Current arthroscopic repair techniques (Fig 2.3) suffer from critical limitations including a tendency to result in mechanically inferior fibrocartilage formation, difficulty in treating patients with multiple or large OCLs, and an inability to treat globalised articular cartilage destruction or OA [69]. Essentially, arthroscopic techniques allow patients with OCLs to be patched up in a similar fashion to filling in a pothole on a road surface. However, the topology and smoothness of the natural joint surface is often never truly restored. Ultimately the underlying osteoarthritic pathology continues to drive the occurrence of more OCLs, as the patched-up joint surface continues to be exposed to ongoing stress and strain, and a full joint resurfacing is required in time. As a result, over 180 000 patients require total joint replacement surgery in the UK annually. Although total hip and knee replacement rank amongst the most successful and cost-effective interventions in medicine, they are nevertheless major procedures with risk of serious complications including infection, haemorrhage, pulmonary embolus and even very rarely death [57, 70]. Particularly in the case of younger patients, incomplete satisfaction and residual symptoms can develop postoperatively, making ongoing management difficult [7-10]. A rising number of patients also face the prospect of requiring revision joint replacement, a technically more complex and costly procedure, with generally inferior clinical results [13, 62, 64-67].

2.3 **The Biofabrication Approach**

Due to the prevalence of cartilage lesions and arthritis worldwide, and limitations of current treatment options, significant efforts have been made to develop novel strategies to aid cartilage repair. As a developing technology, 3D biofabrication offers a novel approach to potentially help ease the treatment burden of cartilage defects. Biofabrication combines raw materials such as living cells, molecules, extracellular matrices, and biomaterials with a range of manufacturing techniques, such as bioprinting, 3D printing and 3D cell culture, allowing the production of complex living and non-living biological products from "the bottom up" [71-74]. Within the following text an overview will be provided of the properties of an "ideal" biofabricated scaffold, followed by a review of biofabrication techniques including bioprinting, bioinks, cell sources and the tissue biofabrication process in general and a review of their recent use in cartilage repair will subsequently be provided.

2.3.1 **The Ideal Biofabricated Scaffold**

Biofabrication strategies can be divided into scaffold-based and scaffold-free approaches. Scaffolds can be defined as 3D porous structures that support cell adhesion and growth, guiding tissue regeneration [75]. A variety of materials and manufacturing methods have been used to produce scaffolds for tissue engineering. However, there are some general properties that all scaffolds seek to obtain, regardless of individual scaffold composition, target cell type or scaffold manufacturing method used.

In general terms, the ideal 3D scaffold is composed of a biocompatible, biodegradable material with similar mechanical properties to the tissue which it is to be implanted in. Scaffolds by

design are not intended to be permanent implants and will ideally facilitate host cells to deposit ECM and replace the scaffold structure over time. The 3D architecture of the scaffold should be highly porous with an interconnected structure to allow cell and nutrient migration. The scaffold surface should also be optimised to facilitate cell attachment, proliferation, and differentiation. Form a surgical point of view, it is also desirable for the scaffold material to be easily manipulated into different shapes and sizes to allow in-situ treatment of individual tissue defects such as cartilage lesions [76-79].

Scaffolds and their breakdown products must above all be biocompatible. This requires scaffold materials to be nontoxic to cells, easily eliminated from the body and to elicit negligible immune response through their presence [80-82]. Controlled biodegradability is also an essential characteristic for a scaffold to achieve; if a scaffold degrades too quickly, mechanical failure could occur. This is particularly relevant in orthopaedics, as an implanted scaffold is likely to undergo a degree of load bearing even if the patient is instructed to rest a treated limb, and scaffold fracture and failure could occur if it is unable to provide mechanical support whilst new tissue is forming. Similarly, if a scaffold does not degrade sufficiently quickly an inflammatory response could be triggered towards the foreign material of the scaffold, impairing tissue regeneration [83].

The microarchitecture of scaffolds is also centrally important in encouraging cell viability and fostering tissue ingrowth. An interconnected pore structure, in the absence of an engineered blood supply, allows inwards diffusion of oxygen and nutrients and outwards diffusion of waste products from the scaffold. Porosity also supports cell migration into the scaffold and improves available surface area for cell-scaffold binding and interaction with surrounding tissues [84-86]. Individual pore size within the scaffold is also an important consideration. It has previously

been shown that scaffold pore density and size significantly impact upon cellular growth and attachment [87, 88]. As pore size decreases, the surface area of the scaffold increases. This increases the availability of scaffold ligands for cells to bind to and interact with. However, if pore sizes become too small, cells may struggle to migrate into the scaffold structure. Scaffolds must therefore be precisely engineered with parameters favourable to the cells and tissue that they will be exposed to. For example, it has been shown that scaffolds implanted *in vivo* with pore sizes close to 300 µm promote osteogenesis due to higher permeability and potential for vascularization, whereas smaller pore sizes closer to 100 µm are more favourable for chondrogenesis [89-91]. Increased scaffold macroporosity has also been shown to improve angiogenesis *in vivo* [92], whilst a degree of microporosity (pores with diameters lower than 10 µm) can improve cell-scaffold interactions, resulting in osteogenic effects [93-95]. Scaffolds therefore need to contain a mixture of macropores allowing cell and osteon ingrowth *in vivo*, and micropores to encourage cell-scaffold ligand interactions [96].

In addition to pore size and overall porosity, mechanoregulatory effects are thought to be key in influencing cartilage tissue growth and cellular differentiation *in vivo*. If a scaffold is unable to replicate the mechanical forces transferred to cells in physiological conditions, cells may lack sufficient stimulation and differentiate towards an undesirable morphology [97-99]. Selecting scaffold materials with similar stiffness to native tissues would therefore seem advantageous [100, 101]. However, scaffold mechanical stiffness and porosity are directly conflicting physical properties, with mechanical strength inversely related to increasing scaffold porosity. In terms of load bearing, important scaffold mechanical properties include Young's modulus (also known as elastic modulus, a measure of the stiffness of a solid material), compressive strength (capacity of a scaffold to withstand loads tending to reduce size) and fatigue strength

(the highest stress that a material can withstand for a given number of cycles without breaking) [80, 102, 103].

Table 2.1 Summary of Desirable Scaffold Properties.

Scaffold Characteristics	Desirable Features
Biocompatibility	• Non-toxic breakdown products. • Non-inflammatory scaffold components, avoiding immune rejection.
Biodegradability	• Controlled scaffold degradation which can complement tissue ingrowth whilst maintaining sufficient support. • Degradable by host enzymatic or biological processes. • Allows invading host cells to produce their own extracellular matrix.
Bioactivity	• Scaffold materials that can interact with and bind to host tissue. • Inclusion of biological cues and growth factors to stimulate cell ingrowth, attachment and differentiation.
Scaffold Architecture	• Interconnected pore structure allowing diffusion and cell migration. • Microporosity to present a large surface area for cell-scaffold. • Macroporosity to allow cell migration and invasion of vasculature • Pore size tailored to target tissue and cells, allowing cell ingrowth without weakening mechanical properties. • Inbuilt vascular channels to enhance angiogenesis *in vivo*.
Mechanical Properties	• Compressive, elastic and fatigue strength comparable to host tissue allowing load bearing and cell mechanoregulation to occur. • Scaffold material that can be readily manipulated in the clinical environment to treat individual tissue defects.

Scaffold bioactivity can also significantly influence cellular regeneration. Bioactivity in this context refers to the capability of a scaffold to affect its biological surroundings. Bioactive scaffolds allow cells to adhere and proliferate, providing stimuli for further growth and/or differentiation. A range of biomaterials have been used to increase the bioactivity of scaffolds for cartilage regeneration, including ECM constituents, polymers, bioceramics, drugs and growth factors. Natural polymers are often derived from extracellular matrix components including collagen and hyaluronic acid, and therefore have low toxicity, high biocompatibility and cell affinity [104]. However, natural polymers can undergo uncontrolled degradation resulting in compromise of mechanical properties in printed constructs. To help address this issue, synthetic polymers can be used either alone or with natural polymers to create a composite scaffold, allowing better control over stiffness and elastic modulus of constructs [105, 106]. Synthetic polymers can also be functionalised with biological molecules, such as arginylglycylaspartic acid (RGD), heparin and hyaluronan, to increase bioactivity and cell adhesion [107, 108]. Growth factors and drugs have also been included within scaffolds to increase bioactivity [109-111].

Growth factors are thought to have a key role in cartilage regeneration and scaffold bioactivity. Growth factors can be described as biologically active polypeptides produced by the body, capable of stimulating cellular division, growth, and differentiation [112]. Articular cartilage development and homeostasis is regulated by a range of growth factors and biomolecules throughout life. Scaffolds designed to regenerate cartilage would therefore seem likely to benefit from inclusion of growth factors; however, inclusion of an individual growth factor in a scaffold is unlikely to achieve complete cartilage development, with numerous interacting growth factors known to influence articular cartilage development [112]. Chondrocyte synthesis of extracellular matrix constituents including proteoglycans, aggrecan and type II

collagen is increased by growth factors, whilst decreased expression of cytokines including interleukin-1 (IL-1) and matrix metalloproteinases (MMPs) leads to lower levels of cartilage ECM degradation.

Transforming growth factor-β (TGF-β) has received significant attention as a growth factor for cartilage regeneration. As a cytokine, TGF-β is secreted by multiple cell types, helping to direct cell proliferation, differentiation, apoptosis and tissue homeostasis [113]. As one of three common isoforms of TGF-β, TGF-β1 has shown the most promise in cartilage regeneration, with an ability to both stimulate chondrocyte synthetic activity and to decrease cartilage ECM breakdown via IL-1 and tumour necrosis factor-α (TNF-α) [114-116]. Following promising *in vitro* results with enhanced cartilage repair found in defects treated with TGF-β1 containing scaffolds, clinical trials have been performed examining TGF-β1 treatment of patients with moderate knee osteoarthritis. Improved pain scores and joint function were found at up to one year following treatment, suggesting significant promise for TGF-β1 as an OA treatment [117, 118].

Perhaps the most extensively studied growth factors within cartilage regeneration so far are the family of bone morphogenic proteins (BMP) [119]. Within the BMP family, BMP-7 has been investigated most frequently with exposure to *in vitro* chondrocytes seen to increase production of cartilage-specific extracellular proteins, including type II and VI collagen, aggrecan, decorin, fibronectin, and hyaluronan [HA] [120, 121]. BMP-7 also modulates the impact of other growth factors, inhibiting the impact of catabolic mediators such as MMPs, IL-1, IL-6, IL-8, IL-11, and tumour necrosis factor [TNF]-α, and increasing the response to anabolic mediators including insulin-like growth factor-1 (IGF-1) and fibroblast growth factor (FGF) [122, 123]. Studies examining treatment of cartilage defects in numerous animal models including sheep and

rabbits have also identified extensive *in vivo* regeneration of subchondral bone and hyaline-like cartilage when BMP-7 was included on scaffolds applied to defects [41, 124-126]. However, risk of bone formation within soft tissues, or heterotopic ossification, is also associated with use of BMPs [127-131]. Vascular endothelial growth factor (VEGF) [132-134], platelet-derived growth factor (PDGF), insulin-like growth-factor 1 (IGF-1), and FGFs provide further examples of growth factors that have been utilised in cartilage and bone tissue engineering [135, 136].

In summary, a range of factors appear to contribute to the success of scaffolds used in tissue regeneration. On occasion, achievement of one desirable scaffold property can come at the detriment of another; for example, producing a mechanically robust scaffold using synthetic polymers can lead to diminished bioactivity, whilst increasing porosity to allow nutrient diffusion and cell ingrowth can weaken overall scaffold strength. Achieving a successful balance *in vivo* between the properties of a scaffold favourable to cellular function, cellular viability and mechanical integrity under load bearing remains challenging [137, 138]. To overcome these challenges, a variety of scaffold manufacturing techniques have been developed, ranging from more conventional options towards more novel biofabrication approaches.

2.3.2 Scaffold Fabrication Methods

A large variety of techniques have been used in the biofabrication of 3D scaffolds, sometimes in combination. In general, it is difficult to create complex scaffold microarchitectures with precise control using conventional techniques. However, the integration into biofabrication of computer-aided design (CAD) modelling and 3D bioprinting has greatly increased scaffold manufacture precision and repeatability, with control over scaffold macro- and microporosity

possible. The advantages and disadvantages of conventional scaffold manufacturing methods and more recent 3D printing techniques will therefore be discussed in the following text.

2.3.3 **Conventional Scaffold Fabrication**

Solvent casting/particulate leaching is a traditional method of scaffold manufacture that begins with dissolution of a polymer in an organic solvent (Fig. 2.4 A). The technique uses porogens, which are substances that can be dispersed into a moulded structure and subsequently dissolved once the structure has set, resulting in the creation of pores. Porogens are added to the polymer solution to create a polymer-porogen network. The polymer is subsequently hardened as the solvent evaporates, with water then used to dissolve the porogen which is often a salt such as sodium chloride. A hardened polymer scaffold with a porous network is left behind, although it is difficult to control pore shape and pore interconnectivity of scaffolds produced by this method [139, 140].

Gas foaming eliminates the use of solvents deployed in solvent casting/particulate leaching methods (Fig. 2.4 B). This technique creates a porous structure through the nucleation and growth of gas bubbles dispersed throughout a polymer. Compression moulding is first used to create solid discs of a scaffold material, such as poly (lactic-co-glycolic acid) (PLGA), within a heated mould. Following this, the discs are saturated with carbon dioxide by exposure to high pressure CO_2 gas (5.5 MPa) for 72 h at room temperature, before solubility of the gas in the polymer is rapidly decreased by reducing CO_2 pressure to atmospheric levels ($P^0 CO_2$). This causes the CO_2 gas to clump together, creating pores. Porosities of up to 93% and pore sizes of up to 100 mm can be obtained using this technique. However, it is difficult to control pore connectivity and pore sizes by gas foaming [140-143].
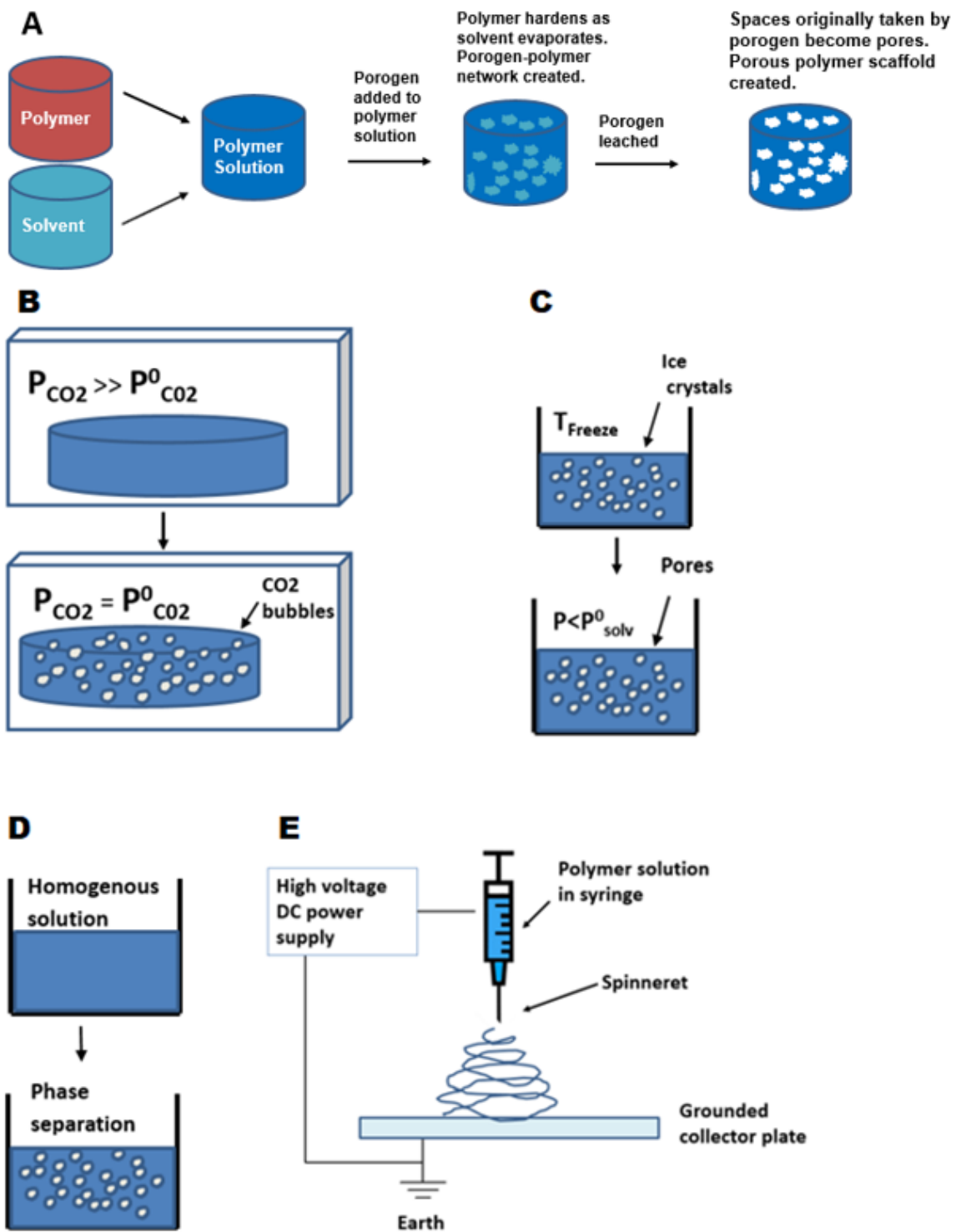
Figure 2.4 Conventional Scaffold Fabrication Techniques: **(A)** Solvent casting-particle leaching process, **(B)** Gas foaming, **(C)** Freeze-drying, **(D)** Phase separation, **(E)** Electrospinning [144].

Freeze-drying begins with freezing of a polymer solution, resulting in the formation of solvent ice crystals surrounded by polymer aggregates (Fig 2.4 C). The surrounding pressure is then reduced via a vacuum, to a level lower than the equilibrium vapor pressure of the frozen solvent (P^0). The solvent is thus triggered to undergo sublimation directly into gas from the solid phase. When the solvent is completely sublimated, a dry polymer scaffold with an interconnected porous structure remains. Emulsification freeze drying can also be used as a primary scaffold fabrication method. The process begins by dissolving polymers/ceramics in a solvent and then mixing with water, to obtain an emulsion. The mixture is poured into a mould and frozen before the two phases can separate. The frozen emulsion is then freeze-dried to remove the solvent and dispersed water, creating pores in a solidified scaffold [145].

Phase separation begins with polymer dissolution in a solvent, at a temperature typically near to or higher than the polymer melting point, allowing formation of a homogenous melt-blend (Fig 2.4 D). The polymer solution is then cast into a desired shape. Subsequent cooling below the solvent melting point and vacuum-drying cause solvent sublimation. A porous scaffold is obtained as the solvent sublimation leaves pores behind in the polymer.

Electrospinning is another popular scaffold fabrication technique with the ability to create nanofibrous interconnected porous scaffolds (Fig 2.4E). This method uses an externally applied electric field to draw charged threads of polymer solutions or polymer melts as thin jets from a capillary tube towards a collector plate. Fibres in the micro- and nanometre range can be created and deposited sequentially to create a scaffold, with potential to include composite materials and biomolecules [146-149].

2.3.4 **3D Printing Techniques**

The traditional methods of scaffold fabrication that have been discussed in brief so far generally offer limited control over pore size, geometry and interconnectivity. Overtime there has been an improvement in the ability to spatially control scaffold microarchitecture and spatial content as technologies such as 3D printing have emerged. In general, 3D printing fabricates objects via layer-by-layer processing of powder, liquid or solid material substrates. Starting from the bottom and building up, each newly formed layer is triggered to adhere to the previous layer, resulting in the creation of construct of gradually increasing size. The structure of a 3D printed object is dictated by a CAD model loaded onto a 3D printer. CAD models describe 3D objects in a series of cross-sectional layers, allowing 3D printers to physically reproduce models through an additive process.

Patient specific CAD models can be created by converting computed tomography (CT) or MRI images of clinical defects into CAD models. Further software is then used to slice CAD models into G-code, which encodes 3D CAD models in a format that can control 3D printers. Parameters such as print speed, layer height, print head temperature and pressure can all be modified and optimised through G-code.
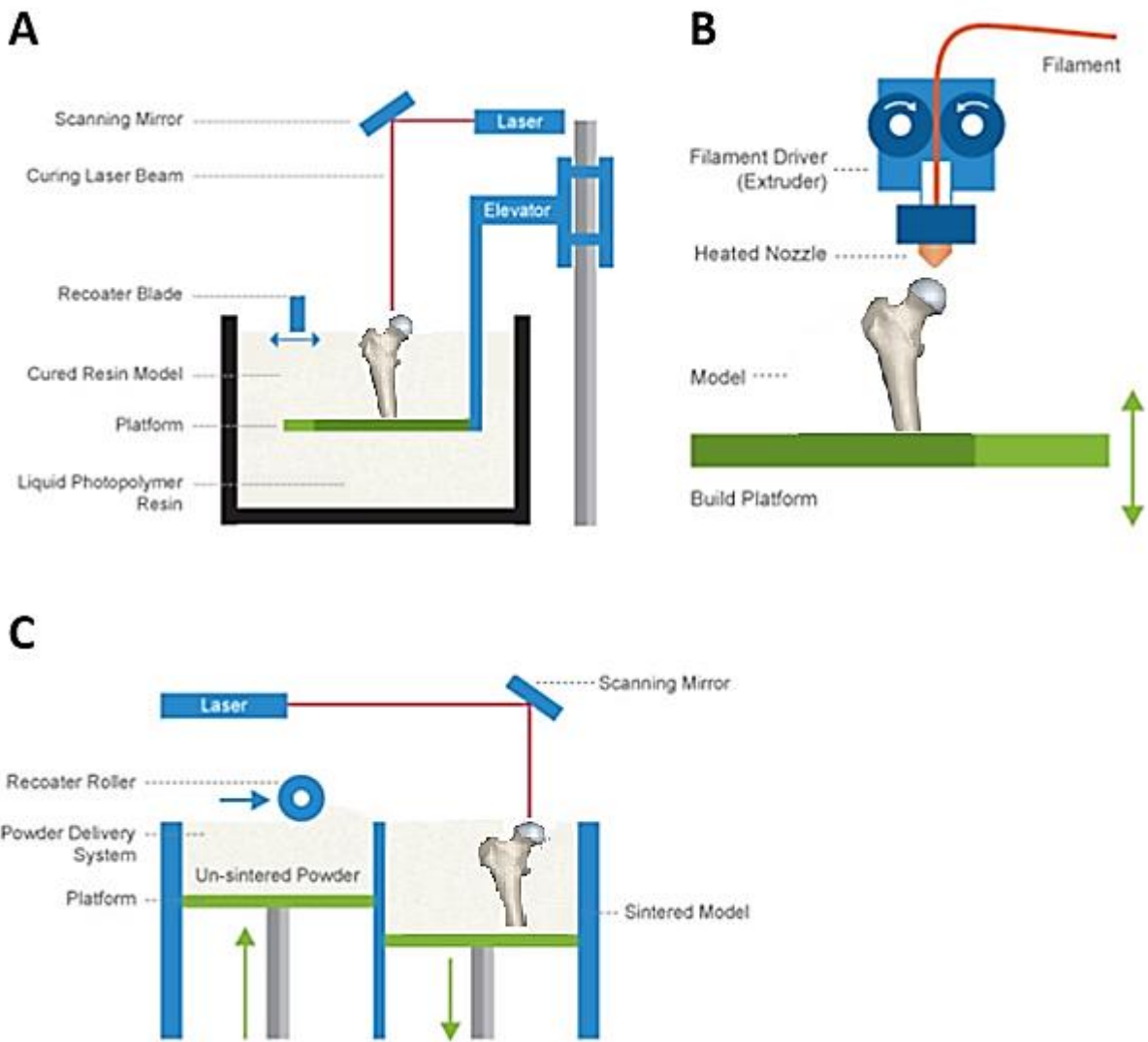
Figure 2.5 Common 3D Printing Techniques. **(A)** Stereolithography **(B)** Fused deposition modelling **(C)** Selective laser sintering [150].

Several 3D printing methods have been adapted into orthopaedic tissue engineering (OTE), with stereolithography (SLA) representing one of the earliest 3D printing techniques to have been developed (Fig. 2.5 A). SLA relies on the directed use of a laser to polymerize ultraviolet (UV)-curable liquid photopolymer resin layer-by-layer, resulting in a solidified 3D model. The UV laser can solidify the model's cross-section, leaving remaining areas in liquid form. After each cross-section, the print platform moves down, covering the solid polymer with another

layer of resin for curing. Excess resin that has not been cured is then removed from the 3D structure, allowing rapid fabrication of a structure that can be cured further in an oven. Whilst SLA can quickly produce scaffolds with controlled architecture and micrometre-level resolution, there is a limited number of materials applicable to this costly technique [151].

Fused deposition modelling (FDM) uses a temperature controlled printhead to deposit thermoplastic material onto a platform in a layer-by-layer manner to build up a 3D construct (Fig 2.5 B). A thermoplastic filament is driven into a heated printhead, causing the filament to melt, allowing thin layers of a semi-molten polymer such as polycaprolactone (PCL) to be precisely deposited sequentially. The molten filament cools in the air of the print environment, allowing filaments to fuse together rapidly to create a scaffold. FDM has been successfully adapted into OTE as method of producing synthetic scaffolds, although the elevated temperatures involved can limit biomaterial inclusion [152, 153].

Selective laser sintering (SLS) involves the use of a computer-controlled laser beam to fuse layer-upon-layer of a powder, sintering the powder material together to build a solid 3D structure (Fig 2.5 C). Some success with this technique has been demonstrated, through the production of bioactive, composite scaffolds with similar mechanical properties to trabecular bone [154, 155]. However, the elevated temperatures involved in the process limit the inclusion of cells and biomaterials directly into SLS scaffolds.

2.3.5 Overview of Bioprinting Approach

Bioprinting involves the use of 3D printing technology to spatially pattern viable living cells and other non-living biologic materials [156]. Bioprinting thus allows the production of complex living and non-living biological products from raw materials such as living cells,

molecules, extracellular matrices, and biomaterials [71, 74, 157]. The general bioprinting approach (Fig. 2.6) begins with selection of cells for inclusion in constructs. Cells for bioprinting can be sourced from commercial cell lines, patient tissue biopsies, blood samples or from donor sources, and expanded in number through culture to maximise cell density on bioprinting [158, 159]. Following culture, cells are encapsulated in a delivery medium or bioink, along with selected biomaterials such as polymers, ceramics and growth factors [73, 160, 161]. Cartridges containing bioink are then loaded into a 3D bioprinter, which dispenses the bioink in a pre-determined 3D geometry according to a CAD model. Bioprinters often have multiple print nozzles, allowing combinations of cells and biomaterials to be included within a printed construct [71, 73, 160, 162-165]. A high degree of spatial control can therefore be achieved over construct architecture and content [166, 167]. Following bioprinting the construct can be cultured *in vitro* for experimental purposes, or potentially implanted *in vivo*. Biologically active culture environments known as bioreactors are also available to help direct and support cell growth within bioprinted constructs towards specific tissue types [168].
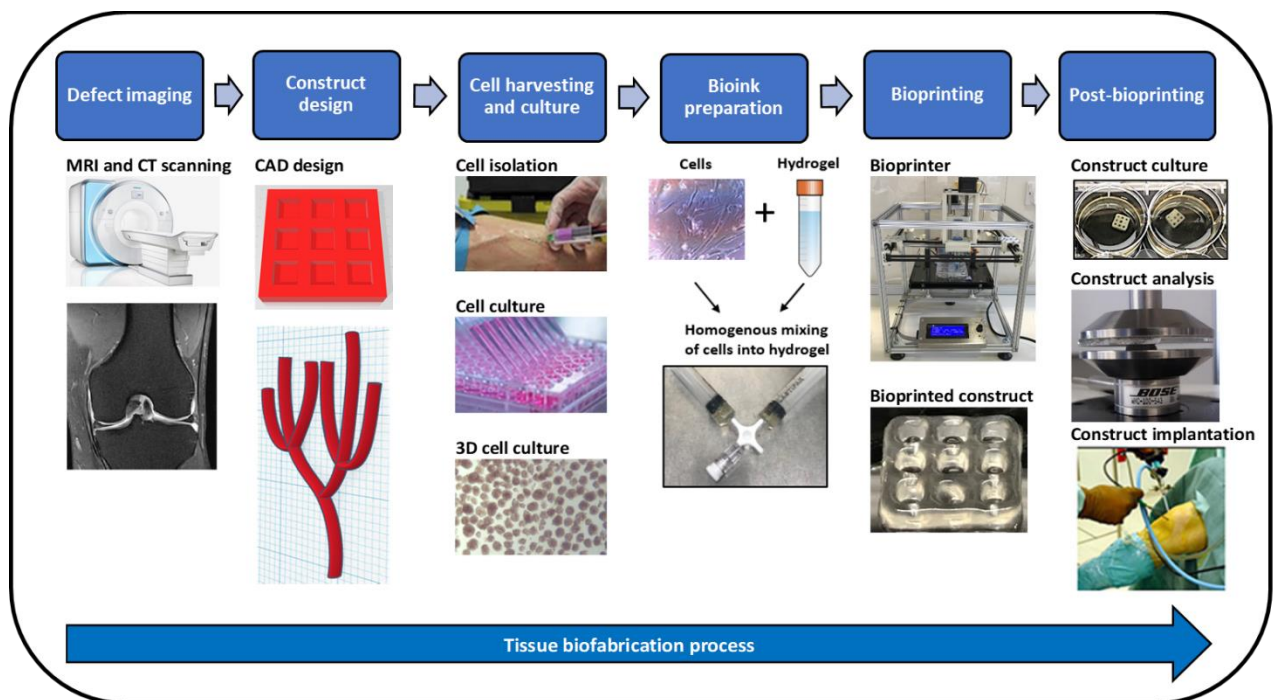
Figure 2.6 Tissue biofabrication process. Patient defects are identified through clinical imaging such as magnetic resonance imaging (MRI) or computed tomography (CT) scanning. Computer aided design (CAD) software can then be used to reconstruct the defect for 3D bioprinting. Cells for bioprinting can be sourced from tissue biopsies, blood samples and from other sources, and expanded in culture to maximise cell density on bioprinting. Following culture, cells are encapsulated in a delivery medium or bioink, along with selected biomaterials such as polymers, ceramics and growth factors. Cartridges containing bioink are then loaded into a 3D bioprinter, which dispenses the bioink in a pre-determined 3D geometry according to a CAD model. Bioprinted constructs can then be matured *in vitro*, analysed or implanted.

2.3.6 Cell Source for Bioprinting

Bodily tissues often possess multiple cell types, all with individual biological functions that ideally are recapitulated in bioprinted tissue. Bioprinting may therefore incorporate multiple

primary cell types when trying to replicate native tissue; alternatively, stem cells can be bioprinted and directed to differentiate to form mature tissue containing different cell types. To minimise the risk of immune response and disease transmission, cells included in bioinks are ideally autologous, derived from a specific patient for their own treatment. For a bioprinted construct to maintain long-term function after transplantation, bioprinted cells must be also able to respond to tissue damage or injury, self-renew and maintain homeostasis [169-171].

Thus far, stem cells used in the biofabrication of bodily tissues have included embryonic stem cells (ESCs), induced pluripotent stem cells (iPSCs) and adult stem cells [172, 173]. Embryonic stem cells originate within the inner cell mass of a blastocyst and have the potential to differentiate into somatic cells of all three germ layers. Consequently, ESCs have the potential to be used to derive all cell types present within soft tissues. Whilst ESCs have high proliferative capacity and pluripotency, they also require complex culture conditions to remain in an undifferentiated and proliferative state and can cause immunogenic reactions [174]. Prolonged culture of undifferentiated ESCs can also result in the development of abnormal karyotypes, with the risk of teratoma formation following implantation *in vivo* [174-176]. ESCs have already been used to help regenerate cartilaginous, vascular and neural tissues amongst others [177-179].

iPSCs are stem cells created through the artificial dedifferentiation of adult somatic cells through exposure to selected transcription factors. iPSCs display similar pluripotency, gene expression profiles and ability to form embryonic bodies as ESCs, whilst overcoming the various ethical issues regarding the use of embryos in research. Whilst iPSCs are considered pluripotent, they have a lower differentiation capacity than ESCs and carry an increased risk of teratoma formation. Safer protocols and virus free iPSCs with reduced carcinoma risk have

been developed, increasing the potential for use of iPSCs in soft tissue and cartilage regeneration in future [176, 180, 181].

Autologous adult stem cells are particularly attractive for inclusion in bioinks, owing to their increased availability relative to ESCs and potential to differentiate into the multiple cell types found in soft tissues. Furthermore, they can be isolated from various tissues including adipose tissue, bone marrow and peripheral blood [182]. Commonly used examples include adipose-derived stem cells (ADSCs) and MSCs, which can be differentiated into chondrocytes, osteocytes, endothelial cells, neural cells and adipocytes [183-187].

Many examples of successfully bioprinted MSCs already exist for the regeneration of cartilage, skin, nerves and blood vessels [164, 188-190]. Within cartilage regeneration, cartilage progenitor cells have also been used, with favourable growth within gelatin methacryloyl (GelMA) based hydrogels found as compared to chondrocytes [191]. Allogenic MSCs are capable of generating a local immunosuppressive microenvironment following implantation, resulting in only a weak immune reaction [192]. Use of autologous MSCs minimises the risk of immune rejection further, although notably for older patients the differentiation and proliferation capacity of autologous MSCs appear to be age-dependent [193, 194]. Following *in vitro* culture, there are also reports that MSCs display unstable phenotypes, reduced chondrogenic matrix formation, undesired mineralisation and cell death on injection [193, 194]. Cell source also appears to influence MSC characteristics, with some reports suggesting that adipose derived MSCs (AD-MSCs) have higher proliferative capacity and apoptosis tolerance compared to bone marrow derived MSCs (BMMSCs) [195, 196]. AD-MSCs can also be harvested at up to 500 times the density of BMMSCs from equivalent volumes of tissue [192,

196], with biopsy from adipose tissue also involving a less painful and invasive procedure with lower risk of morbidity [159].

Following selection of a cell source, the additional step of 3D cell culture may also be performed to create aggregates of cells for printing. Cell aggregates or spheroids have superior intercellular communication and extracellular matrix development when compared to cells grown in 2D culture, potentially accelerating the growth of printed constructs towards functional tissue after bioprinting [197, 198]. There are several examples of bioprinted spheroids used in the fabrication of cartilage, blood vessels and nerves [199-204].

2.3.7 **Bioinks**

Cells are usually encapsulated within a bioink prior to bioprinting. Bioinks provide cellular protection during the bioprinting process and mimic the extracellular matrix environment, providing a scaffold that supports the adhesion, proliferation and differentiation of cells following bioprinting [73]. Bioinks are most often created from hydrogels, which can be defined as gels constructed from networks of crosslinked, hydrophilic polymer chains. Hydrogels are able to absorb up to 1000 times their original dry weight in aqueous medium to form hydrophilic three-dimensional networks, ideal for supporting cell growth [205]. The high-water content of hydrogels makes them highly permeable to oxygen, nutrients and other water-soluble compounds crucial for supporting cell growth. Within orthopaedic tissue engineering, hydrogels have been shown to facilitate angiogenesis, osteoconductivity, cell adhesion and matrix integration [167, 206-208]. Hydrogels can be derived from natural polymers (including collagen, gelatin, alginate, chitosan, hyaluronic acid and agarose) or synthetic materials. Natural polymers are often derived from ECM components including collagen and hyaluronic acid and therefore have low toxicity, high biocompatibility and cell affinity [104, 210-213].

Combinations of naturally derived polymers such as gelatin and alginate have also been incorporated into bioinks to improve printability and bioactivity [214]; decellularized extracellular matrix (dECM) has also shown promise as a source of bioink due to its capability to inherit the intrinsic cues from a native ECM [215]. However, natural polymers can undergo uncontrolled degradation, resulting in compromise of mechanical properties within printed constructs. To help address this issue, synthetic polymers can be used either alone or with natural polymers to create composite hydrogels, allowing better control over stiffness and elastic modulus of bioprinted constructs [105, 106, 216]. Synthetic polymers can also be functionalised with natural biological molecules such as RGD to increase bioactivity and cell adhesion [107, 108, 217]. Bioactivity of bioinks can be increased further by addition of growth media, biomaterials, drugs, growth factors and nutrients [208, 218-220]. Further features, such as tuneable mechanical stiffness, thermal and UV crosslinking and tailored degradability have been included in synthetic hydrogels for tissue engineering [208, 221-224]. A range of compounds have also been added to bioinks to modulate printability, mechanical properties, immune response and growth factor delivery, including clay [225] , hydroxyapatite [226] and modified chitin [227]. Within cartilage and soft tissue engineering, hydrogels have been shown to facilitate cartilage regeneration, angiogenesis, neurogenesis, cell adhesion and matrix integration [228-233].

2.3.8   **Bioprinting Techniques**

Successful bioprinting relies in part on combining a suitable bioprinting technique with an appropriate bioink. A variety of different techniques have been used to bioprint cells with high cell viability achieved following printing. Commonly used bioprinting techniques include inkjet, laser-assisted, microvalve and extrusion bioprinting [71, 74, 220, 234-236].

Inkjet bioprinting (or drop-on-demand bioprinting) uses thermal or acoustic forces to eject droplets from a pint head nozzle (Fig. 2.7 A). Thermal inkjet printers use heat to generate a pressure pulse within a print head for a brief period, causing ejection of a droplet of bioink. Other systems rely on piezoelectric crystals, which become mechanically stressed by the application of a voltage and as a result change shape. This generates an acoustic wave which in turn creates enough pressure to eject droplets from a nozzle. The technology is adapted from desktop inkjet printers, with benefits including low cost, wide availability and high print speed. However, limitations include frequent nozzle clogging, risk of exposing cells and materials to thermal and mechanical stress and nonuniform droplet size. The liquid droplet deposited is also of low viscosity, relying on further gelation or crosslinking to create a solid structure [237-239].
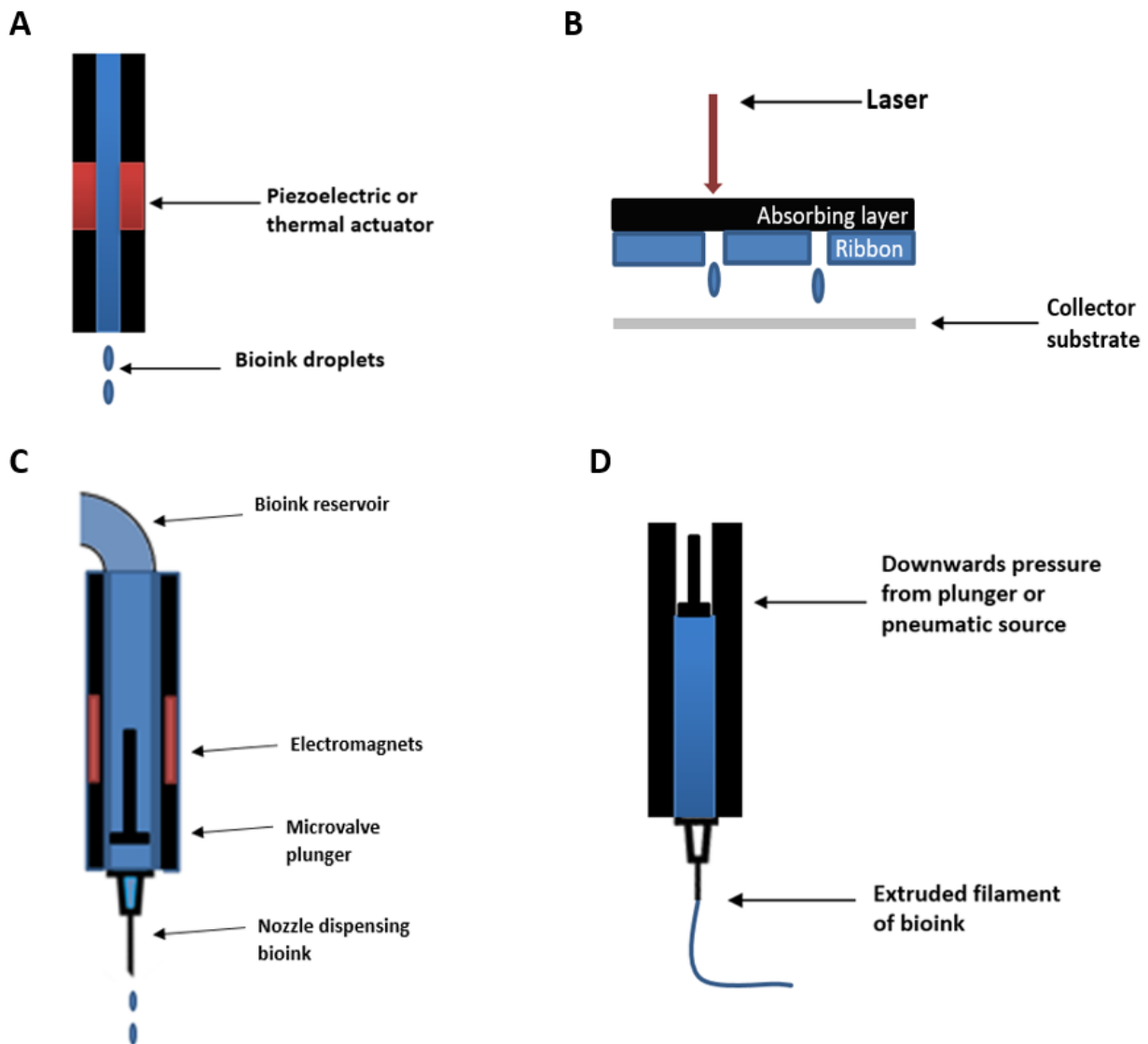
Figure 2.7 Common bioprinting techniques: **(A)** Inkjet. **(B)** Laser-assisted. **(C)** Microvalve. **(D)** Extrusion bioprinting.

Laser-assisted bioprinting (LAB) systems avoid the use of a nozzle (Fig. 2.7 B); instead, they rely on a pulsed laser beam to generate a high-pressure bubble, which in turn propels cell-containing materials toward a collector substrate from an initial print material "ribbon." LAB systems are highly precise and allow cells to be placed within 5 µm of a template, with cell-containing skin substitute materials created using the technology [240]. Some limitations of

LAB include potential heat-induced damage to cells, difficulty of creating 3D structures, high system costs and the time-consuming nature of creating ribbons with high cell and biomaterial concentrations [241].

Microvalve bioprinting is a droplet-based system where fluids under a constant pneumatic pressure are dispensed from cartridge tips by opening and closing a small valve (Fig. 2.7 C). The valve in question can be controlled mechanically, electrically or magnetically. Microvalve systems can print cells including MSCs with high viability and functionality, with deposition of other biomaterials also possible such as polymers and growth factors [235, 236, 242].

Extrusion bioprinters deposit continuous filaments of materials rather than individual droplets (Fig. 2.7 D). Pneumatic or mechanical pressure is applied to a syringe, causing controlled bioink extrusion through a nozzle. A significant advantage of this approach is the ability to deposit very high cell densities, with some studies manging to purely print cells, for example as filaments of cartilage [243]. A broad range of bioinks have been successfully extrusion bioprinted, using cell-laden hydrogels containing tissue spheroids, tissue strands, cell pellets and decellularized matrix components. Extrusion bioprinting also allows for a relatively high print speed to be achieved, improving potential for scalability and clinical translation. Challenges include achieving high print resolution; cell survival decreasing with increasing print pressure, nozzle gauge, and shear stress and development of printable bioinks [161].

2.4 **Techniques to Support Development of 3D Structures Following Biofabrication**

3D biofabrication technologies have undergone rapid development and innovation over the last decade [71, 74]. Bioinks that incorporate beneficial physical and biological characteristics have been combined with multi-material and multi-nozzle bioprinting to fabricate increasingly

complex structures [244]. However, biofabrication of cartilage and soft tissue constructs remains challenging as bioinks generally lack the load bearing capacity to support their own weight without incorporation of harsh mechanical enhancement strategies [160, 245]. A key challenge has been balancing bioink rheological properties required for printability and structural integrity with bioink biocompatibility needed to ensure cellular viability and proliferation after bioprinting [73, 218, 246].

To address this challenge, elegant approaches have been developed that rely on the use of either dissolvable scaffolding materials or biodegradable materials as sacrificial structures to support soft bioinks following bioprinting. Such techniques allow bioinks that would otherwise move and flow after bioprinting to be maintained in position and therefore be bioprinted with greater predictability. Cellular production of extracellular matrix and crosslinking processes can be allowed to occur before removal of supporting structures, leading to the development of complex, heterogenous, soft tissue constructs with maintained structural integrity [170, 247-249].

2.4.1 Fugitive Inks

Dissolving "fugitive" hydrogels including the co-polymer pluronic F-127 have frequently been used to provide temporary support to mechanically weaker, cell-containing bioinks (Fig. 2.8 A) [250]. Typically, the fugitive hydrogel is bioprinted within or around a less viscous secondary bioink to provide support; once the secondary bioink has gained sufficient structural integrity, either through cellular deposition of ECM or via chemical or UV cross-linking following bioprinting, the fugitive hydrogel is dissolved via thermal or chemical means. Fugitive hydrogels have also been utilised to aid the creation of complex 3D vasculatures within multicellular constructs. The fugitive hydrogel is bioprinted alongside other bioinks to create a

43

multicellular construct; following bioprinting, the fugitive hydrogel is then liquified and removed through a variation in temperature or chemical dissolution, leaving patent channels behind within the construct that can be developed into vasculature or perfused with culture media [248].

2.4.2   **Support baths – The FRESH Technique**

Support baths have been developed that allow the bioprinting of low viscosity bioinks to occur (Fig. 2.8 B). This approach typically involves bioprinting into a secondary support bath; once cross-linking of the printed bioink has occurred, the support bath can be liquefied, leaving behind a cross-linked structure. A notable example of this approach is provided by Hinton *et al.,* who developed a novel technique allowing bioprinting of complex structures from low viscosity bioinks, termed freeform reversible embedding of suspended hydrogels (FRESH) [251].

2.4.3   **Removable Rods and Needles – The Kenzan Method**

Removable rods and needles have also been used to provide structural support to bioprinted tissue constructs [252-254]. Itoh *et al.* deployed metallic needles in a circular array to create a temporary scaffold for supporting cell spheroids (Fig. 2.8 C). Termed the Kenzan method, this approach permitted the fusing together of smooth muscle cell and fibroblast spheroids (650 μm, diameter) during culture in a bioreactor, with later removal of the support needles leaving a rigid tubular structure behind [255, 256]. Norotte *et al*. used agarose rods in place of metallic needles to support the fusing together of high cellular density cylinders into a tubular construct (Fig. 2.8 D). This process achieved a reduction in printing times when compared to individual spheroid assembly [257].

2.4.4 **Use of Biodegradable Materials to Guide Cell Growth**

Biodegradable nanofibers have also been used to direct cellular growth towards mature tissue [252, 258, 259]. Choi *et al.* electrospun blended PCL/collagen nanofibers and seeded them with human skeletal muscle cells. Unidirectionally oriented nanofibers significantly induced muscle cell alignment and myotube formation as compared to randomly oriented nanofibers. This technique therefore has potential to provide implantable functional muscle tissues for patients with muscle defects.

2.4.5 **Coaxial Printing**

The process of coaxial printing has also been employed by several research groups to create microtubular, soft tissue constructs [260, 261]. A coaxial nozzle contains an inner core and an outer concentric shell; concurrent extrusion of two chemicals or bioinks can therefore occur, producing a tubular structure with an inner core and outer shell (Fig. 2.8 E). By extruding a cross-linking agent as the inner core, the outer shell can be rapidly cross linked to form a self-supporting hollow tube [262, 263]. Jia *et al.* added an additional outer shell to their coaxial nozzle to allow cross-linking perfusion from two directions [264]. Whilst coaxial printing can create very long conduits in a minimal amount time, production of complex, bifurcated, anatomical structures with the microscale layers seen in native tissue remains challenging using this technique.

2.4.6 **Scaffold-Free Approaches – Use of Spheroids, Cell Sheets and Tissue Filaments**

Scaffold-free approaches to the biofabrication of soft tissues have also been developed. Okano *et al.* developed a successful method of fabricating cell sheets without the use of biodegradable scaffolds. Cell culture on temperature-responsive dishes allowed intact cell sheets to be

harvested by simply switching the temperature from 37°C to room temperature, thereby avoiding the use of proteolytic enzymes (Fig. 2.8 F). Cell sheet engineering allows for tissue regeneration by direct transplantation of single cell sheets to host tissues; alternatively multi-layered cell-sheets can be biofabricated *in vitro* prior to clinical use [265]. Larger constructs including vascular grafts have been successfully fabricated by placing layer upon layer of cell sheets together [266, 267]. By avoiding the use of additional bioinks or scaffolds, this approach minimises the risks of host inflammatory responses occurring [268]. In a similar approach to fusing sheets of cells together, smaller micro-units of cell laden hydrogels have been used as building blocks to create larger tissue constructs in a "micro-masonry" concept [269, 270]. This approach allows for a high degree of modularity, as hydrogels of different compositions that embed different cells can be mixed and deposited with a high degree of precision [271].

Cell pellets, spheroids and tissue strands have also been used as building blocks to create more complex tissue constructs. Various methods have been used to assemble cell aggregates or spheroids, including culture moulds, cell suspensions and hanging droplet techniques [197, 199, 272, 273]. Spheroids bioprinted in close proximity have successfully fused and matured together to form larger tissue constructs, including functional thyroid gland tissue [274, 275]. Tissue filaments have also been successfully bioprinted to create larger patches of tissue, with Yu *et al.* bioprinting chondrocyte filaments together to form a larger, fused cartilage patch [243]. Cellular fibres have also been woven together to create cellular fibre scaffolds [276].

2.4.7 Moulding, Dip-Coating and Rod Support Methods

Moulding techniques have also been used to direct the maturation of 3D tissue constructs (Fig. 2.8 G). Pacak *et al.* cast a mixture of skeletal muscle cells, type 1 collagen, Matrigel™ and NaHCO$_3$ onto silicon moulds. After one to two days, solidified myoblast-containing tissue

constructs could be harvested for *in vitro* use [277]. Tabriz *et al.* developed a rapid method of moulding tubular structures by dip-coating metal bars covered in cell-laden alginate hydrogels into cross-linking reagents, including calcium chloride or barium chloride (Fig. 2.8 H). Following cross-linking, cell-laden hollow tubular structures could be released from the metal bars [209, 278]. This methodology was further developed by Wilkens *et al*., who introduced motors to rotate and dip the rods (Fig. 3I). This approach gave a high level of control over individual layer thickness within vessels, with use of rod-supports allowing successful production of a structural configuration closely resembling natural blood vessels (Fig. 10B). However, the technology could also be applied to allow development of other layered soft tissues, potentially even including cartilage [279].

A Fugative Inks

Self supporting network printed

Encapsulated in cell laden hydrogel

Network ink evacuated and endothelialised to create vascularised tissue

B FRESH printing

Bath gel behaves as a rigid material at low shear stresses, supporting printed material, and a viscous fluid at high shear stresses, permitting nozzle movement.

Cell laden gel is printed into the supporting hydrogel in complex tubular geometries.

Elevation of temperature melts the hydrogel leaving the self-supporting printed structure

20°C

20°C

37°C

C Kenzan method

Circular array of needles

Cell spheroids printed onto needles

Tubular structure arranged

Culture in bio reactor fuses spheroids together and allows removal of needles

D Use of biodegradable materials to guide cell growth

Cell laden tubes deposited alongside inert support tubes

Cell laden tubes allowed to fuse with support from inert tubes

Inert support tubes removed to produce cell-laden, tubular structure

E Use of coaxial nozzle

Inner core

Outer shell

Support core and/or cross-linking agent

Cell laden bio-ink

Dual material cylinder extruded from adapted nozzle with an inner core and outer shell

Outer shell cross-linked through contact with inner core material

Cross-linking agent drained away or sacrificial core removed to create tubular structure

Figure 2.8 3D biofabrication techniques allowing bioadditive manufacture of soft tissue structures. **(A)** Vasculature network creation via fugitive inks. **(B)** Freeform reversible embedding of suspended hydrogels (FRESH) printing. **(C)** Kenzan printing of cell spheroids onto needles. **(D)** Use of biodegradable materials to guide tissue formation. **(E)** Coaxial tube or filament formation from a modified nozzle. **(F)** Use of cell sheets to create layered constructs. **(G)** Use of moulds to allow cell-laden hydrogels to develop into constructs. **(H)** Dip-coating to create tubular structures. **(I)** Rod support printing. Adapted from Holland *et al*. [280].

2.5 Biofabrication of Cartilage

2.5.1 Challenges of Bioprinting Cartilage

The layer-by-layer approach used in many biofabrication strategies to regenerate tissue seems well suited to the task of recreating the intricate, layered structure of cartilage. However, several challenges exist when using a hydrogel-based approach to printing cartilage. To enable high resolution and consistent printing, hydrogels must be optimised to display rapid gelation, minimal extrudate swell post-printing and shear-thinning properties to minimise shear-stresses on cells during bioprinting [72, 73]. The high-water content of hydrogels can also have mixed benefits; whilst this allows replication of the hydrated environment of the native ECM, this often leads to poor mechanical properties [245, 281, 282] . Attempts have therefore been made to create composite bioinks for cartilage regeneration, capable of integrating the mechanical strength of synthetic, viscous hydrogels with the biocompatibility provided by lower-viscosity, naturally derived hydrogels [164, 283-286].

2.5.2 Biofabrication of Cartilage Using Natural Polymer Bioinks

Use of natural polymers in bioinks has attracted great interest within cartilage regeneration due to favourable properties including biomimicry, biocompatibility and biodegradability. As a further benefit, natural polymers often contain biofunctional molecules on their surface that can aid cell attachment, integration and differentiation on scaffolds. Naturally occurring polymers that have been investigated in cartilage regeneration include collagen, gelatin, alginate and hyaluronic acid. However, use of naturally occurring polymers can also be subject to limitations including presence of pathogenic impurities such as endotoxin [180], lack of tuneability of degradation rates and degradation related inhibition of local cells. Mechanical properties of

natural polymers can also be suboptimal for cartilage regeneration, although crosslinking of polymers can enhance structural properties.

As a biocompatible and readily available hydrogel, alginate has been incorporated into several investigations of cartilage biofabrication [164, 287]. Alginate has desirable properties such as biocompatibility, low toxicity, relatively low cost, and crucially for 3D bioprinting, a capacity to undergo rapid gelation by addition of divalent cations such as Ca^{2+} [288, 289]. The US Food and Drug Administration (FDA) also previously approved alginate for a number of clinical trials [290, 291]. More than 200 different alginates are currently manufactured and in fact alginate is a whole family of linear copolymers made from blocks of (1,4)-linked β-D-mannuronate (M) and α-L-guluronate (G) residues. The blocks are composed of consecutive G residues (GGGGGG), M residues (MMMMMM), and alternating G and M residues (GMGMGM). Alginates extracted from different sources differ in M and G contents as well as the length of each block. The G-blocks of alginate are believed to primarily participate in intermolecular cross-linking with divalent cations, and the mechanical properties of alginate gels typically are enhanced by increasing the length of G-block and molecular weight [292].

Numerus successful attempts at bioprinting cartilage using alginate exist. Yang *et al.* used sodium alginate (SA) with collagen type I (COL) or agarose (AG) to encapsulate and 3D bioprint chondrocytes. Mechanical strength was improved in both SA/COL and SA/AG groups compared to SA alone. Further analysis showed that SA/COL effectively suppressed dedifferentiation of chondrocytes and preserved the phenotype. Markestedt *et al.* also 3D printed a nanofibrillated cellulose/ alginate (NFC/A) bioink containing human chondrocytes (Fig. 2.9). The shear thinning of the NFC and fast crosslinking of alginate allowed microvalve bioprinting to occur with high fidelity and stability. Taking MRI and CT data, they managed

to bioprint anatomically accurate scale models of human ears and sheep meniscus with high cell viability seen after 7 days [293]. Nguyen *et al.* also designed bioinks containing nanocellulose with alginate (NFC/A), comparing performance to bioinks composed of nanocellulose with hyaluronic acid (NFC/HLA). NFC was chosen to help mimic the collagen bulk in cartilage matrix, whilst hyaluronic acid was included as a major component in native cartilage [294]. Human-derived iPSCs and irradiated human chondrocytes were encapsulated in the bioinks and bioprinted using a microvalve 3D bioprinter. In the case of NFC/HLA, low proliferation and phenotypic changes away from pluripotency were seen in the iPSCs. However, in the case of the NFC/A constructs, hyaline-like cartilaginous tissue with collagen type II expression was seen after 5 weeks. A marked increase in cell number within the cartilaginous tissue was also detected. The NFC/A bioink therefore appeared suitable for bioprinting iPSCs and chondrocytes to support cartilage production.
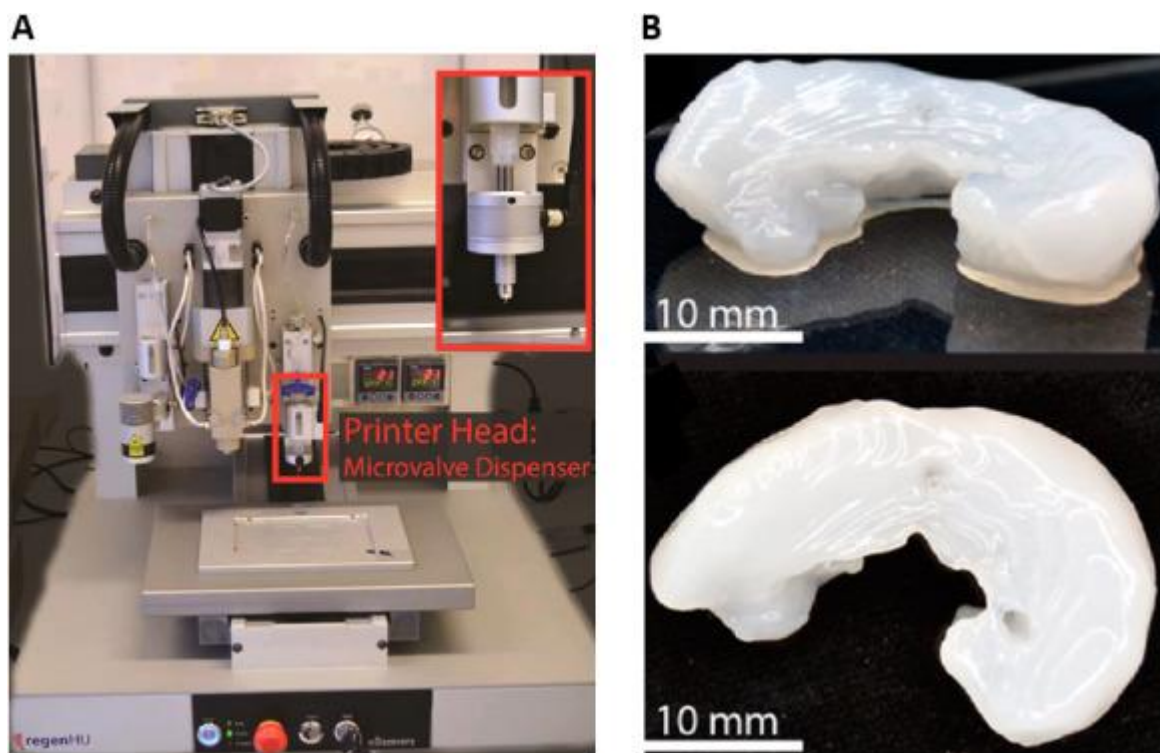
Figure 2.9 Microvalve bioprinting of cartilaginous structures. **(A)** The RegenHu 3D Discovery (Switzerland) bioprinter with microvalve print-head shown. **(B)** 3D printed knee meniscus using nanocellulose with alginate (NFC/A) bioink containing chondrocytes. Adapted from Markestedt *et al.* [293].

A further study combined oxidized alginate and HLA in a composite hydrogel (AL/HLA) for cartilage regeneration, with *in vivo* analysis in mice performed [295]. Six weeks after chondrocyte-loaded AL/HLA gels were injected subcutaneously into mice, effective cartilage regeneration was found histologically. Substantial secretion of glycosaminoglycans and chondrogenic marker genes was also found, compared to control scaffolds. A similar scaffold composed of alginate and low molecular weight HLA was produced by Park *et al.*, with calcium crosslinking performed [232]. Once again, AL/HLA scaffolds triggered chondrocyte differentiation to a much higher degree than found in pure alginate scaffolds. Scaffold stiffness was also found to be critical in triggering chondrocyte differentiation, with low scaffold stiffness leading to diminished chondrocyte differentiation. It was therefore concluded that hydrogels require defined polymer compositions and mechanical properties, to best regulate chondrocyte differentiation and phenotype.

Amongst the natural polymers used in orthopaedic tissue engineering (OTE), collagen ranks amongst the most frequently adapted into scaffolds. Collagen composes 90% of the total weight of bone ECM proteins and forms a key component of cartilage ECM. Although there are approximately twenty-nine known types of collagen, type I collagen has been used perhaps the most frequently within OTE due to the lack of immune reactivity associated with usage of it [164]. As part of the normal ECM it is inherently biocompatible, biodegradable and can stimulate cell proliferation and differentiation [254, 296-299]. Furthermore, the mechanical and

degradation properties of collagen can be tailored through the process of crosslinking [164, 300]. However, in common with other natural polymers, collagen has mechanical properties that are insufficient for creating a load-bearing scaffold [216]. Collagen is therefore often combined with more robust materials within OTE to create composite scaffolds.

Perdisa *et al.* demonstrated the osteoinductive potential of collagen-hydroxyapatite (Col-HA) scaffolds in a prospective clinical study involving patients with patellar osteochondral defects [301]. Cell-free Col-HA scaffolds were implanted into knee or patellar osteochondral lesions (Fig. 2.10), with MRI imaging performed 24 months following surgery. The composite scaffold utilised a three-layered approach in other biomimetic scaffolds such as by Grigolo *et al.*[302]; the cartilaginous layer was made of type I collagen with a smooth surface; the intermediate layer had a combination of type I collagen (60%) and HA (40%); and the lower layer was a mineralised blend of type I collagen (30%) and HA (70%), mimicking subchondral bone composition. Patient functional outcome scores improved significantly at 12 and 24 months follow up, with MRI showing complete filling of the cartilage in 87.0% of the lesions, complete integration of the graft in 95.7% of lesions, and intact repair tissue surface in 69.6% of patients. However, osteophytes or more extensive bony overgrowth was also documented in 8% of the patients, though no correlation was found between MRI findings and clinical outcome (Fig 2.10).

Figure 2.10 Osteochondral scaffold, sized and press-fit into a patella defect. Adapted from Perdisa *et al.* [301].

Collagen has also been blended with other less robust polymeric materials to aid cartilage regeneration. Choi *et al.* blended type-II collagen (Col II) and chondroitin sulphate (CS) with chitosan to create a composite hydrogel for cartilage regeneration [303]. Riboflavin was then used to crosslink the hydrogel using visible blue light. Increased chondrogenesis, MSC proliferation and ECM deposition was triggered by the addition of Col II or CS to the chitosan hydrogel. It was observed that Col II had the greatest impact on chondrogenesis, suggested to be related to chondrocyte integrin $\alpha10$ binding to Col II and therefore increasing cell-matrix adhesion. Lee *et al.* blended HLA with collagen and fibrinogen to create a composite hydrogel, which was then used to encapsulate MSCs. The MSC laden composite hydrogel was then

applied into rabbit osteochondral knee defects; after 24 weeks, defect healing was observed to occur, with hyaline-like cartilage formation observed and significant production of glycosaminoglycans and type II collagen also detected, demonstrating strong therapeutic potential [304].

Different types of collagen have also been mixed together to aid cartilage regeneration. Bernhardt *et al.* used joint freeze-drying and crosslinking processes to produce biphasic scaffolds from biomimetically mineralized salmon collagen and fibrillated jellyfish collagen. By varying cell densities, applying alginate to the chondral section, pre-differentiating cells and using osteochondral medium, chondrogenic and osteogenic differentiation was supported in scaffolds fabricated exclusively from marine collagens [297].

As a biomacromolecule produced from denatured collagen, Gelatin methacrylate (GelMA) based bioinks have gained increasing popularity within biofabrication due to excellent biocompatibility, photocrosslinkability, and tuneable mechanical properties, whilst retaining some of the motifs present in native ECM crucial for promoting cellular adhesion and growth [305-308].

In an attempt to maintain the bioactivity gained from including collagen in constructs whilst simultaneously enhancing structural properties, the bioprintabiltiy of composite alginate methacrylate (AlgMA)/GelMA hydrogels was developed. When used as a lone bioink, high GelMA concentrations (i.e., >15% w/v) have frequently been required to allow maintained structural fidelity following bioprinting. This in turn is associated with higher viscosity and sheer stresses during bioprinting, often leading to lower cell viability [305-307]. Combining AlgMA with GelMA could therefore allow sufficient hydrogel viscosity for bioprinting to be achieved with lower GelMA concentrations, especially with the potential for triple crosslinking

of AlgMA to be performed. Furthermore, previous work has found alginate to support the development of hyaline-like cartilage following 3D bioprinting when compared to GelMA [309].

Costantini *et al.* printed 3D biomimetic hydrogel scaffolds consisting of differing combinations of GelMA, chondroitin sulfate amino ethyl methacrylate (CS-AEMA) and hyaluronic acid methacrylate (HAMA) [310]. Using a two coaxial-needle bioprinting system, they achieved a high cell density, high cell viability and high printing resolution post-printing. Bioinks were loaded with MSCs, with addition of 4% alginate and 0.3 M CaCl$_2$ also performed to aid crosslinking. All the employed hydrogels exhibited enhanced chondrogenic differentiation of bone marrow derived-MSCs after 3 weeks of culture in chondrogenic medium. A composite hydrogel of alginate, GelMA and CS-AEMA appeared to be the best candidate for neocartilage formation, as it supported the highest levels of collagen production. These findings are in keeping with several examples where gelatin or GelMA has been mixed with alginate, leading to improved cell growth [305, 311, 312]. Compared to use of GelMA alone, some groups have also found improved cellular differentiation and growth with inclusion of alginate; it is thought that the improved mechanical properties offered by inclusion of alginate promote cell spreading, proliferation and differentiation by helping to mimic the stiffness of the native ECM more closely [311, 312].

Daly *et al.* evaluated the printing properties and capacity to support the development of either hyaline cartilage or fibrocartilage *in vitro* of a range of commonly used hydrogel bioinks (agarose, alginate, GelMA and BioINK™) [297]. Alginate and agarose hydrogels seeded with MSCs best supported the development of hyaline-like cartilage, whilst GelMA and BioINK™ (a PEGMA based hydrogel) supported the development of a more fibrocartilage-like tissue.

GelMA demonstrated superior printability, generating structures with greater fidelity, followed by the alginate and agarose bioinks. High levels of MSC viability were observed in all bioinks post-printing (~80%).

Focussing more on the role of cell type in successful cartilage biofabrication, Levato *et al.* used GelMA-based hydrogels to investigate the results of bioprinting articular cartilage-resident chondroprogenitor cells (ACPCs), MSCs and chondrocytes for cartilage regeneration [313]. ACPCs outperformed chondrocytes in terms of neo-cartilage production and compared to MSCs, ACPCs had lower gene expression levels of hypertrophy marker collagen type X, and the highest expression of PRG4, a key factor in joint lubrication. By combining ACPC- and MSC-laden bioinks, a bioprinted model of articular cartilage was generated, consisting of defined superficial and deep regions, each with distinct cellular and extracellular matrix composition. The novel ACPC-laden hydrogel appeared to be a suitable substrate for chondrogenesis and was capable of directing cells towards a superficial zone phenotype.

2.5.3 Synthetic Polymer Bioinks for Cartilage Engineering

Whilst natural polymers used in bioinks provide bioactivity and aid biomimicry of the native ECM, synthetic polymers provide superior mechanical strength and structural integrity [164]. Several attempts have therefore been made to combine the mechanical performance of synthetic polymers with the favourable bioactivity of natural polymers in composite bioinks [73, 244]. Synthetic polymers that have been used frequently within orthopaedic tissue engineering (OTE) include PCL, polylactic acid (PLA), polyglycolic acid (PGA), and copolymers of PLA-PGA (PLGA). These poly(α-ester)s have key characteristics of being biodegradable, nontoxic and biocompatible [164, 300].

PCL has been widely incorporated into OTE attempts. Advantages of this polyester include biocompatibility, relatively slow degradation rate, less acidic breakdown products in comparison to other polyesters and potential for load-bearing applications [252, 283, 314-318]. In terms of OTE, the high mechanical strength and slow degradation rate of PCL are particularly advantageous characteristics, potentially allowing a degree of load bearing to occur whilst native tissue gradually regenerate with a scaffold [216, 319-321]. However, due to the poor cellular adhesion properties of PCL, numerous attempts have been made to create PCL composites with improved bioactivity [155, 216, 314, 317, 320, 322-325].

Bahcecioglu *et al.* recently attempted to engineer meniscus replacements, impregnating a PCL meniscus scaffold with agarose (Ag) and GelMA hydrogels in the inner and outer regions, respectively [283]. After incubating the constructs loaded with porcine fibrochondrocytes for 8 weeks, significant Ag-enhanced GAG production and GelMA enhanced collagen production was demonstrated. Furthermore, incorporation of hydrogels was shown to protect cells from mechanical damage under dynamic loading conditions. In summary, a meniscus-like structure was engineered with potential for clinical use.

Kim *et al.* used a combination of 3D printing, electrospinning and a physical punching process to create composite PCL/alginate constructs with nanofibrous content and improved mechanical strength (Fig. 2.11). Electrospun layers of PCL/alginate were sandwiched by layers of micro-sized PCL struts; the final scaffold was then punched to create micro-sized pores travelling through the consecutive layers of electrospun and 3D printed material. Compared to pure PCL scaffolds, PCL/alginate composite scaffolds showed significantly enhanced cell viability at 7 days, alkaline phosphatase (ALP) activity and calcium deposition at 14 days and

greatly increased water absorption due to the improved hydrophilicity contributed by the scaffold alginate content [321].
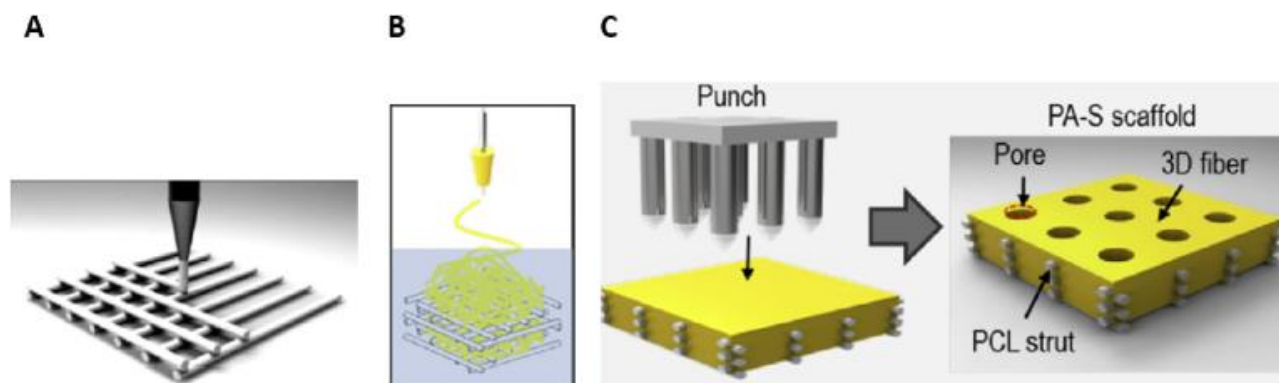
Figure 2.11 PCL/Alginate scaffold fabrication method. **(A)** 3D printing of micro-sized PCL struts **(B)** electrospinning of PCL/alginate onto PCL struts **(C)** punching process to create micro-sized pores in final PCL/alginate (PAS-S) scaffold. Adapted from Kim *et al.* [317].

Shim *et al.* used a multi-headed 3D bioprinter to create MSC-laden, collagen and hyaluronic acid hydrogel constructs reinforced by PCL. Designed to replicate an osteochondral plug, the biofabricated constructs appeared to integrate well with local bone and cartilage and remain mechanically stable following implantation in a rabbit knee. A porous, 3D PCL network was initially printed and an MSC-rich atelocollagen solution with added recombinant bone-morphogenic protein 2 (rhBMP-2) was dispensed into the bottom 4mm of the PCL network, to create an osteogenic layer. Immediately above the osteogenic layer, a hyaluronic-acid-based solution containing MSCs and TGF-β was dispensed to create a 1mm thick top layer to support chondrogenesis. Integration with host tissues was demonstrated by strong positive staining for calcium deposition, collagen deposition, cell viability and observation of excellent neo-cartilage formation comparted to PCL control scaffolds [326]. Malda *et al.* reinforced a GelMA

hydrogel matrix with PCL microfibers produced using a melt-electrospinning direct writing process [327]. This approach allowed for the production of PCL filament diameters as small as 5 μm, whilst the stiffness and deformation profile (shape of the stress–strain curve) of GelMA could be tailored to that of native cartilage by PCL reinforcement. Favourable cell viability was also found after at least 7 days of *in vitro* culture.

A range of other thermoplastic polymers similar in nature to PCL have also been incorporated into OTE attempts. Castro *et al.* also attempted to create a construct capable of replicating the osteochondral interface. Using a custom-built stereolithography 3D printer and tailored nano-ink, they created a construct with cartilaginous and osseous layers. A cartilaginous layer was created from polyethylene glycol (PEG) diacrylate hydrogel, core-shell PLGA nanospheres and chondrogenic TGF-β1). An osseous layer was also fabricated from nano-crystaline hydroxyapatite nanoparticles. Human bone marrow derived MSCs were directed to undergo chondrogenic and osteogenic differentiation *in vitro* within the biomimetic, graded 3D printed osteochondral construct [328].

Groll *et al.* utilised a UV crosslinking approach and a synthetic polymer to optimise the printability of hyaluronic acid with for chondrogenesis. Allyl-functionalized poly(glycidol)s (P(AGE-*co*-G)) was chosen as a cytocompatible cross-linker for thiol-functionalized hyaluronic acid, with incorporation of PCL and high molecular weight HLA performed to create mechanically stable and robust constructs for articular cartilage regeneration [315]. Embedding of human and equine MSCs in the gels and subsequent *in vitro* culture showed promising chondrogenic differentiation after 21 d for cells from both origins.

Gao *et al.* used inkjet bioprinting to co-print an acrylated PEG hydrogel with acrylated peptides [188]. Human MSCs were included in the composite hydrogel, which was exposed to ultraviolet

light to initiate simultaneous photopolymerization of the hydrogel during printing. The resulting scaffold demonstrated excellent cell viability of 87.9 ± 5.3% 24 hours after printing. Printed constructs containing MSCs were cultured for 21 days in chondrogenic media. Chondrogenic gene expression and compressive moduli were seen to significantly increase from day 7 to 21, with significant collagen and extracellular matrix deposition seen. The compressive modulus of the printed PEG-Peptide hydrogel exceeded 500 kPa, which is more than 100 times that reported for some natural hydrogels [329, 330].

2.5.4 **Scaffold-free Approaches**

Although biofabricated scaffolds are frequently used to facilitate cartilage biofabrication, self-assembly approaches have also been developed recently which use increasingly novel techniques to direct cartilage tissue development.

Yu *et al.* developed an interesting approach in bioprinting "tissue strands" without a hydrogel support to facilitate fabrication of biomimetic cartilaginous tissues (Fig. 2.12). Initially, harvested chondrocytes were expanded in number and then microinjected into long, tubular alginate capsules created using a co-axial nozzle. The chondrocytes were allowed to aggregate within the tubular alginate capsules, developing long strands of cylindrical cartilaginous tissue. Once matured, the tissue strands were released by dissolving the alginate tubes, leaving stands of cartilage which could then be 3D bioprinted through a specially adapted extrusion nozzle. Strands of cartilage printed in a layer-by-layer fashion were seen to unite and form larger cartilaginous structures. This approach therefore facilitated rapid chondrocyte fusion and maturation through self-assembly, enabled tissue bioprinting in solid form, did not need a liquid delivery medium during extrusion and facilitated native-like scale-up cartilaginous tissues to be developed [202].

In a further novel, self-assembly approach, Parfenov *et al.* performed scaffold-free, nozzle-free and label-free magnetic levitation of tissue spheroids to form cartilaginous tissue [331]. Chondrospheres produced from primary sheep chondrocytes using non-adhesive culture were exposed to gadolinium (Gd^{3+}) in culture media. Subsequently a magnetic field was produced, and with the aid of mathematical modelling, chondrospheres were predictably directed to move into a pre-designed 3D morphology, controlled by the magnetic field. Assembly of the chondrospheres into a 3D tissue construct was seen to occur, showing the promise of magnetic levitation for rapid 3D tissue biofabrication.
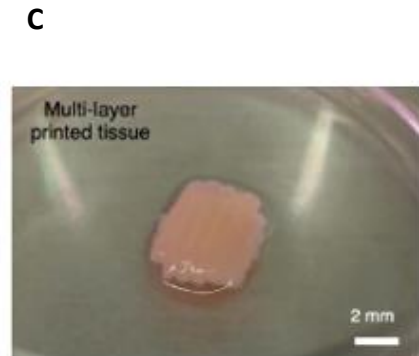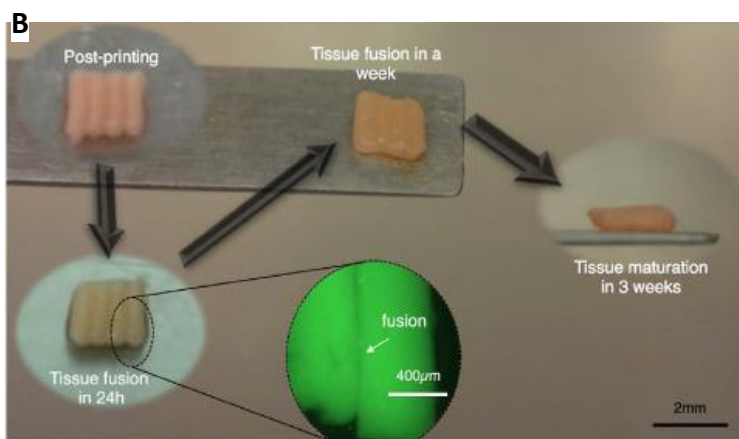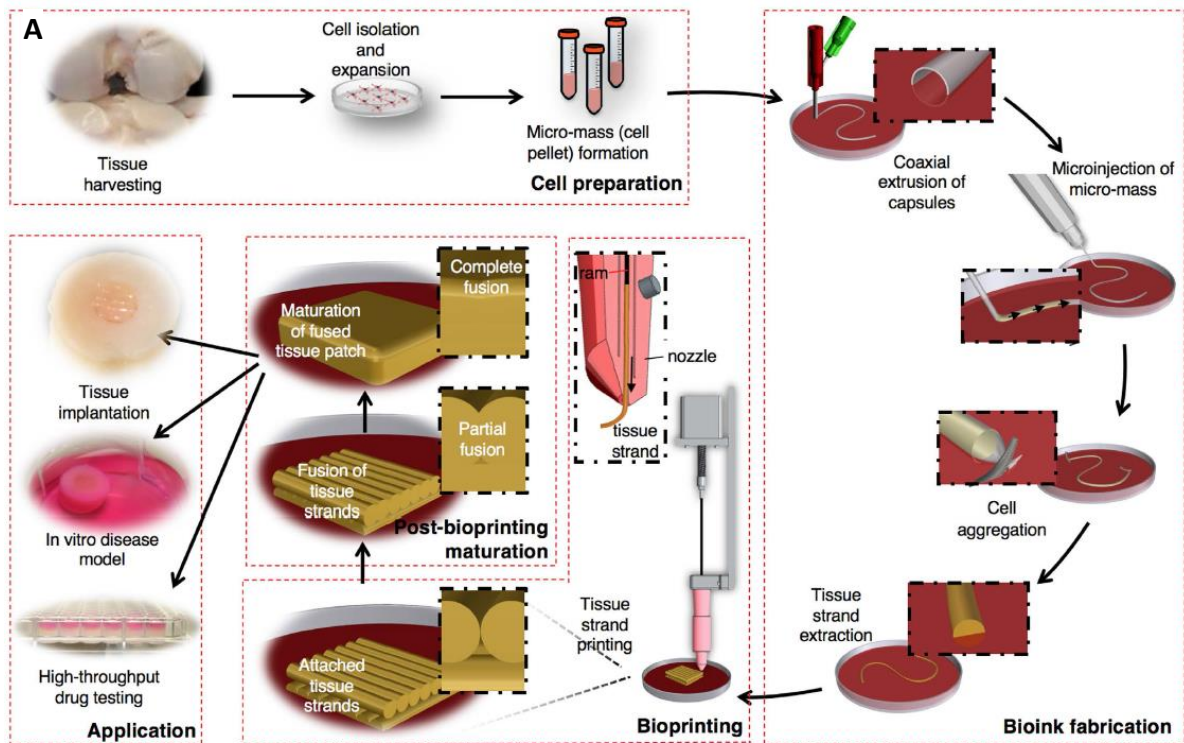
Figure 2.12 Biofabrication of cartilage using co-axial bioprinting and tissue strands. (A) Schematic elucidating the concept of tissue printing using tissue strands as a new bioink. (B) Images of printed tissue morphology over 3 weeks of incubation. (C) 3D bioprinted tissue patches prepared for 4 mm × 4 mm osteochondral defect with 2 mm thickness. Adapted from Yu *et al.* [202].

2.5.5 **Injectable Hydrogels for Cartilage Regeneration**

Injectable hydrogels for cartilage regeneration have attracted significant interest due to potential clinical benefits including the ability to perform minimally invasive injections and the capacity to mould hydrogels in-situ to match irregular patient defects [332-334]. Several natural and synthetic bioactive materials have been used to create injectable hydrogel scaffolds for cartilage regeneration. Examples that have been used successfully include hyaluronic acid, chitosan, collagen, elastin, alginate, glycopeptides [335-341] and synthetic polymers [342, 343].

Choi *et al.* created an injectable type-II collagen (Col II) and chondroitin sulphate (CS) composite hydrogel for cartilage regeneration [303]. The composite gel was crosslinked by exposure to visible blue light (VBL) in the presence of riboflavin. Whilst unmodified chitosan hydrogel supported proliferation and deposition of cartilaginous ECM by encapsulated chondrocytes and mesenchymal stem cells, incorporation of Col II or CS into chitosan hydrogels further increased chondrogenesis. Col II was found have the biggest impact on chondrogenesis and cell proliferation *in vitro*, thought to be related to integrin α10 binding to Col II, increasing cell-matrix adhesion.

Lee *et al.* created a composite collagen/HLA /fibrinogen hydrogel, which they inserted into rabbit osteochondral knee defects along with MSCs. Histological analysis of the scaffolds found glycosaminoglycans and type II collagen production within the extracellular matrix. After twenty-four weeks, the defects had been repaired with hyaline-like cartilage, demonstrating the strong therapeutic potential of this composite hydrogel [304].

HLA has a known ability to aid chondrocyte differentiation, ECM deposition and proliferation [344-348]. These effects are at least partly achieved by the presence of chondrocyte surface

receptors including CD44, which directly bind to HLA [349-351]. There have been several examples of injectable HLA-based hydrogels designed to take advantage of these properties.

Park *et al.* created an injectable HLA and methacrylated glycol chitosan (MeGC) hydrogel by photo-crosslinking with a riboflavin photoinitiator under visible light [352]. Increasing the crosslinking time significantly enhanced the compressive modulus of the hydrogels, although encapsulated cell viability also reduced. Incorporation of HLA into MeGC hydrogels also increased chondrocyte proliferation and deposition of cartilaginous extracellular matrix.

Chen *et al.* developed an injectable HLA/RGD-functionalized pectin hydrogel for cartilage tissue engineering [223]. Pectins are natural polysaccharides found in most primary cell walls and have excellent hydrophilic properties. They have been used within cartilage regeneration to act an ECM alternative, helping to immobilize cells [353, 354]. *In vitro* analysis found significant production of collagen, glycosaminoglycans and aggrecans with high cell viability after encapsulation in the HLA/RGD hydrogel. After 8 weeks of implantation in mice, the scaffold was well tolerated, with minimal inflammation and integration with surrounding subcutaneous tissues seen.

Yu *et al.* created an injectable, double cross-linked HLA/PEG hydrogel [355]. Enzymatic crosslinking resulted in fast gelation of the HLA/PEG hydrogel in 5 minutes, leading to the formation of an injectable material. ATDC-5 chondrocytes encapsulated in the hydrogel showed high viability and proliferation. The hydrogel could also recover from repeated compression and restore initial shape. Although *in vitro* analysis is required, the cell-friendly and anti-fatigue properties appear favourable for cartilage regeneration.

Guo *et al.* prepared hydrogels of HLA/chondroitin sulphate/collagen for cartilage regeneration [356]. This was achieved via collagen self-assembly and crosslinking of chondroitin sulphate-methacrylate (CSMA) and HLA-methacrylate (HAMA). An interpenetrating polymeric network structure was achieved through this process, partly replicating the structure of native cartilage extracellular matrix. The composite hydrogel was found *in vitro* to upregulate cartilage-specific gene expression and promote chondrocyte secretion of glycosaminoglycans and type II collagen.

Composite injectable hydrogels for cartilage regeneration have also been produced from degradable synthetic polymers such as PEG and poly (L-glutamic acid) [200, 342, 357-359]. HLA/PEG-based injectable hydrogels were prepared via a dual cross-linking by Dubbini *et al.,* with thermal gelation at occurring at 37 °C [360]. Through altering polymer content, degree of vinyl sulfonation and degree of thiolation it was possible to alter the gelation kinetics, mechanical properties, swelling and degradation times of the scaffolds. The composite hydrogels also supported MSC and fibroblast growth *in vitro* over 21 days.

2.5.6 **Summary of Techniques and Materials Used in Orthopaedic Tissue Engineering and Reconstruction**

A range of tissue engineering techniques (Table 2.2) and materials (Table 2.3) have been applied to attempt regeneration and reconstruction of orthopaedic tissues. A summary of their comparative benefits and limitations are displayed below.

Table 2.2 Summary of Tissue Engineering Technologies

Manufacturing Method	Benefits	Potential Limitations
Solvent casting/particulate leaching	• Relatively simple technique that allows creation of scaffolds with regular porosity, controlled composition and pore size.	• Use of organic solvents precludes cells and biomolecules being included directly in scaffolds. • Can be difficult to control pore shape and interconnectivity. • Limited thickness of structures and mechanical properties achievable.
Gas Foaming	• Eliminates use of chemical solvents.	• High pressures involved prohibits inclusion of cells and bioactive molecules directly into scaffolds. • Temperature labile materials may be denatured during compression moulding step. • Difficult to control pore sizes and ensure interconnectivity.
Emulsification Freeze-Drying	• Does not require use of solid porogen.	• Requires use of organic solvents. • Small pore size and porosity often irregular. • Long processing time.
Phase Separation	• Eliminates leaching step of porogen. • Can be combined with other techniques easily.	• Small pore sizes limit use. • Use of organic solvents inhibits use of bioactive molecules or cells during scaffold fabrication.
Electrospinning	• Creates scaffold with large surface area for cell attachment. • Simple and inexpensive technique.	• Organic solvents may be required, which can be harmful to cells. • Limited mechanical properties. • Difficult to incorporate precise microarchitecture into constructs.
3D Printing & Bioprinting • **SLA, SLS, FDM** • **Inkjet, microvalve, laser-**	• Complex 3D shapes with high resolution, controlled pore size & morphology can be fabricated. Improved capacity to incorporate vascular structures into constructs. • Some methods allow use of high cell concentrations.	• Some techniques are limited by printable materials. • Set up costs can be expensive for machinery.

| | assisted, microextrusion | |

Table 2.3 Comparison of Materials Used Within Orthopaedic Tissue Reconstruction

Material	Benefits	Potential Limitations
Hydrogels	• High water content/growth media inclusion allows for cell encapsulation and growth • Mechanical properties can be modified through crosslinking • Controlled drug/growth factor release possible • Ease of patterning via 3D printing to mimic tissue microarchitectures	• Mechanical properties limit use in load bearing constructs • Optimising printing conditions for individual hydrogels can be time consuming • Physical manipulation of constructs can be difficult • Loading evenly with cells can be challenging
Polymers	• Natural polymers can be derived from extracellular matrix, ensuring high biocompatibility and low toxicity • Biodegradable • Often contain biofunctional molecules on their surface • Synthetic polymers offer improved control over physical properties	• Natural polymers generally lack mechanical properties for load bearing • Pathological impurities such as endotoxin may be present in natural polymers • Synthetic polymers are often hydrophobic and lack cell recognition sites
Ceramics	• Osteoconductive and osteoinductive properties allow strong integration with host tissue • Similar composition to host bone mineral content • Can be delivered as granules, paste or in an injectable format	• Hard and brittle when used alone • May display inappropriate degradation/resorption rates, with decline in mechanical properties as a result

Bioactive glasses	• Osteoconductive, osteoinductive properties • Adapted into clinical prosthesis already	• Inherent brittleness • Difficult to tune resorption rate • Manipulation of constructs into 3D shapes to treat specific defects challenging • Potential for release of toxic metal ions
Metals	• Biocompatible • Superior strength • Superior mechanical properties can be advantageous in situations where slow bone growth likely	• Superior modulus can lead to stress-shielding • Poor biodegradability may result in further surgery/impairment of tissue ingrowth • Secondary release of metal ions may cause local and distal toxicity

2.6 **Growing Worldwide Arthroplasty Demand and Prosthetic Joint Infections**

Despite the promise and growing scale of biofabrication research, clinical translation remains limited, and an increasing number of patients with symptomatic arthritis are undergoing total joint replacement. Following Sir John Charnley's development of his pioneering total hip arthroplasty (THA) in 1961, the indications for joint replacement have rapidly expanded, with life-enhancing surgery now performed on millions of people worldwide each year suffering from diseased or damaged joints [15, 16, 58, 361-364]. In addition to hip and knee replacement, shoulder, elbow, and ankle arthroplasties are now available. The total number of patients with existing arthroplasties in place therefore continues to increase. Increasing demand is expected to continue, with exponential growth of up to 637% predicted for primary procedures by 2030 [365, 366].While the majority of joint arthroplasties provide pain-free function, a minority of around 1-2 % of patients will experience the devastating complication of prosthetic joint infection (PJI), defined as infection involving the joint prosthesis and adjacent tissue. With an increasing number of joint replacements being performed worldwide, the number of PJIs continues to increase [367-369]. Management of PJI is directed at removing infection from

within the joint and restoring function. This often requires complex treatment strategies including multiple surgical revisions with removal of implants and long-term antimicrobial treatment. This translates into significant morbidity for patients and even risk of mortality in cases where PJI results in systemic infection or sepsis developing. The economic impact of PJI is also significant, with the cost to treat a single PJI up to 6-fold the cost of the primary implantation [370, 371].

2.6.1 Pathogenesis of PJI and Organisms Commonly Involved

Intra-operative contamination with microorganisms is thought to account for around two thirds of PJIs [372]. Following surgery, wound infection can also progress to involve the prosthesis, due to incompletely healed superficial and deep tissue planes. Early infections are often the result of virulent species such as *Staphylococcus aureus,* whilst less invasive organisms such as coagulase-negative staphylococci may present several months or even years after surgery with subtle signs and symptoms including unexplained joint pain and implant loosening on radiographs [372].

Unfortunately, following implantation prosthetic joints are also susceptible to haematogenous seeding of bacteria from distal primary infections. Common primary sources of infection and related bacteria include skin and soft tissue infections (e.g. *Staphylococcus aureus*), respiratory tract infections (e.g. *Streptococcus pneumoniae*), gastrointestinal infections (e.g. *Salmonella, Bacteroides*) and urinary tract infections (e.g. *Escherichia coli, Klebsiella, Enterobacter* spp.). The risk of seeding is higher when a patient develops a bacteraemia in the context of a virulent organism; *S. aureus* bacteraemia is thought to be associated with a 30 to 40% risk of hematogenous seeding of *in situ* arthroplasties [373]. This compares to a reported risk of only

3 to 10% risk of infection of native joints during *S. aureus* bacteraemia, highlighting the susceptibility of prosthetic implants to hematogenous seeding [374-376].

2.6.2 Role of Biofilm in Implant Infections

Central to the pathogenesis of prosthetic joint infection is the formation of bacterial biofilm. Biofilms can be defined as 3D structured communities of bacterial cells enclosed in a self-produced polymeric matrix, attached to a solid surface or substratum [377-379] . Nearly all (99.9%) micro-organisms have the ability to form biofilm, allowing bacteria to adhere and grow on a wide range of biological and inert surfaces, including joint replacements, heart valves and a range of native bodily tissues [380, 381]. Within the protective environment of a biofilm, bacteria increase their tolerance to host immune defences and antibiotics up to 1000%, whilst their ability to exchange genetic information is also greatly increased [382, 383]. Bacteria in established biofilms also have low growth rate and can develop resistant subpopulations (so-called "persisters"). Eradication of infection once biofilm has formed is therefore hugely challenging, and often leads to chronic infection, requiring surgical removal of implants, prolonged antimicrobial therapy and can even lead to mortality [384]. The presence of foreign material such as a joint implant reduces the minimal infecting dose of bacteria such as *S. aureus* more than 100,000-fold, as bacteria are able to adhere to the avascular implant surface with diminished threat from circulating immune cells and antimicrobials [385]. In the United States of America alone, there are 17 million new biofilm-associated bacterial infections that lead to estimated health care costs of $94 billion and 550,000 deaths each year [7].

2.6.3 Biofilm Formation

Biofilm formation can be described as a step-wise process, beginning with the irreversible attachment of bacteria to inanimate and living surfaces (Fig 2.14). Once microorganisms have

gained access to a joint, they are able to immediately begin adhering to the implant or native joint surface. Cellular proliferation and cell to cell adhesion occurs, leading to formation of microcolonies and initial deposition of extracellular matrix containing polysaccharides, proteins, and/or extracellular DNA. Biofilm composition and level of production can vary between and even within organism types. Once established, the biofilm undergoes structural maturation and may develop water-filled channels within the matrix, facilitating nutrient transport [386]. Gene expression also changes as bacteria communicate through cell-to-cell signalling in a process known as quorum sensing (QS), altering processes including sporulation, virulence factor secretion and biofilm formation [387, 388]. Mature biofilm formation takes around four weeks to occur; during this process, gradual accumulation of waste products and depletion of resources can occur, causing micro-organisms to enter a slow- or non-growing (stationary) phase. Eventually regions of the biofilm spontaneously disperse as bacteria enzymatically dissolve the matrix. Dispersed cells can quickly revert to their planktonic (free swimming) form to colonise other sites in the body, whilst retaining properties such as antimicrobial resistance [389].

①:Reverible attachment
②:Irreversible adhesion to a substratum
③:Microcolony formation occurs
④:Maturation of the biofilm
⑤:Biofilm dispersion and bacteria detachment
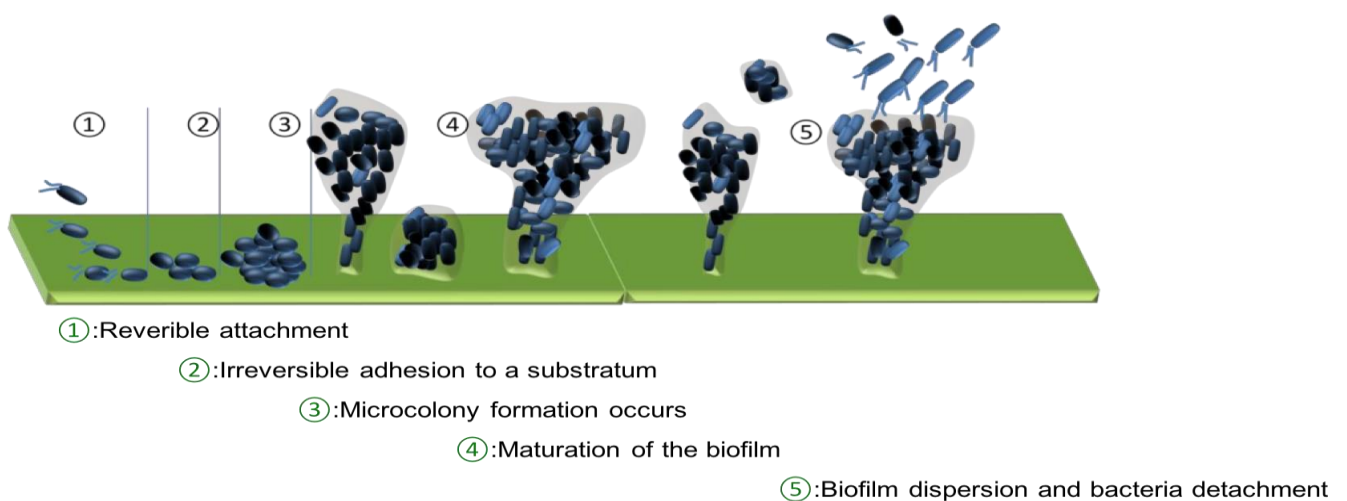
Figure 2.14 Biofilm maturation is a complex developmental process involving five stages. 1. Single free-floating eukaryotic cells land on a surface and begin to attach. 2. Bacterial cells aggregate and become irreversibly attached to the surface through secretion of an extracellular polymeric substance (EPS), comprised of sugars, proteins, and nucleic acids like DNA. 3. Growth and division of bacteria occurs along with secretion of further layers of EPS. 4. The biofilm matures, developing increasingly complex internal organisation and structure. 5. Segments of the biofilm disperse, releasing bacteria to undertake further colonization [379].

2.6.4 Diagnosis of PJI

Diagnosis of PJI can be performed using a combination of diagnostic tests and physical examination. Clinically patients may present with systemic features of an acute infection, including fever, with localising signs and symptoms also present including joint pain, joint effusion, erythema, warmth and persistent wound leak or dehiscence. More indolent or chronic infections may present with subtler signs, such as chronic pain and evidence of implant loosening on radiographs. However, similar features can be found in the context of aseptic failure of an implant. More overt features such as a discharging sinus tract or evidence of pus or a collection around the joint may also be evident [385, 390].

Investigations performed for PJI include blood tests, histopathology, microbiology and imaging studies. Blood tests such as white blood cell count (WBC), erythrocyte sedimentation rate (ESR), C-reactive protein (CRP) or procalcitonin (PCT) can all suggest the presence of an acute infection; however, all lack sufficient sensitivity or specificity to diagnose or exclude PJI, and in the context of recent surgery are often raised due to post-surgery inflammation [380, 385, 391].

Joint aspiration is a more targeted investigation, with the sensitivity of synovial fluid culture from aspirated fluid reported to range from 45% to 75% and a specificity of 95%. However, it can require up to 14 days incubation to detect some low-virulent and difficult-to-detect pathogens. Aspiration of deeper joints such as the hip often requires radiological guidance, whilst aspiration of prosthetic joints should ideally be performed in a sterile environment such as an operating theatre to reduce risk of iatrogenic introduction of infection into a joint. Further analysis of synovial fluid leukocyte count and percentage of granulocytes represents a simple test for PJI, with a cut-off at 2000 leukocytes/µl and 70% granulocytes reported to help differentiate between PJI and aseptic failure [392, 393]. Synovial fluid can also be analysed for the presence of Alpha (α)-defensin, an antimicrobial peptide released by activated neutrophils in response to bacterial infection. Qualitative analysis can be performed of α-defensin using disposable test kits that provide results within 10 minutes, with reported sensitivity ranging from 54 to 77% and a high specificity of 99% [394, 395].

In patients requiring surgical debridement, multiple intra-operative tissue samples are usually taken and sent for culture, with reported sensitivity ranging from 65% to 94% [392, 396]. Further analysis of surgical tissue samples can be performed using histopathology, with the number of neutrophils visualised on high magnification of samples used to diagnose PJI with high reported sensitivity and specificity [392, 393]. Contrastingly, superficial wound swabs or samples taken from sinus tracts are often misleading as they detect superficial colonizing bacteria rather than the infecting micro-organisms in deeper tissue accessed during surgery. Implants that are removed during surgery can also be sent for culture alongside tissue samples; sonication can be performed in water with low-frequency ultrasound waves to detach biofilm from the implant surface, with the resultant fluid cultured. Sonication fluid can yield a sensitivity of 79% and a specificity of 99% for the diagnosis of PJI. However, there is potential

for false-negative results to occur when implants with antibiotic-loaded bone cement are sonicated, and most modern bone cements are routinely antibiotic-loaded [393, 397, 398]. In addition to being sent for culture, sonicated and synovial fluid can also be subjected to polymerase chain reaction (PCR). PCR can identify pathogens in synovial or sonicated fluid with a high sensitivity (>80%) and (90%) specificity in patients on antibiotics. However, limitations include high costs and susceptibility to contamination [385, 399, 400]. Testing synovial fluid for the presence of leucocyte esterase offers a further point-of-care test with high sensitivity (>80%) and (>90%) specificity for PJI. However, nearly 30% of test strips in one study were unreadable due to blood, debris, or provided indeterminate results [401, 402].

Imaging of the affected joint can also help support a diagnosis of PJI, although is rarely a definitive test. Plain radiographs are neither sensitive nor specific but can detect established features of PJI including periprosthetic lucency, effusion, adjacent soft tissue gas or fluid collection, or new periosteal bone formation [403]. More advanced imaging modalities such as CT and MRI allow evaluation of periprosthetic tissues for signs of infection and produce more detailed images than plain radiographs. However, imaging artefact can occur in the presence of metal implants and evaluation of bony structures is often sufficient on plain radiographs. Nuclear medicine (NM) imaging techniques can also be utilised; three-phase bone scintigraphy is perhaps the most widely used NM imaging technique. Three-phase bone scintigraphy relies upon uptake of a radioactive isotope-labelled compound such as technetium-99m (^{99m}Tc) into bone. The labelled ^{99m}Tc accumulates in areas of high metabolic activity and emits gamma rays that can be detected by a gamma camera. However, the technique lacks specificity as asymptomatic patients frequently have uptake detected by imaging in the early years after

surgery [404]. Overall, it serves to help rule out infection rather than definitively diagnose PJI, and is therefore of more limited clinical utility [404].

2.6.5   Limitations of Current Techniques of Diagnosis

Despite the range of modalities available for investigating PJI, the gold standard for PJI diagnosis remains culture of periprosthetic tissue or synovial fluid. Bloods tests, imaging modalities and analysis techniques previously discussed suffer from limitations in investigating PJI including lack of specificity, high cost, limited availability, patient exposure to radiation and susceptibility to contamination. Unfortunately, up to 20% of patients develop culture-negative PJI with no bacterial diagnosis reached, even with synovial fluid culture and sampling of periprosthetic tissue. This makes elimination of infection and use of appropriately targeted antimicrobials more challenging and can lead to increased morbidity and mortality for patients [385, 394, 405-407]. Demand for a novel technique to diagnose PJI therefore exists; a cost-effective test that could non-invasively diagnose PJI due to specific bacteria in a rapid and reproducible manner at the bedside or clinic would represent a major step forward in PJI diagnostics.

2.6.6   Raman Spectroscopy – A Potential Novel Option for Diagnosis?

Raman spectroscopy is a molecular spectroscopic technique that utilizes the interaction of light with matter to gain insight into the chemical make-up of compounds. Raman can probe the chemical composition of materials and detect vibrational, rotational, and other states in a molecular system. Detection of bacterial species and bacterial biofilms in samples has already been demonstrated using Raman technology [408-410] . In brief, Raman spectroscopy works by shining a monochromatic light source onto a sample and detecting the scattered light. Most

scattered light is at the same frequency as the excitation source; however, a small amount of the scattered light shifts in energy from the input laser frequency because of interactions between the incident electromagnetic waves and the vibrational energy levels of the molecules in the sample. Plotting the intensity of the shifted light against the frequency produces a Raman spectrum of the sample [411-413]. Unfortunately, very weak signal is generated using conventional Raman spectroscopy as very few incident electromagnetic waves, or photons, undergo a Raman shift. Alternative techniques have been developed to enhance signal, including Surface enhanced Raman spectroscopy (SERS) and Spatially offset Raman spectroscopy (SORS), that can generate signal intensities 10^{10} to 10^{11} magnitude greater than conventional Raman [414]. Spatially offset Raman spectroscopy (SORS) is a technique that allows Raman signals to be obtained at depth by offsetting the point of collection of the scattered light from the laser-illumination, allowing highly accurate chemical analysis beneath obscuring barriers [415, 416]. Surface enhanced Raman scattering (SERS) also allows enhancement of several orders of magnitude of Raman signal by modifying the surface upon which an analyte material is to be placed. When a molecule is adsorbed onto a metal NP surface, enhancement in scattering of the molecularly specific Raman reporter is observed, allowing greatly enhanced signal detection [415, 417]. SERS has already been applied by by Haisch *et,al*. to perform chemical analysis of a biofilm matrix using SERS-active silver nanoparticles [418]. Surface enhanced Raman scattering with spatially offset Raman spectroscopy (SESORS) combines the benefits of SORs and SERs to achieve even greater interrogation of samples at depth [419]. Raman has the clinical benefit of being a potential non-invasive test, avoids use of ionizing radiation and has already shown potential for detection of different bacteria and related biofilm [408-410]. Successfully applying it to aid the novel diagnosis of PJI could therefore be of great clinical benefit.

2.6.7 Current Methods of Antimicrobial Sensitivity Testing (AST) and Related Limitations in Biofilm Infections

Following successful diagnosis of an infecting organism, it is important to determine the effectiveness of any planned antimicrobial therapy. Whilst the effectiveness of antimicrobial therapy can be predicted once the infecting organism is known, the presence of resistance can confound "best guess" treatment plans. The minimum inhibitory concentration (MIC) of antimicrobial agents (defined as the lowest concentration of an antimicrobial agent at which visible bacterial growth is inhibited after overnight incubation) is frequently calculated during AST to assess antimicrobial efficacy and bacterial resistance [10]. Methods to determine the MIC based on 2D planktonic cultures of bacteria are well established [11]. However, determining the minimal biofilm eradicating concentration (MBEC) in biofilm infections is much more challenging. This is primarily because *in vivo* biofilm formation is 3D in architecture, which differs to most currently available laboratory models that tend to involve 2D biofilm culture [12-14]. AST of planktonic bacteria therefore tends to give misleading results that do not necessarily reflect the increased antimicrobial tolerance of bacteria living in a 3D biofilm [15, 16]. This has significant clinical implications; for example, antimicrobial agents are usually chosen on the basis of their efficacy against 2D planktonic cultures which are more sensitive to treatment than 3D biofilms. Clinically this is well demonstrated by cystic fibrosis patients, where treatment of *P.aeruginosa* infection with antibiotics originally developed against planktonic cultures often becomes ineffective once biofilm formation occurs [15]. To develop novel antimicrobials capable of disrupting biofilm formation and resistance in future, 3D *in vitro* biofilm models more representative of clinical infection are therefore required.

2.6.8 Potential Role for A Novel 3D Biofilm Model

Frequently used 2D biofilm culture methods attempt to simulate the *in vivo* environment by focusing on replicating selected parameters including nutrients and, importantly, fluid flow including drip flow [16], rotating disk [17], microfluidics [18], and flow chamber architecture [19]. Unfortunately, none of these methods mimic the complexity of the 3D microenvironment and host defense mechanisms [20] and are unable to produce biofilm thicknesses beyond 100 µm [21, 22]. In contrast to the current *in vitro* models, *in vivo* biofilms can grow beyond 1000 µm in size and are often found embedded within a host's extracellular matrix, leading to interactions with the host immune system which can further alter biofilm morphology and size [1, 23].

3D bioprinting has developed rapidly as a technique that can deposit living cells and biomaterials in user-defined patterns to build complex tissue constructs "from the bottom up" [24-27]. While there are elegant approaches on 3D bioprinting bacteria and their aggregates [28-32], there has been no report on demonstrating the formation of mature bacteria biofilms. However, the capacity to reliably and reproducibly 3D bioprint bacterial biofilms have several potential benefits. Embedded bacteria have been shown to have increased metabolic activity, antimicrobial resistance (AMR) and plasmid stability compared to bacteria grown in 2D [32, 33]. 3D bioprinted bacterial biofilms therefore could potentially mirror *in vivo* bacterial growth and behavior more closely than traditional 2D models, increasing the potential to investigate critical bacterial processes including QS and antimicrobial biofilm penetration [34, 35]. 3D bioprinting also increases the potential to produce biofilm constructs with predesigned dimensions, with a high degree of control possible over biofilm thickness and dimensions. Other benefits of 3D bioprinting biofilm include the potential creation of microbial fuel cells [35], biosensors [36] and biotechnological applications [37-39].

2.7 **Summary and Research Aims**

The overall aim of this thesis is to utilise a 3D biofabrication approach to study two pressing areas within clinical orthopaedics; the regeneration and reconstruction of osteochondral tissue, and the study and treatment of bacterial biofilms that aid infection of joint replacements and propagation of antimicrobial resistance.

On reviewing currently available osteochondral biofabrication methods it is apparent that several ongoing challenges exist. The high-water content of hydrogels that are commonly used can have mixed benefits; whilst allowing replication of the hydrated native ECM, they often display poor mechanical properties [245, 281, 282]. To enable high resolution and consistent bioprinting, soft hydrogels must therefore be engineered to combine properties including rapid gelation, shear-thinning and minimal post-printing swell with mechanical stability within culture conditions [72, 73]. To this end, focus will be placed on developing a composite bioink targeting osteochondral defect repair capable of fusing mechanical stability within culture with the biocompatibility often provided by lower-viscosity, naturally derived hydrogels [164, 283-286]. To enhance the complexity and scale of constructs biofabricated using our composite bioink, techniques such as FRESH bioprinting (Fig. 2.8.B) will also be examined. FRESH bioprinting allows post-bioprinting crosslinking to be performed within a temporary gelatin support matrix, and thus minimises the mechanical properties that bioinks must possess prior to bioprinting. Development of a hydrogel that can undergo combined methods of crosslinking (including UV and ionic crosslinking) will also be explored, to enhance the stability of hydrogel constructs post-bioprinting. A final aim will be to apply our composite bioink in an injectable format to aid treatment of osteochondral defects *in vitro*.

Focussing on investigation of AMR, a key aim of this thesis will be to biofabricate clinically relevant 3D bacterial biofilms that facilitate investigation of biofilm growth, antimicrobial treatment and joint infection detection. It is hoped that some of the approaches that are developed in our attempts at biofabrication of osteochondral tissue can also be translated to aid successful 3D bioprinting of bacteria. Previous literature has developed elegant approaches to 3D bioprinting bacteria, often using alginate bioinks, without demonstrating mature biofilm formation [28-32]. By developing a novel bacterial bioink with optimised crosslinking and therefore enhanced stability in culture, we hope to demonstrate formation of mature 3D bioprinted bacterial biofilms and then investigate 3D biofilms further.

3 Materials and Methods

3.1 Biofabrication for Osteochondral Regeneration

3.1.1 Mesenchymal Stem Cell Culture

Human bone marrow derived mesenchymal stem cells (hBMMSCs) were commercially sourced (Donor ID – 28940, Lot No - 0000483199, Date Cryopreserved - 10th June 2015, Lonza) at passage 3. Cells were initially seeded at a density of 5,000 cells per cm^2 in tissue culture flasks and maintained in Dulbecco's Modified Eagle Medium (Gibco™ DMEM, low glucose, GlutaMAX™ Supplement, pyruvate) supplemented with 10% fetal bovine serum (FBS) and 1 mg/mL penicillin and 1 U/mL streptomycin (Life Technologies, Paisley, UK). hBMMSCs were incubated in 36.0-37.5°C, $5.0\pm0.5\%$ CO_2 and 90% humidity with medium changed every 3 days. At near 90 percent confluency, cells were passaged. hBMMSCs were harvested between passage number 3 and 7 for use in experiments in this thesis.

3.1.2 Osteogenic Differentiation of Mesenchymal Stem Cells

Osteogenic media was prepared from commercial osteogenic basal medium (Lonza, Slough, UK) supplemented with hMSC osteogenic SingleQuots™ (Lonza, Slough, UK) which consisted of growth factors and supplements (dexamethasone, ascorbate, mesenchymal cell growth supplement (MCGS), L-glutamine, penicillin/streptomycin, b-glycerophosphate). Tissue culture flasks were seeded with 3.1 x 10^3 hBMMSCs per cm^2, with 0.3ml of temperature equilibrated low-glucose D-MEM containing 10% FBS and 1% Penicillin-Streptomycin also added per cm^2 of tissue culture area (Life Technologies, Paisley, UK). Cells were allowed to adhere to the tissue culture area for 24 hours before the supplemented DMEM was replaced with osteogenesis induction medium. Osteogenesis media

was replaced every 3-4 days for 3 weeks. Control hBMMSCs were fed with supplemented low-glucose DMEM on the same schedule.

3.1.3 Adipose Derived Stem Cell Culture

Adipose-Derived Stem Cells (ADSCs) were received from University of Glasgow Centre for Cell Engineering. ADSCs were initially seeded at a density of 5 000 cells per cm^2 in tissue culture flasks and cultured in Alpha Minimum Essential Medium (Gibco™ MEM α, no nucleosides) supplemented with 10% FBS and 1% penicillin/streptomycin (Life Technologies, Paisley, UK). ADSCs were incubated at 37°C, 5% CO_2 and 90% humidity with medium changed every 3-4 days. At near 90 percent confluency, cells were passaged. ADSCs were harvested between passage number 3 and 7 for use in experiments in this thesis.

3.1.4 Human Chondrocyte Culture

Primary human chondrocytes (HCs) isolated from normal human hip and knee joint articular cartilage were commercially sourced at passage 2 (product number C-12710, lot number 445Z012.3, PromCell, Germany). HCs were initially seeded at a density of 10 000 cells per cm^2 in tissue culture flasks and cultured in chondrocyte growth medium (product number C-27101, PromoCell, Germany) supplemented with 1% penicillin/streptomycin (Life Technologies, Paisley, UK). HCs were incubated at 36.0-37.5°C, 5.0±0.5% CO_2 and 90% humidity with medium changed every 2 -3 days. At near 90 percent confluency, cells were passaged. HCs were harvested between passage number 3 and 7 for use in experiments in this thesis.

3.1.5 Spheroid Creation

Cell spheroids were created from hBMMSCs, ADSCs and HCs using a methodology adapted from Dhalmann *et al.* [1]. The following technique allowed the micro-structure present on the bottom surface of an Aggrewell™ 400Ex micro-well plate (Stem Cell Technologies, Grenoble,

France) to be replicated onto an agarose mould. Cells were then seeded onto the agarose micro-well mould and allowed to mature into spheroid bodies.

3.1.5.1 Creation of Silicon Masters

Silicone masters were generated by a soft lithography method, producing templates with a defined pattern that would allow the subsequent production of agarose micro-wells (Fig. 3.1). Commercially available AggreWell 400 Ex 6-well plates (Stem Cell Technologies, Grenoble, France) were used as template. Each well contained a structured PDMS surface with an array of approximately 4700 inverse-pyramidal microwells. Approximately 15 mL of 1:1 mixed addition-curing duplicating silicone with hydrophilic properties (Hydrosil A & B from Siladent, Goslar, Germany) was mixed and decanted into each well. Trapped air was removed from liquid silicone by centrifugation at 55g for 30 s using an Eppendorf 5810R cell culture centrifuge with a swing bucket rotor (Hamburg, Germany). Centrifugation also promoted interdigitation of the curing silicon with the inverse pyramidal microwells. After curing for approximately 20 minutes, the resulting solidified silicon master was carefully released from the Aggrewells 6-well plate (Fig. 3.1 A). Reusable silicone masters were washed thoroughly with cell culture grade water, heat sterilized (autoclaved for 20 min at 121°C), and air dried in a sterile laminar flow hood prior to each experiment.

3.1.5.2 Creation of Agarose Microwells

As a non cell-adhesive substrate, 3 % (w/v) agarose powder (NEEO ultra quality, Roth, Karlsruhe, Germany) was dissolved by boiling in DMEM (DMEM, low glucose, Life Technologies, Paisley, UK), avoiding water evaporation. Liquid agarose/DMEM was directly filter-sterilized (0.2 μm pore size, Corning® syringe filters) and cooled to approximately 65°C. Liquid agarose/DMEM was then aliquoted into 6-well plates

(Corning® Costar® TC-Treated Multiple Well Plates, Life Technologies, Paisley, UK) using 5 mL/well. The structured surface of a sterilized silicon master was carefully placed on top of the liquid agarose-DMEM, and silicone masters allowed to sink down. 6-wells were partially immersed in ice water to aid agarose solidification (Fig. 3.1 B). After agarose solidification and silicon master removal, resulting agarose microwell plates, i.e. mirror-inverted patterned agarose-DMEM surfaces, were equilibrated for 12 h or overnight within the appropriate cell culture medium at 37^{0C} prior to any cell culture (Fig. 3.1C).

3.1.5.3 Seeding Agarose-DMEM Microwells with Cells

hBMMSCs, ADSCs or HCs were harvested and resuspended to get a final concentration of 4.7×10^5 cells/ml in relevant cell media (low glucose DMEM, MEM α or chondrocyte growth media depending on cell type). 1ml of cell suspension was aliquoted into each well of a 6 well plate. The resulting seeding density was calculated as 100 cells and 0.2 µl medium per microwell. Plates were incubated for up to 3 days at 36.0-37.5°C, $5.0 \pm 0.5\%$ CO_2 and 90% without medium change. On day 3, spheroids were detached from the agarose surface by gentle tapping and collected in the centre of the dish by slow orbital movements. For harvesting, a lateral part of agarose-DMEM was cut away using a sterile scalpel, and spheroids were washed into the resulting gap and aspirated using a 1ml pipette.

(A) Creation of Silicone Masters

Structured surface on bottom of Aggrewell™ plate

Hydrophilic Silicone solution

Solidified silicone master is peeled off the bottom.

(B) Creation of Agarose Microwells

Liquid agarose/DMEM dispensed into 6-well

Silicone Master applied

Silicone master is peeled from solid agarose

Ice water surrounding 6-well helps cure liquid agarose inside prior to removal of silicone master
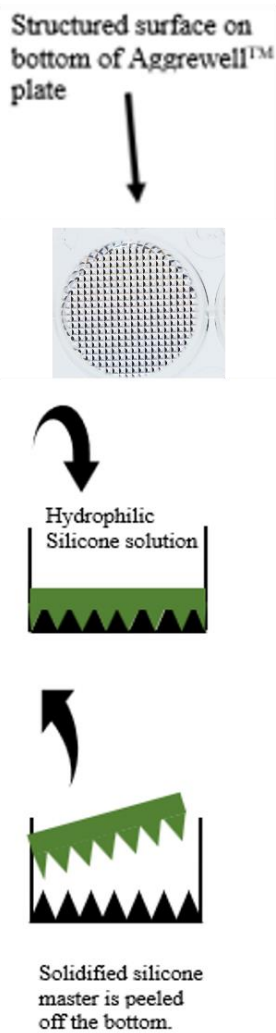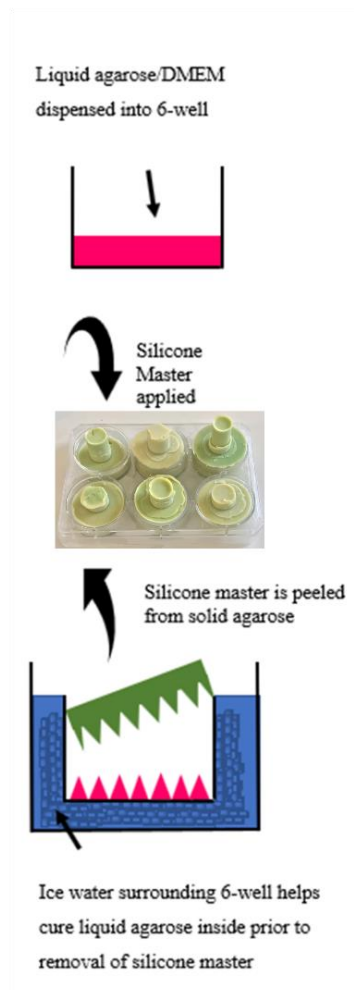
(C) Spheroid Body Development

Agarose wells seeded with cells (A), and cells allowed to mature over 24 (B), 48 (C) and 72 hours (D).
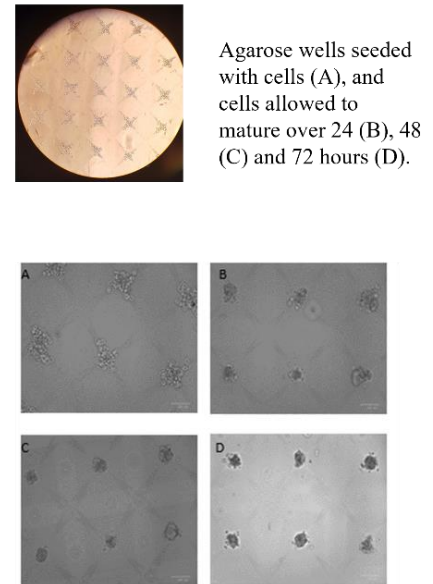
Figure 3.1 Formation of spheroids using microwells. **(A)** Hydrophilic silicone is cast onto the structured bottom surface of an Aggrewell™ plate and centrifuged to release bubbles. Once set, silicone master is peeled off. **(B)** 3% (w/v) agarose solution is aliquoted onto the bottom of a 6-well plate. A sterilised silicone master was placed on top of Agarose solution and 3% (w/v) agarose solution was left to solidify and silicone master is peeled off, leaving a mirror inverted patterned agarose surface. **(C)** Agarose wells are equilibrated with cell culture media, seeded with a calculated density of cells,

and centrifuged to force cells to settle into the wells. Spherical aggregates are then harvested from the culture wells at around 72 hours incubation.

3.1.6 **3D printing system**

A commercially sourced FDM-based 3D printing system (Stealth-330 model by ROKIT, South Korea) was used to print thermoplastic polymer scaffolds from substrates including PCL and PLA (Fig. 3.2). The FDM printer had a build size of 290 x 180 x 260 mm, a high efficiency particulate air (HEPA) and activated carbon filter, a metal 0.4 mm-diameter nozzle and a 40 x 30 cm printing bed with a maximum print layer resolution of 25 µm.

3.1.7 **Design and 3D Printing of Biocompatible Thermoplastic Scaffolds Using Polylactic Acid (PLA) and Polycaprolactone (PCL)**

Scaffolds with varying porosity and dimensions were designed using Autodesk® Netfabb® software (Autodesk®, Inc, USA) and exported as a Standard Tessellation Language (STL) file. Open-source slicer software (NewCreatorK slicing software, 3EDISON, South Korea) was then used to load the STL files and generate G-code files; G-code is a form of numerical control (NC) programming language that can control the actions of automated machines including 3D printers. A built-in USB port on the 3D printer allowed upload of G-codes files. Alteration of the G-code allowed 3D printing parameters including layer thickness, infill pattern, infill density, print speed and extrusion multiplier to be carefully selected and optimised.

A range of structures were printed with PCL and PLA to optimize print settings; a range of print speeds, layer heights, structure infills and temperatures were trialled for PCL and PLA. Larger structures including proximal tibia and knee replacement inserts were printed from anatomically accurate CAD models (Fig. 3.2 D) with reliable and repeatable print settings found; this permitted gradually larger scale models to be fabricated (Fig. 3.2 E).

For printing PCL, optimum print results were found with the nozzle temperature set to 170°C and the print bed temperature to 45° C. The printing speed was adjusted to 40 mm/s, the filament input flow to 60%, model fill density to 90% and finally, the layer height to 0.1 mm. For printing PLA, nozzle temperature was set to 230°C and the print bed temperature to 85° C, with all other settings kept constant. PCL filament was used with >99% purity and 1.145 g/cm^3 density (3D4Makers, Haarlem, Netherlands). PLA filament was used with >99% purity and 1.25 g/cm^3 density (3D4Makers, Haarlem, Netherlands). The filament was fed into the 3D printer and the scaffolds were printed under non-sterile conditions. Scaffolds with a range of pore sizes were successfully printed from PLA and PCL (Fig. 3.2 C).
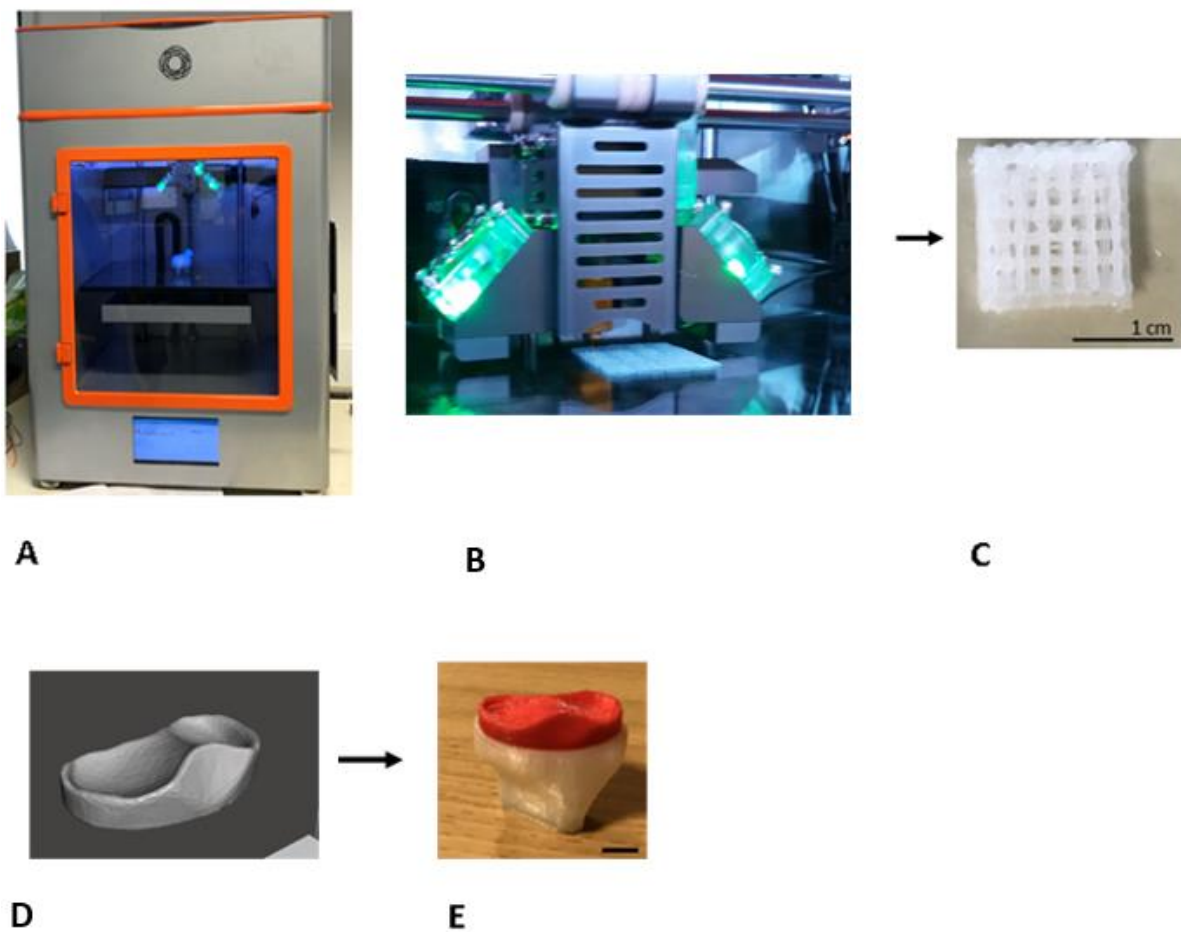
Figure 3.2 Optimising FDM 3D printing. **(A)** ROKIT Stealth 3000 3D printer during motion. **(B)** Close up of print bed during PCL scaffold printing. **(C)** example of PCL scaffold produced by ROKIT. **(D)** CAD model of proximal tibia knee replacement component. **(E)** 3D printed proximal tibia and knee replacement produced from CAD model using PLA. Scale bar = 1cm

3.1.8 Scaffold Surface Treatment with Sodium Hydroxide (NaOH)

PCL scaffolds were immersed in NaOH in an attempt to improve surface hydrophilicity. Initially, two incubation time points (1, 4 h) and two different concentrations of NaOH (Sigma-Aldrich) (1 and 4 M) were examined. 3D printed scaffolds were immersed in NaOH solution and placed on an orbital shaker (70 RPM) at room temperature for the desired immersion time. Following this, the treated PCL scaffolds were washed three times in deionised (DI) water and soaked in DI water overnight. Before cell seeding, the scaffolds were sterilized by soaking in 70% ETOH for 30 min and washed extensively with PBS.

3.1.9 Bioprinting Systems

For printing hydrogels, two different extrusion-based systems were utilized. Both bioprinters produced 3D constructs by coordinating the motion of a syringe dispenser. The dispenser deposits extrudate consisting of cell-containing hydrogel, or bioink, on a stationary Z-platform. As successive layers of extrudate are deposited, the z-platform moves downwards allowing structures to be bioprinted from the bottom up, layer-by-layer.

In initial work a commercially sourced, pneumatic micro-extrusion based system was used (Inkredible 3D Bioprinter, Cellink, Sweden). The Inkredible has 2 pneumatic-based extrusion printheads with adjustable print nozzle diameters, a UV LED curing system (365 or 405 nm), build volume of 130 x 80 x 50 mm, print layer resolution of 100 μm and adjustable print pressure ranging from 5 to 400 kPa (Fig 3.3).

A three-axis (X-Y-Z), single nozzle 3D extrusion bioprinter was subsequently developed in our lab (Fig 3.4). This system utilises a mechanically driven print syringe to produce micro-extrusion through adjustable print nozzle diameters. This contrasts with the pneumatic pressure used to drive the syringe in the Inkredible bioprinter.

Bioprinting designs with varying porosity and dimensions were created using Autodesk® Netfabb® software (Autodesk®, Inc, USA) and exported as an STL file. Open-source slicer software (Slic3r software version 1.2.9, Rome, Italy) was used. This allowed print settings including layer thickness, infill pattern, infill density, print speed and extrusion multiplier to be carefully selected and adjusted prior to printing different hydrogel bioinks. Prior to usage the bioprinters were sterilized via 30 mins UV exposure and thoroughly wiped down with 70% ethanol. Sterility was maintained during bioprinting by placing the bioprinter in a laminar flow cabinet. Sterile 5ml leur-lock syringes containing bioink were attached to 25 gauge, 0.5inch long, standard blunt needles or 30 gauge, 1.25 inch long, standard blunt needles (Thermofischer,UK) and loaded into the bioprinter, allowing bioprinting onto sterile culture plates to occur.
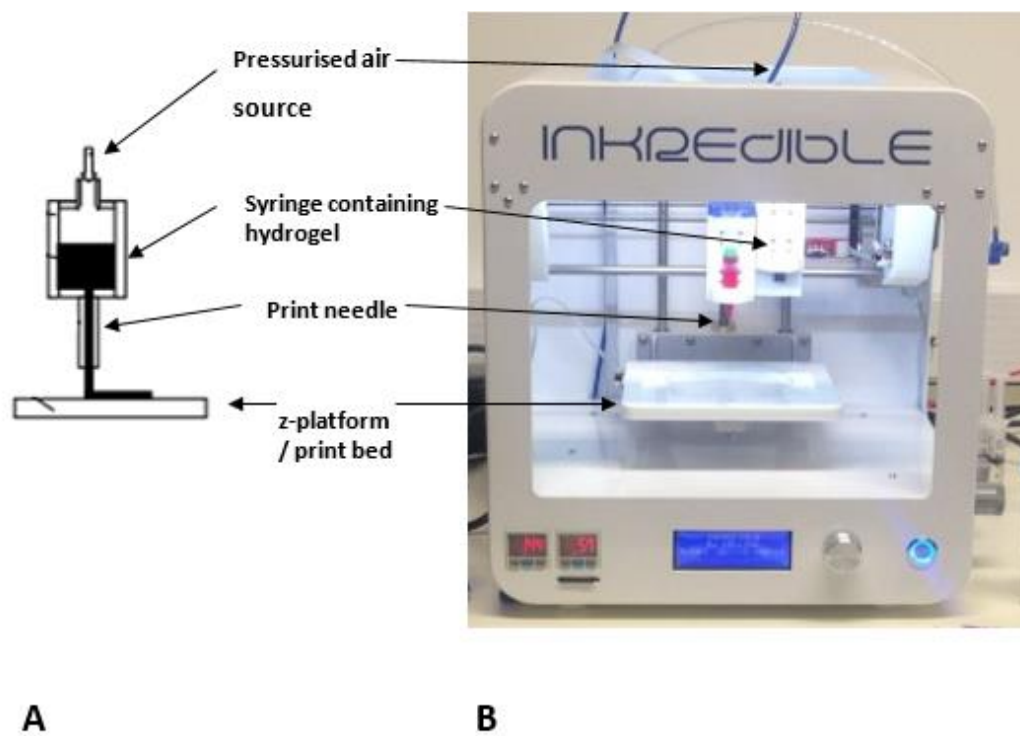
Figure 3.3 (A) Schematic of pneumatic extrusion **(B)** and commercially sourced Inkredible bioprinting system which uses pneumatic extrusion.
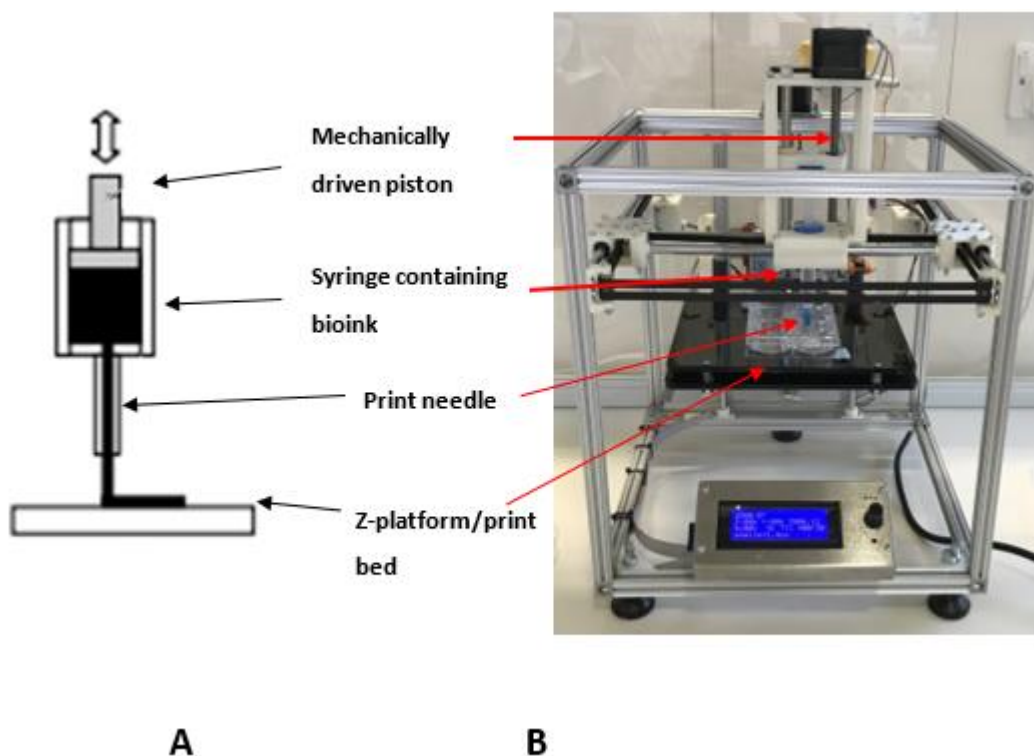
Figure 3.4 (A) Schematic of mechanical extrusion system and **(B)** custom-built mechanical extrusion bioprinter.

3.1.10 **Biofabrication Techniques to Support Construct Development Post-Printing**

Three main techniques were utilised with different hydrogels in this thesis to support hydrogel constructs prior to crosslinking. The FRESH technique, use of sacrificial hydrogel and hydrogel moulding were all used in combination with different hydrogels and crosslinking processes to produce cellular constructs.

3.1.10.1 **Freeform Reversible Embedding of Suspended Hydrogels (FRESH) Method**

Biomaterials such as collagen and alginate often lack sufficient viscosity to retain shape following bioprinting without further crosslinking or structural support being provided. The FRESH method, which stands for freeform reversible embedding of suspended hydrogels,

allows for biofabrication of complex designs with low viscosity, soft biomaterials [2]. Biomaterials such as alginate and collagen can be printed into complex geometries within a gelatin slurry support bath, which supports the hydrogels and allows them to retain print morphology as they are deposited. Once bioprinting is finished, the support bath that surrounds the deposited alginate can be removed through exposure to warmed calcium chloride ($CaCl_2$) or phosphate buffered solution (PBS) solution. This melts away the gelatin slurry surrounding the deposited hydrogel, whilst simultaneously thermally or ionically crosslinking the bioprinted alginate or collagen, leaving behind a cross-linked 3D structure (Fig. 3.5).

3.1.10.1.1   **Gelatin Slurry Preparation**

A glass mason jar containing 250ml deionized water was pre-heated to 45ºC. The water was then mixed with 10g gelatin (Type A, Thermo Fisher Scientific) and 0.4g $CaCl_2$ (Sigma-Aldrich). The solution was mixed on a hot plate with a stir bar at 40ºC until the gelatin fully dissolved. The solution was then gelled for 12 hours at 4°C in a 500-ml mason jar (Ball Inc, USA). A solution of 1L 0.16 wt% $CaCl_2$ (Sigma-Aldrich) was also made and placed in the refrigerator.

3.1.10.1.2   **Blending Gelatin**

The mason jar containing gelled gelatin was removed from the refrigerator and filled to the brim with 250 ml of 0.16 wt% $CaCl_2$ at 4°C. This ensured as little air as possible was trapped within the mason jar, prior to it being attached to a consumer-grade blender (Oster® Heritage Blend™ 400 Blender, USA). The mason jar contents were then blended (at "pulse" speed) for a period of 90 s. After blending, the gelatin solution was pipettable and not overly viscous/gelatinous. The blended gelatin slurry was loaded into 50-ml conical tubes and centrifuged at 4200 rpm for 2 min, causing slurry particles to settle out of suspension. The

supernatant was removed and replaced with 0.16 wt% $CaCl_2$ at 4°C. The slurry was then vortexed back into suspension and centrifuged again. This process was repeated until no bubbles were observed at the top of the supernatant, which indicated that most of the soluble gelatin was removed. At this point, gelatin slurries could be stored at 4°C. For FRESH bioprinting, the slurry was poured into a petri dish or a container large enough to hold the object to be printed. Any excess fluid was removed from the gelatin slurry support bath using Kimwipes (Kimberly-Clark), which produced a slurry material that behaved like a Bingham plastic. All 3D bioprinting was performed using gelatin blended for 90s.

3.1.10.1.3 **FRESH Bioprinting**

Alginate or collagen-based bioinks were extrusion bioprinted directly into the prepared gelatin slurry using the following bioprinting settings:

25G straight print needle; layer thickness, 0.1 mm; infill pattern, rectilinear; infill density, 25%; speed, 20 mm/s; extrusion multiplier 0.7.

During bioprinting, a warm (40-50°C) 1% w/v $CaCl_2$ bath was set up. The container of the bath was larger than the petri-dish containing gelatin slurry, allowing full submersion of the slurry following FRESH printing to be performed. Exposing the bioprint within a slurry to a high concentration of $CaCl_2$ caused simultaneous crosslinking of the alginate and melting of the gelatin slurry. Melted slurry could then be pipetted away, and bioprinted constructs removed and placed in culture.
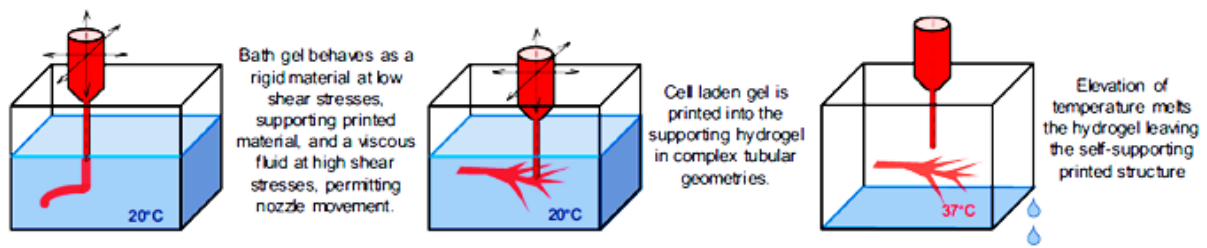
Figure 3.5 Freeform reversible embedding of suspended hydrogels (FRESH) method. Extrusion bioprinting occurs into a gelatin slurry support bath that behaves as a Bingham plastic. At high print speed, the extruding print needle is able to pass through the slurry with minimal resistance. However, once extruded, bioink is held in place by the surrounding slurry. By exposing the slurry to warmed solution such as calcium chloride, simultaneous crosslinking of extruded bioink and melting of the gelatin slurry is achieved, releasing a crosslinked structure.

3.1.10.2 **Sacrificial Ink – Pluronic F-127**

The co-polymer Pluronic® F-127 was used to provide temporary support to mechanically weaker hydrogels including alginate and collagen prior to crosslinking [3]. As previously described F-127 printed at room temperature as a hydrogel can be triggered to undergo a sol-gel transition through a reduction in temperature to $4^{\circ C}$ [3-5]. It is therefore well suited to being printed as a supporting structure around less viscous hydrogels such as collagen.

Concentrations of Pluronic® F-127(Sigma-Aldrich, UK) ranging from 20% to 40% wt% were prepared by dissolving F-127 in deionized distilled water (ddH$_2$O). This was performed by adding F-127 powder stepwise to ddH$_2$O in a glass beaker with a stir bar. The solidified paste that developed was then cooled to 4°C so that it became a liquid, with subsequent filtering performed (0.45 μm pore size, Corning® syringe filters) prior to any cell printing. Supporting

pluronic structures were then bioprinted at room temperature (Fig. 3.6 A) using the following settings:

Inkredble bioprinter: 25G straight print needle; layer thickness, 0.2 mm; infill pattern, rectilinear; infill density, 25%; speed, 10 mm/s; extrusion multiplier 1.0; pneumatic pressure 70 kPa; printed at room temperature.

Custom bioprinter: 25G straight print needle; layer thickness, 0.2 mm; infill pattern, rectilinear; infill density, 25%; speed, 10 mm/s; extrusion multiplier 1.0; printed at room temperature.

This allowed collagen or alginate-based bioinks to be 3D bioprinted or pipetted inside the supporting pluronic structure (Fig. 3.6 B). Once UV, thermal or ionic crosslinking of deposited collagen or alginate-based bioink was performed to increase stability (Fig. 3.6 C), cooling was performed of the structure for 30 minutes in a refrigerator at 4°C to trigger liquefication of the surrounding F-127 structure, leaving behind a cross-linked construct [6]. F-127 was then pipetted away as a liquid and the construct washed x 3 with PBS prior to incubation in culture media.
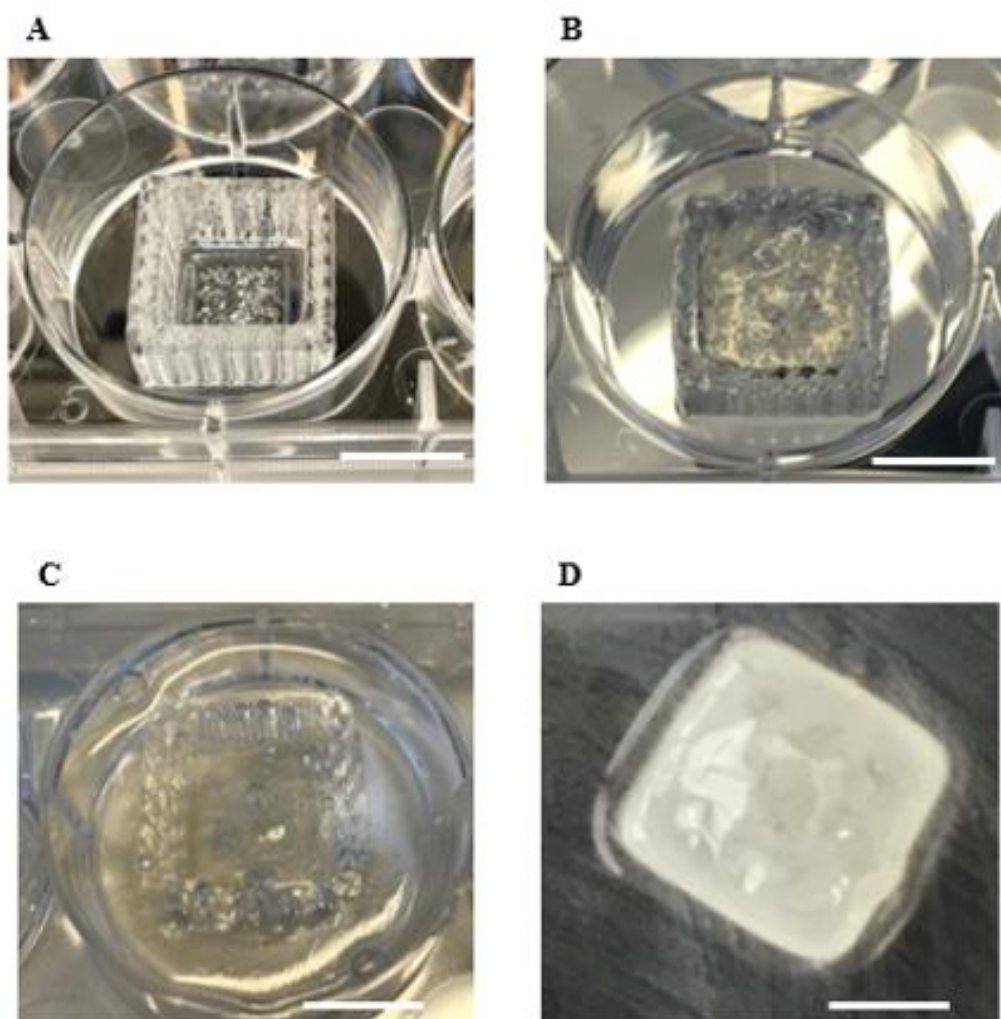
Figure 3.6 Use of sacrificial F-127 to mould hydrogels. **(A)** An initial supporting F-127 structure is bioprinted. **(B)** Alginate or collagen-based hydrogel is pipetted or bioprinted inside the surrounding F-127 structure **(C)** Crosslinking of the collagen (via thermal and/or UV crosslinking) or alginate (via ionic and/or UV crosslinking) is performed **(D)** The surrounding F-127 is removed by cooling to 4°C, leaving behind a 3D construct. Scale bar represents 1 cm.

3.1.10.3   **Preparation of Agarose Moulds Using PLA Inverse**

To allow reproducible and precise moulding of hydrogels into 3D constructs *in vitro*, a soft lithography technique was developed incorporating the use of 3D printed PLA stamps and agarose substrate (Fig. 3.7). As a non-cell-adhesive substrate, 3 % (w/v) agarose powder

(NEEO ultra quality, Roth, Karlsruhe, Germany) was dissolved by boiling in ddH$_2$O. Liquid agarose was then aliquoted into 6-well plates (Corning® Costar® TC-Treated Multiple Well Plates, Life Technologies, Paisley, UK) using 2 mL/well. 3D printed stamp designs were produced using PLA (using printing settings detailed in Section 3.1.7), sterilised through submersion in 70% EtOH and allowed to dry within an aseptic environment (Bassaire Class I hood). 3D printed stamps were then carefully placed on top of liquid agarose within the culture wells and allowed to sink down, so that the agarose fully surrounded the stamp design, and the agarose was allowed to cure at 4$^{°C}$. After agarose solidification and PLA stamp removal, resulting agarose moulds were equilibrated for 12 h or overnight within the appropriate cell culture medium at 37$^{°C}$ prior to any cell culture. Bioinks produced from alginate or collagen could then be deposited in the moulds, crosslinked in situ and then removed as 3D structures.
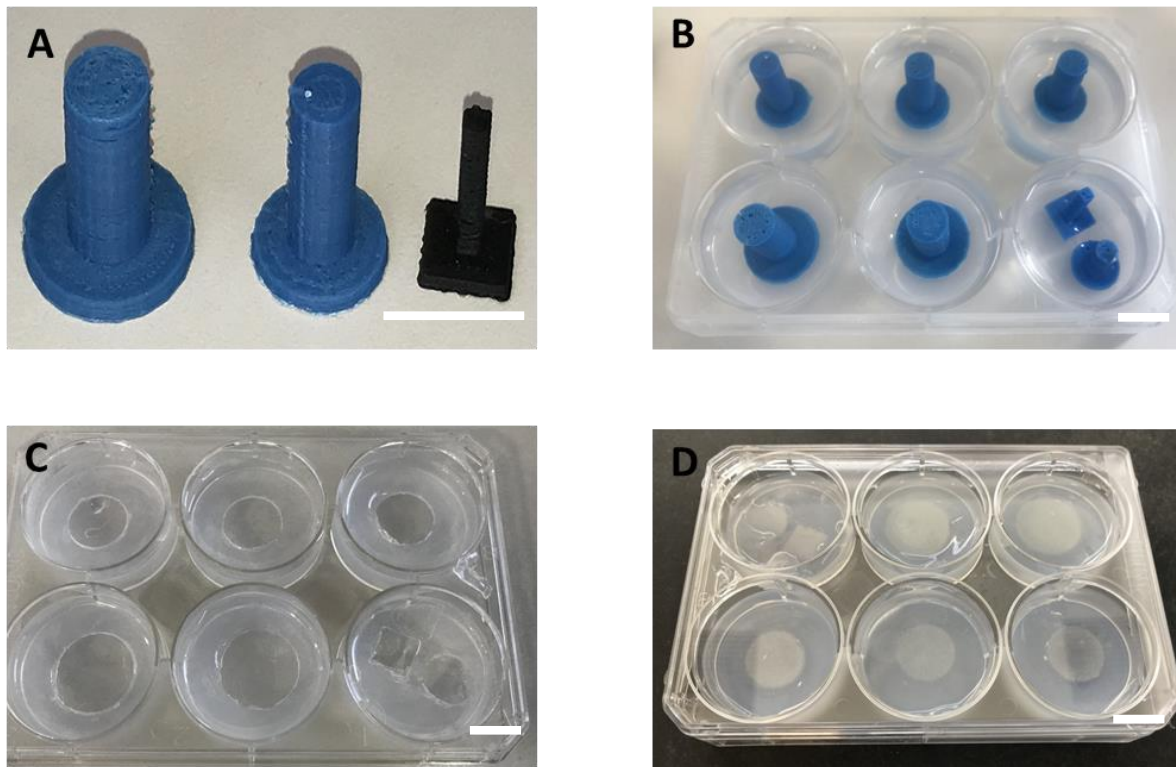
Figure 3.7 Use of agarose and PLA stamps to mould hydrogels. **(A)** 3D printed PLA stamps **(B)** Stamps inserted into agarose **(C)** Removal of stamps from agarose after agarose has cured creates inverse of stamp design in agarose substrate **(D)** Hydrogel deposited into agarose mould in regions where stamps were previously inserted, leading to creation of hydrogel discs of desired size. Scale bars represent 1cm.

3.1.11 Individual Hydrogel Preparations and Bioprinting Parameters

The procedure for preparing each bioink used in this thesis and the bioprinting settings used for each bioink are detailed in the following section.

3.1.11.1 Addition of Cellular Content to Bioinks

To produce a bioink with a homogenous, high density of ADSCs, hBMMSCs or HCs, a cell pellet was first prepared through centrifugation of passaged cells at 300G for 5 mins. The pellet

was then pipetted back and forth in 0.5ml of hydrogel, and then aspirated into a 5ml syringe. Connection to a further 5ml syringe containing 0.5ml of chosen hydrogel allowed repeated, gentle syringe mixing back and forth to occur via a three-way tap, producing 1ml of hydrogel in total with a homogenous cellular content (Fig. 3.8). The bioink was then vortexed for no more than 15s to further homogenize the suspension prior to bioprinting.

3.1.11.2 **Protanal Alginate Hydrogel Preparation and CaCl$_2$ Crosslinking**

Powdered Protanal (Protanal LF 10/60 FT, 89.00 g/mol, FMC Biopolymers Girvan, UK) was dissolved in ddH$_2$O through use of a magnetic stirrer to produce alginate stock solutions with a range of wt% concentrations (1%, 2%, 3% & 4%). CaCl$_2$ (Sigma- Aldrich) solutions with a range of wt% concentrations (0.1%, 0.2%, 0.3% & 0.4%) were prepared through dissolution in ddH$_2$O. Alginate and CaCl$_2$ solutions were sterilised using a 0.2 μm pore size syringe filter (Corning®, Sigma-Aldrich) within an aseptic environment (Bassaire Class I hood). Equal volumes of alginate and CaCl$_2$ solution were then aspirated into separate 5ml leur-lock syringes, the syringes connected via a three way tap to form a closed system, and direct mixing back and forth performed repeatedly between the syringes (Fig. 3.8). This allowed homogenous mixing of Protanal and CaCl$_2$ solutions, leading to uniform CaCl$_2$ crosslinking of Protanal occurring. Crosslinking was performed to improve the printability of the alginate compared to non-crosslinked alginate.

Figure 3.8 5ml syringes containing Protanal and $CaCl_2$ solutions connected via a three-way tap. Repeated mixing between the syringes allows a homogenous mixture to be produced, leading to uniform $CaCl_2$ crosslinking.

3.1.11.3   Bioprinting Settings for $CaCl_2$-Crosslinked Protanal

Bioprinting of different Protanal hydrogels was performed using the following bioprinting settings: 25G straight print needle; layer thickness, 0.1 mm; infill pattern, rectilinear; infill density, 25%; speed, 20 mm/s; extrusion multiplier 0.7; pneumatic pressure 70 kPa.

3.1.11.4   Sodium Alginate Preparation

Sodium alginate (Sigma Aldrich, UK) hydrogel was prepared through dissolution at 2% w/v in sterile, deionised water using a magnetic stirring plate. Sterilisation of the hydrogel was then performed by passing it through a 0.2 μm syringe filter (Corning® filters, Sigma Aldrich, UK). To produce an alginate hydrogel with a homogenous distribution of a chosen cell type, a cell pellet of a chosen cell type was first pipetted back and forth in 0.5ml of alginate, and then aspirated into a 5ml syringe. Connection to a further 5ml syringe containing 0.5ml of alginate

hydrogel allowed repeated, gentle syringe mixing back and forth to occur, producing 1ml of hydrogel in total, with a cell density of approximately 1 x cell pellet content/ml.

3.1.11.5 Sodium Alginate Bioprinting Settings

Bioprinting using alginate 2% w/v was performed using the following settings: FRESH bioprinting; 30G straight print needle; layer thickness, 0.06 mm; infill pattern, rectilinear; infill density, 25%; speed, 20 mm/s; extrusion multiplier 0.6.

3.1.11.6 Methacrylated alginate (AlgMA) and Photoinitiator (Irgacure®2959) Hydrogel Preparation

Protanal (FMC Biopolymer) was methacrylated at a maximum degree of methacrylation in a collaborating laboratory (Soochow University, Suzhou, *China)* using previously described chemical functionalization techniques [7-10]. Briefly, this involved dissolution of Protanal (FMC Biopolymer) in ddH$_2$O to produce a 2 % (w/v) Protanal solution. The Protanal solution was adjusted to pH 8 by adding 0.5 M NaOH solution. Methacrylic anhydride (Sigma, St. Louis, MO) at 20-fold excess was added to the alginate solution slowly at 4°C and the pH periodically adjusted to 8 using NaOH. The solution was allowed to react for 24 hours at 4°C. The modified alginate was purified via dialysis against sterile water (Sigma Aldrich) for 48 hours to remove excess methacrylic anhydride before the final AlgMA product was recovered through lyophilization. A hydrogel for bioprinting was then produced by dissolving AlgMA (0.2 g) and 0.5% wt of the photoinitiator 1-[4-(2-hydroxyethoxy) phenyl]-2-hydroxy-2-methyl-1-propan-1-one (Irgacure®2959) (Sigma Aldrich) in ddH$_2$O (10 ml) with the aid of a magnetic stirring plate. Care was taken to avoid light exposure to the solution during preparation by covering the mixing beaker with tin foil and performing preparation in a darkened culture hood.

3.1.11.7   Bioprinting Settings for AlgMA/ Ig 2959

Bioprinting using AlgMA/ Ig 2959 was performed using the following bioprinting settings: 25G straight print needle; layer thickness, 0.1 mm; infill pattern, rectilinear; infill density, 25%; speed, 20 mm/s; extrusion multiplier 0.7.

3.1.11.8   Secondary Ionic and UV Light Cross-linking of AlgMA/ Ig 2959 Constructs

Barium chloride ($BaCl_2$) powder (Sigma-Aldrich, UK) was dissolved in sterile, deionised water to produce a 20 mM or 40mM $BaCl_2$ solution and then autoclaved at 121 °C for 30 min prior to experimental usage. Following FRESH bioprinting of AlgMA/ Ig 2959, constructs were cross-linked by submersion in $BaCl_2$ solution warmed to 40°C for 2 min, with concurrent exposure to a 20 mW cm^{-2} 365nM UV light source at 5cm for 60 seconds also performed. This allowed $BaCl_2$ and UV-crosslinking of AlgMA/ Ig 2959 constructs to be simultaneously performed, whilst the 40°C warmth of the $BaCl_2$ solution allowed release of constructs to occur from the gelatin slurry print bath which melted away. Cross-linked constructs were then rinsed in PBS three times prior to incubation in culture media under standard conditions (36.0-37.5°C, 5.0±0.5% CO_2 and 90% humidity). Culture media was replenished every second or third day.

3.1.11.9   Biogelx Standard (Biogelx S) and Biogelx Arginylglycylaspartic Acid (Biogelx RGD) Hydrogels

Samples of Biogelx S and Biogelx RGD lyophilised powder were commercially supplied (Biogelx, Newhouse, Scotland). Biogelx hydrogels consist of a peptide-based gelator (the structural element of the hydrogel) and a surfactant-like molecule that presents carboxylate functionality, enabling subsequent cross-linking upon exposure to divalent cations (Ca^{2+}) present in tissue-culture media. Specifically, it contains the gelator fluorenyl-9-methoxycarbonyl-diphenylalanine (Fmoc-F_2) and the surfactant-like Fmoc-serine (Fmoc-S).

Biogelx S represents a standard Fmoc-F$_2$/S preparation, whilst Biogelx RGD is a version functionalised with the RGD motif, designed to increase cell adhesion and proliferation within the hydrogel.

Biogelx S hydrogel was prepared by initially mixing 232 mg of lyophilised powder with 3.75ml of sterile water using a magnetic stirring plate. The reconstituted material was left overnight at 4°C to allow peptide self-assembly to fully occur. Following overnight incubation, 1.25ml of MEM α media was mixed with the 3.75ml of Biogelx S solution via by brief pipetting to produce 5ml of hydrogel. Air bubbles were abolished by putting the mixture in a bath sonicator at room temperature for approximately 5 mins.

Biogelx RGD hydrogel was prepared by initially mixing 332 mg of lyophilised powder with 3 ml of sterile water using a magnetic stirring plate. The reconstituted material was left overnight at 4°C to allow peptide self-assembly to fully occur. Following overnight incubation, 2ml of MEM α media was mixed with the 3ml of Biogelx RGD solution via by brief pipetting to produce 5ml of hydrogel. Air bubbles were abolished by putting the mixture in a bath sonicator at room temperature for approximately 5 mins.

Cellular content was added to Biogelx S and Biogelx RGD hydrogels as per previously described methodology (3.11.1.1).

3.1.11.10 **Biogelx Bioprinting Settings**

Bioprinting using Biogelx S and Biogelx RGD hydrogel was performed using the following bioprinting settings: 25G straight print needle; layer thickness, 0.1 mm; infill pattern, rectilinear; infill density, 25%; speed, 10 mm/s; extrusion multiplier 1.2

3.1.11.11   Preparation of Methacrylated Gelatin (GelMA)

GelMA was prepared using previously described chemical functionalization techniques [11-14]. Gelatin (type A, 300 bloom, Sigma-Aldrich) was dissolved in PBS at 50 °C at 10% (w/v) through use of a magnetic stirrer. Methacrylic anhydride (MA; Sigma-Aldrich, St. Louis, MO, USA) in solution form was added to the gelatin solution at a rate of 0.5 mL/min (50 °C) while mixing to reach a ratio of 0.6 g MA/g gelatin. The reaction was allowed to proceed for 4 h at 50 °C before being diluted 5-fold with PBS (50 °C) to stop the methacrylation reaction. Dialysis was then performed against deionized water at 40 °C for 7 days using a 12–14 kDa cut-off dialysis membrane (Sigma Aldrich). After dialysis, GelMA was filtered through 0.2 µm filters (Merck Millipore) under aseptic conditions and pH adjusted to 7.4. The solution was then lyophilized for 72 h to obtain a GelMA sponge. GelMA hydrogels at 10 and 15 wt% were prepared by dissolving the GelMA sponge in PBS with 0.5 wt% of the photoinitiator Ig 2959 through the use of a magnetic stirrer at 40 °C. Care was taken to avoid light exposure to the solution during preparation by covering the mixing beaker with tin foil. Cellular content was added to the composite hydrogels as per previous methodology (3.11.1.1).

3.1.11.12   Bioprinting Settings for GelMA/ Ig 2959

Bioprinting using GelMA/ Ig 2959 was performed using the following bioprinting settings: 25G straight print needle; layer thickness, 0.1 mm; infill pattern, rectilinear; infill density, 25%; speed, 20 mm/s; extrusion multiplier 0.7.

3.1.11.13   Secondary Ionic and UV Light Cross-Linking of GelMA/ Ig 2959 Constructs

Following FRESH bioprinting, GelMA/ Ig 2959 constructs were released from the support bath through submersion in PBS warmed to 40°C for 5 min. Constructs were subsequently UV-

crosslinked through exposure to a 20 mW cm^{-2} 365nM UV light source at 5cm for 60 seconds. Cross-linked constructs were then rinsed in PBS three times prior to incubation in culture media under standard conditions (36.0-37.5°C, 5.0±0.5% CO_2 and 90% humidity). Culture media was replenished every second or third day.

3.1.11.14 Composite AlgMA/GelMA Bioinks

Composite bioinks were created by mixing different volumes of AlgMA and GelMA hydrogels of varying concentrations. For instance, 5ml of composite AlgMA/GelMA hydrogel was initially created by directly mixing 2.5ml of 2 wt% AlgMA/0.5% Ig 2959 with 2.5ml of 2 wt% GelMA/0.5% Ig 2959. This was achieved through aspirating 2.5l of AlgMA/0.5% Ig 2959 into a 5ml syringe. Connection to a further 5ml syringe containing 2.5ml GelMA/0.5% Ig 2959 allowed repeated, gentle syringe mixing back and forth to occur, producing a final hydrogel of 1% AlgMA/1% GelMA/0.5% Ig 2959. This methodology was used to produce a range of different composite hydrogels with varying AlgMA and GelMA concentrations. Cellular content was added to the composite hydrogels using the methodology as previously described (3.11.1.1).

3.1.11.15 Bioprinting Settings for AlgMA/ GelMA/Ig 2959

Bioprinting of AlgMA/GelMA/ Ig 2959 composite hydrogels was performed using the following bioprinting settings: FRESH bioprinting; 25G straight print needle; layer thickness, 0.1 mm; infill pattern, rectilinear; infill density, 25%; speed, 20 mm/s; extrusion multiplier 0.7.

3.1.11.16 Secondary Ionic and UV Light Cross-Linking of AlgMA/GelMA/ Ig 2959 Constructs

Following FRESH bioprinting, AlgMA/GelMA/ Ig 2959 constructs were further crosslinked through submersion in 20mM or 40 mM $BaCl_2$ warmed to 40°C for 2 min. Constructs were

concurrently UV-crosslinked through exposure to a 20 mW cm^{-2} 365nM UV light source at 5cm for 60 seconds. Crosslinked constructs were then rinsed in PBS three times prior to incubation in culture media under standard conditions (36.0-37.5°C, 5.0±0.5% CO_2 and 90% humidity). Culture media was replenished every second or third day.

3.1.11.17   **Preparation of Collagen Gels and Bioinks**

Type I collagen was extracted from rat tails and used to produce collagen gels that could be used in cell culture and in the formation of composite hydrogels for 3D bioprinting.

3.1.11.18   **Extraction of Acid-Soluble Collagen I**

Rat tails were harvested from adult animals scarified within a separate experiment at The University of Strathclyde. The outer rat tail skin was dissected away with a scalpel to expose the inner tendon. The exposed tendon was then cut flush at the vertebrae, pulled away from the attached vertebrae and the overlying tendon sheath removed. Tendons were then washed in sterile distilled water, weighed and placed into 0.5 M acetic acid (14.3ml glacial acetic acid in 500ml sterile distilled water). A 1% w/v extraction was performed (i.e. 1g tendons into 100ml 0.5M acetic acid) and incubation performed for 48 hours at 4°C. The resulting solution was filtered through 4 layers of sterile gauze using a sterile bottle top filter (500ml) to remove any debris. The solution was then dialysed against 0.1X DMEM in distilled water (50ml 10x in 5l) for 48 hours at 4°C with dialysis water changed. The dialysate was then placed into sterile centrifuge bottles (250ml) and centrifugation performed at 10 000 rpm for 2 hours at 6°C. To calculate the concentration (mg/ml) of collagen produced, 3ml of the solution was pipetted into 3 pre-weighed 100mm petri dishes and the collagen allowed to dry at 37°C, before reweighing of dry content.

3.1.11.19   **Collagen Gel Preparation**

4ml of 5 mg/ml collagen was added to 0.5 ml 1M HEPES buffer (Sigma Aldrich, UK) and 0.5 ml of DMEM/NaOH (2:1 mixture prepared from 8ml of DMEM and 4ml of 0.4M NaOH). Once the three constituents were mixed in a sterile beaker, the pH was adjusted through the dropwise addition of 1M NaOH. For the solution to form a gel the pH needs to be 8.0 to 8.5, indicated by the solution turning pink due to phenol red present within the DMEM.

3.1.11.20   **AlgMA/Col Composite Hydrogel Preparation**

Composite bioinks were created by mixing different volumes of AlgMA 4% stock solution and collagen solution of 4 mg/ml concentration. For instance, 5ml of composite AlgMA / Col hydrogel was initially created by directly mixing 2.5ml of 4 wt% AlgMA /0.5% Ig 2959 with 2.5ml of 4 mg/ml collagen solution. This was achieved through aspirating 2.5l of AlgMA / 0.5% Ig 2959 into a 5ml syringe. Connection to a further 5ml syringe (Fig. 3.8) containing 2.5ml of 4 mg/ml collagen/0.5% Ig 2959 solution allowed repeated, gentle syringe mixing back and forth to occur, producing a final hydrogel of 1% AlgMA /0.5% Ig 2959/ 2 mg/ml Col. This methodology was used to produce a range of different composite hydrogels with varying AlgMA and Col concentrations. Cellular content was added to the composite hydrogels using the methodology as previously described (3.11.1.1).

3.1.12 **Analysis of Biofabricated Constructs**

Analysis of biofabricated constructs was performed with an emphasis placed on investigating cell growth, viability and overall construct stability.

3.1.12.1   **Image Analysis of Samples**

All assays with cellular content were performed in triplicate prior to analysis unless otherwise stated. To evaluate cell viability and growth within bioprinted constructs, images were taken at

selected timepoints following bioprinting using a Nikon Eclipse TE300 Epifluorescent Inverted Microscope. Bioprinted constructs were removed from culture conditions and cross-sectional samples for analysis cut away using a scalpel blade. Cross sectional samples were washed 3X with PBS to remove residual culture media and then immersed in 1 ml of PBS. Two fluorescent stains were then used to determine cell viability; propidium iodide (1µg/ml), which cannot penetrate the membrane of living cells, was used to stain for dead cells; fluorescein diacetate (FDA) (5µg/ml) was used to stain for live cells. A volume of 0.01ml of propidium iodide (PI) was added to each construct submerged in 1ml PBS, and after 45 minutes incubation at room temperature, 0.005ml of fluorescein diacetate was added. Constructs were then imaged using brightfield, FITC and TRITC settings after incubation with fluorescent stains. Live/dead imaging was performed in different areas of cross-sectional samples (e.g. superficial, mid and deep zones of vertically cut samples), and a minimum of three samples were analysed for selected time points. Mean live/dead percentages were then derived after live and dead cells were counted using ImageJ. Density of live/dead staining was also used as an alternative measure of cell growth and viability. This was calculated by evaluating the relative total area of green/live staining present in captured cross-sectional images to total area of red/dead staining visible on images with quantification performed using ImageJ software [15] (National Institutes of Health, New York, NY, USA).

3.1.12.2 **Calcium Deposition Assays**

Staining solution was prepared by dissolving 2 g Alizarin Red S (Sigma-Aldrich, Irvine, UK) in 90 ml distilled water, with subsequent mixing and adjustment of the pH to 4.1–4.3 with 2M hydrochloric acid as necessary. The final volume of solution was then brought up to 100 ml with distilled water and filtered. Cells or cell-containing constructs for analysis were removed from the incubator, spent medium aspirated and gentle washing performed with PBS

without Ca^{2+}/Mg^{2+} (Life Technologies, Paisley, UK). PBS was then aspirated and paraformaldehyde fixation solution (Sigma-Aldrich, Irvine, UK) added to cover the cellular sample. After at least 30 min the fixation solution was aspirated, and the samples washed with ddH_2O. The ddH_2O was then aspirated and enough filtered alizarin staining solution added to cover the samples. Samples immersed in alizarin were then incubated at room temperature in the dark for 15 min, until staining intensity was visible. The alizarin staining solution was then aspirated and samples washed four times with ddH_2O. The distilled water was then aspirated and PBS added to cover the stained samples. Samples were then analysed immediately with an AE31 Elite Trinocular microscope (by Motic), using the 10x0.25 lens.

3.1.12.3 **Alkaline Phosphatase Assay**

One BCIP/NBT tablet (SigmaFast^{TM} BCIP-NBT; Sigma Aldrich, Irvine, UK) was dissolved in 10 ml distilled water to prepare a substrate solution. 0.05% Tween 20 (Sigma-Aldrich) was added to PBS, without Ca^{2+}/Mg^{2+} (Life Technologies, Paisley, UK) to prepare a washing buffer. Cells were removed from the incubator and culture medium aspirated, with subsequent washing performed with PBS. The PBS was then aspirated, and enough paraformaldehyde (Sigma-Aldrich) added to cover the samples for analysis. After 60–90 seconds the paraformaldehyde was gently aspirated, and the cells washed with Tween washing buffer. The washing buffer was then removed and enough BCIP/NBT substrate solution added to cover the sample. Incubation at room temperature in the dark for 10 min was then performed. The substrate solution was then aspirated, and the samples washed again with washing buffer. The washing buffer was aspirated, and PBS then added to cover the

cellular monolayer. Cells were analysed immediately with an AE31 Elite Trinocular microscope (by Motic), using the 10x0.25 lens.

3.1.12.4   Evaluation of Scaffold Porosity

The porosity and pore sizes of printed scaffolds was evaluated with an AE31 Elite Trinocular microscope (by Motic), using the 10x0.25 lens. For each scaffold, images were recorded of the scaffold top and bottom surface. In every image taken, the four central pores of the scaffold were measured. Quantification was performed using ImageJ software (National Institutes of Health, New York, NY, USA). Theoretical porosity of scaffolds was calculated by comparing the calculated weight of a 1 cm^3 non-porous, solid scaffold (given the known density of the print substrates PCL and PLA) to the measured weight of a scaffold of a measured volume.

$$\% \text{ Porosity} = \frac{\text{Theoretical weight of 1 cm}^3 \text{ of solid scaffold}}{(1/\text{volume of scaffold in cm}^3) \times \text{measured weight of scaffold}} \times 100\%$$

3.1.12.5   Water Contact Angle

The contact angle of selected hydrogels was measured to allow comparison of wettability, or the relative hydrophilicity, of different hydrogels. Water droplets were dispensed by a syringe positioned above the sample surface, and the contact angle obtained with a high-resolution camera arranged perpendicular to the sample surface. Image analysis using ImageJ allowed static contact angle measurement.

3.1.12.6   Biomechanical Testing of Hybrid Scaffolds

The mechanical stiffness of selected scaffolds and hydrogels was analysed using a BOSE ElectroForce 3230 system and WinTest4.1 software. A 450N load cell was assembled, with displacement limits set at -2 mm (min) and 2 mm (max) and load limits set at -400N (min) and

40N (max). The displacement and the load were calibrated at 0 mm and -0.1N, respectively. A ramp up period of 5 seconds, hold period of 30 seconds and ramp down period of 5 seconds was performed, corresponding to a 40 second test with 400 scan points. This allowed generation of a displacement/time graph and a load/displacement graph for each scaffold. The experiments were performed in triplicates unless otherwise specified
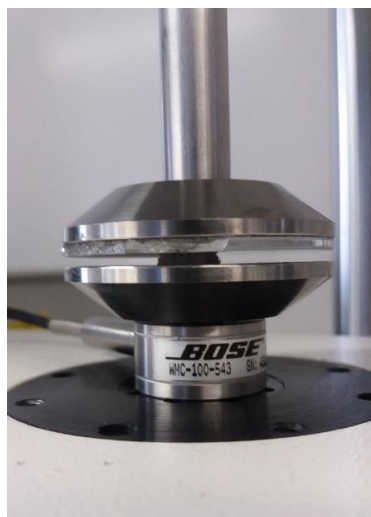

Figure 3.9 The BOSE ElectroForce 3230 system performing an unconfined compression test on an alginate/PCL scaffold. The bottom plate is stationary whilst the top plate generates displacement.

3.1.12.7 **Mechanical Performance Test of Hydrogel**

Further mechanical testing of hydrogels was performed in a collaborating laboratory (Orthopedic Institute at Soochow University, Suzhou, China). Cylinders of selected hydrogels with a diameter of 4.5 mm and a height of 4 mm were initially prepared. The hydrogel cylinders were then subjected to a compression test via a mechanical testing machine (HY-0580, Shanghai Heng Wing Precision Instrument Co., Ltd., Shanghai, China). This allowed generation of a stress-strain curve at up to 30% deformation, with the slope of the curve at 0–

10% deformation recorded as the compressive modulus. Compression tests were performed at 2 mm min^{-1}. The experiments were performed in triplicates unless otherwise specified.

3.1.12.8 Scaffold Degradation Analysis

Constructs were analysed at selected time points during *in vitro* culture to examine for weight loss suggestive of degradation, or weight increases suggestive of scaffold swelling. Constructs were initially weighed prior to being placed in culture media and incubation in standard culture conditions. Constructs were then removed from culture at selected time points, blotted dry to remove excess culture media using Kimberly-Clark Kimtech *Kimwipes* (Sigma Aldrich, UK), and weight measurements made before constructs were placed back into culture conditions.

3.1.12.9 In vitro Model of Osteochondral Regeneration

The capacity for different bioinks to repair osteochondral defects *in vitro* was analysed using animal tissue model. Three different biofabrication strategies were also utilized to aid repair of osteochondral defects.

Freshly prepared chicken knee samples were sourced from a local abattoir. The articular surface of the knee samples was exposed through debridement of surrounding soft tissue, and samples washed x 3 with PBS to remove any debris. Osteochondral defects were then created in the articular surfaces using a metal punch, allowing circular defects of diameter 10mm and depth 1 to 3mm to be prepared. Removed osteochondral tissue was measured using calipers to confirm diameter and depth.

Bioinks containing HCs or hBMMSCs were then used to repair the defects via 2 main different biofabrication strategies. Firstly, 10mm x 10mm x 1 mm cylindrical constructs were bioprinted using selected bioinks. Following bioprinting, constructs were crosslinked with UV light and/or through exposure to BaCl$_2$ solution. Constructs were then placed directly into the defects to fill

them up. Secondly, bioinks were manually injected directly into the defects, and cross-linked in situ with UV light and/or through exposure to $BaCl_2$ solution.

3.1.13 Statistical Analysis

This was performed using Statistical Package for Social Sciences version 27.0 (SPSS Inc., Chicago, Illinois). Univariate analysis was performed using parametric (Student's t-test: paired and unpaired) and non-parametric (Mann-Whitney U test) tests, as appropriate, to assess continuous variables for significant differences. One or two way analysis of variance (ANOVA) with post-hoc analysis (Tukey's HSD) where appropriate was used to compare continuous variables with multiple groups (e.g. cell viability in different composite bioinks). Significant differences were accepted at $p < 0.05$. All experiments were performed in triplicate unless otherwise stated, with mean and standard deviations (SD) displayed for selected time points of analysis.

3.2 Developing 3D Bioprinted Bacterial Biofilms

3.2.1 Preparation of Bioink for Bioprinting Bacteria

Brain Heart Infusion (BHI) broth (Sigma-Aldrich, UK) powder was dissolved in sterile deionized water to produce a 37 g/ L BHI Broth and then autoclaved. UV-sterilised sodium alginate powder (Protanal LF10/60FT, FMC Biopolymer, UK) was then dissolved in BHI Broth to produce a 4% (w/v) Protanal solution. The Protanal solution was subjected to magnetic stirring until reaching homogeneity and then sterilised through heating to boiling point (95°C). Solutions consisting of 4% w/v Protanal and 0.4% w/v $CaCl_2$ were then mixed with a volume ratio of 1:1 to create a partially cross-linked 0.2% $CaCl_2$: 2% Protanal hydrogel using a 3-way connector (Fig. 3.8). The hydrogel solution was vortex mixed at room temperature at 1500 rpm

for 5 min to produce a homogeneous, partially cross-linked alginate hydrogel. Protanal hydrogels were then stored at 4 °C prior to usage to prevent the growth of contaminants.

3.2.2 Bacterial Strains and Growth Media

Bacterial strains were universally cultured in Brain Heart Infusion (BHI) broth at 37°C whilst shaking. Strains used included *Escherichia coli* (*E.coli* clinical isolate, ATCC 25922), *Pseudomonas aeruginosa* (*P. aeruginosa,* PAO1, wild type strain, ATCC 47085), Methicillin-sensitive *staphylococcus aureus* (MSSA, clinical isolate, ATCC 29213) and Methicillin-resistant *staphylococcus aureus* (MRSA, clinical isolate, ATCC 700788). Chosen strains were routinely maintained on BHI agar (Sigma-Aldrich, UK) plates and stocks kept frozen in glycerol (50% v/v) at -80°C.

3.2.3 Bacterial Bioink Preparation

Bacterial strains taken from glycerol stocks were streaked on to a BHI agar plate and incubated at 37°C overnight. The following day a single colony was inoculated into 5 mL of BHI broth and incubated overnight at 37°C, with 200 rpm shaking (Mini shaker, Cleaver). The overnight cultures were harvested in the stationary phase after 18 h cultivation. The bacteria were collected by centrifugation (3,000 rpm, 4°C, 5 min) and washed three times with 9% sodium chloride (NaCl) to remove residual BHI medium. In all experiments, the concentration of bacteria was determined by optical density (OD) spectrometry (Eppendorf BioPhotometer) and inoculated at 1.0 at wavelength 600 nm ($OD_{600nm}=1.0$). The inoculated suspension of each strain was prepared in 10 mL of 9% NaCl in a 50 mL centrifuge tube prior to addition to hydrogel (Fisher Scientific, UK) and the bacteria re-harvested via centrifugation of the 50ml tube (3,000 rpm, 4°C, 5 min). Following centrifugation 9% NaCl supernatant was discarded, and bacterial

cell-pellets were then re-suspended in 500 µL of 0.2% CaCl$_2$: 2% sodium alginate hydrogel solution with a micropipette and dispensed into a 5 mL Luer-lock syringe (Fisher Scientific, UK). Connection to a further 5 mL Luer-lock syringe containing 4.5 mL 0.2% CaCl$_2$: 2% sodium alginate hydrogel warmed to 37°C allowed repeated, gentle mixing to be carried out back and forth between syringes containing bacteria and hydrogel (100 mixes back and forth), producing 5 ml bioink with homogeneously distributed bacteria.

3.2.4   Construct Design and Bioprinting Settings

3D models consisting of a solid or lattice 10 mm x 10 mm square design with increasing vertical thicknesses (0.25 mm, 0.5 mm, 1 mm, 2 mm, 4 mm) were produced using Autodesk® *Netfabb*® software (Autodesk®, Inc, USA) and exported as an STL file. Open-source slicer software (Sli3er, Version 1.2.9) was used to load the STL files and generate G-code files using the following settings for bioprinting: layer thickness, 0.1 mm; infill pattern, rectilinear; infill density, 25%; speed, 10 mm/s; extrusion multiplier 1.2. G-code files corresponding to solid and lattice constructs with differing vertical thicknesses were then loaded onto the bioprinter.

3.2.5   Bioprinting

A three-axis (X-Y-Z), single nozzle 3D extrusion bioprinter developed in our laboratory was used for bioprinting bioink loaded with different bacteria. This bioprinter represents an adapted, extrusion-based version of a previously developed microvalve-based bioprinter used in our lab to bioprint human cells including induced pluripotent stem cells [26, 39, 40]. Briefly, the bioprinter produces 3D constructs by coordinating the motion of a mechanically-driven syringe (Fig. 3.4). The dispenser deposits extrudate consisting of hydrogel on a stationary Z-platform. As successive layers of extrudate are deposited, the z-platform moves downwards allowing structures to be bioprinted from the bottom up, layer-by-layer. Prior to use, the bioprinter was

sterilized via UV exposure and wiped down with 70% ethanol. Sterility was maintained during bioprinting by placing the bioprinter in a laminar flow cabinet. Sterile 5 mL Luer-lock syringes containing bacterial bioink were attached to 25G printing nozzles and loaded into the bioprinter, allowing bioprinting into sterile 6-well culture plates to occur.

3.2.6   Secondary Cross-linking of Constructs

Ethylenediaminetetraacetic acid (EDTA), $CaCl_2$ and $BaCl_2$ powders (Sigma-Aldrich, UK) were sterilised with UV light (three 30 min cycles). Solutions of 0.4% w/v $CaCl_2$, 10 mM $BaCl_2$, 20 mM $BaCl_2$, 40 mM $BaCl_2$ and 110 mM EDTA (Sigma-Aldrich, UK) were prepared in sterile deionised water. All solutions were then autoclaved at 121 °C for 30 minutes prior to experimental usage.

Following bioprinting, constructs were cross-linked by submersion in ionic solutions of either 10, 20 or 40 mM $BaCl_2$ for 2 mins. Cross-linked constructs were then rinsed in PBS to incubation in BHI medium under standard culture conditions (37 °C, 5% CO_2, and 95% relative humidity). BHI media was replenished every second or third day and culture was performed atop a compact fixed-angle platform rocker (Grant Bio™ PMR-30 Compact Fixed-Angle Platform Rocker, Fisher Scientific, UK), to increase flow of media around the bioprinted constructs.

3.2.7   Analysis of Results

Analysis of bacterial growth, development of biofilm and response of biofilms to antimicrobial treatment was performed. All assays with bacterial content were performed in triplicate prior to analysis unless otherwise stated.

3.2.7.1 **Colony-forming Units (CFU)**

Colony-forming units (CFU) were used to determine the number of viable bacteria in constructs at selected time-points following bioprinting. To achieve this, constructs were first dissolved by submersion in 110 mM EDTA for 1 hour. Samples of the resultant broth were then serially diluted in 10-fold increments using 9% NaCl and plated onto BHO agar plates. After incubation at 37°C for 24h, visible colonies were counted.

3.2.7.2 **Fluorescence Staining for Biofilm Viability**

A commercial Film Tracer™ LIVE/DEAD™ biofilm viability kit (Thermo Fisher, UK) was used for the assessment of biofilm viability based on staining with the membrane potential sensitive dye propidium iodide (PI) (490 nm excitation, red emission) and the nucleic acid stain SYTO-9 (488 nm excitation, green emission). In principle, bacteria with intact cell membranes stain fluorescent green, whereas bacteria with damaged membranes stain fluorescent red. Bacterial constructs were washed with sterile distilled water and then incubated with SYTO-9 (6.7 µM) and PI (40 µM) in 35 mm glass bottomed imaging dishes (Ibidi) at room temperature (RT) for 45 min to allow stain penetration prior to imaging.

3.2.7.3 **Microscopy**

A Leica Microsystems TCS SP8 CARS microscope utilising a 25x magnification objective (HC FLUOTAR L 25x/0.95 W) and water immersion was used to perform CSLM imaging. Standard light microscopes often struggle to image biofilm of more than 3-4 µm thickness as biofilm material above and below the focal plane tends to scatter light and interfere with direct measurement [16]. Contrastingly, CSLM allows optical sectioning of biofilms and with image analysis 3D reconstruction is possible. To minimise or eliminate artefacts associated with

simultaneous dual wavelength excitation, all dual labelled biofilms were sequentially scanned, frame-by-frame, first at 488 nm (Argon laser, 70 µW) then at 561 nm (DPSS laser, 80 µW). Line averaging (x2) was used to capture images with reduced noise. Fluorescence emission was then sequentially collected in the green and red regions of the spectrum respectively. Images were captured in a two-dimensional (2D) projection. For analysing spatial separation in the z-direction (thickness), step sizes between 40-140 µm were used in z-stacks and 3D reconstructions were performed using Leica Confocal Software (LCS, Leica Microsystems). Five image stacks (typically 700 x 700 µm images over a depth of 40 - 140 µm) were acquired randomly from three independent constructs per $BaCl_2$ concentration per time point (15 stacks in total). The image stacks were then analysed using MATLAB 2016A software.

3.2.7.4 **Image Processing, Analysis and Statistics**

Thresholding and quantification of fluorescence imaged along the Z-axis was performed using MATLAB 2016a software. Initially fluorescent images were imported to the software and the green channel was extracted. An unsupervised k-means segmentation method was applied to analyse the channel [17], where k was set to be 3, which allowed separation of the cellular and background signals. The cells were then counted and analysed using a labelling connected component method to identify individual microcolony groups [18]. Finally, the mean and standard deviation of the numbers of microcolony groups, group areas, and area variations were calculated for statistical purposes.

3.2.7.5 **Antibiotic Susceptibility Testing (AST)**

The susceptibility of 2D bacterial cultures and 3D bacterial biofilms to antimicrobial treatment was compared, with the penetration of antimicrobials into a 3D biofilm also evaluated.

3.2.7.5.1 Investigating the Minimum Inhibitory Concentration (MIC) of 2D Bacterial Cultures using a Broth Microdilution Method

Corning 96-well microtiter plates (Sigma-Aldrich, UK) were used to allow the MIC of the antimicrobial methicillin sodium salt (Sigma-Aldrich, UK) against MRSA and MSSA. Methicillin concentrations ranging from 0.02 to 5 mg/mL were produced by serial dilution. MRSA and MSSA inoculums (OD 1.0) were then prepared as previously described (3.3.3) above. 50 µL of increasing strengths of methicillin solution and 50 µL of inoculated suspension were then dispensed into consecutive wells of the microtiter plates. The 96-well plates were then sealed with an anaerobic film (Thermo Fisher Scientific, UK) and incubated under anaerobic conditions at 37°C for 24 hours. The optical density of inoculated culture wells was then measured using a plate reader (Multiskan Go, Thermo Scientific). MICs were taken as the lowest concentration of an antimicrobial agent at which visible growth was inhibited.

3.2.7.5.2 Investigating the Minimal Biofilm Eradication Concentration (MBEC) of 3D Bacterial Cultures using a Broth Microdilution Method

Methicillin stock solution of 20 mg/mL was prepared in sterile dH_2O and diluted in BHI broth to obtain solutions with preliminary concentrations ranging from 2.5 to 10 mg/m. Investigation of the response of 3D biofilm constructs to methicillin was then performed by exposing a series of porous, 1 mm MRSA or MSSA constructs to increasing concentrations of methicillin. MRSA and MSSA constructs were cultured for 14 days prior to methicillin exposure to allow dense biofilm formation to occur. Mature MRSA and MSSA biofilm constructs were then transferred into sterile Corning® 6-well plates (Sigma-Aldrich, UK) and incubated in 3 mL volumes of either 2.5, 5 or 10 mg/mL methicillin solution. Positive-control wells containing fresh BHI

broth and MRSA or MSSA constructs were also set up without methicillin. The 6-well plates were sealed with an anaerobic film (Thermo Fisher Scientific, UK) and incubated under anaerobic conditions at 37°C for 24 hours. The optical density of inoculated culture wells was then measured using a plate reader (Multiskan Go, Thermo Scientific). MBECs were taken as the lowest concentration of an antimicrobial agent at which biofilm eradication was seen.

3.2.7.6 Biofilm Antimicrobial Penetration Test

3D bioprinted *E.coli* biofilm constructs of 1mm and 2mm thickness and porous design were cultured for 5 days to allow significant biofilm formation to occur. Biofilm constructs were then washed x 3 with phosphate buffered saline (PBS) solution to remove non-adherent bacteria. Antibiotic disks containing 30 µg tetracycline (Oxoid, UK) were then placed on top of *E.coli* biofilm constructs and incubated at 37°C for 7 days within BHI broth. The tetracycline disks located on top of the biofilm constructs were replaced daily to maintain consistent delivery of antibiotic. Biofilm constructs were then imaged after 7 days to analyse antimicrobial penetration.

3.3 Combining 3D Biofilms with a Novel Method for Identifying Orthopaedic Joint Infection: Surface Enhanced Spatially Offset Resonance Raman Spectroscopy (SESORRS)

3.3.1 Use of Raman Spectroscopy

Raman spectroscopy was chosen as a novel method to detect bacterial biofilms located within a joint infection model. As spontaneous Raman scattering is very weak, surface enhanced Raman scattering with spatially offset Raman spectroscopy (SESORS) was utilised as this combines the benefits of SORs and SERs to achieve even greater spectroscopic interrogation

of samples at depth [19]. SESORs combined with resonant Raman reporters, "surface-enhanced spatially offset resonance Raman spectroscopy" (SESORRS) was utilised to attempt detection of the binding of gold nanoparticle (AuNP) labelled biofilms at tissue depth within the following experiment.

3.3.1.1 Raman Measurements Including Handheld Device

Baseline Raman and SERS spectra were measured using Snowy range Raman instruments (SnRI, USA) with 638nm and 785 nm laser excitation wavelength and 45 mW laser power. SORS and SESORS measurements were taken using a handheld "Resolve" instrument (Cobalt Light Systems Ltd, UK) with average laser power 459 mW at 830 nm. The Resolve instrument is a handheld Raman device that allows through barrier Raman Spectroscopy to be performed (Fig. 3.14). The system can identify materials by comparing captured spectra to inbuilt spectral libraries, enabling rapid chemical identification through a wide range of sealed non-metallic containers, barriers, and packaging to be performed. All captured spectra were processed using the "rubberband" function on MatLab, allowing baseline correction to be performed before further analysis.
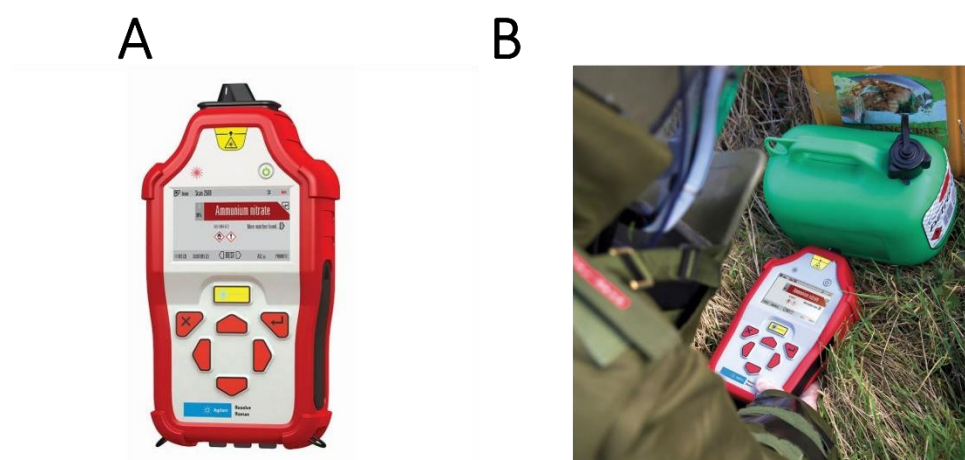
Figure 3.10 (A) Resolve handheld through-barrier identification system. A simple interface with large buttons makes it friendly to laboratory use through protective gear. **(B)** Example of Resolve instrument in use to detect chemicals within plastic container.

3.3.2 Summary of Functionalisation of Gold Nanoparticles with DNA Aptamers and Chalcogenpyrylium Raman Reporter Dyes

Gold nanoparticles were functionalised in a two-step process by collaborators to allow detection of bacterial biofilms via Raman spectroscopy. In brief, gold nanoparticles (AuNPs) were initially fabricated according to previously described methodology [20]. AuNPs were then chemically functionalised with commercially sourced DNA aptamers that bind specifically to MRSA or *E. coli* according to a previously described methodology [21], allowing them to bind specifically to *E. coli* or MRSA within 3D bacterial biofilms. Further functionalisation of the AuNPs was performed through the addition of chalcogenpyrylium Raman reporter dyes to their surface. Previous work has shown the potential for chalcogenpyrylium dyes conjugated to large AuNPs to generate strong Raman responses, allowing successful detection of tumour cells bound to Raman reporters at tissue depths of 25 mm [22, 23]. To detect MRSA and *E.coli* biofilms, chalcogenpyrylium Raman reporters with absorbance wavelengths of 823 nm (dye 823) and 815 nm (dye 815) were selected to detect biofilm.

Stepwise Gold Nanoparticle Functionalisation
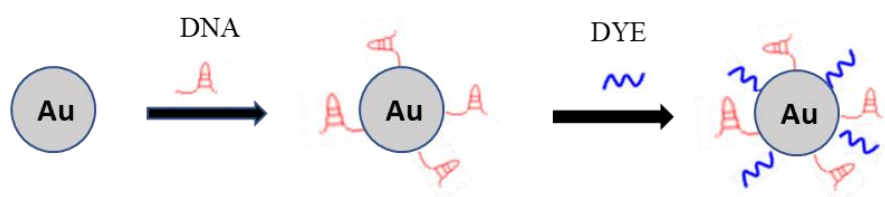
Bacterial Binding to Nanoparticle-DNA-Dye Complex
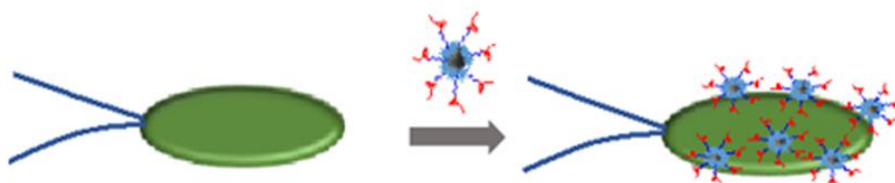
Figure 3.11 Gold nanoparticles were synthesised and then functionalised in a stepwise fashion with DNA and then chalcogenpyrylium Raman reporter dyes. This allowed nanoparticle-DNA-dye complexes to bind directly to bacteria in a targeted fashion according to the DNA aptamer included in the complex.

3.3.3 Overview of Experimental Set Up

A sandwich-like joint infection model consisting of pork bone (bottom), 3D bioprinted biofilms (middle) and porcine tissue (top) was created. 3D bioprinted biofilms were incubated overnight with AuNPs functionalised with aptamers and chalcogenpyrylium dyes and then removed from culture and washed with HBSS x 3. Lean porcine tissue was purchased from a local butcher and cut into sections with an average thickness of 3 mm. 3D biofilm constructs were then placed directly on top of a porcine bone sample and increasing thicknesses of lean porcine tissue placed

on top of the biofilms in 3 mm increments. Control bioink scaffolds of the same dimensions and containing no bacteria were also produced within the model to allow comparison. With every increase in lean tissue thickness placed on top of the biofilms, SORS and SESORS measurements were taken using a handheld Resolve instrument from Cobalt Light System (830 nm). The tissue model was brought into contact with the nose cone of the SORS instrument, and the stage was moved around in x-y plane in order to detect the biofilm through the tissue barrier. The total tissue penetration thicknesses achieved was measured using a calliper. Previous research has shown the greatest level of offset that can be used when performing through-barrier detection with the handheld Cobalt Light System (830 nm) is 8 mm offset [24]. Therefore, all measurements were carried out using 8 mm offset, 5 accumulations and 2.0 s integration time.

(A) Biofilm Placed on Bone

(B) Soft Tissue Over Biofilm/Bone

Increasing
Vertical
Thickness
of Porcine
Soft Tissue

Porcine Bone

Biofilm beneath
overlying soft tissue

Porcine Bone
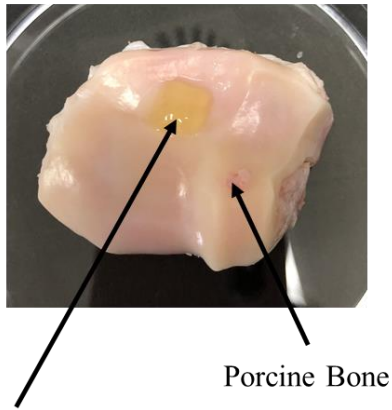
Biofilm exposed to
functionalised AuNPs
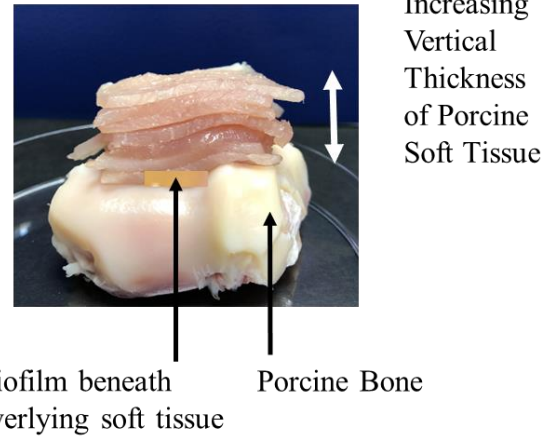
(C) Handheld Raman Device Over Biofilm/Tissue

Biofilm/bone/soft tissue
underneath Raman Device

Figure 3.12 Joint infection model. **(A)** Initially, a 3D bioprinted, 1cm thick bacterial biofilm was placed on top of a porcine femoral condyle after overnight exposure of the biofilm to

AuNPs functionalised with aptamers and chalcogenpyrylium dyes. **(B)** Increasing layers of soft tissue were placed on top of the biofilm, to create a sandwich model with the biofilm submerged below over 2cm thickness of soft tissue. **(C)** A hand-held portable SORS instrument (handheld Resolve instrument from Cobalt Light System (830 nm) was placed directly above the bone-biofilm-soft tissue construct, to investigate detection of biofilm under depth of soft tissue.

4   Chapter 4 – Development of Initial 3D Biofabrication Approaches for Osteochondral Regeneration

4.1 Acknowledgement of Collaboration

All experimental work included in this chapter was performed by the author. Initial mechanical testing was performed in collaboration with Eleni Farmaki (MSc student, University of Strathclyde).

4.2 Introduction

The smooth, sliding motion of articulating joints during locomotion relies upon articular cartilage (AC) that can be found coating opposing joint surfaces. AC is a highly specialised connective tissue that provides a lubricated surface with a low frictional coefficient, minimising friction between opposing joint surfaces. Viscoelastic properties and an intricate structure also allow AC to shield underlying bone from some of the mechanical stresses applied during locomotion. Despite being only 2 to 4mm thick, AC has a deceptively intricate structure that can be divided into four zones extending from superficial to deep zones based on the orientation of type II collagen fibres and proteoglycan content. However, AC is devoid of blood vessels, nerves or lymphatics and has limited cellular content resulting in a poor intrinsic capacity for healing and repair [105]. Once AC sustains damage from aetiologies including acute trauma and repetitive overloading, full recovery of structure and function is unlikely, and significant alteration of native biomechanics can occur [1]. Symptoms of pain, instability and mechanical locking can develop, leading to arthroscopic (keyhole) surgery being performed in over 150 000 patients annually in the UK [108].

Several techniques can be deployed to treat cartilage defects surgically. Unfortunately, current arthroscopic repair techniques (Fig. 2.3) have critical limitations including a tendency to result

in mechanically inferior fibrocartilage formation, ongoing pain and morbidity, and an inability to treat globalised AC destruction [2, 3]. Over 180 000 patients therefore require total joint replacement surgery in the UK annually, a major operation which can result in incomplete satisfaction and residual symptoms, particularly in younger patients [4-9]

As demand for arthroplasty surgery continues to grow significantly worldwide, the need for a novel, cost effective treatment option for arthritis and osteochondral defects tailored to the individual patient has therefore never been greater. As a developing technology, 3D biofabrication offers a novel approach to help ease the treatment burden of AC defects. Biofabrication involves combining biological constituents such as cells, growth factors and biomaterials with precise biomanufacturing techniques such as 3D cell printing, known as "bioprinting". Complex tissue constructs can therefore be created, or biofabricated, "from the bottom up." The overall aim of this chapter is to develop and optimise a 3D biofabrication approach that can target the regeneration and reconstruction of osteochondral defects. Key to this will be the identification and optimisation of successful biofabrication techniques, biomaterials and cell sources that can be applied to osteochondral regeneration.

4.3 **Results and Discussion**

4.3.1 **3D Biofabrication of PCL Scaffolds and Hybrid Hydrogel/ PCL Scaffolds**

Initial work focussed on the use of FDM to 3D print porous scaffolds. FDM uses a temperature controlled printhead to deposit thermoplastic material onto a platform in a layer by layer manner to build up a 3D construct (Fig. 2.5 B). Once print conditions were optimised to reproducibly 3D print scaffolds with a defined structure, attention was focussed on improving

biocompatibility of scaffolds though surface modification and creation of hybrid polymer-hydrogel scaffolds.

4.3.2 Osteogenic Differentiation of hBMMSCs

To confirm the pluripotency of hBMMSCs used in experimental work, initial growth of hBMMSCs was performed for 21 days growth in osteogenic inducing media. Following 21 days culture, hBMMSCs were found to have significantly increased calcium deposition and alkaline phosphatase activity ($p < 0.001$) on staining compared to control hBMSCs grown in non-inducing DMEM media (Fig. 4.1), after secondary analysis of images using ImageJ software (Table 4.1). In combination with an observed change in cell morphology, this was highly suggestive of osteogenic differentiation of hBMSCs occurring.

Table 4.1 Analysis of hBMMSC Osteogenic Staining

		Staining Intensity	Std. Deviation	T-test (Independent Samples)
Alizarin	Induced MSCs	12.36	3.73	
	Control MSCs	0.48	0.75	$p < 0.001$
ALP Activity	Induced MSCs	8.66	0.31	
	Control MSCs	0.47	0.47	$p < 0.001$
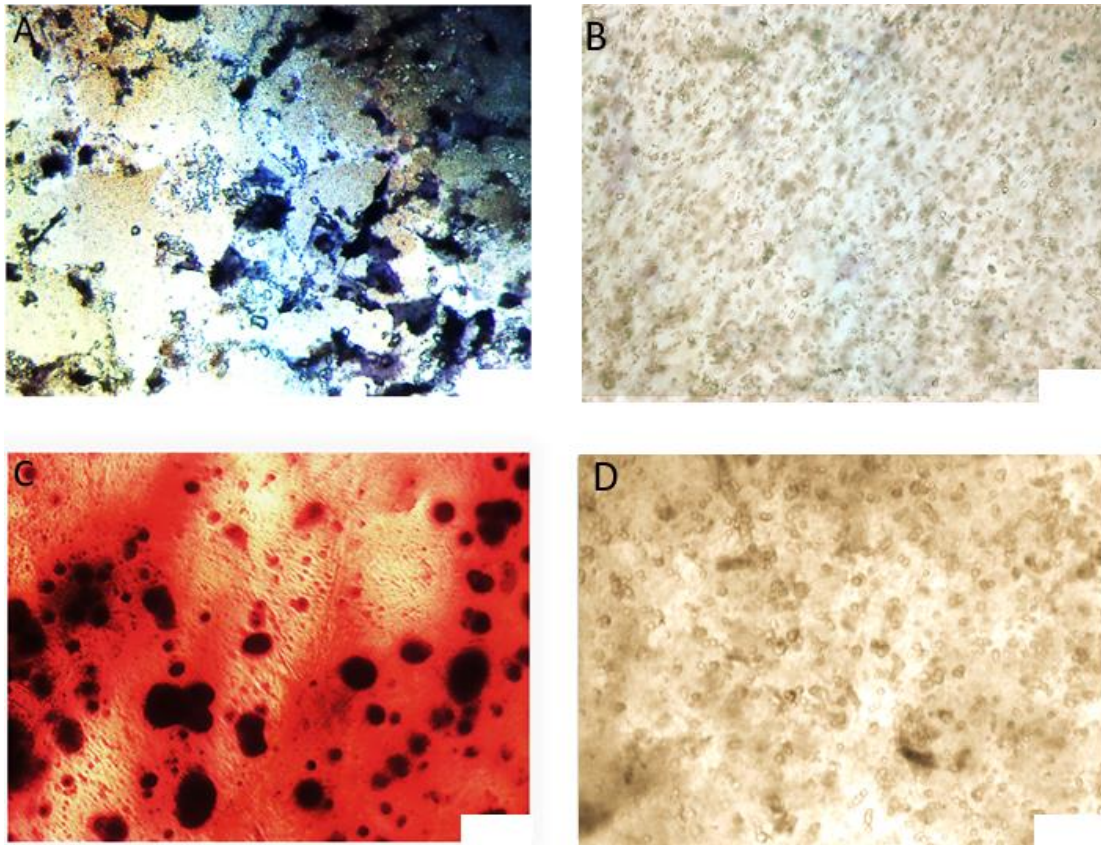
Figure 4.1 (A) ALP staining in induced hBMMSCs after 21 days (B) ALP staining in control hBMMSCs after 21 days (C) Alizarin Red S staining in induced hBMMSCs after 21 days (D) Alizarin Red S staining in control hBMMSCs after 21 days. Scale bar = 100μm.

4.3.3 Use of PCL to Create Scaffolds

PCL was chosen as the initial scaffold substrate having been widely used previously in tissue engineering for the fabrication of 3D scaffolds. Initially a range of structures were printed with PCL to establish optimal print settings; a range of print speeds, layer heights, structure infills and print temperatures were trialled to optimise print results. Optimal print settings allowed PCL scaffolds to be reproducibly 3D printed with defined pore sizes and thicknesses (Fig. 4.2). Measurement of the scaffolds confirmed pore sizes of 265.7 ± 30.7 μm, vertical thickness of 3.0 ± 0.1 mm, width 10.0 ± 0.1 mm and calculated overall porosity of 50 ± 1 %.
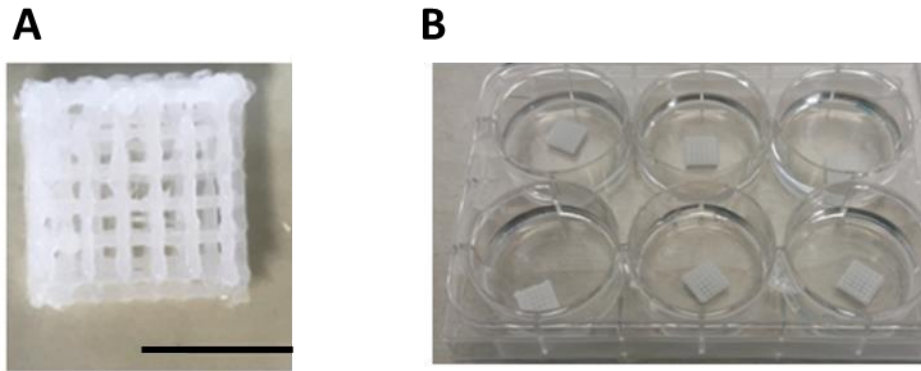
Figure 4.2 3D printing PCL using an FDM approach. **(A)** 3D printed PCL tissue scaffold. Scale bar = 1cm **(B)** PCL scaffolds within 6-well culture plate.

4.3.4 **Surface Modification**

To improve hydrophilicity and biocompatibility of PCL scaffolds, immersion in NaOH solution was performed prior to cell culture. PCL scaffolds printed with consistent dimensions as previously described were exposed to NaOH in different concentrations and for different durations. MSC cells were then seeded at a density of 1×10^5 cells/ml onto PCL scaffolds and observed over 24 hours, with comparison made to cells seeded onto non-NaOH exposed PCL scaffolds. Exposure of PCL scaffolds to NaOH prior to MSC seeding led to significantly greater cell viability at 24 hrs ($p < 0.05$), with no benefit found to increasing exposure beyond 1M NaOH or 1 hr duration of immersion (Fig 4.3).
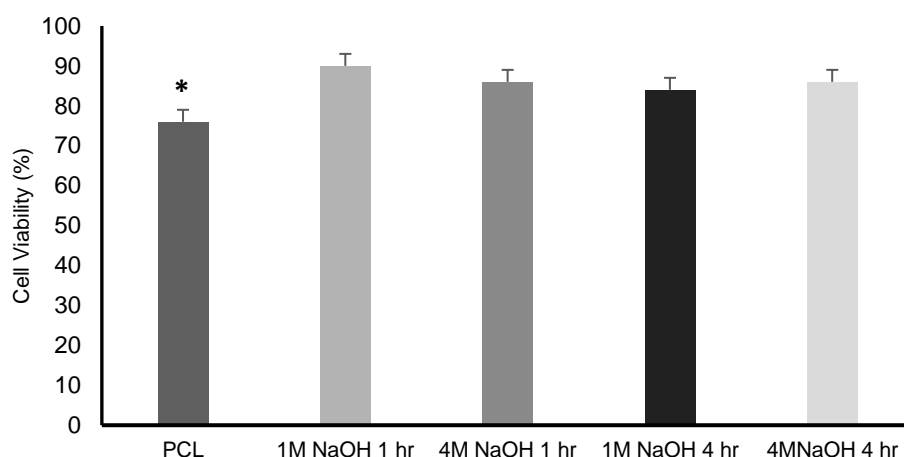
Figure 4.3 Viability of MSC cells seeded onto PCL scaffolds at 24 hours. Greater cell viability was found at 24 h on PCL scaffolds treated with NaOH, compared to non-exposed PCL scaffolds (*$p<0.05$, ANOVA). No significant difference was found between scaffolds treated with different strengths of NaOH, or by increasing time of NaOH exposure ($p>0.05$, ANOVA).

4.3.5 Creation of Hybrid PCL-Hydrogel Scaffolds

Biofabrication of hybrid scaffolds consisting of PCL scaffolds combined with more bioactive hydrogels has led in some cases to improved cellular growth within constructs [10-13]. To examine this, PCL scaffolds treated with 1M NaOH for 1 hr and printed to previously defined pore sizes and thicknesses were combined with different hydrogels to create hybrid scaffolds.

4.3.6 Cell Viability in Hybrid Scaffolds

Initially hBMMSCs encapsulated in 1% alginate (Protanal LF10/60FT, FMC Biopolymer, UK) or Biolgelx S hydrogel at a density of 1 x 10^5 cells/ml were dispensed onto PCL scaffolds to ensure scaffolds were fully coated with hydrogel (rationale for use of alginate and Biogelx S covered in section 4.8.5). For comparison, identically prepared control PCL scaffolds were also seeded with hBMMSCs suspended in DMEM media at a density of 1 x 10^5 cells/ml. Cells were allowed to adhere to scaffolds for 2 hours post-seeding, before immersion in DMEM

media and culture in standard conditions. Cellular growth and viability were observed over 7 days within the scaffolds (Fig. 4.4). PCL/Alginate and PCL/Biogelx scaffolds appeared to retain a far larger number of cells following seeding and foster greater cellular adhesion compared to PCL control scaffolds. Significantly higher cell viability ($p<0.05$, ANOVA) was found in PCL/Alginate and PCL/Biogelx scaffolds compared to control PCL scaffolds (Fig. 4.5) from 24 hours onwards of cell culture.
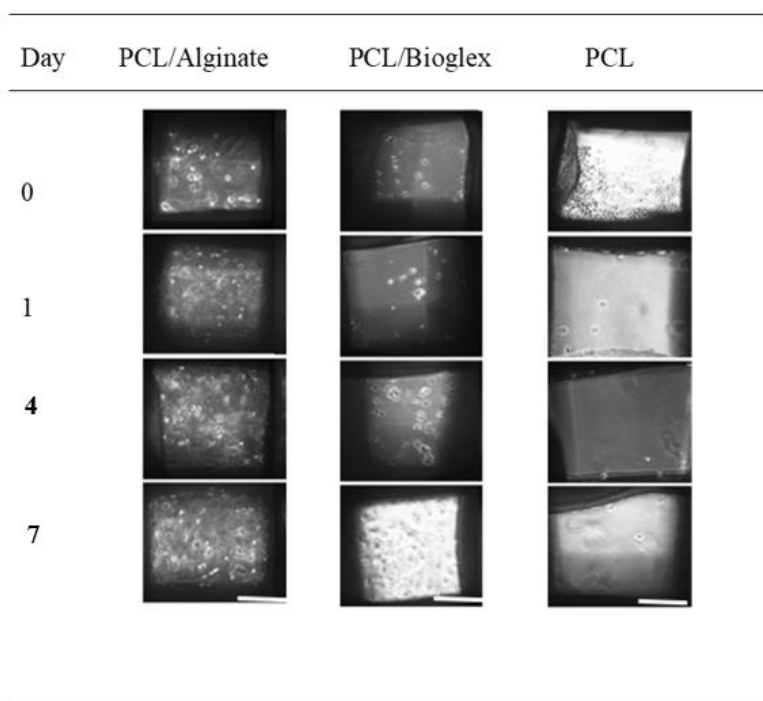
Figure 4.4 Cell retention seen in hybrid and non-hybrid scaffolds over 7 days. Images taken of cells within pores of hybrid PCL/Alginate, PCL/Biogelx and PCL scaffolds. Greater cell growth and retention was evident in hybrid scaffolds compared to PCL scaffolds. Scale Bar = 100 µm.

A

	PCL /Alginate	PCL/Biogelx	PCL
Day 7 Live Stain			
Day 7 Dead Stain			
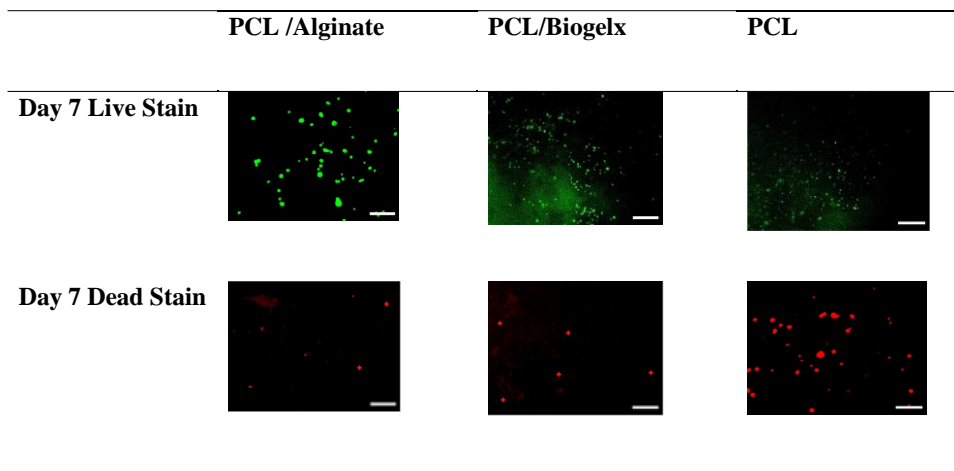
B
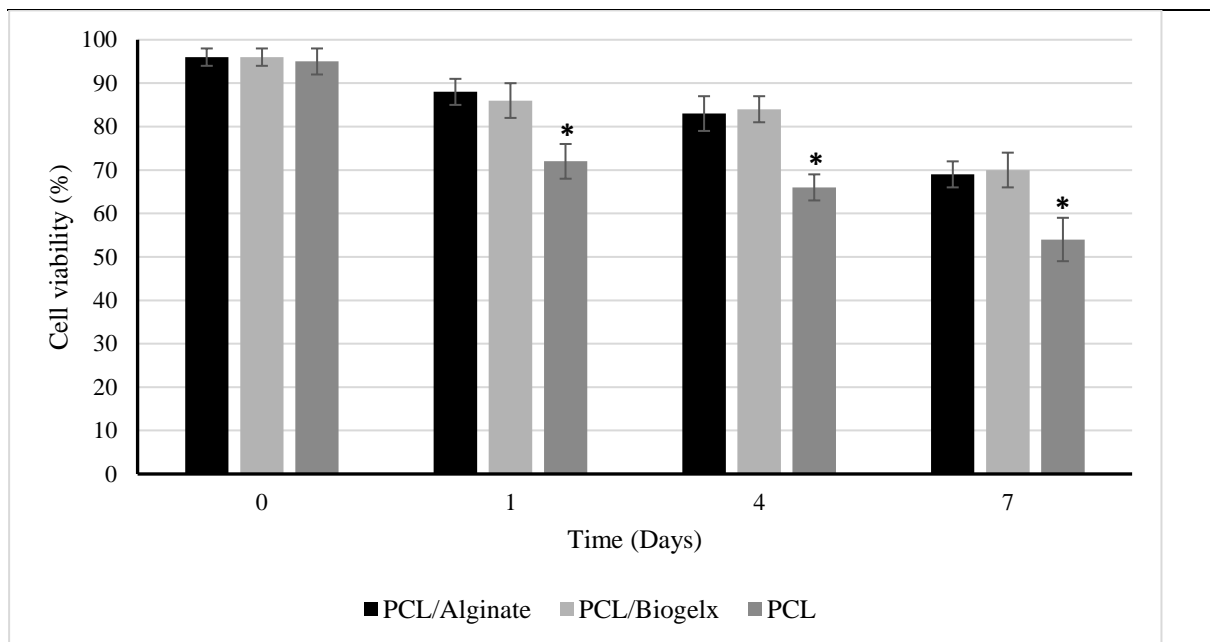
Figure 4.5 hBMMSC viability over 7 days in different scaffolds. (A) Significantly higher cell viability was supported in hybrid hydrogel-PCL scaffolds compared to PCL scaffolds seeded with cells. (B) Significantly lower cell viability (*p<0.05, two-way ANOVA) was found in

control PCL scaffolds at up to 7 days culture compared to hybrid PCL/Alginate and PCL/Biogelx scaffolds from 24 hours onwards of cell culture.

4.3.7 Mechanical Performance of Hybrid Scaffolds

Unconfined compression testing was performed on PCL/Alginate, PCL/Biogelx and PCL scaffolds following production. It was found that significant differences existed between scaffolds (p<0.01, ANOVA), with PCL/Alginate found to have the stiffest mechanical properties and PCL the weakest (Fig. 4.6 and 4.7).
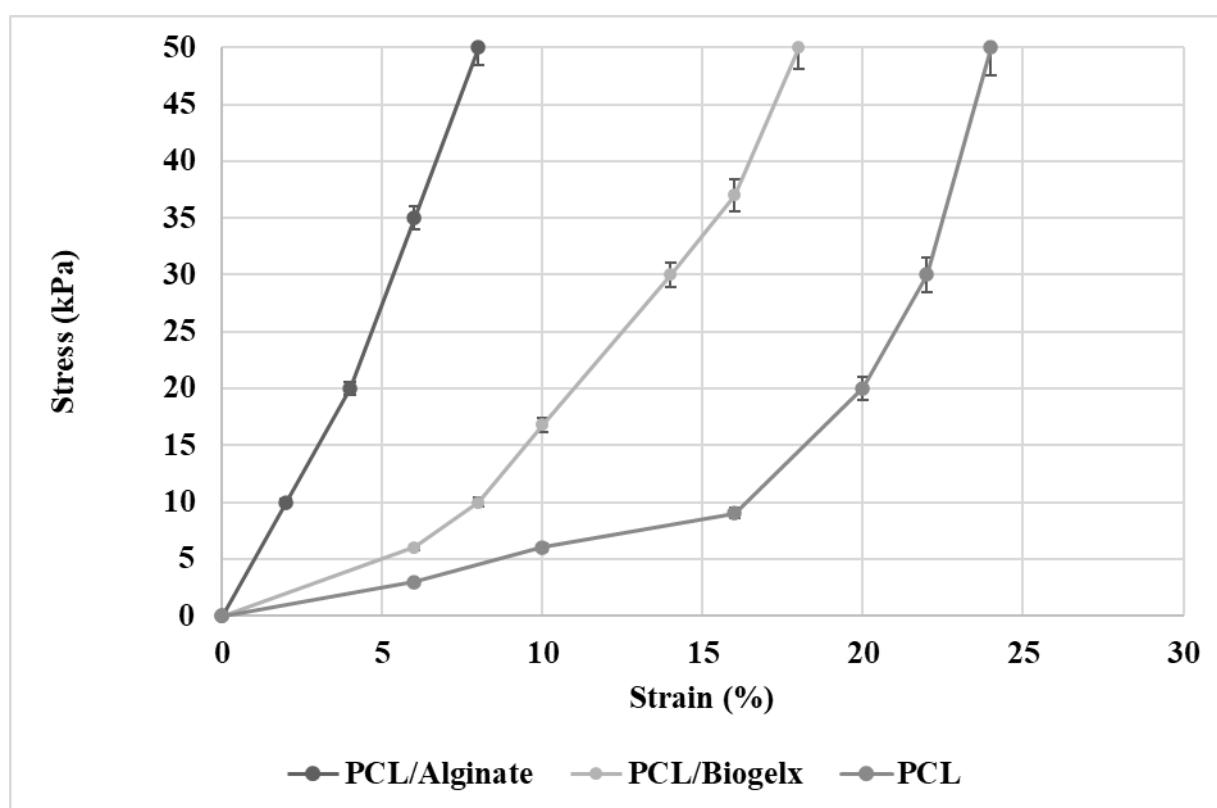
Figure 4.6 Stress/strain curve derived from unconfined compression testing performed on 1mm thick PCL/Alginate, PCL/Biogelx and PCL scaffolds. Significant differences were noted between scaffolds (two-way ANOVA, p<0.01), with PCL/Alginate found to have the stiffest mechanical properties and PCL the weakest.
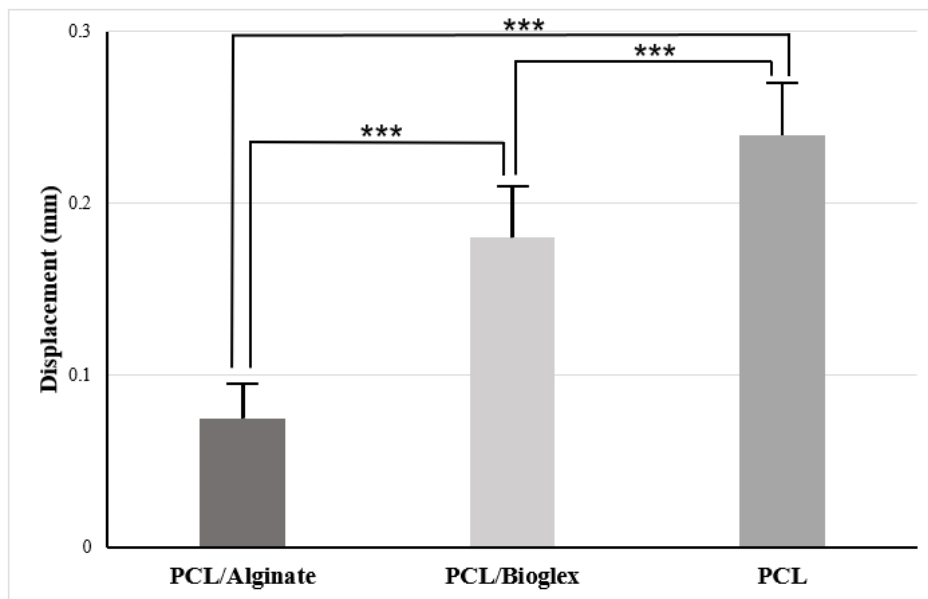
Figure 4.7 Maximum displacement found to have occurred during unconfined compression testing on 1mm thick scaffolds. PCL/Alginate was found to demonstrate significantly less displacement than either PCL/Biogelx or PCL scaffolds during testing conditions (*** $p<0.01$, ANOVA).

4.3.8 Initial Hydrogel Bioprinting

A range of hydrogel materials were used to print constructs using the Inkredible 3D extrusion printer (Fig. 4.8 A). F-127 of varying concentrations from 20% to 40% was 3D bioprinted at room temperature; concentrations of 40% F-127 printed at 70- 80 kPa extrusion pressure were found to give stable prints capable of maintaining 3D structure. Gradually more complex structures were designed and bioprinted, including an anatomical human nose model (Fig. 4.8 D). Ultimately, F-127 is recognised as having poor biocompatibility and has greater utility as a sacrificial or supporting hydrogel in larger constructs [14-17]. Attempts were therefore made to develop bioprinting using other hydrogels capable of supporting cellular growth.
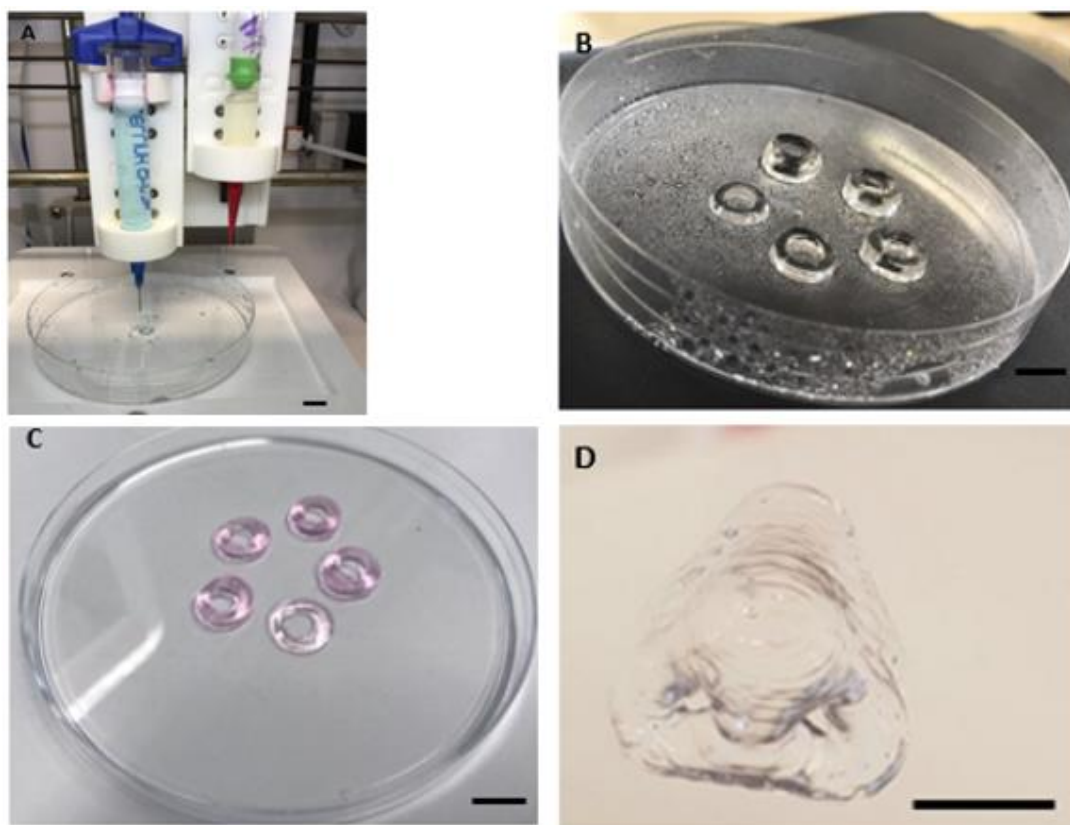
Figure 4.8 Initial Extrusion Bioprinting Attempts. **(A)** Inkredible bioprinter printing hydrogel structure **(B)** Alginate rings of increasing height bioprinted using 2% Alg/ 0.2% CaCl$_2$ **(C)** Bioprinted Biogelx ring structures **(D)** Bioprinted pluronic nose structure close-up. Scale bars = 1cm.

Initially alginate was chosen as a biocompatible and readily available hydrogel for bioprinting cells. A range of Protanal alginate (1% w/v to 6% w/v) and CaCl$_2$ concentrations (0.1% to 0.4%) were combined to develop a bioprintable, partially cross-linked hydrogel (Table 4.2). It was apparent that the viscosity of the Protanal hydrogel increased with rising concentrations of either Protanal or CaCl$_2$. The blends produced from 4% and 3% Protanal were significantly more viscous than 1 % and 2 % Protanal. However, as the Protanal hydrogel became more viscous, print nozzle blockages became more frequent and print pressures increased,

representing high shear stress conditions suboptimal for cell viability during bioprinting [2]. Centrifuging Protanal/$CaCl_2$ mixtures at 2000 rpm for 2 minutes and performing overnight refrigeration of hydrogel at 4°C prior to addition of cells helped to remove air bubbles and increase bioink homogeneity and printability.

Biogelx S was also examined as an alternative bioink to alginate-based hydrogels with the expectation that it could have superior bioactivity. Following optimisation of Biogelx S bioprinting settings (Fig. 4.8 C), comparison was made with 2% Protanal/ 0.2% $CaCl_2$ and 2% Protanal/ 0.0.15% $CaCl_2$ as two of the most readily bioprintable partially-crosslinked alginate bioinks. Ultimately, 2% Protanal/ 0.2% $CaCl_2$ appeared to give the best combination of bioprintability (Table 4.2) and cell viability when 10 x 10 x 1mm porous constructs containing hBMMSCs were bioprinted (Fig. 4.9).

Table 4.2 Bioprintability of Protanal alginate /$CaCl_2$ pre-crosslinked compositions

Alginate (%)	CaCl$_2$ (%)				
	0.4	0.3	0.2	0.15	0.1
1%	*	*	*	*	*
2%	*	**	***	***	**
3%	*	**	**	**	**
4%	*	*	*	**	**
6%	*	*	*	*	*

*Poor **Satisfactory ***Very Good
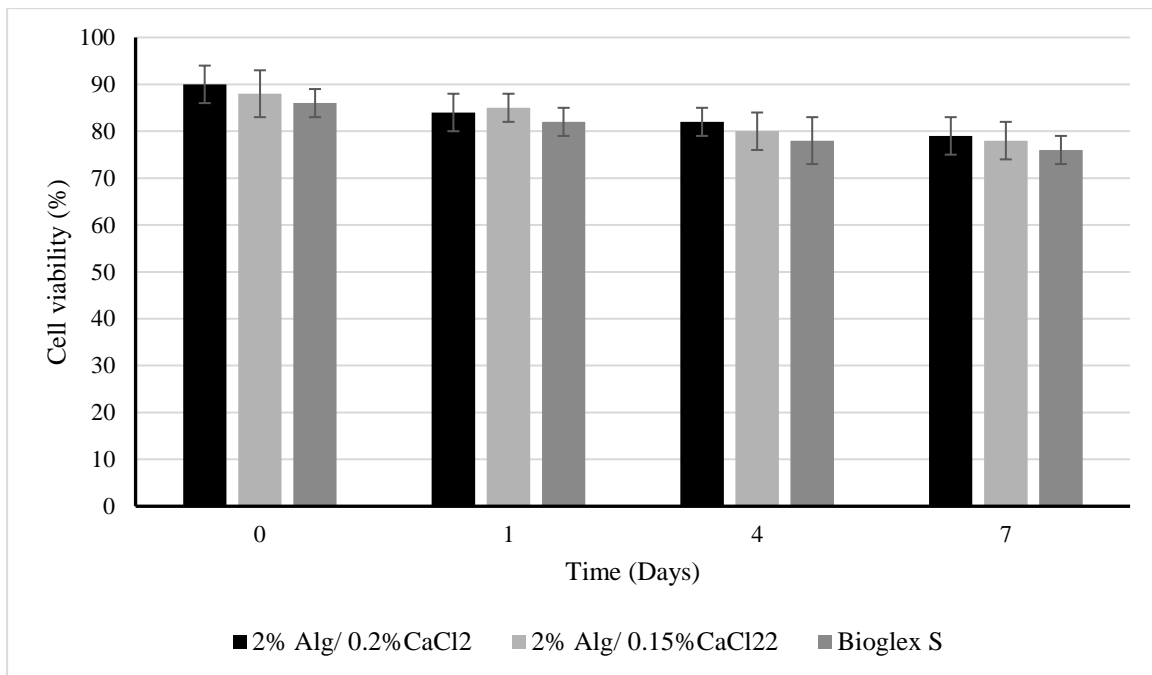
Figure 4.9 Morphology and Viability of Bioprinted hBMMSC/Bioink Constructs**. (A)** Examples of 10 x 10 x 1mm porous constructs containing hBMMSCs bioprinted using 2% Protanal/ 0.2% $CaCl_2$ (left) and Biogelx S (right). Similar morphology is evident following bioprinting the same design using the two different bioinks confirming bioprintabiltiy. Scale bar = 1cm **(B)** Viability of hBMMSCs within the different bioinks displayed over 7 days. No significant difference in cell viability was found between the bioinks used (p>0.05).

4.3.9 **FRESH Bioprinting of Alginate Constructs**

Having established stability and viability of bioprinted constructs to 7 days, attention turned to increasing the complexity and scale of bioprinted constructs. Alginate constructs of increasing size and complexity were successfully bioprinted by combining an extrusion bioprinter with the FRESH method of bioprinting (Fig. 4.11). Bioprinting settings were optimised over successive bioprinting attempts, with individual layer heights of 0.06 mm and a 30G needle initially used to bioprint constructs including knee replacement, blood vessel and ear models (Fig. 4.11). Although ADSC viability was satisfactory following bioprinting at a density of 1 x 10^5 cells/ml (Fig. 4.12), use of a 30G needle did appear to cause slight impairment in cell viability when compared to use of a 25G needle previously (Fig. 4.9 B). Analysis of constructs was performed to 7 days as beyond this point constructs became more fragile and began to partially fragment and disintegrate. This was likely due to loss of alginate crosslinking as calcium leached from constructs into surrounding cell media [18].
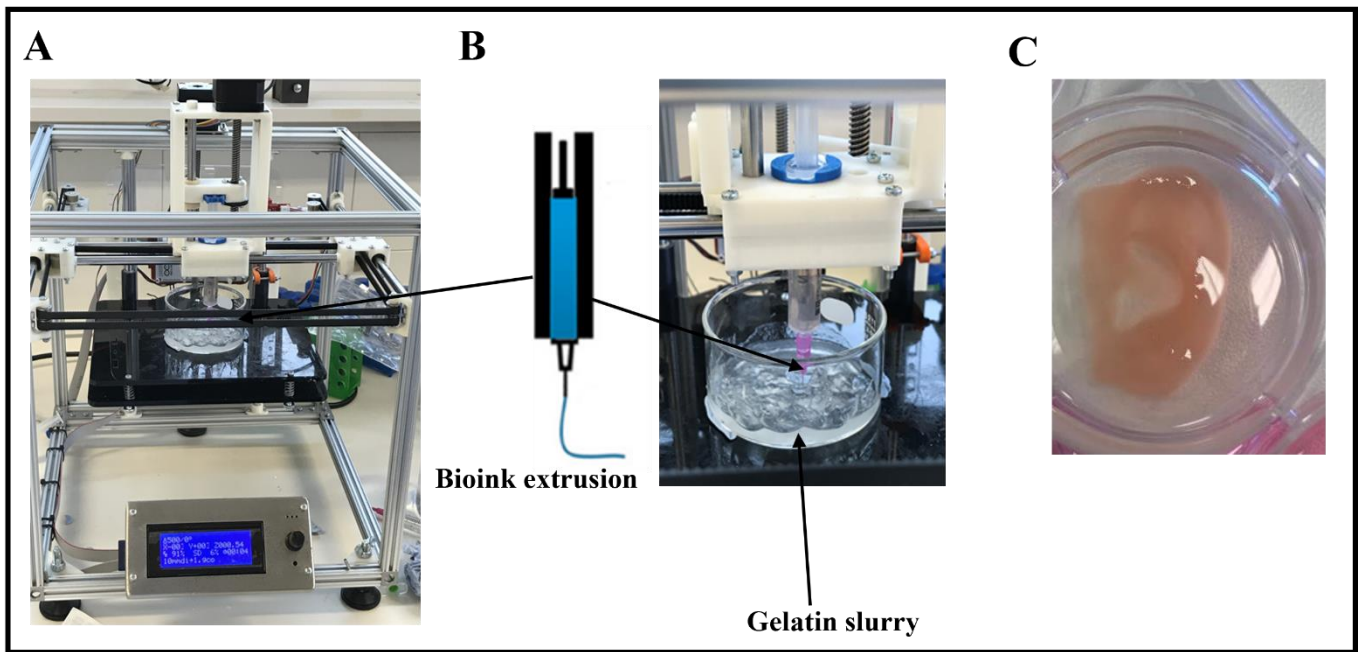
Figure 4.10 Schematic demonstrating FRESH bioprinting process. **(A)** A three-axis (X-Y-Z), single nozzle custom built 3D cell bioprinter used for bioprinting different bioinks laden with cells. **(B)** The bioprinter produces 3D constructs by coordinating the motion of a mechanically-driven syringe. The syringe extrudes filaments of bioink onto a stationary Z-platform (z-platform is black surface seen in A and B of above schematic). As successive layers of extrudate are deposited, the z-platform moves downwards allowing structures to be bioprinted from the bottom up, layer-by-layer. Bioprinting using the FRESH method involves depositing bioink in a gelatin slurry, seen at the bottom of the glass dish. **(C)** Once bioprinting is finished, the support bath that surrounds the deposited hydrogel can be removed through exposure to warmed calcium chloride solution. This melts away gelatin whilst simultaneously crosslinking bioprinted alginate, releasing a cross-linked alginate structure.
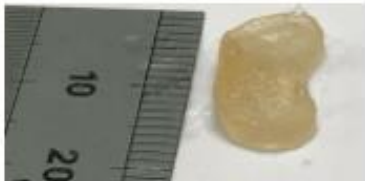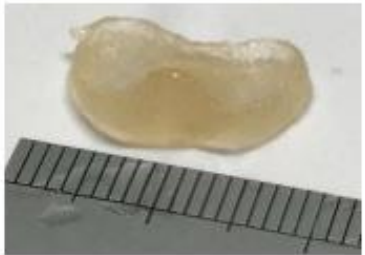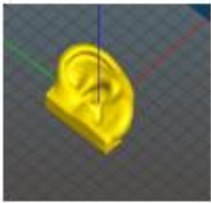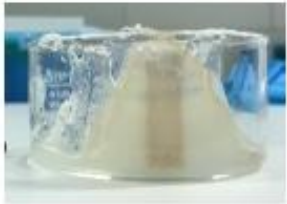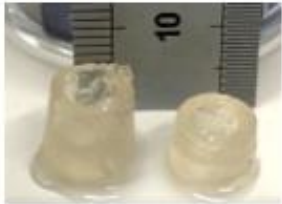
CAD File	Construct within FRESH support bath	Construct released from FRESH support bath
Knee replacement		
Ear		
Vessels		

.

Figure 4.11 Bioprinting of structures using the FRESH method. Initial computer aided design (CAD) models are created for the 3D bioprinter. Models are then bioprinted into a gelatin

support bath and released through addition of warm 100 mmol $CaCl_2$ solution to leave cross-linked alginate structures.
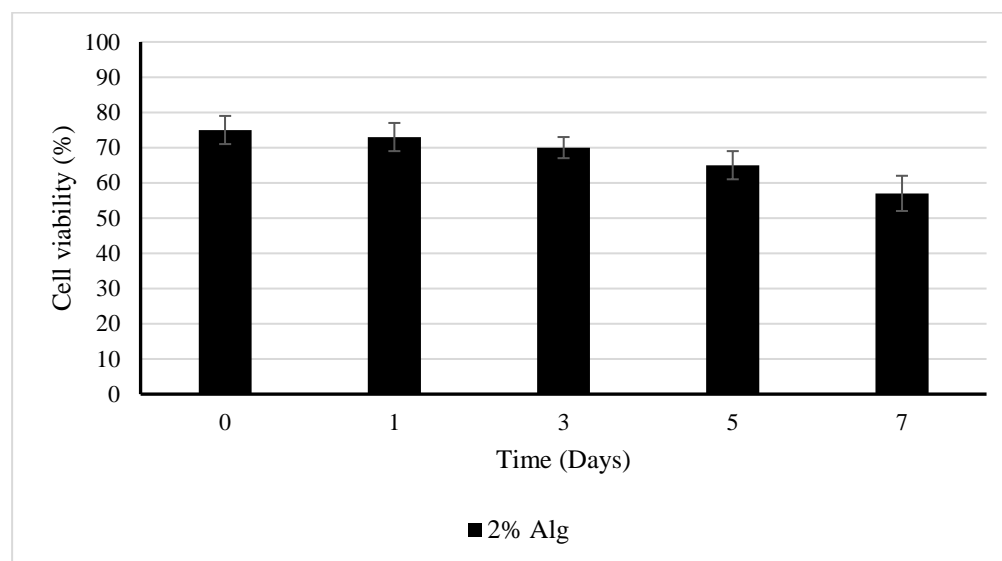
A

Post-printing	24 Hours	72 Hours	7 days
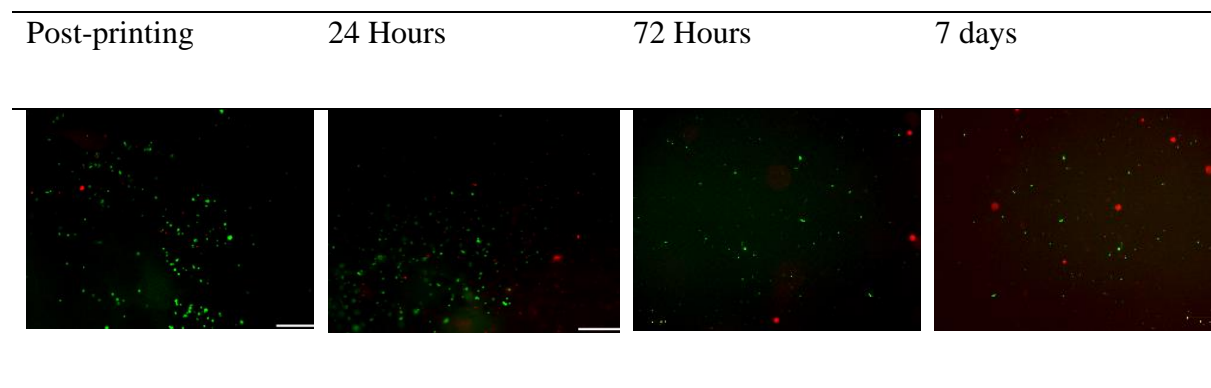
B

Figure 4.12 Viability of FRESH-bioprinted ADSCs in 2% alginate using 30G needle. **(A)** Live/dead imaging of FRESH-bioprinted ADSCs printed within a blood vessel model show good initial viability, with increasing presence of dead cells. **(B)** Initial post-printing cell viability (75%) appeared to be lower than in previous bioprints where 25G needles were used,

presumably due to increased sheer stresses. Viability analysis beyond 7 days was restricted by deteriorating construct integrity.

4.3.10 **FRESH Bioprinting of UV-Crosslinkable Methacrylated Alginate (AlgMA) Constructs**

Following successful FRESH bioprinting of alginate structures, methacrylated alginate (AlgMA) was investigated as an alternative bioink. Due to the low viscosity of non-UV crosslinked AlgMA, extrusion bioprinting was again performed using the FRESH method, with 10mm x 10mm x 1mm porous constructs bioprinted using 25G needles. It was expected that the potential to perform both UV- and ionic crosslinking could increase construct stability within extended cell culture. Furthermore, use of a 25G needle was expected to reduce shear stresses to cells during bioprinting and therefore improve cell viability compared to use of a 30G needle.

4.3.11 **Impact of Crosslinking Conditions on AlgMA Stability**

The impact of different crosslinking conditions on the stability in culture of bioprinted AlgMA was first examined (Fig. 4.13 A). Use of $CaCl_2$ alone for crosslinking following bioprinting led to insufficient stability, whilst combining dual ionic crosslinking ($CaCl_2$ and $BaCl_2$) with UV-crosslinking led to the lowest overall rates of degradation.

Table 4.3 Impact of Crosslinking Conditions on AlgMA Stability in Culture.

|	Day 7 – Gross Integrity	Day 14 - % Degradation
100mM $CaCl_2$	Degraded	Degraded – 100%
40mM $BaCl_2$	Intact	33 ± 8
100mM $CaCl_2$ & 40 mM $BaCl_2$	Intact	34 ± 12

| 100mM CaCl$_2$, 40 mM BaCl$_2$ +UV | Intact | 28 ± 8 |

4.3.12 **Impact of UV-Crosslinking on Cell Viability**

The impact of UV-crosslinking on cell viability was also examined (Fig. 4.13). When constructs were exposed to UV light for 60s and ionic crosslinking conditions kept constant, it was found that cell viability was not significantly impaired compared to non-UV exposed AlgMA constructs over a 14-day period ($p > 0.05$) (Fig. 4.13 B).
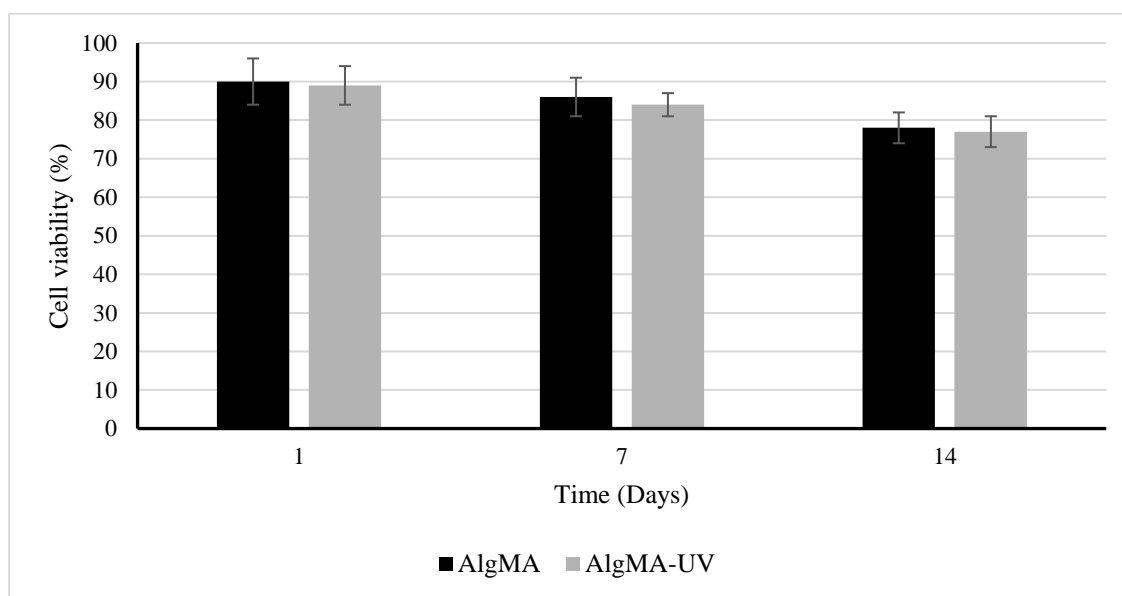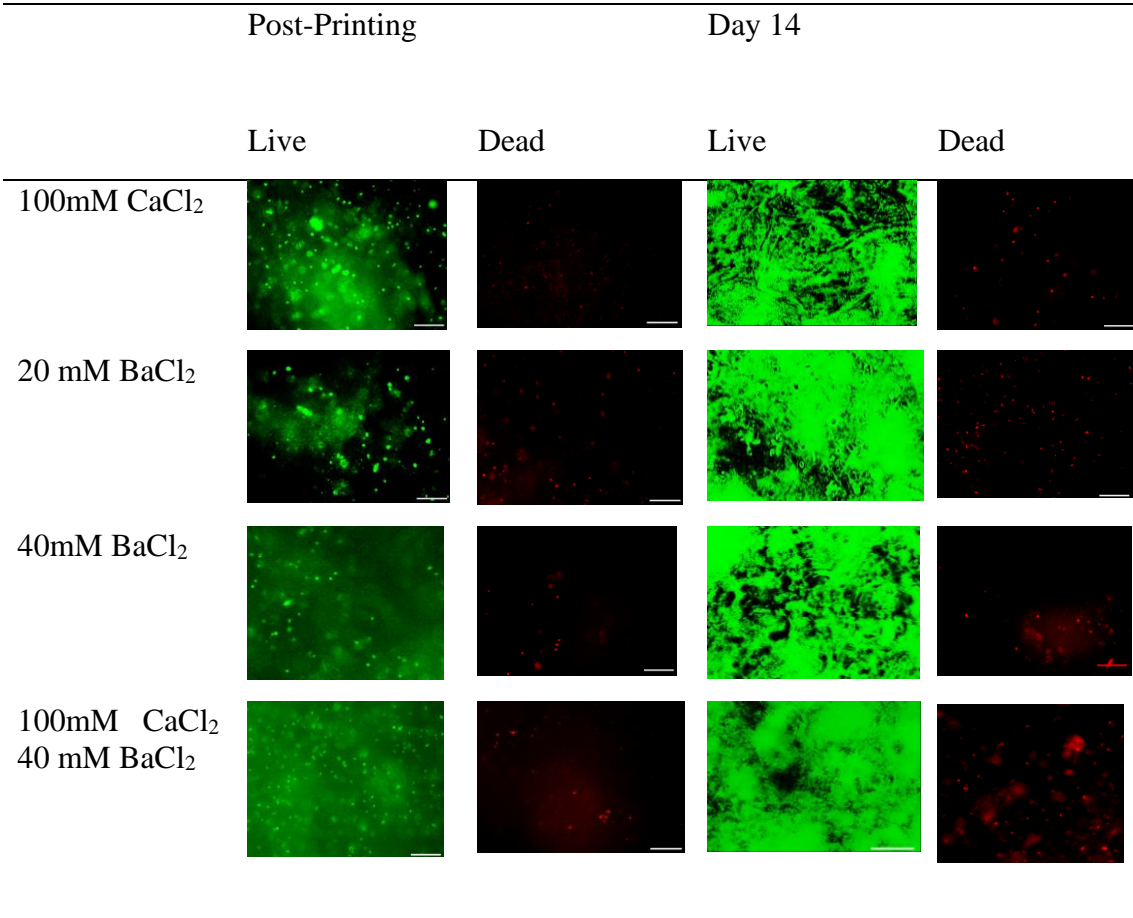
A
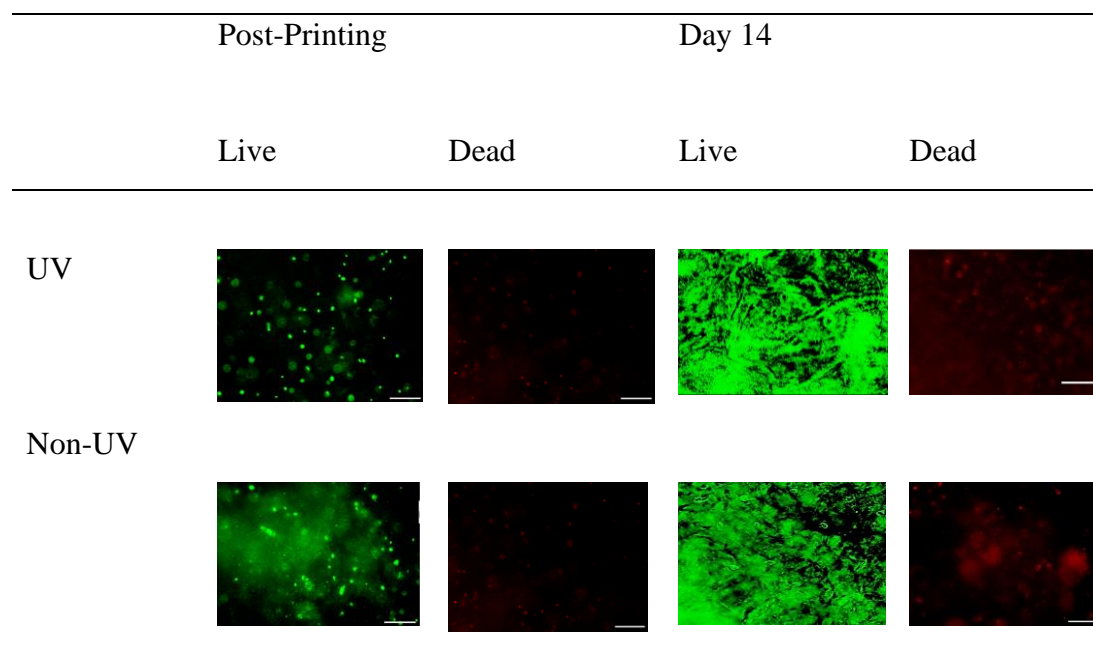
B

Figure 4.13 Impact of UV-crosslinking on cell viability. **(A)** Live/dead imaging of UV- and non-UV exposed 100 mM $CaCl_2$/40 mM $BaCl_2$ AlgMA constructs up to 14 days following bioprinting demonstrated good cell growth in both constructs, **(B)** with no significant difference in cell viability demonstrated (p>0.05).

4.3.13 Combining Different Ionic Crosslinking Conditions with UV Crosslinking – Impact on Cell Viability

UV-crosslinking of AlgMA constructs was combined with different ionic crosslinking conditions during the FRESH bioprinting process, allowing the impact of different ionic crosslinking conditions on AlgMA construct biocompatibility to be examined. Following extrusion into a gelatin support bath, constructs were crosslinked using either $CaCl_2$, $BaCl_2$, or a sequential combination of both, with all constructs exposed to 60s UV crosslinking. No

significant difference in cell viability was observed between different crosslinking conditions,

with good cell growth demonstrated in all four constructs after 14 days (Fig. 4.14).
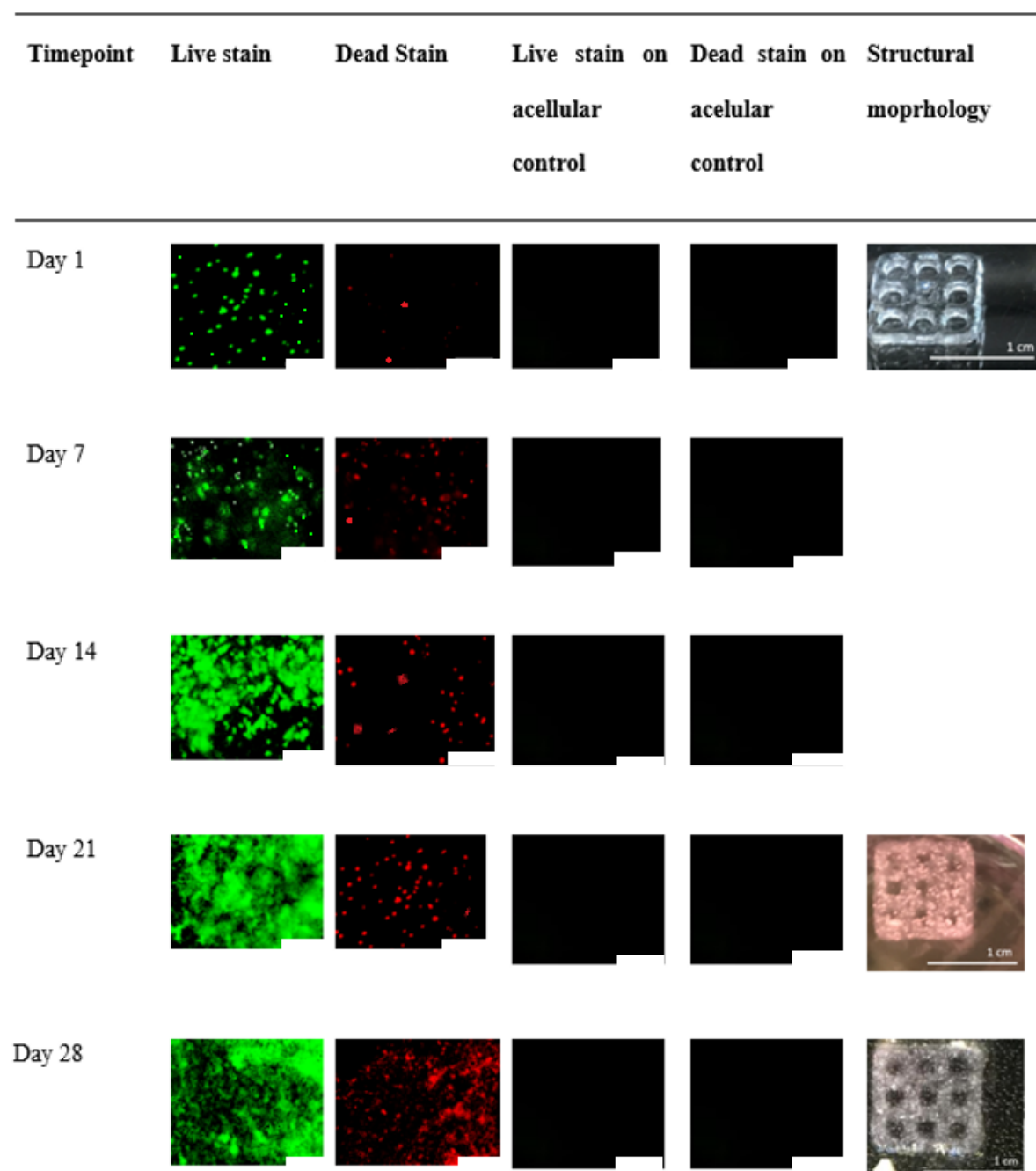
A

	Post-Printing		Day 14	
	Live	Dead	Live	Dead
100mM CaCl$_2$				
20 mM BaCl$_2$				
40mM BaCl$_2$				
100mM CaCl$_2$ 40 mM BaCl$_2$				

B
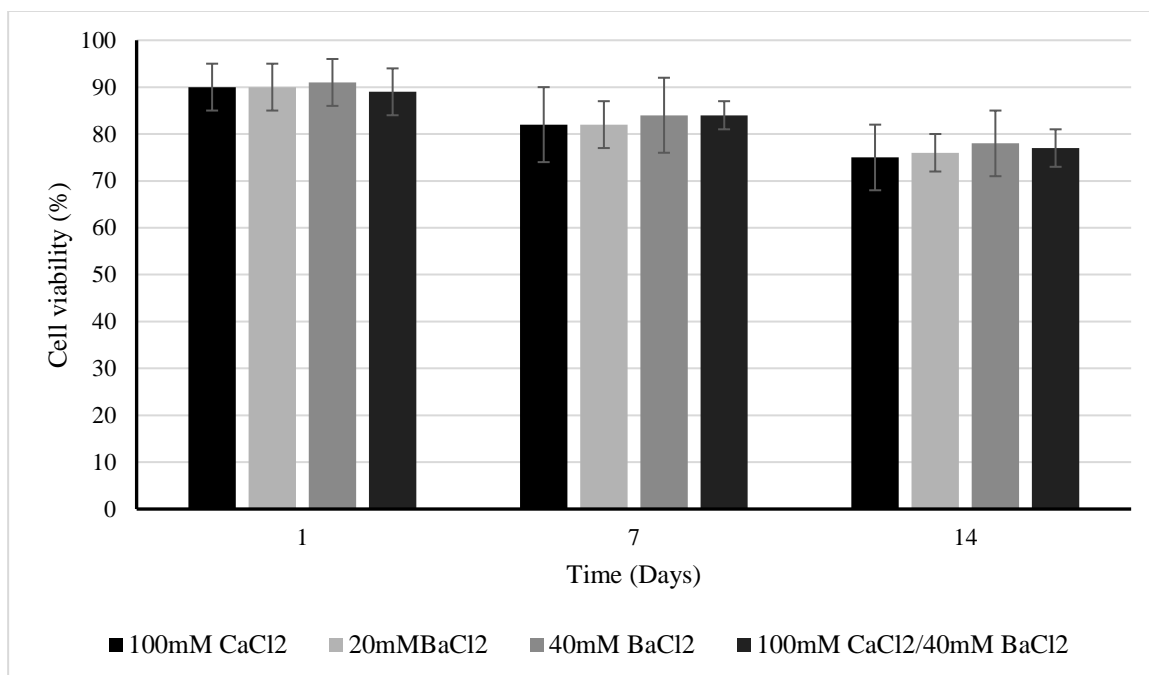
Figure 4.14 Impact on cell viability of combining different ionic crosslinking conditions with UV crosslinking. **(A)** Live/dead imaging of UV and ionically crosslinked AlgMA constructs up to 14 days following bioprinting demonstrated good cell growth in all constructs, **(B)** with no significant difference in cell viability demonstrated ($p>0.05$). Scale bars represent 100 μm.

4.3.14 Extended Culture of Triple Crosslinked AlgMA Constructs

Over 28 days of culture, triple crosslinked (UV/100mM $CaCl_2$/40 mM $BaCl_2$) 2 % w/v AlgMA/ 0.5% Ig 2959 constructs maintained their initial bioprinted design, whilst appearing to support healthy ADSC growth and proliferation (Fig.4.15).

A

Timepoint	Live stain	Dead Stain	Live stain on acellular control	Dead stain on acelular control	Structural moprhology
Day 1					
Day 7					
Day 14					
Day 21					
Day 28					

.

B
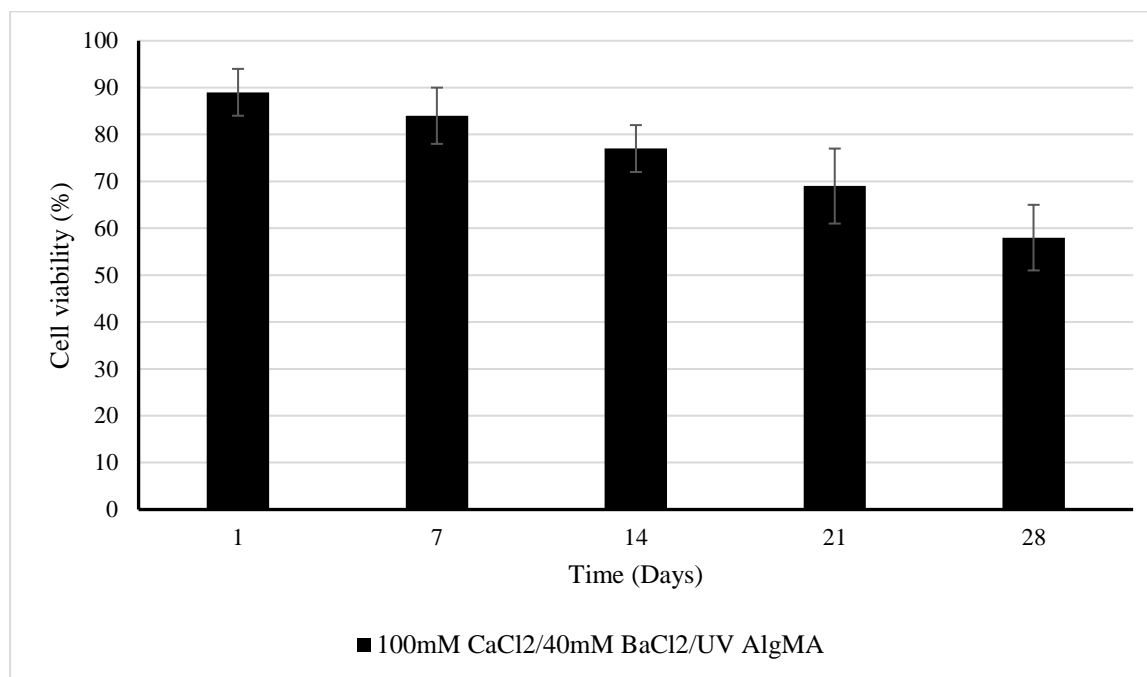
Figure 4.15 Cell viability and structural morphology of triple-crosslinked AlgMA loaded with ADSCs at a density of 1 x 10^6 cells/ml. **(A)** Live/dead imaging of UV and ionically crosslinked AlgMA constructs up to 28 days following bioprinting demonstrated good cell growth, well maintained structural morphology and **(B)** strong cell viability. Scale bars represent 100 μm.

4.3.15 **Bioprinting Biogelx Standard Preparation Hydrogel (Biogelx S)**

Biogelx S was examined as an alternative bioink to AlgMA with the expectation that it could have superior bioactivity.

To allow comparison, extrusion bioprinting of 10mm x 10mm x 1mm porous constructs was performed using Biogelx S, with the hydrogel viscous enough to be bioprinted without use of the FRESH method. Over 3 weeks of culture, constructs grossly maintained their initial bioprinted design although became more friable, whilst appearing to support strong ADSC growth and proliferation. However, by one month construct integrity had deteriorated

significantly, and constructs were much more friable during analysis and physical manipulation compared to crosslinked AlgMA constructs (Fig. 4.16).
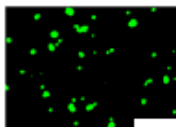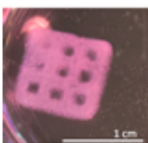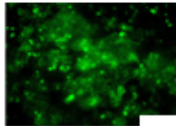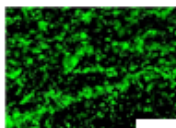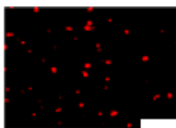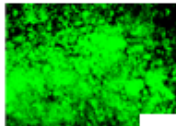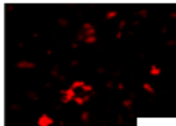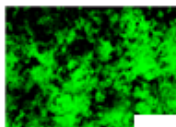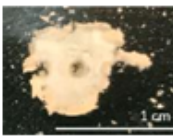
Timepoint	Live stain	Dead Stain	Live stain on acellular control	Dead stain on acelular control	Structural moprhology
Day 1					
Day7					
Day 14					
Day 21					
Day 28					

Figure 4.16 Cell viability and structural morphology of bioprinted Biogelx S loaded with ADSCs at a density of 1×10^6 cells/ml. Strong cell viability is seen up to 21 days, with more

dead cells found after 6 weeks of culture. Bioprinted constructs retained shape and structural integrity initially, before beginning to disintegrate. Scale bars represent 100 μm.

4.3.16 **Bioprinting biogelx RGD preparation hydrogel (Biogelx RGD)**

Biogelx RGD adds to the composition of Bioglex S by including the tripeptide Arg-Gly-Asp (RGD). RGD was originally identified as the sequence within fibronectin that mediates cell attachment and has subsequently been identified in a number of other proteins that support cell adhesion, cell-substratum and cell-cell interactions [19]. Addition of RGD to the standard Biogelx hydrogel therefore was expected to boost biocompatibility and cell growth. To investigate this extrusion bioprinting of 10mm x 10mm x 1mm porous constructs was again performed. Over 3 weeks of culture, constructs maintained their initial bioprinted design, whilst appearing to support strong ADSC growth and proliferation up to 3 weeks, similar to that seen in Biogelx S hydrogel constructs. However, after 3 weeks construct integrity again significantly deteriorated (Fig. 4.17).
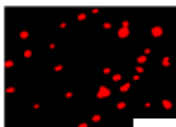
Timepoint	Live stain	Dead Stain	Live stain on acellular control	Dead stain on acelular control	Structural moprhology
Day 1					
Day 7					
Day 14					
Day 21					
Day 28					
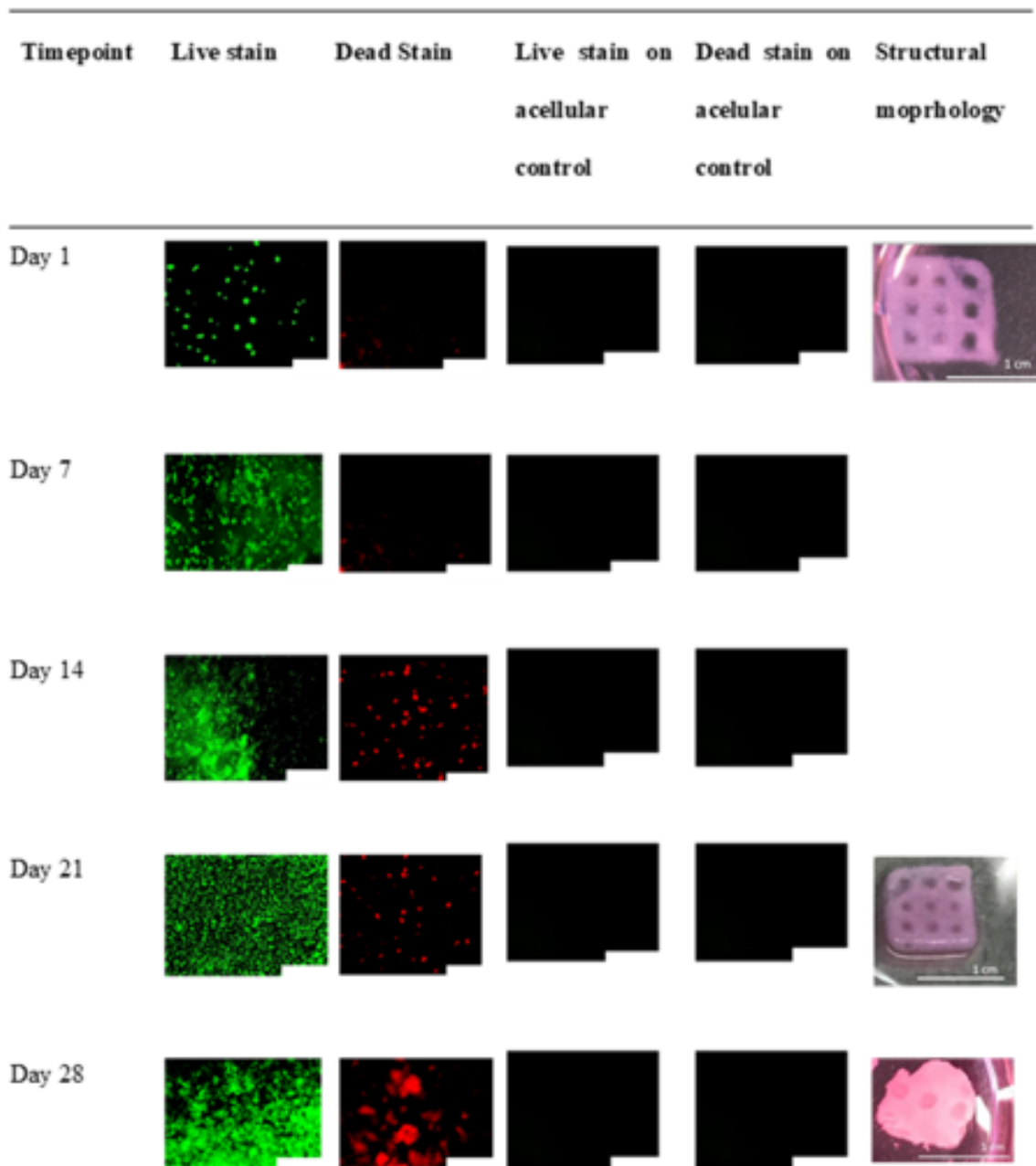
Figure 4.17 Cell viability and structural morphology of bioprinted Biogelx RGD loaded with ADSCs at a density of 1 x 10^6 cells/ml. Strong cell viability and proliferation is seen up to 21 days, with more dead cells found after one month of culture. Bioprinted constructs retained shape and structural integrity initially, before beginning to disintegrate. Scale bars represent 100 μm.

4.3.17 Comparison of Biocompatibility and Stability of AlgMA and Biogelx Constructs

In summary, it was apparent that the best stability in culture was offered by FRESH-bioprinted triple-crosslinked AlgMA constructs. However, comparison of cell viability found that Biogelx RGD had significantly improved viability compared to Biogelx S and AlgMA between 14 and 28 days of culture ($p<0.05$) (Fig. 4.18). However, Biogelx RGD and Biogelx S constructs began to lose significant structural properties during extended culture (Fig. 4. 16 and 4.17). Attention was therefore turned to producing a bioink that could potentially combine biocompatibility with stability in culture.
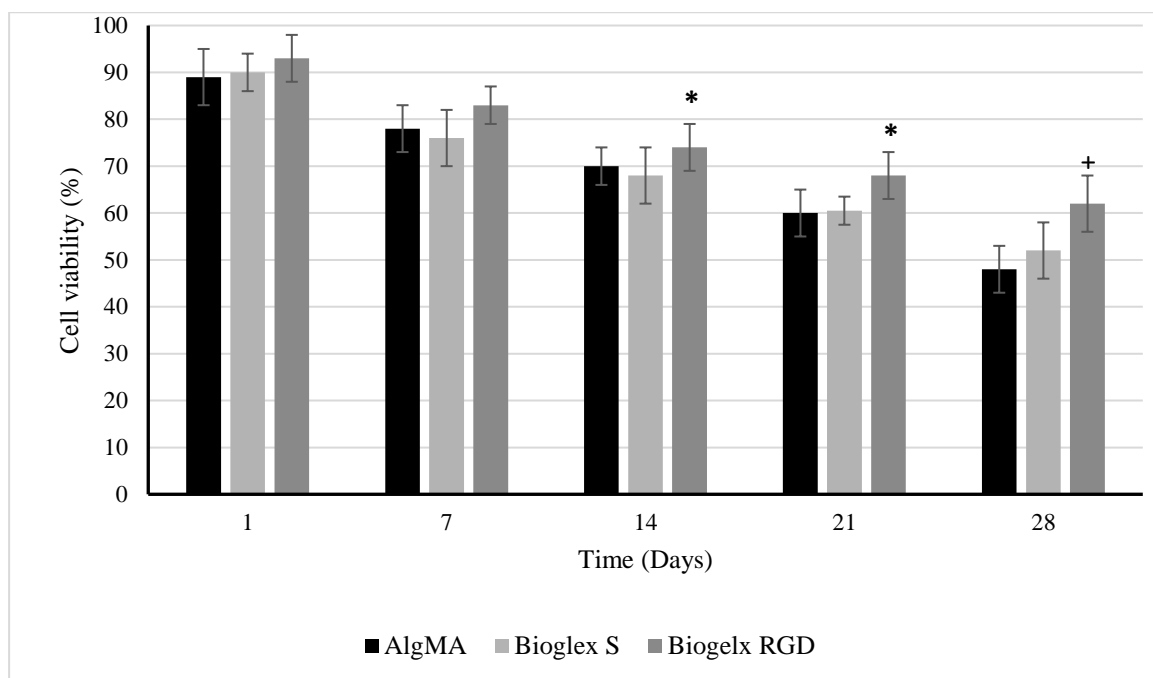
Figure 4.18 Comparison of cell viability between AlgMA and Biogelx preparations. Addition of RGD to Bioglex hydrogel led to significantly higher cell viability at 14 days of culture and beyond (*<0.05) compared to AlgMA and Bioglex S. However, both Biogelx S and Bioglex RGD had visible signs of degradation at 28 days whilst AlgMA scaffolds remained intact.

4.3.18 Incorporation of Collagen into Bioinks

As the most the most abundant macromolecule with the ECM of cartilage and bone, collagen represents an obvious choice for inclusion in a bioink directed at osteochondral regeneration. As part of the native ECM it is inherently biocompatible, biodegradable and has been shown to help stimulate cell proliferation and differentiation as it includes amongst other motifs a high density of RGD sequences that facilitate cell adhesion and cell differentiation [20, 21]. However, in common with other natural polymers, collagen has mechanical properties that are insufficient for creating a load-bearing scaffold and is also prone to degradation [22, 23]. The following section therefore developed production of a collagen hydrogel to allow formation of a bioink, and also examined combining collagen with AlgMA to create a composite bioink.

4.3.19 Collagen Hydrogel Production

Type I collagen was initially extracted from rat tails (Methods 3.1.11.18). To calculate the concentration (mg/ml) of collagen produced, 3ml of the extract solution was pipetted into 3 pre-weighed 100mm petri dishes and the collagen allowed to dry at 37°C before reweighing of the collagen precipitate. The initial dry weight of collagen extracted was calculated as 5 ± 0.3 mg/ml.

Collagen gels were prepared (Methods 3.1.11.18) and different methods then used to biofabricate structures using the resulting hydrogels. Collagen gelation occurs as temperatures increase towards room and body temperature at 37°C [24]. Due to the lack of a temperature control on our 3D bioprinter printhead, initial strategies to biofabricate 3D collagen structures therefore focused on moulding techniques instead of bioprinting. This circumvented the potential issue of bioprinter nozzle blockages occurring due to gelation of collagen within the bioprinter nozzle during bioprinting.

4.3.20 **Use of Soft Lithography to Biofabricate Collagen Structures**

Two separate approaches were utilised to produce 3D structures using collagen gels. Initially, silicon moulds were produced by stamping liquid silicone with a 3D-printed PLA design. Once the silicon cured, this allowed collagen to be injected into the inverse mould produced. Collagen gel was allowed to cure via crosslinking at 37°C before 3D collagen structures were physically released from the silicone mould and placed into further incubation in culture conditions (Fig. 4.19 A). Unfortunately, the collagen structures became fragile in nature during prolonged culture and began to fragment.

In a similar approach, 3D printed PLA stamps were used to create mould designs in liquid agarose. Once the agarose had set, PLA stamps were removed allowing collagen to be injected into the stamp design left behind. Collagen was again allowed to crosslink at 37°C before release from the mould and further incubation in culture conditions. Again, collagen structures demonstrated evidence of fragmentation during prolonged culture (Fig. 4.19 B).

Despite structural integrity of the moulded collagen constructs visibly deteriorating within culture conditions over a 7-day period (Fig. 4.19), cell viability remained high in remaining construct materials after 7 days of culture. Initial viability of ADSCs encapsulated in the collagen gel at a density of 1 x10^5 cells/ml was $95 \pm 3\%$, whilst at 7 days $82 \pm 5\%$ of cells remained viable (Fig. 4.20).

(A)

Collagen applied to mould   Release of construct from mould   Construct at 7 days

(B)

PLA stamps inserted into liquid agarose   Removal of PLA stamps to leave inverse in mould   Collagen injected to moulds

Release of constructs from moulds   Construct at 7 days
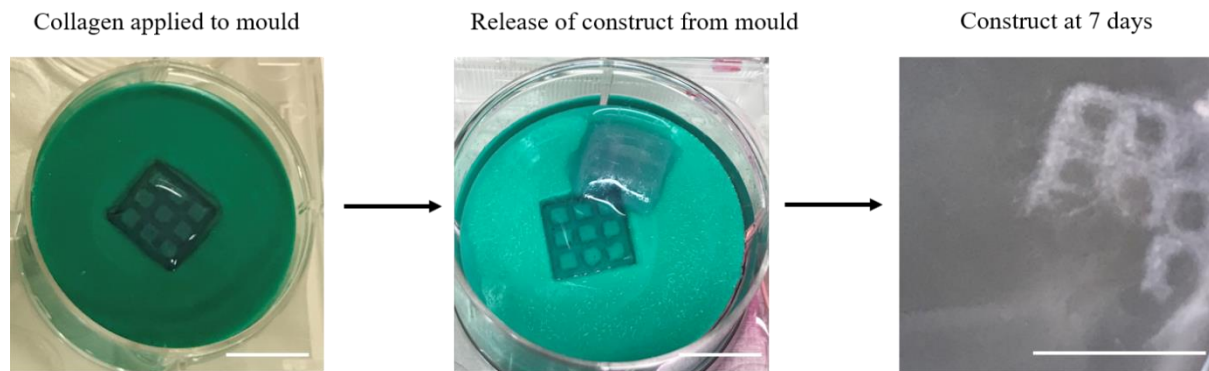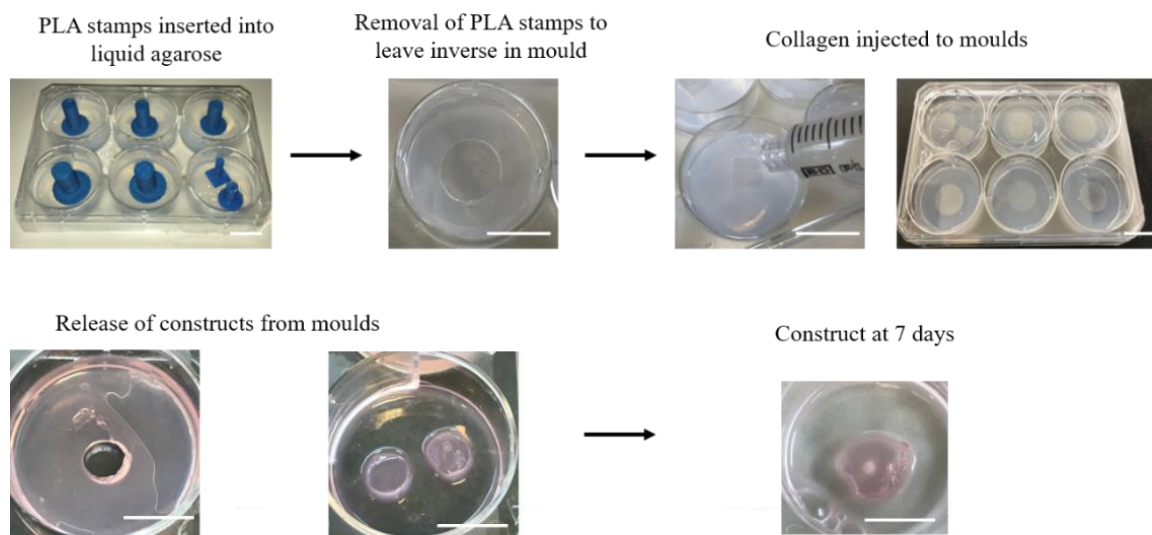
Figure 4.19 Moulding techniques to produce collagen structures. **(A)** Silicon inverse moulds were used as part of a soft lithography technique to produce porous collagen scaffolds. Collagen injected into the mould was allowed to crosslink at 37^{oc} before release from the mould and further incubation in culture conditions. **(B)** A further inverse moulding technique was utilised, with 3D printed PLA stamps used to create mould designs in liquid agarose. Once the agarose had set, PLA stamps were removed allowing collagen to be injected into the stamp design left

behind. Collagen was again allowed to crosslink before release from the mould and further

incubation in culture conditions. Scale bar represents 1cm.

A

Post-printing	24 Hours	72 Hours	7 days
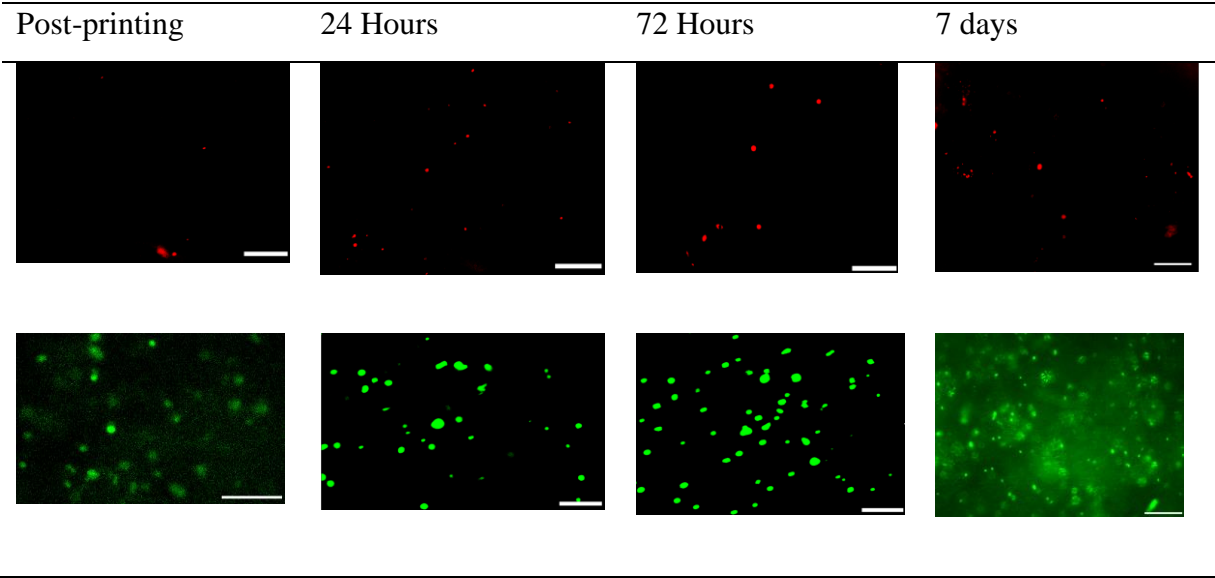
B
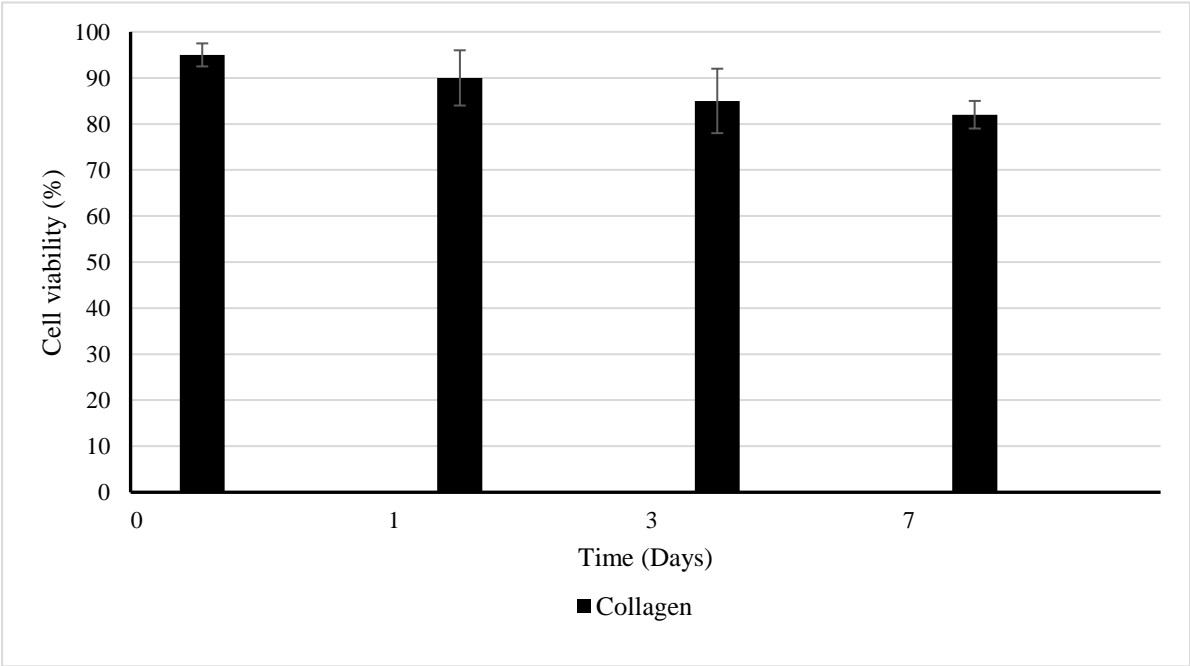
Figure 4.20 Viability of ADSCs within moulded collagen structures. **(A)** Live/dead imaging of ADSCs within collagen constructs. **(B)** Despite structural integrity deteriorating within culture conditions, cell viability remained high after 7 days of culture.

4.4 **Discussion**

4.4.1 **Choice of cell type**

MSCs and ADSCSs were used throughout experiments due to their multipotent potential to differentiate into cell types found in musculoskeletal tissues, including chondrocytes and osteocytes. Compared to pluripotent cell sources, such as such as embryonic stem cells (ESCs), MSCs and ADSCs have increased availability and reduced ethical considerations, making them a more feasible cell source for clinical tissue regeneration. ADSCs can reportedly be harvested at up to 500 times the density of BMMSCs from equivalent volumes of tissue [25, 26]. Furthermore, adipose tissue biopsy in patients also involves a less painful and invasive procedure with lower risk of morbidity than bone marrow biopsy [27]. Some reports also suggest that ADSCs have higher proliferative capacity and apoptosis tolerance compared to BMMSCs and are less affected by patient age in their capacity for proliferation and differentiation [25, 28]. MSCs are however recognised as being capable of producing a variety of ECM molecules that are critical for cartilage function, including collagens (Cols), fibronectin, proteoglycans, and glycosaminoglycans (GAGs), as well as a variety of cytokines [29] and have been extensively research within cartilage regeneration [2, 26, 30-33].

4.4.2 Initial Use of an FDM Approach and PCL Filaments

The primary aim of this research was to design and optimise a 3D biofabrication methodology capable of supporting 3D osteochondral regeneration. Initial work focussed on the use of PCl and an FDM 3D printer to produce a porous scaffold that could be seeded with cells. Advantages of PCL include biocompatibility, relatively slow degradation rate, less acidic breakdown products in comparison to other polyesters and potential for load-bearing applications [34-37]. However, previous studies have demonstrated the benefit of modifying PCL to improve bioactivity [10, 13]. Initial exposure of PCL scaffolds to NaOH was performed to improve hydrophilicity of scaffolds as PCL is recognised as having a relatively low surface hydrophilicity, which ultimately impairs cellular adhesion [38]. Immersion of PCL in NaOH causes surface hydrolysis and disruption of ester linkages along the PCL polymer backbone, increasing exposure of hydroxyl and carboxylic acid groups on the PCL surface that can form hydrogen bonds with water molecules [10, 23]. However, prolonged NaOH exposure can lead to unchecked breakdown of scaffold structure and mechanical integrity [38, 39]. Exposure of PCL scaffolds to NaOH prior to MSC seeding led to significantly greater cell viability at 24 hrs ($p<0.05$), with no benefit found to increasing exposure beyond 1M NaOH or 1 hr duration of immersion. This is in keeping with previous studies that found immersion of PCL scaffolds in up to 4M NaOH led to improved cell attachment and viability, without significant change in material properties [40, 41].

PCL scaffolds were then modified further, through the creation of hybrid hydrogel/PCL scaffolds. The hydrophilic nature of hydrogels allows them to absorb up to 1000 times their original weight in water into a three-dimensional network, ideal for supporting cell growth. At the same time, they are highly permeable to oxygen, nutrients and other water-soluble compounds, making them attractive materials for inclusion in tissue engineering constructs [42,

43]. Alginate was chosen for use in a hybrid scaffold as a biocompatible and readily available hydrogel that has previously been incorporated into several investigations of cartilage biofabrication [23, 44, 45]. Biogelx S was chosen as a novel supramolecular biomaterial with tuneable mechanical properties, that has previously been shown to facilitate chondrogenic differentiation of MSCs in 3D culture [46]. It was notable that hybrid scaffolds incorporating alginate and Biogelx S hydrogel both had superior cell viability compared to control PCL scaffolds. This result was likely the result of improved biocompatibility, cell affinity and replication of the native ECM imparted by the inclusion of hydrogels compared to use of PCL alone.

Previous studies have successfully utilised hybrid scaffolds combining hydrogels such as alginate with synthetic polymer scaffolds for cartilage and osteochondral regeneration [47, 48]. Alternative methods of adding natural polymer content to PCL scaffolds have also been developed. Kim et al. melted PCL and alginate powders together before extruding the melted composite through a print nozzle to create a 3D scaffold via an FDM approach [47]. Compared to a pure PCL scaffold fabricated by the same method, PCL/alginate scaffolds showed increased osteoblast cell viability, calcium deposition, ALP activity and greater cell-seeding efficiency over 7 days in culture. However, applying this approach to include other natural polymers and motifs is subject to limitations, as the melt process and high print nozzle temperatures required for PCL is likely to denature many natural polymers. Electrospinning PCL together with polymers including alginate has also allowed for the creation of scaffolds with enhanced cell adhesion, improved cell viability, optimised mechanical properties and cellular differentiation [49]. However, electrospinning can suffer from limitations including poor cell infiltration and migration as a result of the close packing of scaffold fibres, risk of toxicity from residual solvent, whilst electrospun scaffolds frequently have low mechanical strength [50].

163

4.4.3   **Rationale for Selection of an Extrusion Based Bioprinting Approach**

Despite initial results with use of an FDM produced PCL scaffold, the desire to include a high density of cells directly within the scaffold architecture (rather than seeding them onto a prefabricated scaffold) led to a change in direction to developing a bioprinting approach. Bioprinting can be used to deposit living cells, extracellular matrices and other biomaterials in user-defined patterns to build complex tissue constructs "from the bottom up." Compared to the conventional tissue engineering method of seeding cells onto a prefabricated scaffold, 3D placement of cells or biological content can be performed with greater precision, increasing capacity to create more complex hierarchical tissue constructs [2, 51-54]. Whilst multiple bioprinting technologies are available, including laser-based, inkjet and microvalve systems, extrusion bioprinting was utilised in this project due to several advantages that it possesses. Extrusion bioprinters typically deposit continuous filaments of materials rather than individual droplets deposited in inkjet and laser-based systems. Pneumatic or mechanical pressure (as utilised within our laboratory) is applied to a syringe, causing controlled bioink extrusion through a nozzle. A significant advantage of this approach is the ability to deposit very high cell densities, with some studies manging to purely print cells, for example as filaments of cartilage [55]. A broad range of bioinks have also been successfully extrusion bioprinted, including tissue spheroids, tissue strands, cell pellets, decellularized matrix components and cell-laden hydrogels. Potential for scalability and clinical translation is increased by the high print speed and size of constructs that can be extrusion bioprinted relative to other bioprinting technologies. There are some limitations to extrusion bioprinting; extruded bioinks must have sufficient viscosity to be self-supporting following bioprinting. In the case of alginate, collagen and GelMA bioprinting, this required adoption of the FRESH method [56], whereby a support

bath provided secondary support and guidance to bioprinted constructs following bioprinting, until cross-linking could occur. However, use of this method results in additional labour related to support bath preparation, and requires optimisation, adding complexity to the bioprinting process. Furthermore, bioprinting so far with the FRESH approach typically has been demonstrated with a single print needle, potentially limiting the contents of bioprinted constructs to a single bioink [56]. Further challenges within extrusion bioprinting include achieving high print resolution; cell survival decreasing with increasing pressure, nozzle gauge, and shear stress and development of printable bioinks. These challenges were partly evident, as earlier use of narrower 30 G needles to bioprint with alginate resulted in increased cell death compared to bioprinting with 25G needles, presumably due to increased shear stresses within the narrow gauge needle [53].

4.4.4   **Initial Choice of Alginate-Based Bioink**

Successful bioprinting relies in part on combining a suitable bioprinting technique with an appropriate bioink [2]. Alginate was chosen as the initial hydrogel for investigation having previously been applied to multiple biomedical applications, due to its biocompatibility, low toxicity, relatively low cost, and crucially for 3D bioprinting, a capacity to undergo gelation by addition of divalent cations such as Ca^{2+} [57, 58]. The US Food and Drug Administration (FDA) also previously approved alginate for a number of clinical trials [59, 60]. More than 200 different alginates are currently manufactured and in fact alginate is a whole family of linear copolymers made from blocks of (1,4)-linked β-D-mannuronate (M) and α-L-guluronate (G) residues. The blocks are composed of consecutive G residues (GGGGGG), M residues (MMMMMM), and alternating G and M residues (GMGMGM). Alginates extracted from different sources differ in M and G contents as well as the length of each block. The G-blocks

of alginate are believed to primarily participate in intermolecular cross-linking with divalent cations, and the mechanical properties of alginate gels typically are enhanced by increasing the length of G-block and molecular weight [61]. Protanal (Protanal LF 10/60 FT, 89.00 g/mol, FMC Biopolymers Girvan, UK) was chosen for inclusion in experimental work as a low viscosity sodium alginate of high-G content. Protanal is well adapted to bioprinting compared to some alternative alginates for two main reasons; low viscosity is recognised to decrease shear stresses exposed to cells during the bioprinting process, whilst a high-G content (over 70%) facilitates rapid crosslinking following bioprinting. Furthermore, it is recognised as having high purity following manufacture; other alginate preparations retain higher levels of potentially pro-inflammatory impurities such as endotoxin and polyphenols following extraction from seaweed [57] .

4.4.5   Development of AlgMA-Based Bioink with Optimised Crosslinking

Initial work relied on the use of calcium crosslinking to maintain stability of alginate constructs following extrusion. However, it is recognised that exchange reactions with monovalent cations such as sodium ions frequently occur in physiological conditions, leading to disruption of divalent crosslinking, loss of mechanical properties and hydrogel disruption [62]. $CaCl_2$ exposure can also result in an extremely fast gelation rate with alginate, creating varying crosslinking densities throughout the construct [63]. This appeared to be the case in initial work, despite partial pre-crosslinking with $CaCl_2$ prior to bioprinting, use of sonication to remove air bubbles and overnight convalescence of hydrogels prior to printing to help improve homogeneity of crosslinking, with construct integrity notably deteriorating as 7 days of culture progressed. This is in keeping with previous work demonstrating significant ion exchange occurring in culture conditions during the first 24 hours after alginate crosslinking [62], and

significant construct deterioration tending to occur in the 7 days following biofabrication of CaCl2-crosslinked alginate structures [64]. Nevertheless, cell viability was promising and in keeping with that reported following similar extrusion and biofabrication attempts using alginate [64].

Attention was therefore turned to developing the bioprintability of AlgMA. The formation of homogeneous, CaCl2-crosslinked alginate structures is challenging due to the rapid reaction rate of CaCl2 crosslinker which favours crosslinking of exposed surfaces over the inner content of an alginate structure. Furthermore, physiological stability is depleted by loss of crosslinking through ion exchange in culture [65]. However, AlgMA is chemically modified with methacrylate groups that can form covalent bonds through free radical polymerization in the presence of UV light and a photoinitiator [45]. Furthermore, as the methacrylated alginate has remaining free carboxylic acid groups, it can also interact with calcium or other divalent cations to form additional crosslinks [66]. Penetration of UV light through the AlgMA hydrogel also potentially helps with improving homogeneity of crosslinking. Performing combined triple crosslinking, via dual ionic (CaCl2, BaCl2) and UV crosslinking, appeared to significantly reduce construct degradation within culture, whilst simultaneously supporting good cell viability. After 14 days and then 28 days, no detectable impact on cell viability was evident following UV exposure. BaCl2 also had a significant impact on improving construct stability compared to use of CaCl2 crosslinking. Previous research has shown Ba^{2+} to bind with greater affinity to alginate than Ca^{2+}, whilst also binding to G- and M-blocks [58]. It has also been shown to significantly prolong stability of biofabricated alginate constructs *in vitro* [64]. However, one potential limitation is the known toxicity of barium in high doses [67]. Further to this, high-G alginate gelled with a combination of calcium and a relatively lower

concentration of barium has been recommended to minimise risk of barium accumulation and leakage into the body, although it has been shown that unbound barium can at least partly be removed through serial washing of constructs prior to culture or implantation [68]. The decision was therefore made to implement a triple crosslinking approach as standard, via dual ionic ($CaCl_2$, $BaCl_2$) and UV crosslinking, with the concentration of barium used lower than in some other reported studies [58, 64, 68]. The increase in construct stability and scaffold mechanical properties induced through triple crosslinking has also previously been shown to lead to increased stiffness and decreased swelling, compared to ionic or UV-alone crosslinked scaffolds. This in turn is thought to be favourable to chondrocyte, MSC and osteogenic cell growth, as it closer replicates the mechanical properties of the native ECM [66, 69]. Furthermore, construct stability appeared to be improved via triple crosslinking, with the lowest levels of degradation found in triple cross-linked constructs. [70]. UV-crosslinking of AlgMA has also previously been shown to support controlled drug delivery from stable 3D constructs [66], whilst a further study demonstrated greater than 80% viability of bovine chondrocytes encapsulated within dual $CaCl_2$ and UV crosslinked AlgMA hydrogels after 7 days of culture. Our results support these findings, with structural integrity and high cell viability within triple crosslinked AlgMA constructs maintained several weeks after bioprinting.

4.4.6   Evaluating Biocompatibility of AlgMA via Comparison to Biogelx Hydrogel

One potential limitation of alginate is the relative lack of cell-binding properties it possesses, potentially hindering cellular proliferation, migration, and higher order organization [59]. With a view to encouraging dense cell growth and ECM deposition in bioprinted constructs, the printability of Biogelx hydrogels was therefore developed. Previous work involving cell culture with Biogelx hydrogels has revealed attractive properties for use in tissue regeneration. Biogelx

S utilises a two-component co-assembly approach comprising a peptide-based gelator (the structural element) and a surfactant-like molecule that presents carboxylate functionality to the surface of fibres, enabling subsequent cross-linking upon exposure to divalent cations (Ca^{2+}) present in tissue-culture media [71]. Specifically, fluorenyl-9-methoxycarbonyl-diphenylalanine (Fmoc-F2) undergoes co-assembly to form a nanofibrous network with the surfactant-like Fmoc-serine (Fmoc-S) [46]. Previous research has shown evidence of serum proteins from cell-culture media and cells interacting with the nanofibrous network, allowing cell attachment to the fibres [46]. By varying co-assembly concentrations within the hydrogel preparation, mechanical stiffness of the hydrogel can be tuned to reach desired targets. Within soft (1 kPa), stiff (13 kPa), and rigid (32 kPa) gels, neuronal, chondrogenic, and osteogenic differentiation, respectively, has previously been achieved [46]. In contrast to AlgMA hydrogels, Biogelx hydrogels also have the ability to form nanofibrous networks, which are thought to be more biomimetic and result in improved interaction with cells than covalently cross-linked structures [46, 72]. With the benefit of RGD inclusion, cell viability was improved in Biogelx RGD hydrogels compared to AlgMA and Biogelx S. This is consistent with previous literature, where RGD modification has led to improved growth of chondrocytes and production of cartilage [73], and osteoblast growth and mineralisation of tissue [74] in RGD-modified hydrogels. However, whilst denser cell growth potentially appeared to develop within Biogelx S compared to AlgMA over 28-day culture, cell viability was not statistically significantly improved. AlgMA constructs also had far superior structural integrity during prolonged culture compared to both Biogelx S and Biogelx RGD.

4.5 **Overall Summary of Results**

The overall aim of this chapter was to develop and optimise a 3D biofabrication approach that can be applied to target the regeneration and reconstruction of osteochondral defects. Key challenges therefore included the identification and optimisation of successful biofabrication techniques, biomaterials and cell sources that could be applied to osteochondral regeneration. Initial attempts deployed an FDM approach to produce PCL scaffolds that could be seeded with hBMMCs. It was apparent that use of hydrogels significantly increased cell viability and had the benefit of greater biocompatibility compared to use of a thermoplastic PCL scaffold alone. Attention therefore turned to development of a bioprinting approach. When alginate was combined with a FRESH bioprinting approach, complexity and scale of constructs could be increased. Stability in prolonged culture was however limited, and so AlgMA was combined with UV and double-ionic ($BaCl_2$ and $CaCl_2$) crosslinking following bioprinting, leading to significantly enhanced bioink stability in culture without impairing cell viability. However, when comparison was made to Biogelx and collagen preparations, improvement in cell viability was seen. To allow successful treatment of OCD defects, it will be necessary to match the accurate bioprinting of complex constructs achieved using a FRESH approach with a biocompatible bioink with enhanced stability in culture. Attention will therefore be turned in the next chapter to producing a bioink that could potentially combine superior biocompatibility with stability in culture.

5   Chapter 5 – Development of Composite Bioinks for Osteochondral Regeneration

5.1 **Introduction**

A key challenge identified within chapter 4, and within the wider field of biofabrication, has been balancing bioink rheological properties required for printability and structural integrity with bioink biocompatibility after bioprinting [1-3]. To address this challenge previous studies have successfully utilised composite bioinks combining synthetic polymers or more robust hydrogels capable of undergoing crosslinking with naturally derived polymers to boost cellular biocompatibility [4, 5].   Initial work with collagen hydrogel in chapter 4 demonstrated promising cell viability. As the most the most abundant macromolecule with the ECM of cartilage and bone, collagen represented a logical choice for inclusion in a hydrogel for osteochondral regeneration. As part of the native ECM it is inherently biocompatible, biodegradable and has been shown to help stimulate cell proliferation and differentiation as it includes a number of motifs capable of facilitating cell adhesion and differentiation, including high density of RGD [6, 7]. However, in common with other natural polymers, collagen has limited mechanical properties and is also prone to degradation [8, 9]. By contrast, AlgMA crosslinked via UV and $CaCl_2$/$BaCl_2$ mechanisms within chapter 4 had robust stability in culture with cell viability only slightly inferior to a non-UV crosslinked comparison Bioglex bioink at 28 days (Fig. 4.18). To create a bioink capable of combining biocompatibility with resilient structural properties in culture, a range of composite bioinks will therefore be created in this chapter by initially mixing a range of collagen and AlgMA preparations. The potential for inclusion of GelMA in composite bioinks will also be explored. As a biomacromolecule produced from denatured collagen, GelMA-based bioinks have gained increasing popularity

within biofabrication due to excellent biocompatibility, photocrosslinkability, and tuneable mechanical properties, whilst retaining some of the motifs present in native ECM crucial for promoting cellular adhesion and growth [10-12].

5.2 **Results**

5.2.1 **Mixing Stock Collagen and AlgMA Hydrogels to Produce Composite Bioinks**

Composite bioinks were created by mixing different volumes of AlgMA 4% w/v stock solution and 4 mg/ml collagen solution (Table 5.1) using 5ml syringes and a 3-way connector (Fig. 4.21), with Irgacure added to achieve a final Ig crosslinking concentration of 0.5%. For instance, 2.5ml of 4 wt% AlgMA was mixed with 2.5ml of 4 mg/ml collagen solution and Irgacure to produce a final hydrogel of 2% AlgMA/0.5% Ig 2959/2 mg/ml Col. Cellular content was added to the composite hydrogels using a 3-way connector (Fig. 3.8) as previously described (3.11.1.1).

Table 5.1 A range of composite bioinks with titrating AlgMA and collagen concentrations created by mixing different ratios of AlgMA 4% w/v stock solution and 4 mg/ml collagen solution using 5ml syringes and a 3-way connector.

Stock Solution Ratios	Title	Bioink Composition
AlgMA 1 : Col 1	A1C1	2% AlgMA/0.5% Ig 2959/2 mg/ml Col
AlgMA 1 : Col 2	A1C2	1.33% AlgMA/0.5% Ig 2959/2.67 mg/ml Col
AlgMA 1 : Col 3	A1C3	1 % AlgMA/0.5% Ig 2959/3 mg/ml Col
AlgMA 1 : Col 6	A1C6	0.5% AlgMA/0.5% Ig 2959/3.43 mg/ml Col
AlgMA 2 : Col 1	A2C1	2.67% AlgMA/0.5% Ig 2959/1.33 mg/ml Col
AlgMA 3 : Col 1	A3C1	3 % AlgMA/0.5% Ig 2959/1 mg/ml Col
AlgMA 6 : Col 1	A6C1	3.43 % AlgMA/0.5% Ig 2959/0.5 mg/ml Col
AlgMA	AlgMA	2 % AlgMA/0.5% Ig 2959

5.2.2 Bioprinting Composite AlgMA/ Col Bioinks

Successful bioprinting of all composite bioinks was possible, allowing creation of 10mm x 10mm x 1mm porous constructs for comparison. It was evident that scaffolds with high collagen content had superior cell viability (***** $p<0.05$, ANOVA) compared to scaffolds with low collagen content and high AlgMA content at 7 days onwards of culture (Fig. 5.2 A and B). However, increasing collagen content also appeared to lead to reduced construct stability in culture (Fig. 5.1). After 14 days, scaffolds with the highest collagen content (A1C6 and A1C3) were found to have demonstrated significantly ($p<0.05$, ANOVA) higher levels of degradation (Table 5.2). This was an expected finding, given that the collagen used was not methacrylated, and so unlike AlgMA could not undergo UV or indeed ionic crosslinking. In turn, this made high collagen-content scaffolds less resistant to degradation in culture conditions.
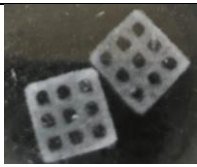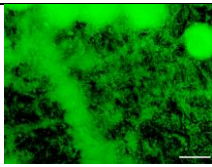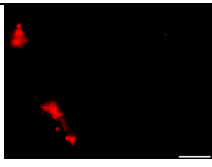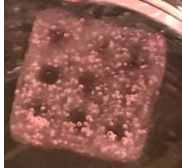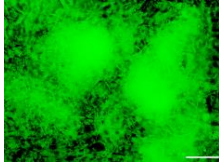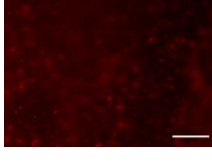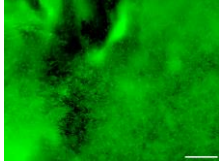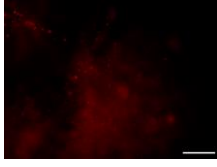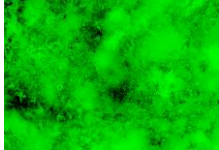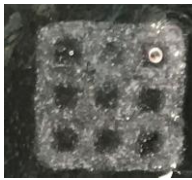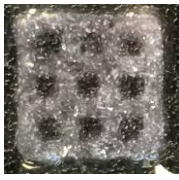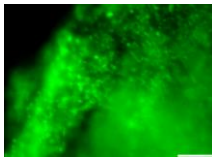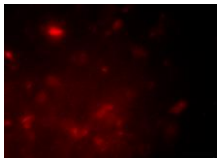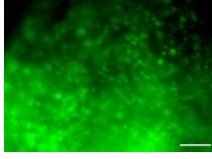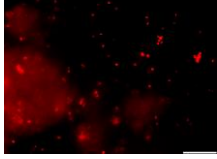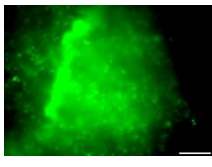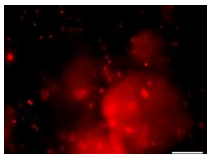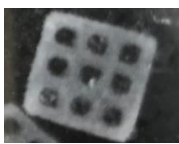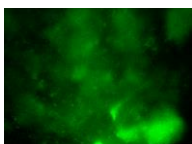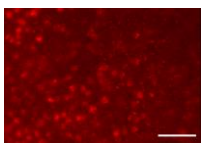
Bioink	Bioprintability	14-day Stability	Day 14 Live Stain	Dead Stain
A1C1				
A1C2				
A1C3				
A1C6				
A2C1				
A3C1				
A6C1				
AlgMA				

Figure 5.1 Cell viability and structural morphology of bioprinted AlgMA/Collagen Composite Bioinks loaded with chondrocytes (1×10^6 cells/ml). Strong cell viability and proliferation is seen up to 14 days, with more dead cells found in bioinks with increasing AlgMA content. Bioprinted constructs retained shape and structural integrity initially, with higher collagen content predisposing to fragility of constructs in culture. Scale bars represent 100 μm.
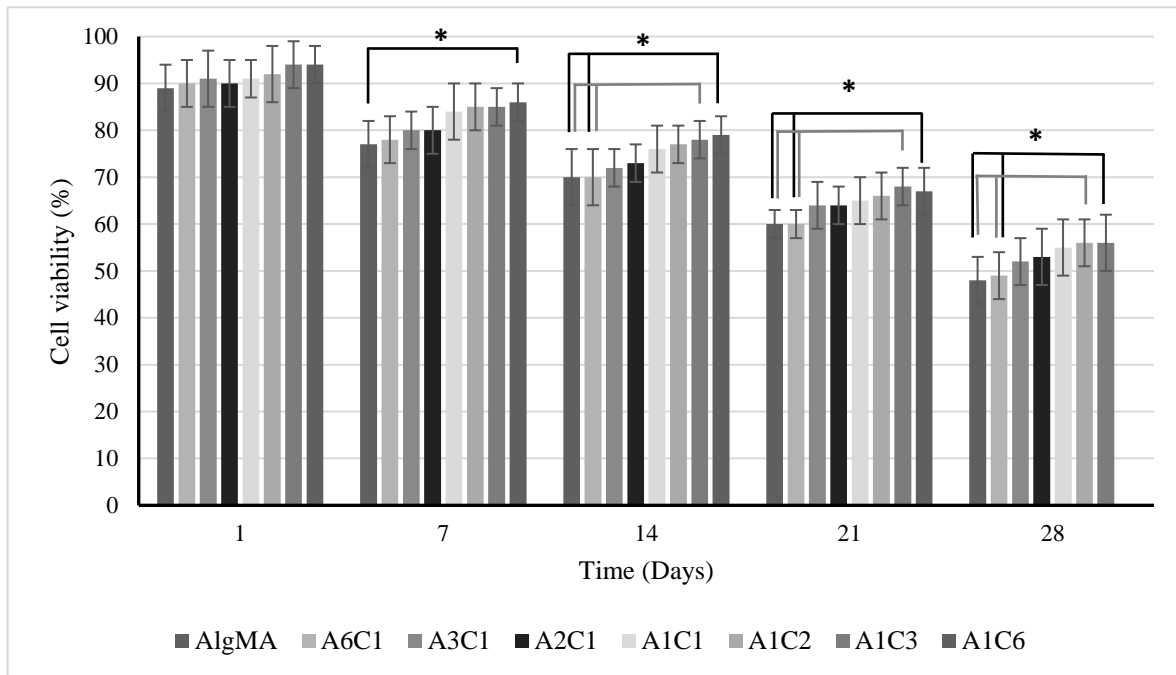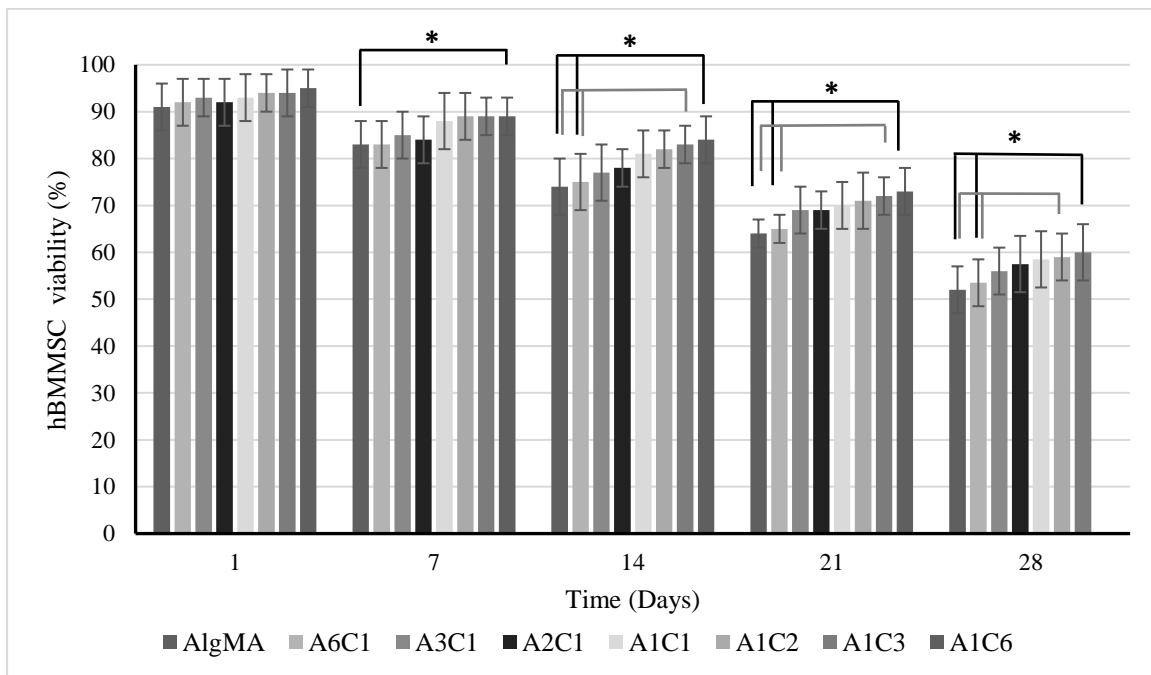
Figure 5.2 Cell viability analysis of composite AlgMA/Collagen bioinks over 28 days. Scaffolds with increased AlgMA content compared to collagen content displayed inferior (A)

chondrocyte and (B) hBMMSC viability (* $p<0.05$, two-way ANOVA, Tukey post-hoc) at 7 days onwards of culture. However, lower AlgMA concentration and higher collagen content also led to decreased structural viability, with analysis of AlgMA 1: Col 6 not possible beyond 21 days as scaffolds disintegrated.

5.2.3   **Composite AlgMA/Col Bioink Fidelity and Degradation Following Bioprinting**

The pore size and vertical thickness of scaffolds was measured following bioprinting with comparison made to an intended design of vertical thickness 1mm and pore size of 0.2mm. Scaffolds with higher AlgMA content tended to conform closer to intended print design. It was also evident that after 14 days scaffolds with higher collagen tended to undergo higher levels of degradation. A1C6 scaffolds experienced significantly (* $p<0.05$, one-way ANOVA, Tukey post-hoc) higher levels of degradation than AlgMA, A1C1, A2C1, A3C1 and A6C1 scaffolds by 14 days. A1C3 scaffolds also had significantly higher levels of degradation compared to AlgMA scaffolds (* $p<0.05$, one-way ANOVA, Tukey post-hoc) (Table 4.5).

Table 5.2 Measured pore size and vertical thickness of AlgMa/Col scaffolds immediately following bioprinting. Scaffold degradation after 14 days of culture also displayed.

Bioink	Vertical thickness (mm)	Pore Size (mm)	Weight loss (% of original)
AlgMA	1.0 ± 0.1	0.22 ± 0.01	28 ± 8
A1C1	1.0 ± 0.1	0.19 ± 0.03	39 ± 9
A1C2	1.1 ± 0.1	0.19 ± 0.04	42 ± 10
A1C3	1.2 ± 0.15	0.18 ± 0.03	47 ± 7 *
A1C6	1.2 ± 0.2	0.17 ± 0.04	63 ± 10 *
A2C1	1.0 ± 0.18	0.19 ± 0.02	36 ± 10
A3C1	1.1 ± 0.2	0.19 ± 0.03	34 ± 11
A6C1	1.0 ± 0.2	0.20 ± 0.02	30 ± 8

5.2.4 Osteochondral Defect Injection with AlgMA/ Col Bioinks

Osteochondral defects 5 x 5 x 1 mm in dimension were injected (or filled with bioprinted patches) with AlgMA/Col bioinks containing chondrocytes or hBMMSCs at a density of 1 x 10^6/ml. Injected defects were patched over more successfully using bioinks with higher AlgMA content, with increasing use of collagen predisposing to breakdown of the injections (Table 5.3). However, higher collagen content also supported improved cell viability and growth (Fig 5.3 and 5.4). A2C1 (2.67% AlgMA/0.033% Ig 2959/1.33 mg/ml Col) appeared to offer a good balance of high cell viability and maintained structural integrity after 14 days of culture. Overall chondrocyte and hBMMSC viability in osteochondral injections was comparable to that of chondrocytes and hBMMSCs 3D bioprinted using the same bioinks.
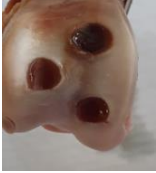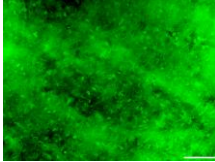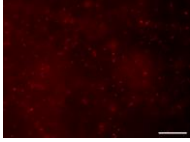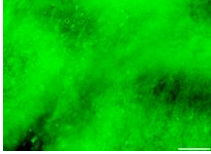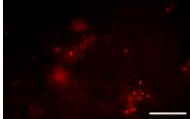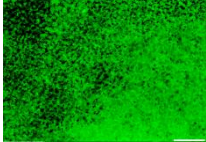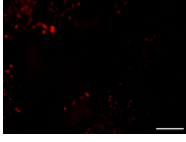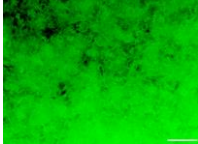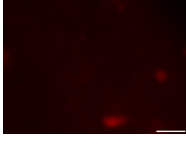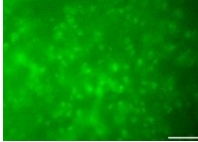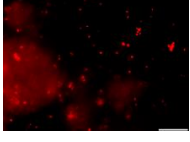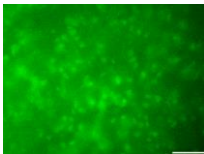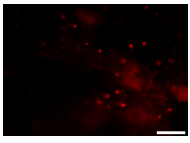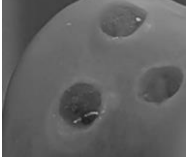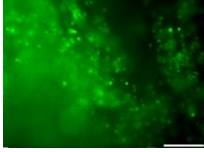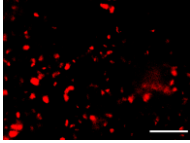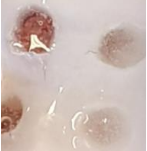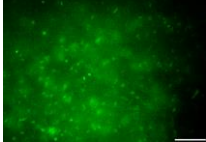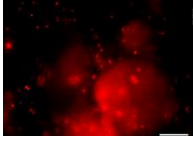
Bioink	Osteochondral Defect Injection	Day-14 Injection Stability	Day-14 Live Stain	Day-14 Dead Stain
A1C1				
A1C2				
A1C3				
A1C6				
A2C1				
A3C1				
A6C1				
AlgMA				

Figure 5.3 Cell viability and morphology of osteochondral defects injected with AlgMA /Col Composite Bioinks loaded with chondrocytes. Strong cell viability and proliferation is seen up to 14 days, with more dead cells found in bioinks with increasing AlgMA content. Higher collagen content predisposed to macroscopic breakdown of osteochondral injections in culture. Scale bars represent 100 μm.
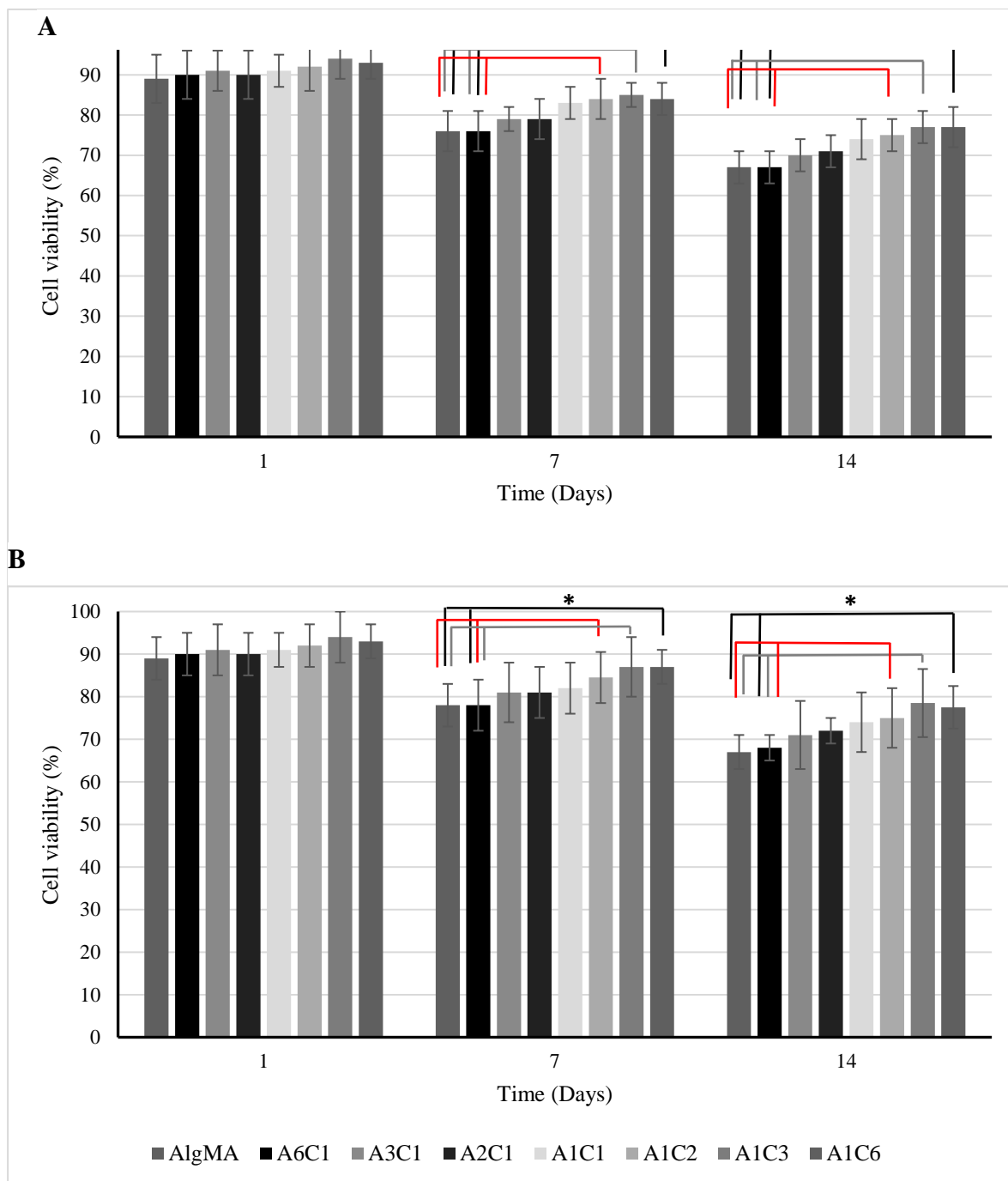
Figure 5.4 Viability of osteochondral defect injections using AlgMA/Col bioinks loaded with (A) chondrocytes and (B) hBMMSCs over 14 days in culture. Constructs with increased AlgMA content (AlgMA, A6C1) had inferior cell viability ($p < 0.05$, two-way ANOVA, Tukey post-hoc) compared to scaffolds with lower AlgMA content and relatively higher collagen

content at 7 days onwards of culture. However, higher collagen content also led to decreased structural viability, with macroscopic evidence of injection breakdown seen in scaffolds with lower AlgMA content and higher collagen content.

Table 5.3 Physical integrity of osteochondral defect injections using AlgMA/Col bioinks loaded with chondrocytes or hBMMSCs over 14 days in culture.

Bioink	AlgMA	A1C1	A1C2	A1C3	A1C6	A2C1	A3C1	A6C1
OCD Injection Integrity	Intact	Slight erosion	Failure	Failure	Failure	Intact	Intact	Intact

5.3 **Use of Gelatin Methacrylate (GelMA) to Produce Composite Bioinks**

Whilst the results of combining AlgMA and collagen to produce bioinks were encouraging, improved biocompatibility achieved through inclusion of collagen came at the expense of a deterioration in construct stability in culture and subsequent loss of integrity of osteochondral defect injections *in vitro*. Maintained stability of constructs is clearly a desirable property when attempting to achieve repair of an osteochondral defect. Patients undergoing cartilage repair surgery are frequently kept non-weight bearing for a number of weeks to support the integrity of an osteochondral repair, and so injected repairs need not be strong enough to allow immediate weight bearing. However, implanted cells still need to be held in place for sufficient time to allow sufficient development of extracellular matrix and regeneration of the host articular surface to occur [13].

As an alternative hydrogel to collagen, gelatin methacrylate (GelMA) has several desirable properties that offer promise for use in cartilage regeneration. Gelatin is a water-soluble protein

manufactured through the denaturation of collagen. Aqueous solutions of gelatin form thermoreversible hydrogels below their upper critical solution temperature of 25–35 °C [14], allowing thermal gelation to aid in the shape retention of bioprinted constructs. Production of GelMA from gelatin via a methacrylation process can be tuned to allow different degrees of methacrylation to occur, with high degrees of methacrylation found to lead to greater compressive moduli following UV crosslinking [14-19]. GelMA also has a high level of biocompatibility; due to a hydrophilic nature, it allows a high water content and permeability to nutrients; possession of integrin-binding motifs, and matrix metalloprotein (MMP) degradation sites allow cell adhesion, proliferation and migration to occur and also help make gelatin biodegradable [20]. Overall, GelMA solutions tend to have a low viscosity at room or body temperature, and so combining GelMA with other more viscous hydrogels such as AlgMA could offer a potential route to production of a biocompatible and stable composite hydrogel in culture [14, 21].

5.3.1   Initial Evaluation of GelMA and AlgMA Composite Bioink Properties

Initially, the water contact angles (WCAs) of AlgMA, AlgMa-GelMA composite hydrogels and a cell culture dish were compared. This gives a measure of the wettability of the hydrogel, which directly influences interaction with cell culture medium, surface proteins and subsequent cellular adhesion. It was apparent that inclusion of GelMA significantly improved properties compared to pure alginate (Fig. 5.5). The WCA of pure AlgMA was less than 10° indicating very high hydrophilicity. By comparison, pure 10% GelMA had a WCA of 82°, indicating hydrophobic properties. Creation of AlgMA-GelMA composite hydrogel led to optimised performance, with the WCAs of AlgMA-GelMA (2%, 5%) far closer to that of a cell culture dish.
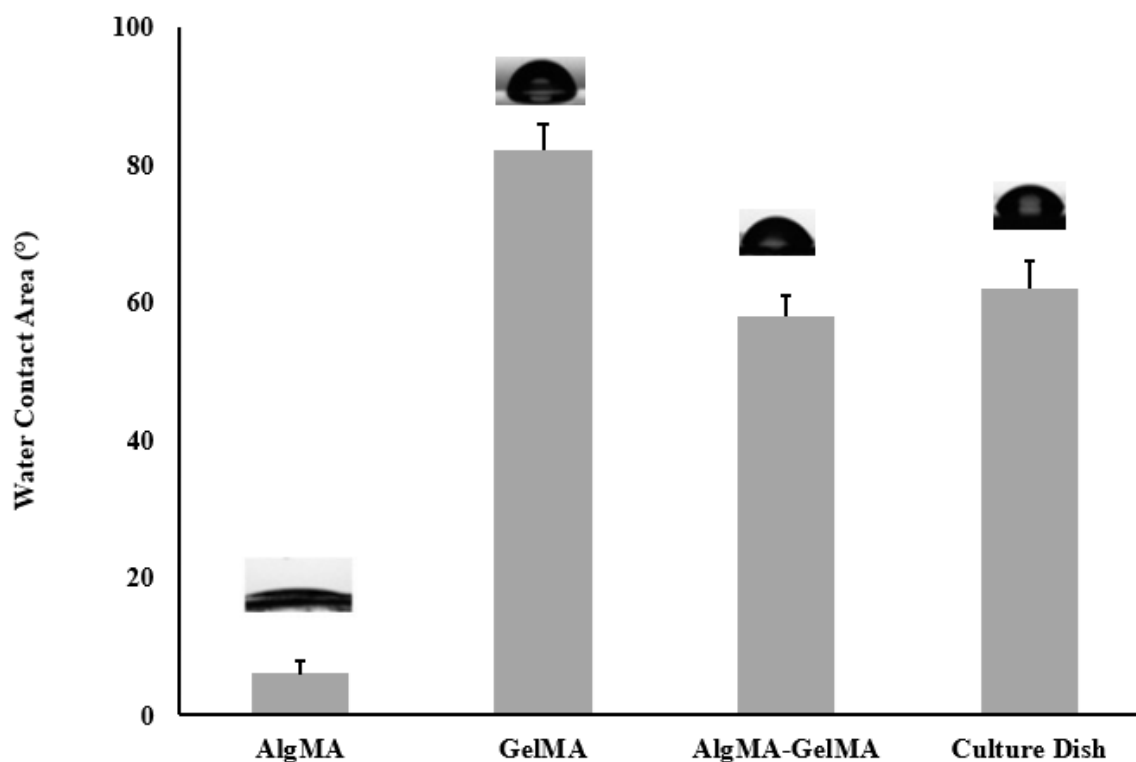
Figure 5.5 The water contact angle of AlgMA (4%), GelMA (10%) and AlgMA-GelMA (2%, 5%) composite hydrogels. Creation of AlgMA-GelMA composite hydrogels led to optimised performance, with the WCA of AlgMA-GelMA (2%, 5%) composite hydrogel close to that of a cell culture dish.

The mechanical properties of AlgMA, GelMA and AlgMA-GelMA composite hydrogels were also compared. The compressive modulus of the composite AlgMA-GelMA hydrogel was significantly improved compared to pure AlgMA and GelMA hydrogels (Fig. 5.6).

(A)
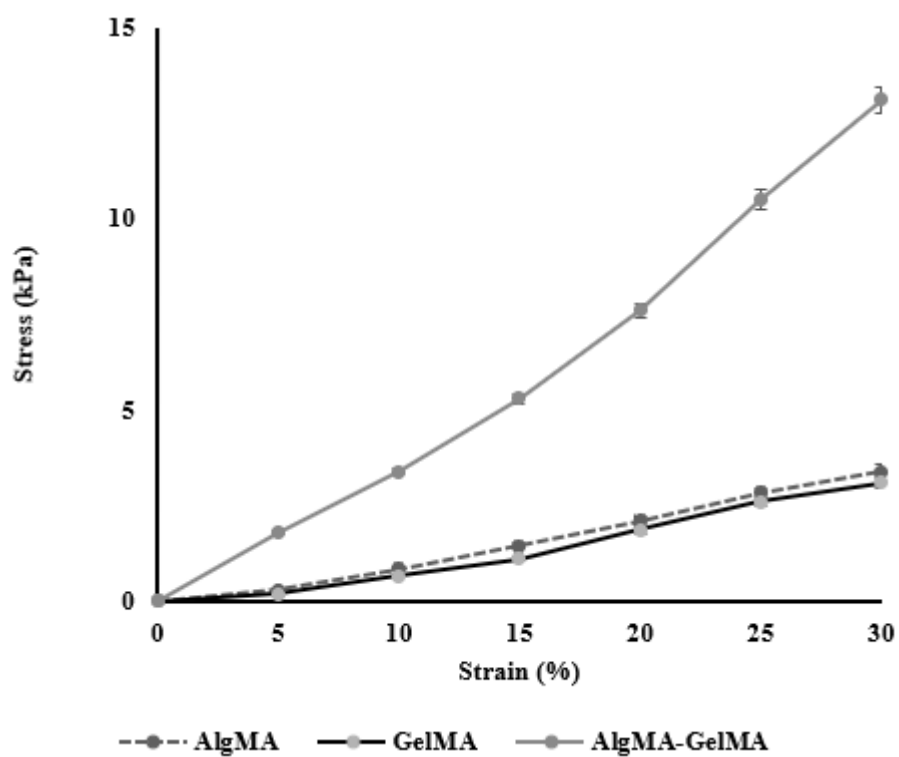
(B)
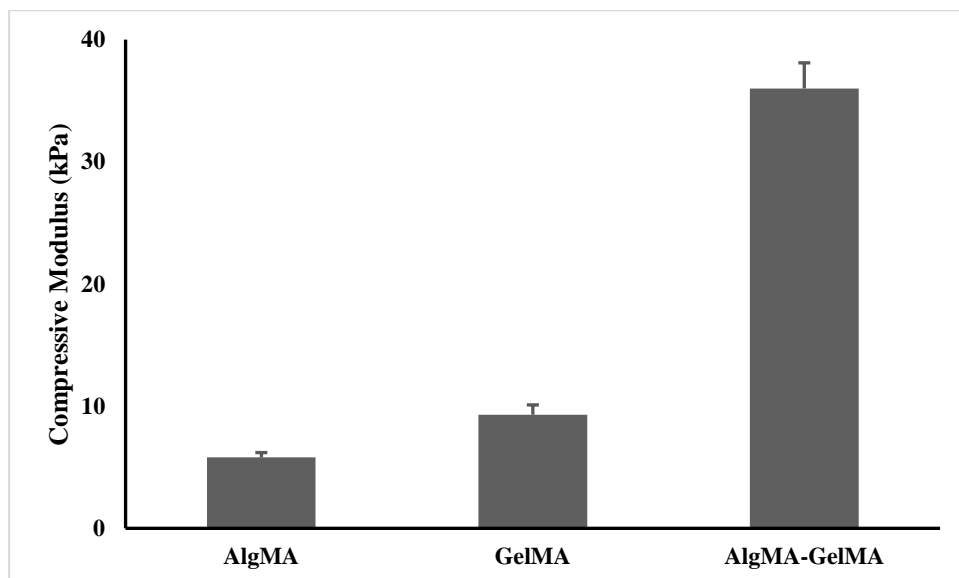
Figure 5.6 Mechanical properties of GelMA (10%), AlgMA (4%) and AlgMA-GelMA (2%, 5%) hydrogels. Stress-strain curves (a) and compressive moduli (b) of GelMA (10%), AlgMA (4%) and Alg-GelMA (2%, 5%) hydrogels. Creation of a composite hydrogel led to improved mechanical properties.

5.3.2   **Mixing Stock GelMA and AlgMA Hydrogels to Produce Composite Bioinks**

Composite bioinks were created by mixing different volumes of stock AlgMA 4% w/v solution and 10 wt% GelMA solution using 5ml syringes and a 3-way connector (Table 5.4). For instance, 2.5ml of 4 wt% AlgMA/0.5% Ig 2959 was mixed with 2.5ml of 10 wt% GelMA/0.5% Ig 2959 solution to produce a final hydrogel of 2% AlgMA/5% GelMA/0.5% Ig 2959. Cellular content was added to the composite hydrogels using the methodology as described for AlgMA.

Table 5.4 A range of composite bioinks with titrating GelMA and AlgMA concentrations were created by mixing different ratios of AlgMA 4% w/v stock solution and 10% w/v GelMA stock solution using 5ml syringes and a 3-way connector.

Stock Solution Ratio	Title	Bioink Composition
AlgMA 1 : GelMA 1	A1G1	2% AlgMA/5% GelMA/0.5% Ig 2959
AlgMA 1 : GelMA 2	A1G2	1.33% AlgMA/6.66 % GelMA/0.5% Ig 2959
AlgMA 1 : GelMA 3	A1G3	1% AlgMA/7.5% GelMA/0.5% Ig 2959
AlgMA 2 : GelMA 1	A2G1	2.67% AlgMA/3.33% GelMA/0.5% Ig 2959
AlgMA 3 : GelMA 1	A3G1	3% AlgMA/2.5% GelMA/0.5% Ig 2959

5.3.3 **Bioprinting Composite AlgMA/ GelMA Bioinks**

Successful bioprinting of all composite bioinks was possible, allowing creation of 10mm x 10mm x 1mm porous constructs for comparison. Through observation of construct stability in culture over a two-week period, it was evident that all composite bioinks facilitated maintained infilling of osteochondral defects and cell growth. Incorporation of GelMA into composite bioinks did appear to result in improved biocompatibility, with a significant trend towards greater cell growth and improved cell viability demonstrated (Fig. 5.7 and Fig. 5.8). Increasing AlgMA content led to a significant decrease in degradation of bioprinted constructs, with GelMA (*p<0.05) found to have a significantly higher degradation at 14 days compared to AlgMA, A2G1, and A3G1 scaffolds. Increasing GelMA content did appear to lead to a slight improvement in print resolution and conformation with bioprint design thickness and pore size (Table 5.5).

Table 5.5 Measured pore size and vertical thickness of scaffolds immediately following bioprinting. Scaffold degradation after 14 days of culture also displayed.

	Vertical thickness (mm)	Pore Size (mm)	Weight loss (% loss of original)
AlgMA	1.0 ± 0.1	0.22 ± 0.01	28 ± 9
A1G1	1.0 ± 0.1	0.19 ± 0.03	34 ± 11
A1G2	1.0 ± 0.05	0.2 ± 0.06	37 ± 10
A1G3	1.0 ± 0.05	0.2 ± 0.03	43 ± 9
A2G1	1.2 ± 0.2	0.18 ± 0.04	32 ± 16
A3G1	1.2 ± 0.18	0.18 ± 0.02	30 ± 10
GelMA	1.0 ± 0.05	0.20 ± 0.05	54 ± 16*

5.3.4 Bioprinting AlgMA/GelMA Composite Bioinks
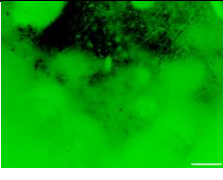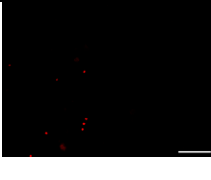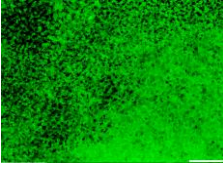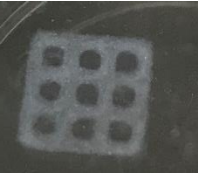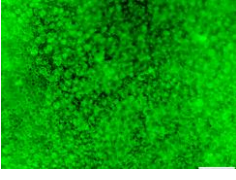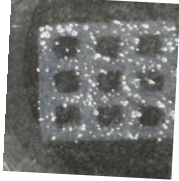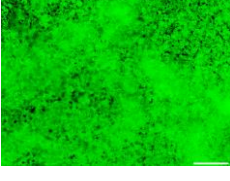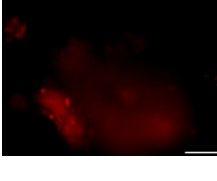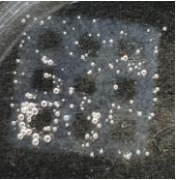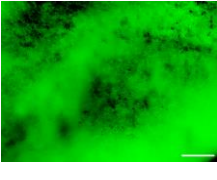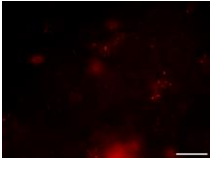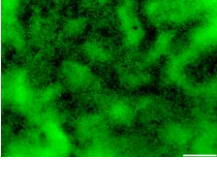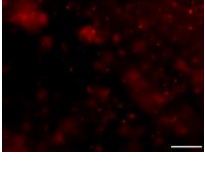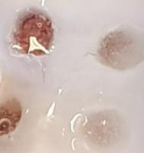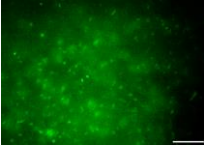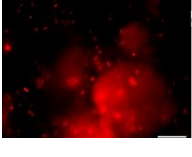
Bioink	Bioprintability	14-day Stability	Day 14 Live Stain	Day 14 Dead Stain
GelMA				
A1G1				
A1G2				
A1G3				
A2G1				
A3G1				
AlgMA				

Figure 5.7 Viability of scaffolds bioprinted using AlgMA/GelMA bioinks loaded with chondrocytes shown over 14 days in culture. Whilst healthy cell growth and maintained scaffold

structure was seen in all scaffolds, there was a trend towards increased cell viability in scaffolds with higher GelMA content. Pure AlgMA scaffolds had relatively inferior cell viability (* $p<0.05$) compared to scaffolds with lower AlgMA content and higher GelMA content at 7 days onwards of culture (Fig. 5.8).

A
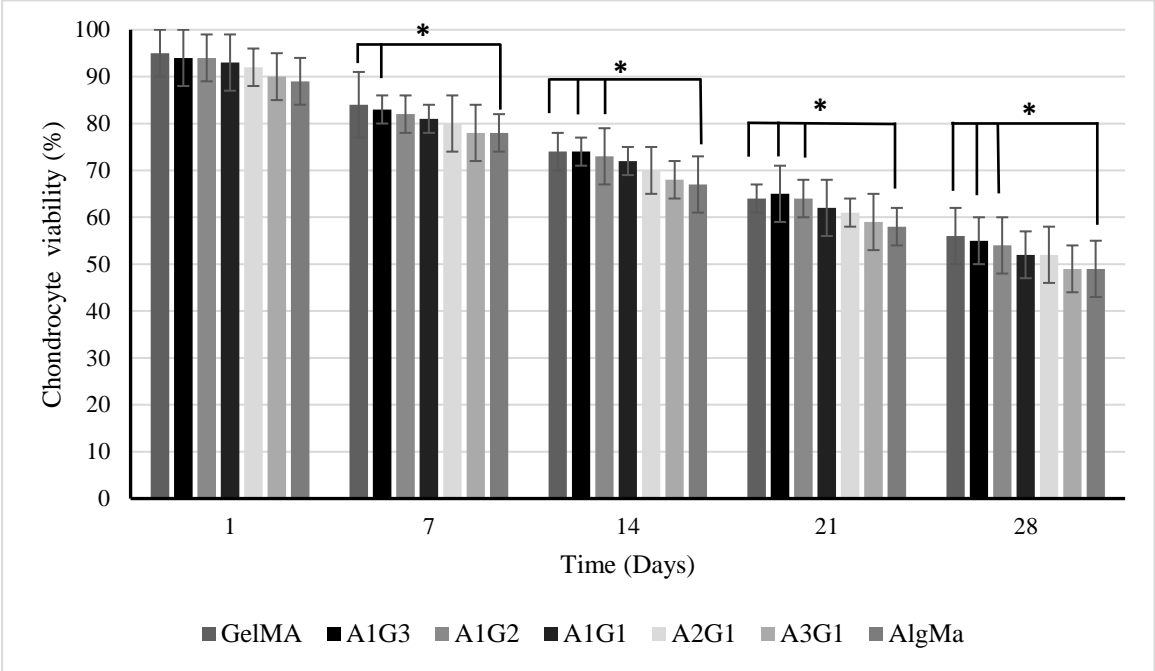
B
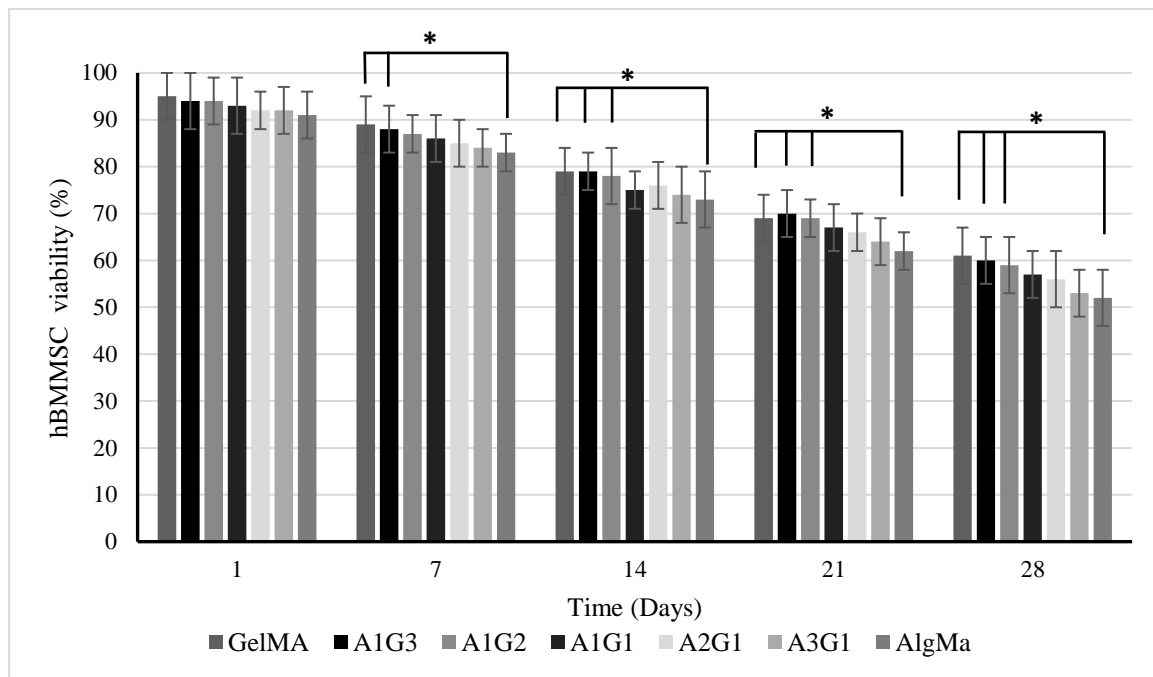
Figure 5.8 Cell viability analysis of composite AlgMA/GelMA bioinks over 28 days. There was a trend towards scaffolds with increased GelMA content having improved (A) chondrocyte and (B) hBMMSC cell viability. Pure AlgMA scaffolds had significantly (*< $p<0.05$, two-way ANOVA) inferior cell viability compared to scaffolds with relatively higher GelMA content at 7 days onwards of culture for both chondrocytes and hBMMSC scaffolds.

5.3.5 Osteochondral Defect Injection with AlgMA/ GelMA Bioinks

Successful injection of OCDs was physically maintained with use of all composite AlgMA/ GelMA bioinks, with only GelMA showing signs of partial breakdown of injections after two weeks of culture (Table 5.6). Incorporation of GelMA into composite bioinks did appear to result in improved biocompatibility, with a significant trend towards greater cell growth and improved cell viability demonstrated (Fig. 5.9 and Fig. 5.10). At 7 days, AlgMA OCD injections had inferior cell viability compared to GelMA OCD infills (*$p<0.05$, ANOVA). By

14 days, AlgMA had significantly inferior cell viability (* $p<0.05$) compared to GelMA, A1G3 and A1G2 scaffolds. A3G1 scaffolds also had significantly inferior cell viability (* $p<0.05$) compared to GelMA and A1G3 scaffolds.
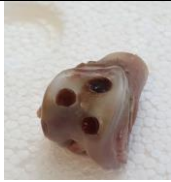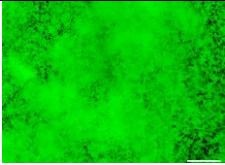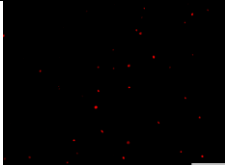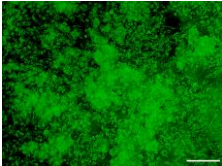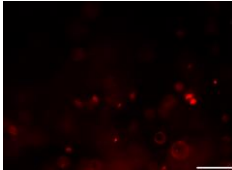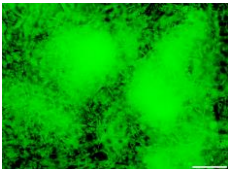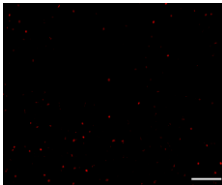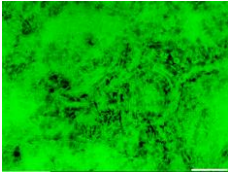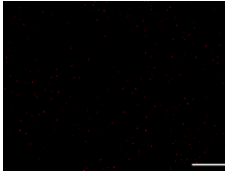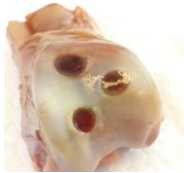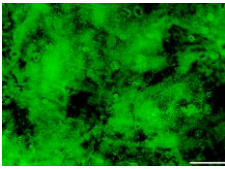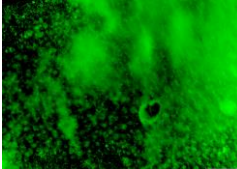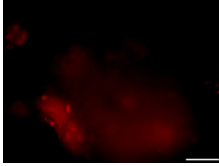
Bioink	Osteochondral Defect Injection	Injection 14-day Stability	Day-14 Live Stain	Dead Stain
GelMA				
A1G1				
A1G2				
A1G3				
A2G1				
A3G1				

Figure 5.9 Viability of osteochondral defect (OCD) injected areas using AlgMA/GelMA bioinks loaded with chondrocytes over 14 days in culture. Increased AlgMA content led to relatively inferior cell viability ($p<0.05$) compared to scaffolds with lower AlgMA content and higher GelMA content at 7 days onwards of culture. However, higher GelMA content also led to decreased structural integrity, with macroscopic evidence of OCD injection breakdown seen when pure GelMA was used.

Table 5.6 Macrosopic integrity of osteochondral injections using AlgMA/GelMA bioinks loaded with chondrocytes over 14 days in culture.

Bioink	AlgMA	A1G1	A1G2	A1G3	A2G1	A3G1	GelMA
Defect Injection Integrity	Intact	Intact	Intact	Intact	Intact	Intact	Slight breakdown

A
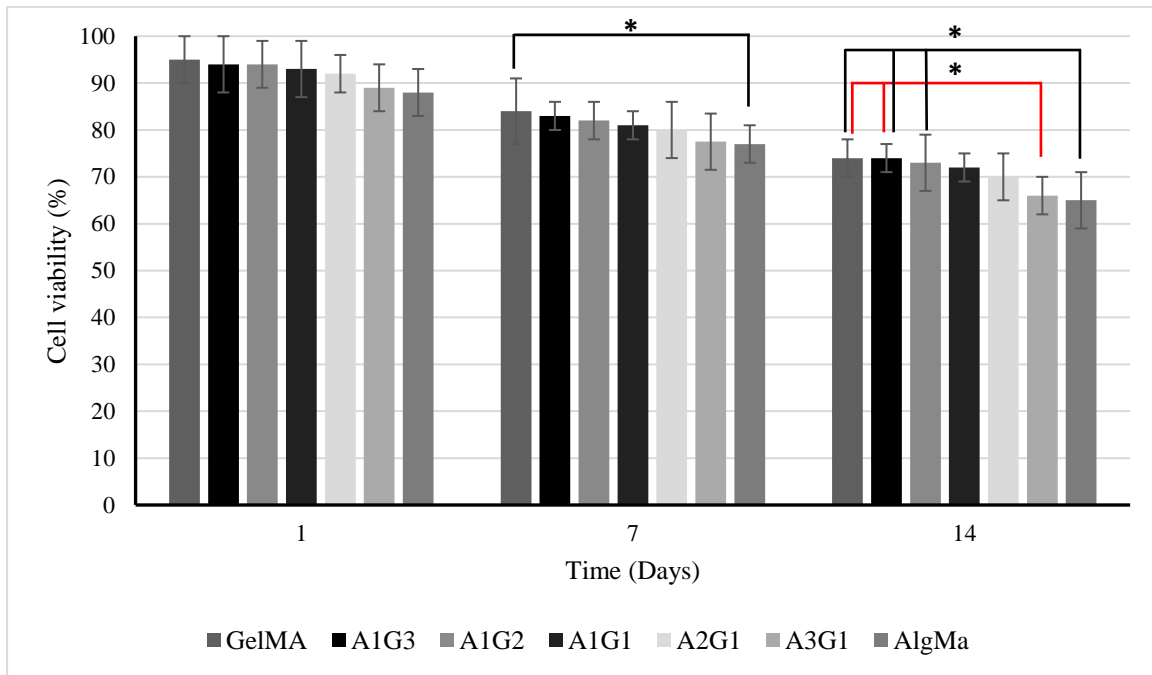
B
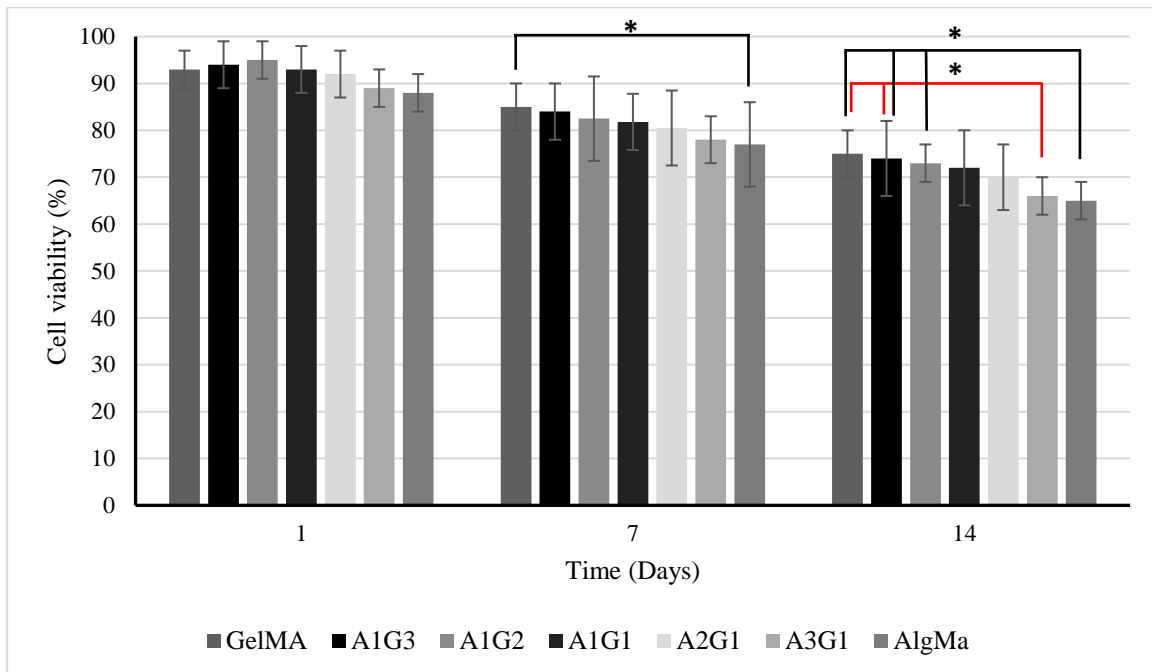
Figure 5.10 Viability of osteochondral defect injections using AlgMA/GelMA bioinks loaded

with (A) chondrocytes and (B) hBMMSCs over 14 days in culture. Injections performed using

bioinks with increased AlgMA content demonstrated a trend towards inferior cell viability. At 7 days, AlgMA OCD injections had inferior cell viability compared to GelMA OCD injections (*p<0.05, two-way ANOVA). By 14 days, AlgMA had significantly inferior cell viability (* p<0.05) compared to GelMA, A1G3 and A1G2 scaffolds. A3G1 scaffolds also had significantly inferior cell viability (* p<0.05) compared to GelMA and A1G3 scaffolds.

5.4 **Creation of Spheroids for Incorporation into Bioinks**

Following optimisation of bioink composite hydrogel content and crosslinking conditions, attention turned to the incorporation of cell spheroids into constructs to potentially increase early cell growth and aggregation. Cell aggregates or spheroids have superior intercellular communication and extracellular matrix development when compared to cells grown in 2D culture, and thus inclusion of spheroids in bioinks instead of initial single cell suspensions could potentially accelerate the growth and development of printed constructs after bioprinting [22]. There are several examples of bioprinted spheroids used in the biofabrication of cartilage, nerves and other soft tissues [23-27].

In the following section a 3D culture system was adapted from methods originally described by Dahlmann *et al.* [28] to produce high volumes of regularly sized ADSC, MSC and chondrocyte aggregates. Aggregates of hBMSCs, ADSCs and chondrocytes were successfully created and harvested from agarose moulds (Fig. 5.11). Spheroids appeared largely matured 48 hours post-seeding in terms of morphology and size of cell body (Fig. 5.11 C), and beyond 72 hours became more difficult to remove from agarose moulds. Despite use of ultra-pure agarose, it remains possible that cells adhered to impurities within the agarose, increasing the difficulty of dislodging them. Once spheroids were harvested, bioinks could be formed containing high

densities of spheroids (Fig. 5.11 E). Spheroids encapsulated in hydrogels maintained high viability following harvesting (Fig. 5.11 F).
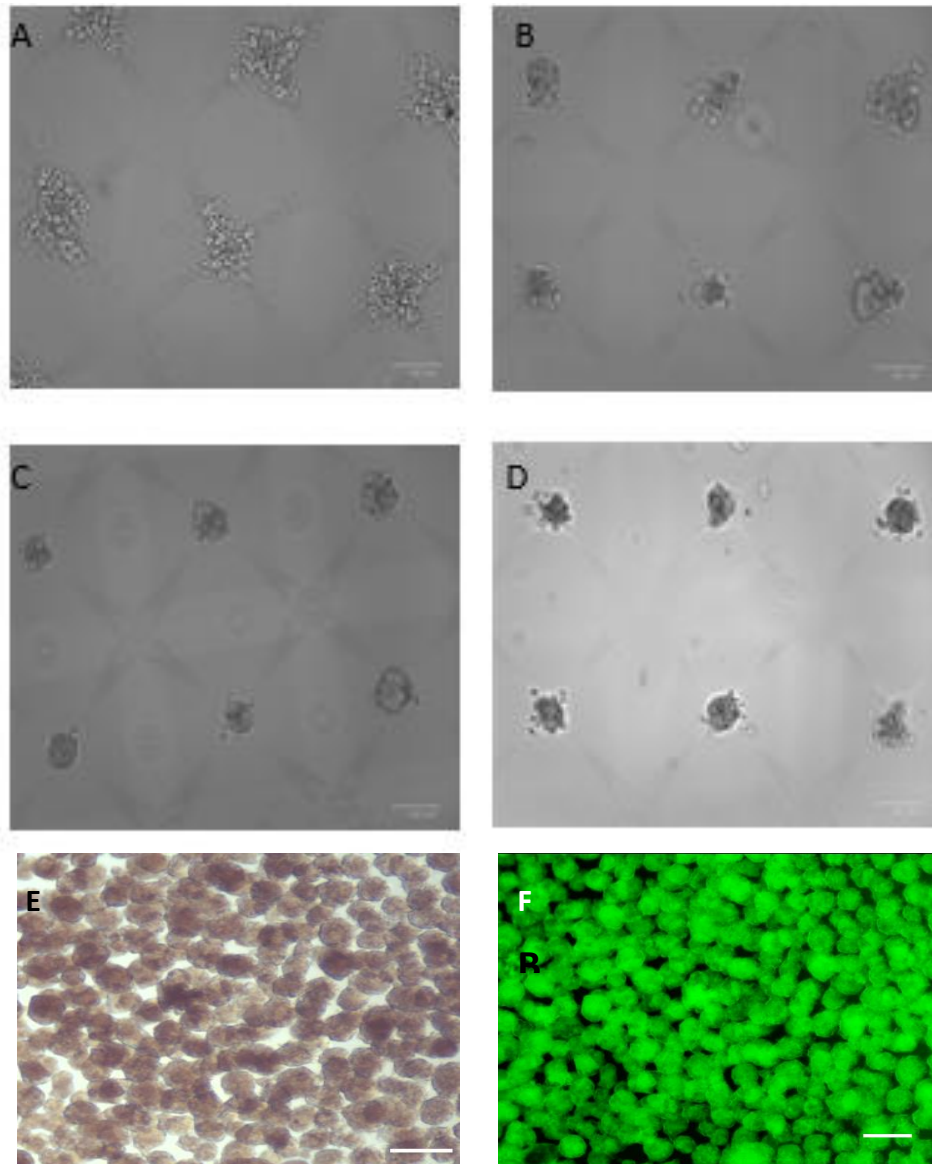
Figure 5.11 Production of Spheroids. **(A)** Seeded hBMSC spheroids in agarose microwells **(B)** hBMSC spheroids at 24 hours **(C)** hBMSC spheroids at 48 hours **(D)** hBMSC spheroids at 72 hours. **(E)** Harvested chondrocyte spheroids immersed in a collagen hydrogel. **(F)** Live staining showing excellent spheroid viability after harvesting and encapsulation in hydrogel. Scale bar = 100μm.

5.4.1 **Bioprinting and Osteochondral Defect Injections using Spheroids**

Comparison was made between the growth of single-cell and spheroid-cell containing bioinks using the A1G2 bioink. A1G2 was selected as the "delivery" bioink having demonstrated a combination of good overall cell viability, low degradation and high bioprint resolution when used to bioprint scaffolds or as an injectable bioink to patch-up OCDs. To allow fair comparison an initial single cell suspension of chondrocytes was prepared at a density of 1 $x10^6$ chondrocytes/ml in A1G2. A spheroid cell suspension was then prepared using 1 $x10^4$ spheroids/ml (equating to around 1 $x10^6$ chondrocytes/ml, as 100 cells were initially seeded into each agarose microwell to allow individual spheroid formation). Cell growth was well supported in both spheroid and single-cell suspension containing bioinks, with cell viability not found to be significantly different at any time point up to 14 days (Fig 5.12 B). However, density of cell growth was significantly improved beyond 3 days of culture ($p<0.001$, t-test) when spheroids were included in bioinks instead of single cell suspensions (Fig. 5.13). When growth was compared between OCD injections and scaffolds produced using the same A1G2 bioink, there appeared to be a slight trend towards improved viability and density of cell growth in bioprinted scaffolds compared to injected OCD repairs for both spheroid and single-cell A1G2 bioinks, however this did not reach statistical significance in either case ($p>0.05$) (Fig. 5.12 and Fig. 5.13).

	Post-Printing	**Day 3**	**Day 7**	**Day 14**
Spheroid				
Single Cell				
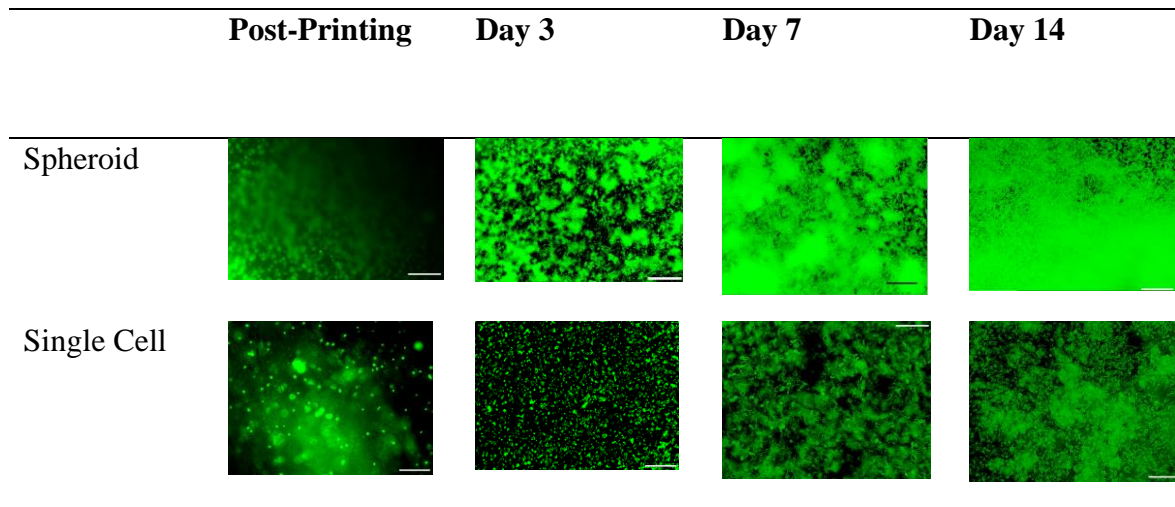
B
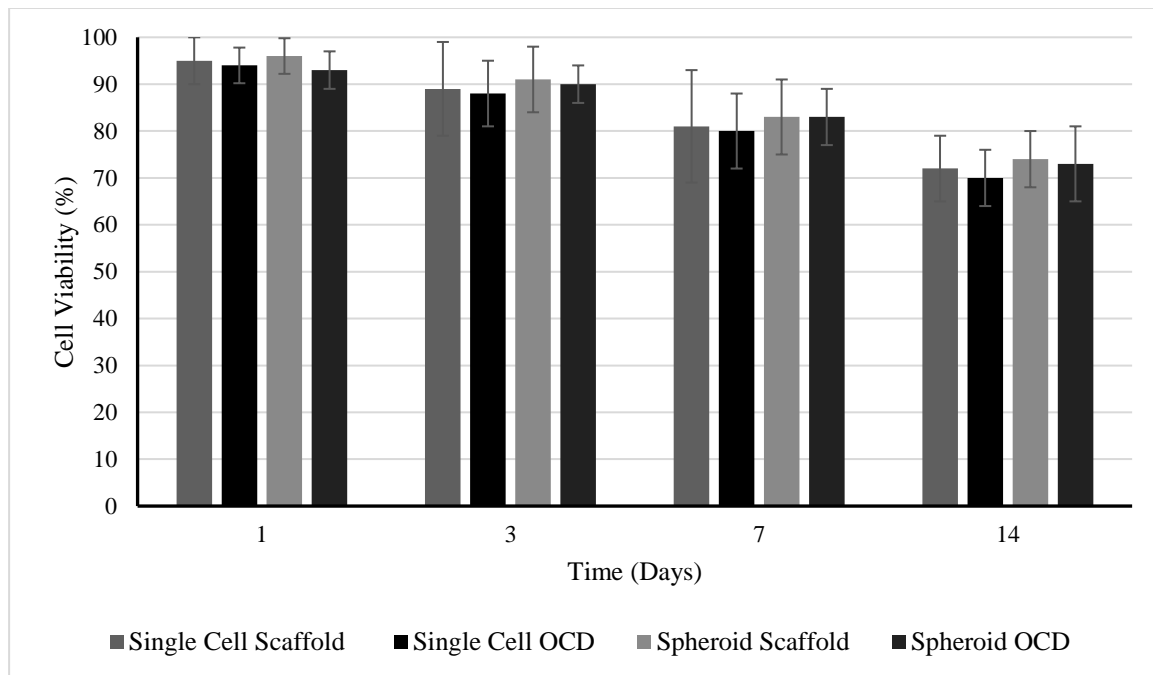
Figure 5.12 Cell viability observed during culture of single-cell and spheroid A1G2 bioinks within 10 x 10 x 1mm scaffolds and 5 x 5 x 1mm osteochondral defects (OCDs). Chondrocytes were loaded into A1G2 bioink at a density of 1×10^6 cells/ml, and either used to bioprint 10 x

10 x 1mm scaffolds or injected into OCDs to repair them. Concurrently, chondrocyte spheroids were loaded into A1G2 bioinks at a density of 1×10^4 spheroids/ml, with approximately 100 cells used to create each initial spheroid, and then used to again either bioprint 10 x 10 x 1mm scaffolds or injected into OCDs to repair them. Whilst there appeared to be a slight trend towards improved viability in in scaffolds compared to OCDs for both spheroid and single-cell A1G2 bioinks, this did not reach statistical significance in either case ($p > 0.05$). Furthermore, no significant difference was found in viability between spheroid or single-cell A1G2 bioinks at any time point.
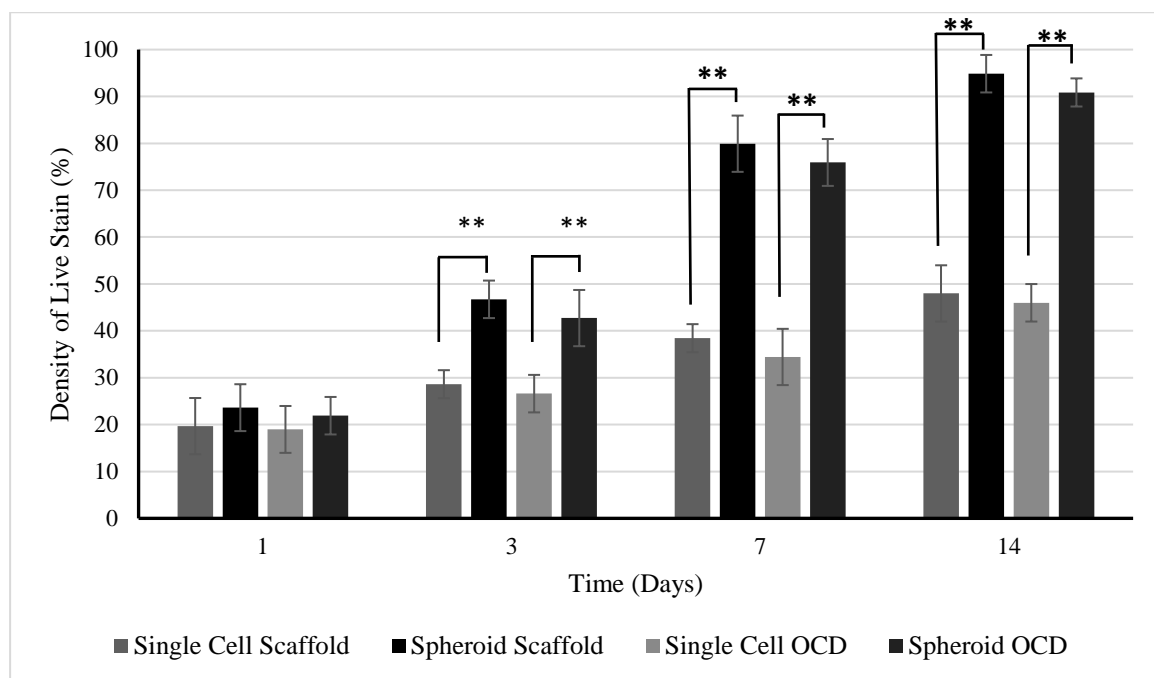
Figure 5.13 Density of cell growth observed during culture of single-cell and spheroid A1G2 bioinks within 10 x 10 x 1mm scaffolds and 5 x 5 x 1mm osteochondral defects (OCDs). At 3 days onwards of culture, significantly (** $p < 0.001$, two-way ANOVA) greater density of chondrocyte cell growth was detected using ImageJ software within spheroid containing scaffolds and OCDs compared to those prepared using single-cell bioinks. Although there was

a slight trend towards higher cell density occurring in scaffolds compared to OCD repairs, this was not statistically significant for either single-cell or spheroid bioinks.

5.5 **Discussion**

5.5.1 **Development of Composite AlgMA/Col Hydrogels**

The comparatively robust structural properties of AlgMA during culture appeared desirable to maintain in a construct intended to aid biofabrication of osteochondral tissue. Attention was therefore turned to combining triple-crosslinked AlgMA with more bioactive hydrogels capable of fusing bioactivity with stability in culture. As the most the most abundant macromolecule with the ECM of cartilage and bone, collagen represented an obvious initial hydrogel for evaluation. As part of the native ECM it is inherently biocompatible, biodegradable and has been shown to help stimulate cell proliferation and differentiation as it includes a number of motifs capable of facilitating cell adhesion and differentiation, including a high density of RGD [6, 7]. However, in common with other natural polymers, collagen has limited mechanical properties and is also prone to degradation [8, 9]. Optimising a balance between AlgMA and collagen content was therefore a key aim of experimental work. It was apparent that higher collagen content supported improved cell viability and growth, with a significant difference found from 7 days of culture onwards. This finding is in keeping with previous research where inclusion of collagen to create Alg/Col hydrogel led to enhanced cell adhesion, accelerated cell proliferation and enhanced expression of cartilage specific genes such as *Acan*, *Col2al* and *Sox9*, whilst expression of fibrocartilage markers was also inhibited [29]. Furthermore, Daly *et al.* reported that alginate best supported the development of hyaline-like cartilage following 3D bioprinting when compared to GelMA and BioINK™ [19]. Previous work also found

alginate to be helpful to the acceleration of proteoglycan synthesis, whilst chondrocyte proliferation was promoted in the presence of collagen [30].

Despite the benefits in cellular growth and viability achieved through inclusion of collagen, it was apparent that high collagen content also impacted significantly upon construct stability in culture. Constructs containing the highest levels of collagen underwent significantly increased degradation whilst triple-crosslinked AlgMA had significantly lower degradation levels. Some studies have reported improvement of some mechanical properties such as elasticity with the incorporation of collagen into alginate bioinks, although this was achieved when much higher concentrations of collagen (15 mg/mL) were used to create composite hydrogels [29]. It may therefore be the case that refining initial collagen extraction and gel preparation to yield higher collagen concentrations offers one potential avenue to counteract this limitation. Further studies have also deployed UV crosslinking of collagen to bolster structural properties [31]. Collagen hydrogel is known to be susceptible to native enzymatic degradation, and so introduction of UV-mediated covalent crosslinking would have the benefit of being able to at least partially resist collagenase-mediated degradation [32]. However, exposure of collagen to UV has recognised potential to cause partial loss of native collagen structure, which may influence attachment, migration, and proliferation of cells on collagen fibres [33]. Overall, A2C1 (2.67% AlgMA/0.033% Ig 2959/1.33 mg/ml Col) appeared to offer a good balance of high cell viability and maintained structural integrity following bioprinting and injection into OCDs.

5.5.2 Development of Composite AlgMA/GelMA Hydrogels

In an attempt to maintain the bioactivity gained from including collagen in constructs whilst simultaneously enhancing structural properties, the bioprintabiltiy of composite AlgMA/GelMA hydrogels was developed. As a biomacromolecule produced from denatured

collagen, GelMA-based bioinks have gained increasing popularity within biofabrication due to excellent biocompatibility, photocrosslinkability, and tuneable mechanical properties, whilst retaining some of the motifs present in native ECM crucial for promoting cellular adhesion and growth [10-12]. When used as a lone bioink, high GelMA concentrations (i.e. >15% w/v) have frequently been required to allow maintained structural fidelity following bioprinting. This in turn is associated with higher viscosity and sheer stresses during bioprinting, often leading to lower cell viability [10-12]. Combining AlgMA with GelMA could therefore allow sufficient hydrogel viscosity for bioprinting to be achieved with lower GelMA concentrations, especially with the potential for triple crosslinking of AlgMA to be performed. Furthermore, previous work has found alginate to support the development of hyaline-like cartilage following 3D bioprinting when compared to GelMA [19].

It was apparent that incorporation of GelMA into composite bioinks resulted in improved biocompatibility compared to AlgMA controls, with a significant trend towards greater cell growth, surface wettability, mechanical properties and improved cell viability demonstrated. These findings are in keeping with several examples where gelatin or GelMA has been mixed with alginate, leading to improved cell growth [10, 34, 35]. Compared to use of GelMA alone, some groups have also found improved cellular differentiation and growth with inclusion of alginate; it is thought that the improved mechanical properties offered by inclusion of alginate promote cell spreading, proliferation and differentiation by helping to mimic the stiffness of the native ECM more closely [34, 35]. Furthermore, use of stiffer hydrogels has been found to be supportive of maintaining the phenotype of bioprinted chondrocytes [36]. As a further example of increased mechanical properties helping promote cellular growth *in vitro*, a further study found that performing both UV and ionic crosslinking led to improved cell growth and spreading compared to use of UV – only crosslinking [35]. This is in keeping our finding that

performing triple (double ionic and UV) crosslinking seemed to support significant cell growth and spreading with a range of composite hydrogels.

A potential benefit of increasing GelMA content appeared to be a slight improvement in print resolution and improved conformation with bioprint design (Table 4.7). This is in keeping with the findings of Aldana *et al.*, where increasing concentrations of GleMA within GelMA/alginate bioinks led to increased bioprint accuracy [10]. Gao *et al.* also recently reported that increasing alginate concentration in gelatin/alginate blends lead to decreased printing accuracy while a high gelatin concentration lead to improved fidelity [21]. However, within the design and bioprinting parameters used within our work, the slight increased accuracy had minimal overall impact on final construct dimensions or on settings used to bioprint different composite AlgMA/GelMA bioinks. Overall, there was a high correlation between bioprint design and measured post-print dimensions irrespective of composite AlgMA/GelMA bioink used, confirming that bioink constructs could keep their shape without significant degradation or diffusion after bioprinting.

One potential limitation of implanting constructs containing AlgMA *in vivo* is that biodegradability is potentially limited by the lack of alginase present within the body. This means that the polymer chains in alginate cannot be fully broken down initially, leaving potential for a foreign body reaction and inflammation to be triggered over time [37]. However, there are numerous examples of alginate being implanted *in vivo* within animal models with no evidence of construct rejection or inflammation occurring at least in the short term [29, 34, 35, 38, 39]. One potential approach to minimise the risk of an immune response being triggered is to perform oxidation of alginate prior to inclusion in a bioink.   [38, 39]. By comparison, GelMA is much more inherently susceptible to biodegradation given it is originally produced

from collagen [10, 12, 36]. It was therefore an expected result that increasing GelMA content led to a significant increase in degradation of bioprinted constructs, with GelMA ($p<0.05$) found to have a significantly higher degradation at 14 days compared to AlgMA, A2G1, and A3G1 scaffolds.

Overall, the composite AlgMA/GelMA bioink appeared to be highly biocompatible and capable of supporting both MSC and chondrocyte cell growth following bioprinting and injection into OCDs. This is in keeping with a range of studies where excellent growth of MSCs, chondrocytes and other cells has been supported by use of alginate/GelMA bioinks, demonstrating the versatility and biocompatibility of this composite bioink [10-12, 34-36]. In addition to supporting the growth of a range of cells, further studies have modified alginate/GelMA bioinks to include biological motifs or drug delivery systems, showing a further avenue to optimise *in vivo* tissue regeneration [34, 40].

5.5.3   Use of Composite Bioinks for Injectable Repair of Osteochondral Defects

One of the key successes of developing AlgMA/Col and AlgMA/GelMA composite bioinks was the potential they allowed for injectable repair of osteochondral defects to be performed. Injectable hydrogels for cartilage regeneration have attracted significant interest as they offer the potential clinical flexibility of performing minimally invasive injections that can be moulded in-situ to match irregular patient defects [41, 42]. Cell viability with the injected repairs was strong over several weeks of culture, with significant cell spreading and density of cell growth seen to develop with use of either MSCs or chondrocytes. Previous literature has shown promising results with use of injectable bioinks, with a range of hydrogels including collagen, fibrinogen, chitosan, alginate, GelMA and also synthetic polymers used to support

growth of MSCs and chondrocytes [41-53]. Having the option to combine an injectable bioink with a bioprinted scaffold within the same patient could potentially be clinically useful. Larger osteochondral defects could be repaired using an initial bioprinted construct with any size mismatches between implanted 3D biofabricated constructs and OCDs "filled in" using an injectable bioink. Furthermore, smaller and more superficial defects not detected or anticipated on clinical imaging pre-operatively could also be treated intra-operatively in a flexible manner using an injectable bioink.

5.5.4   **Rationale for Choice of Cells**

As the main cell type within cartilage, chondrocytes were a logical choice for inclusion in experimental work. Use of a fully differentiated adult cell type in biofabricated constructs has the advantage of avoiding the need to stimulate differentiation of stem cells into desired cell types within tissue constructs. Current approved surgical treatment options for OCDs such as ACI and M-ACI also utilise chondrocytes, both of which have published long-term follow up and clinical results proving safety and efficacy. This potentially makes gaining clinical approval for the use of biofabricated constructs containing chondrocytes easier than for implants containing MSCs or ADSCs. MSCs do however have several potential benefits and so were also included in experimental work. They are recognised as being capable of producing a variety of ECM molecules critical for cartilage function, including collagens (Cols), fibronectin, proteoglycans, and glycosaminoglycans (GAGs), as well as a variety of cytokines [54] and have been extensively researched within cartilage regeneration [55-60].

5.5.5   **Incorporation of Cell Spheroids**

A further significant finding was the increased density of cell growth observed with use of MSC and chondrocyte spheroids within bioprinted constructs and injected OCD repairs. Cell aggregates or spheroids are recognised as having superior intercellular communication and extracellular matrix development when compared to cells grown in 2D culture, potentially accelerating cellular growth and ECM development with constructs after biofabrication [22]. There are several examples of bioprinted spheroids having been successfully used in the biofabrication of cartilage, blood vessels and other soft tissues [23-27]. A notable example is provided by Yu *et al*., where hollow alginate capsules created using a co-axial system were deployed to facilitate aggregation of chondrocytes into long strands of cylindrical cartilaginous tissue. Once matured, the tissue strands were released by dissolving the alginate tubes, leaving stands of cartilage which could then be 3D bioprinted to form larger cartilaginous structures which could be deployed in toxicology testing and within *in vitro* analysis [61, 62]. An especially novel approach was developed by Parfenov *et al.* to allow fusing of spheroids into cartilaginous tissue to occur. Chondrocyte spheroids were exposed to gadolinium (Gd^{3+}) in culture media, before a magnetic field was produced, and with the aid of mathematical modelling, chondrospheres were predictably directed to move into a pre-designed 3D morphology, controlled by the magnetic field [63]. In a perhaps more straightforward approach, we adapted a 3D culture system from methods described by Dahlmann *et al.* [28]. This approach was easily scalable, cost-effective and allowed production of high volumes of regularly sized chondrocyte and MSC spheroids. Subsequent harvesting and centrifuge of spheroids allowed easy production of a bioink with a high density of spheroids that was notable for leading to a significant increase in density of cell growth, compared to when cells grown in 2D culture were used. Further research has examined the role of co-culturing MSCs and

chondrocytes together; chondrogenesis of MSCs has found to be improved in co-culture, thought to be related to the paracrine secretion by chondrocytes of factors including TGF-β, IGF-1, BMP-2 and FGF-2[64]. Furthermore, the relationship appears to be synergistic, with direct co-culture in 3D found to enhance the proliferation and phenotype preservation of chondrocytes whilst enhancing chondrogenic differentiation of MSCs [65-68].

5.5.6 Key Limitations

There are some limitations to our findings and room for development of experimental methods. A more detailed analysis of the mechanical properties of biofabricated constructs would have been informative, particularly to allow comparison between different composite bioinks and the impact of varied crosslinking conditions. However, prolonged analysis of the stability of constructs during culture was achieved and in some respects, this is as equally important. Biofabricated constructs need not be robust enough to allow weightbearing to occur immediately following *in vivo* implantation*,* as it is commonplace to restrict weightbearing following cartilage repair procedures within patients to protect the repair as healing occurs. More important is the ability for biofabricated constructs to retain 3D integrity and thereby facilitate 3D cell growth and ECM development within OCD repairs *in vivo.* To this end, performing *in vivo* analysis of biofabricated constructs would have provided invaluable information about overall levels of bioink and construct biodegradation and biocompatibility. Added to this, deeper scrutiny of cell behaviour *in vitro* would also have added important information. Specifically, analysis of gene expression would have allowed closer monitoring of the phenotype of chondrocytes during culture, as within suboptimal conditions chondrocytes are recognised to undergo progressive de-differentiation and produce fibrocartilage rather than articular hyaline cartilage, particularly as they are subjected to passaging during culture [69].

Preservation of chondrocyte phenotype has been found to be favoured by stiffer GelMA constructs and culture in 3D, and so use of a triple crosslinked AlgMA/GelMA bioink is likely to be favourable to phenotype preservation. Furthermore, attempting chondrogenic differentiation of MSCs and ADSCs included in constructs would have provided significant proof of concept if successfully achieved. Use of histology and more sophisticated imaging techniques, such as confocal and scanning electron microscopy would also have provided more detailed information about cell spreading, microporosity and internal structure of scaffolds. Analysis of total DNA content would have also provided a further quantitative method of examining density and volume of cell growth during culture.

5.5.7   Conclusions

The overall aim of this chapter was to apply 3D biofabrication to target the reconstruction of osteochondral defects. To this end, novel composite AlgMA/Col and AlgMA/GelMA bioinks that can be triple-crosslinked following bioprinting or injection were developed. Following bioprinting or injection into osteochondral defects, optimised versions of the composite bioinks supported high chondrocyte and MSC viability, with accelerated cell growth seen with inclusion of cell spheroids into bioinks ($p < 0.05$). UV and double-ionic ($BaCl_2$ and $CaCl_2$) crosslinking deployed following bioprinting significantly prolonged bioink stability in culture without impairing cell viability. Bioprinted constructs successfully maintained shape in culture over 28 days, whilst injected OCD patch-repairs demonstrated sustained cell viability and maintained macroscopic structure over a 14-day period *in vitro*. This offers further evidence for a new approach to treating AC defects in the future.

Future work using the composite bioinks could look to increase bioactivity through inclusion of further biological cues and chondrogenic or osteogenic growth factors. Inclusion of an osteogenic base layer to create a biphasic or even triphasic construct as has been attempted elsewhere in the literature could help to improve mimicry of native anatomy, potentially speeding the integration of constructs into osteochondral defects *in vivo* [8, 55]. Enhanced maturity of constructs and closer replication of the *in vivo* environment during culture could also be achieved through use of a bioreactor, whilst spheroid creation could also be optimised further and potentially automated. Ultimately increasing the scalability and throughput of the biofabrication process to allow cost-effective and patient-specific treatment to be delivered into the clinical environment remains the overall key challenge.

6 Chapter 6 – Developing 3D Bioprinted Bacterial Biofilms - A Novel Method for Studying Clinical Orthopaedic Infection

6.1 **Introduction**

Three dimensional (3D) bioprinting has developed rapidly as a technique that can deposit living cells and biomaterials in user-defined patterns to build complex tissue constructs on demand "from the bottom up" [1, 2]. Whilst bioprinting has been utilised to produce 3D constructs for tissue-engineering [3, 4], few attempts have been made at 3D bioprinting bacteria [5-9]. The potential to bioprint and study 3D bacterial constructs could have great clinical significance at a time when antimicrobial resistance (AMR) is rising to dangerously high levels worldwide. According to the World Health Organization (WHO), urgent action is required to avoid a "post-antibiotic era", in which common infections and minor injuries can once again kill [10]. Future strategies to overcome AMR are likely to include targeting the 3D process of biofilm formation, a key bacterial survival mechanism against antibiotics and other environmental threats. Biofilms can be defined as structured 3D communities of bacterial cells enclosed in a self-produced polymeric matrix, attached to a solid surface or substratum [11] . Nearly all (99.9%) micro-organisms have the ability to form biofilm, allowing bacteria to adhere and grow on a wide range of biological and inert surfaces, including joint replacements, heart valves and bodily tissues [12, 13]. Within the protective environment of a biofilm, bacteria increase their resistance to host immune defences and antibiotics up to 1000%, whilst their ability to exchange genetic information is also greatly increased [14, 15]. Eradication of infection once biofilm has formed is therefore hugely challenging, and often leads to chronic infection, requiring surgical removal of implants, prolonged antimicrobial therapy and even mortality [16]. In the United

States of America alone, there are 17 million new biofilm-associated bacterial infections that lead to estimated health care costs of $94 billion and 550,000 deaths each year [17].

Biofilm formation can be described as a stepwise process, beginning with the irreversible attachment of bacteria to inanimate and living surfaces (Fig. 6.1). Following attachment, bacteria begin to divide, forming microcolonies and producing extracellular polysaccharides that define a biofilm. Once established, the biofilm undergoes structural maturation and may develop water-filled channels within the matrix, facilitating nutrient transport [18]. Gene expression also changes as bacteria communicate through cell-to-cell signalling in a process known as quorum sensing (QS), altering processes including sporulation, virulence factor secretion and biofilm formation [19, 20]. Finally, regions of the film spontaneously disperse as bacteria enzymatically dissolve the matrix. Dispersed cells can quickly revert to their planktonic form to colonise other sites, whilst retaining properties such as AMR [21].

① :Reverible attachment
② :Irreversible adhesion to a substratum
③ :Microcolony formation occurs
④ :Maturation of the biofilm
⑤ :Biofilm dispersion and bacteria detachment
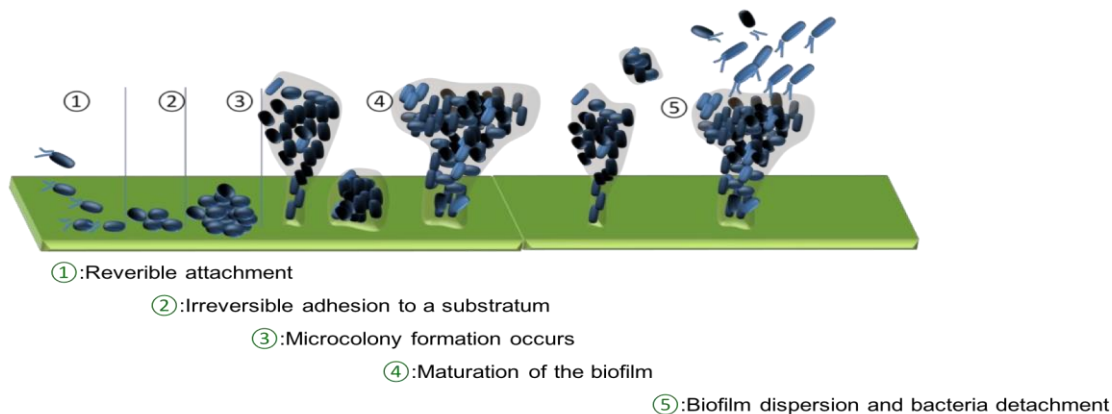
Figure 6.1 Biofilm maturation is a complex developmental process involving five stages. 1. Single free-floating eukaryotic cells land on a surface and begin to attach. 2. Bacterial cells aggregate and become irreversibly attached to the surface through secretion of an extracellular polymeric substance (EPS), comprised of sugars, proteins, and nucleic acids like DNA. 3.

Growth and division of bacteria occurs along with secretion of further layers of EPS. 4. The biofilm matures, developing increasingly complex internal organisation and structure. 5. Segments of the biofilm disperse, releasing bacteria to undertake further colonization [22].

Current biofilm culture methods tend to be 2D in nature and attempt to replicate the nature of the *in vivo* environment by focussing on factors relevant to biofilm formation such as provision of materials, nutrients or fluid flow; available methods include drip flow [23], rotating disk [24], microfluidic [25], and flow chamber based culture [26]. Unfortunately, none of these methods are able to entirely mimic the complexity of the 3D microenvironment and host defence mechanisms [27] and struggle to produce biofilm thicknesses beyond 100 µm [28, 29]. In contrast to current *in vitro* models, *in vivo* biofilms can grow beyond 1000 µm in size and are often found embedded within a host's extracellular matrix, leading to interactions with the host immune system which can further alter biofilm morphology, complexity and size [30, 31]. Within the clinical environment, the minimum inhibitory concentration (MIC) of antimicrobial agents (defined as the lowest concentration of an antimicrobial agent at which visible bacterial growth is inhibited after overnight incubation) is frequently calculated during antimicrobial susceptibility testing (AST) to assess antimicrobial efficacy and bacterial resistance [32]. Methods to determine the MIC are traditionally based on 2D planktonic cultures of bacteria [33]. However, *in vivo* biofilm formation is three dimensional (3D) in nature, making it difficult to accurately determine the minimum biofilm eradicating concentration (MBEC) in well-established biofilm infections, as current laboratory models tend to involve 2D biofilm culture that underestimates the increased antimicrobial tolerance of 3D biofilms [23, 34-37]. This mismatch has significant clinical implications; for example, antimicrobial agents are usually chosen based on their efficacy against 2D planktonic cultures which are more sensitive to treatment than 3D biofilms. Clinically this is well demonstrated by treatment of *P.aeruginosa*

infection, where treatment with antibiotics originally developed against 2D cultures often becomes ineffective once biofilm formation occurs [37]. To develop novel antimicrobials capable of disrupting biofilm formation and resistance in future, 3D *in vitro* biofilm models more representative of clinical infection are therefore required to allow effective drug screening. Concern about AMR is compounded by the fact that it has been 30 years since a new class of antibiotics was last introduced [38].

One potential technological solution is offered by 3D bioprinting, which has developed rapidly as a technique that can deposit living cells and biomaterials in user-defined patterns to build complex tissue constructs "from the bottom up" [39-42]. Whilst there have been elegant attempts to 3D bioprint bacteria and their aggregates [9, 43-46], as yet there has been no report demonstrating the formation of mature bacteria biofilms following bioprinting. However, the capacity to reliably and reproducibly 3D bioprint bacterial biofilms could have several potential benefits. Embedded bacteria have been shown to have increased metabolic activity, AMR and plasmid stability compared to bacteria grown in 2D [47, 48]. 3D biofilms therefore potentially mirror *in vivo* bacterial growth and behaviour more closely than traditional 2D models, increasing the potential to investigate processes including bacterial quorum sensing, antimicrobial biofilm penetration and MBECs [48, 49]. 3D bioprinting also increases the potential to produce biofilm constructs with predesigned dimensions, with a high degree of control possible over biofilm thickness and dimensions. Other benefits of 3D bioprinting biofilm include the potential creation of microbial fuel cells [50], biosensors [51] and biotechnological applications [51-53]. Other benefits of 3D bioprinting biofilm include the potential creation of microbial fuel cells [54], biosensors [55] and biotechnological applications [52].

In the following section a novel 3D biofilm bioprinting technology that facilitates rapid biofabrication of 3D bacterial biofilms is introduced, with controlled size and structure of 3D biofilms achieved using gram negative, gram positive, aerobic and anaerobic species. Bioprinting of biofilm constructs with thicknesses greater than previously available *in vitro* models is also demonstrated. The formation of mature bioprinted 3D biofilms and their response to *in vitro* AST is also examined, allowing comparison of the antimicrobial tolerance of 2D cultures versus 3D printed biofilms to be performed for the first time.

6.2 **Project Acknowledgments**

6.3 **Results**

6.3.1 **Reproducible Bioprinting of 3D Bacterial Bioink with Controlled Dimensions**

Successful bioprinting relies in part on combining a suitable bioprinting technique with an appropriate bioink. To achieve this, a bacteria-friendly bioink was developed with reliable bioprinting characteristics. The schematic in Figure 5.2 presents a general overview of our methodology of bacterial bioink bioprinting, using a biocompatible bioink and stepwise ionic crosslinking process. Alginate is a widely adopted hydrogel for bioprinting and was chosen as the main component of our bacterial bioink due to its biocompatibility, low toxicity, low cost and ease of use [40, 56, 57]. Cross-linking a sodium alginate (Protanal 10/60) hydrogel with calcium chloride created a hydrogel (0.2% $CaCl_2$: 2% Protanal) with viscosity sufficient to allow bioprinting of free-standing structures ranging in size and thickness. Cultured bacteria were mixed into the partially crosslinked hydrogel to produce a bioink with homogenous bacterial concentration. An extrusion bioprinter using mechanical extrusion was then used to extrude the bioink to produce constructs with predesigned dimensions. Measured scaffold thickness following bioprinting correlated well with the intended CAD file thickness (Table 6.1). Bioprinting resolution with the hydrogel could be increased to produce more intricate structures using a 32g print needle, corresponding to a maximum resolution of 0.108 µm (Table 6.1). Further cross-linking following bioprinting via exposure to solutions of barium chloride was performed, allowing prolonged culture and observation of constructs (up to 28 days).
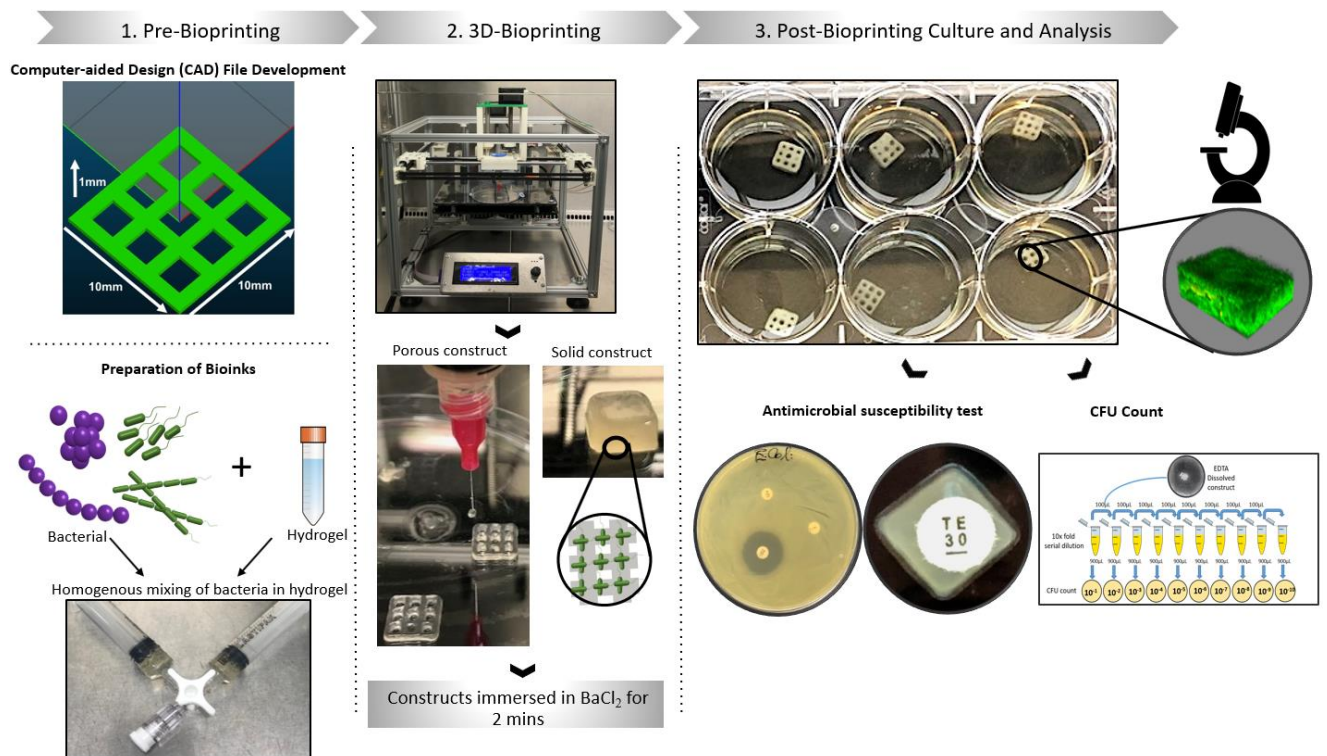
Figure 6.2 Schematic of bacterial biofilm bioprinting process. Initial designs to be bioprinted are produced using computer-aided design (CAD) software. Following this, a partially cross-linked hydrogel is produced by mixing sodium alginate and calcium chloride together. Bacteria are then mixed into the hydrogel to produce a bioink with homogenously distributed bacteria. 3D bioprinting is then performed, using a custom-built bioprinter that uses mechanical force to extrude bioink from a syringe that is moved in the x-y-z plane. Bioprinted constructs of solid and porous design are then immersed in solutions of $BaCl_2$ for 2 mins to secondary cross-link the constructs. Following bioprinting and immersion cross-linking, the constructs are cultured in bacterial growth media, allowing analysis to be performed at selected time points.

Table 6.1 Measured 3D scaffold thickness following bioprinting compared to intended CAD file thickness. Scale bars = 1cm.

Solid Construct

CAD thickness	0.25 mm	0.5 mm	1 mm	2 mm	4 mm
Bioprinted thickness (mm)	0.33 ± 0.06	0.63 ± 0.09	1.1 ± 0.06	2.2 ± 0.19	4.2 ± 0.29
Thickness after BaCl$_2$ crosslinking (mm)	0.27 ± 0.11	0.57 ± 0.08	1.2 ± 0.24	2.2 ± 0.29	4.1 ± 0.27

Porous Construct

CAD thickness	0.25 mm	0.5 mm	1 mm	2 mm	4 mm
Bioprinted thickness (mm)	0.29 ± 0.06	0.51 ± 0.08	1.0 ± 0.13	2.2 ± 0.24	4.1 ± 0.31
Thickness after BaCl$_2$ crosslinking (mm)	0.28 ± 0.09	0.56 ± 0.08	1.1 ± 0.12	2.0 ± 0.23	4.2 ± 0.19

Bioprinted Construct Morphology	Solid	
	Porous	
	Max. resolution (0.108 μm)	

6.3.2 Developing Stability in Culture of Bacterial Bioink Through Double Ionic Crosslinking

The complex structure of 3D biofilms found in clinical infection take significantly longer to develop and mature than 2D *in vitro* biofilm models that can be produced in overnight culture [58, 59]. Achieving sufficient stability and longevity in culture of bioprinted bacterial bioink was therefore an essential step to allow time for bacteria to proliferate and deposit their own extracellular matrix, a central component of mature biofilm structure. In previous work we developed the stability of alginate bioinks to allow successful long-term 3D cell culture and differentiation of stem cells [40, 57]. This was achieved via double ionic cross-linking alginate with calcium and then barium cations in a stepwise process [57]. Whilst other cations including strontium have been utilized for this purpose, barium appears to give the strongest cross-linking effect, optimizing construct mechanical stability [60]. We therefore applied this approach to achieve extended bacterial bioink stability (>4 weeks) in culture. As demonstrated in Table 6.1, initial cross-linking of Protanal alginate hydrogel with $CaCl_2$ created a hydrogel with sufficient viscosity to allow successful bioprinting of free-standing structures of both solid and porous design, ranging in thickness from 0.25 mm to 4mm. By performing cross-linking prior to bioprinting, rather than extruding alginate onto a calcium-coated culture surface as performed in other literature, greater homogeneity of hydrogel cross-linking was achieved; this is essential to achieve optimal printability [43]. Further cross-linking was performed following bioprinting by exposure of constructs to increasing concentrations of $BaCl_2$, which helped to extend the stability of constructs from within a week (with calcium-only cross-linking) to over 4 weeks in culture (Fig. 6.3).
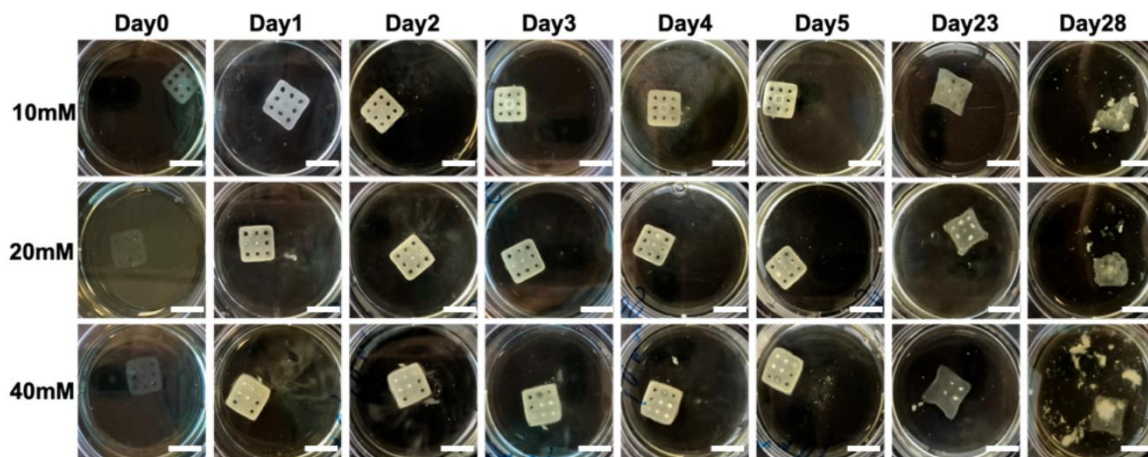
Figure 6.3 Stability of 1mm, porous scaffolds containing MRSA during culture following crosslinking with increasing BaCl$_2$ concentrations from 10 to 40 mM. Scale bars represent 1cm. Constructs crosslinked with 20 or 40 mM BaCl$_2$ had superior longevity in culture compared to constructs exposed to 10 mM BaCl$_2$.

6.3.3 Thickness And Structure of Bioprinted Constructs Influences Biofilm Formation

To examine the ideal 3D construct design and thickness for supporting bacterial growth following bioprinting, two different construct designs in a range of thicknesses were bioprinted containing *E. coli* and bacterial growth observed over 14 days (Fig. 6.4 A). It was apparent that *E. coli* biofilm formation (or bacterial density) was greater in thinner (0.25 mm to 1 mm) constructs compared to thicker (4mm) construct designs (p<0.001, ANOVA) (Fig. 6.4 C). Unfortunately, thinner constructs of 0.25 mm and 0.5 mm thickness were not robust enough to allow physical manipulation and CLSM imaging to be performed after 14 days culture. This was presumed to be due to leaching of cations (Ca^{2+} and Ba^{2+}) from the thin, relatively high-surface area constructs into surrounding culture media, resulting in decreased cross-linking; this is likely to have been exacerbated by regular media changes and culture atop a rocking device, increasing outwards diffusion of cations from the bacterial bioink construct. In 4 mm thick

constructs, reduced biofilm formation was also observed in solid compared to porous constructs (p=0.038, t-test) (Fig. 6.4 B).

It seems likely that porous construct designs facilitate greater fluid transport, enhancing nutrient and oxygen diffusion processes in comparison to non-porous, solid constructs. This would explain why the aerobic bacteria *E.coli* failed to proliferate and produce significant biofilm in the thick, solid constructs, with the optimal structure for *E.coli* appearing to be a 1 mm porous construct.
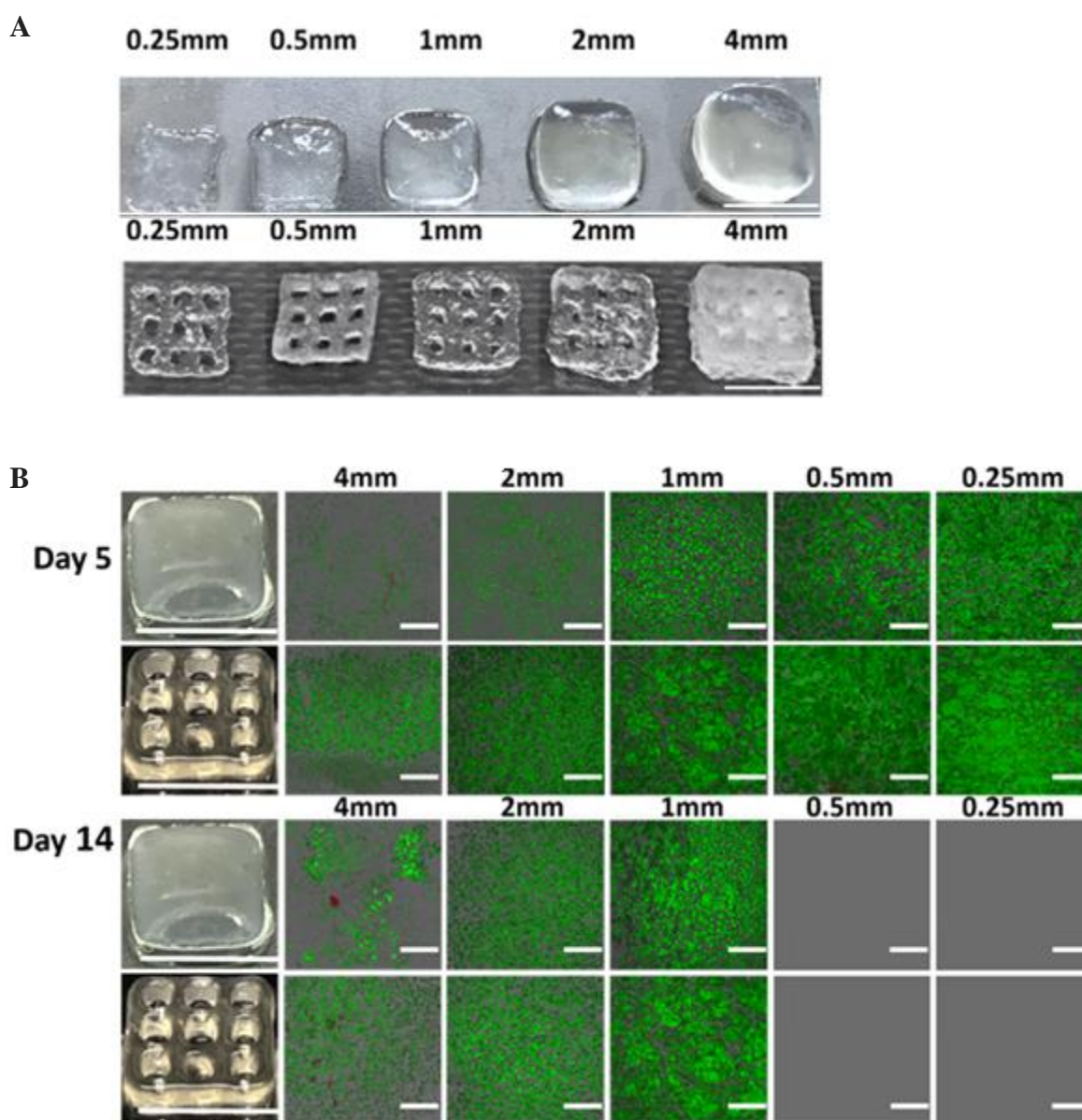
Figure 6.4 Influence of construct structure and thickness on biofilm formation. **(A)** Constructs with vertical thicknesses increasing from 0.25mm to 4mm were sequentially bioprinted and cross-linked by exposure to 20mm $BaCl_2$. Measured thickness correlated well with designed vertical thickness after measurement with digital callipers (Table 6.1). Scale bar represents 1cm. **(B)** Comparison of bacterial growth in solid and porous 1mm constructs containing *E.Coli* was made. Initial analysis at 5 days found that growth in solid constructs was slower than in

corresponding porous constructs. At 14 days, 1mm constructs appeared to have the best biofilm formation, whilst 0.5mm and 0.25mm constructs had insufficient mechanical integrity to allow analysis. Scale bar represents 100 microns.

6.3.4 **Optimizing Crosslinking Conditions for Biofilm Formation**

Having established for aerobic bacteria that porous constructs of at least 1m thickness and crosslinked with at least 20 mM $BaCl_2$ maintained stability in culture, the influence of $BaCl_2$ cross-linking concentration on bacterial growth was analysed over 28 days. Porous, 1mm constructs containing MRSA were exposed to a range of $BaCl_2$ concentrations. Initial CFU analysis found significantly higher bacterial growth in 20 mM and 40 mM constructs compared to constructs exposed to 10 mM of $BaCl_2$ after 4 days of culture ($p<0.001$, ANOVA) (Fig 6.5 A). Quantitative analysis of biofilm formation captured using CLSM (Fig. 6.5 B) was then performed over 28 days of culture using MATLAB2016a. It was found that maximum density of biofilm formation was significantly greater in 20 mM and 40 mM constructs compared to constructs exposed to 10 mM of $BaCl_2$ ($p<0.001$, ANOVA) (Fig 6.5 C). This was presumed due to increased leaching of bacteria as a result of lower (Ba^{2+}) cross-linking density in 10 mM constructs.

A CFU Count

B

C Biofilm Denisty
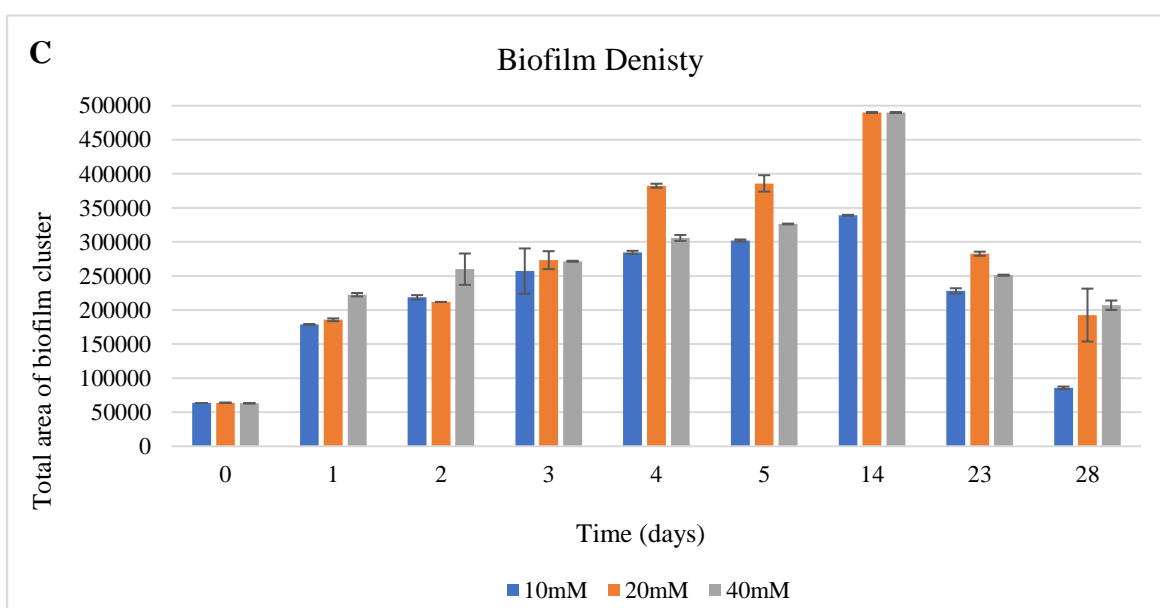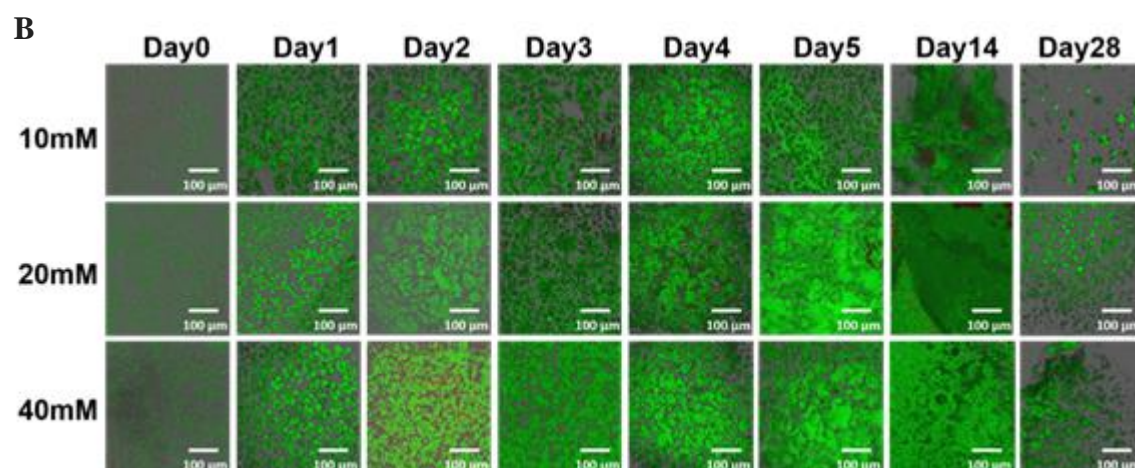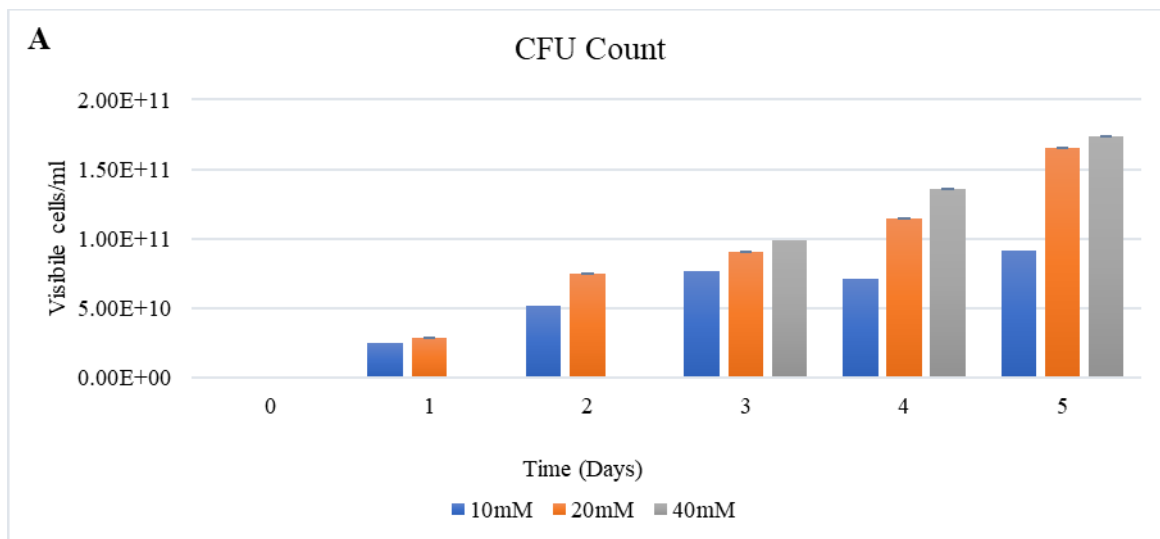
Figure 6.5 Optimising crosslinking conditions for biofilm formation. **(A)** Constructs were sampled daily for 5 days, with exposure to EDTA triggering dissolution of the bacterial bioink construct. This allowed CFU analysis to be performed on released bacteria from constructs. It was notable that from day 4 onwards, 20 and 40 mM $BaCl_2$ constructs had significantly greater bacterial growth ($p<0.001$, ANOVA). Analysis of 40 mM $BaCl_2$ constructs was not possible for the first 3 days as EDTA exposure was unable to sufficiently dissolve the construct and release bacteria. (B) Porous, 1mm constructs containing MRSA were exposed to a range of $BaCl_2$ concentrations. Growth within all constructs was initially strong; however, maximum density of biofilm formation was significantly greater in 20 mM and 40 mM constructs compared to constructs exposed to 10 mM of $BaCl_2$ ($p<0.001$, ANOVA). **(C)** Quantification of biofilm formation over time was performed using unsupervised k-means segmentation and a labelling connected component function on MATLAB to threshold areas of biofilm formation out from background noise on images. The resultant graph of biofilm area produced over time demonstrates that maximum density of biofilm formation was significantly higher in 20mM and 40mM constructs ($p<0.001$, ANOVA), compared to 10 mM constructs.

6.3.5   Capturing the *In vitro* Life Cycle of Biofilm in 3D

Biofilm formation is reported to occur in a five-step lifecycle (Fig. 6.6 A) [61]. However, due to factors including limited biofilm thickness, current *in vitro* models are unable to readily facilitate observation of the five-step process and complex microarchitecture development that occurs during biofilm formation [62].

We therefore attempted to observe the biofilm life cycle in 3D by taking advantage of the favourable conditions for biofilm formation provided by porous, 1mm MRSA constructs cross-linked with 20 mM $BaCl_2$. CLSM imaging of MRSA biofilm formation allowed correlation

with the natural process of biofilm formation to be made. The recognised phases of biofilm formation could be observed, with aggregation of microcolonies at day 2, maturation of biofilm between days 5 and 14, and eventual biofilm dispersion seen at day 23 onwards (Fig. 6.6 B).

To the best of our knowledge, this is the first time the processes involved in mature 3D biofilm formation have been observed *in vitro* in true 3D and following bioprinting. Direct correlation to the 5-step process governing biofilm formation in 2D can be made, offering a novel method to study biofilm behaviour and response to antimicrobial treatment in 3D.
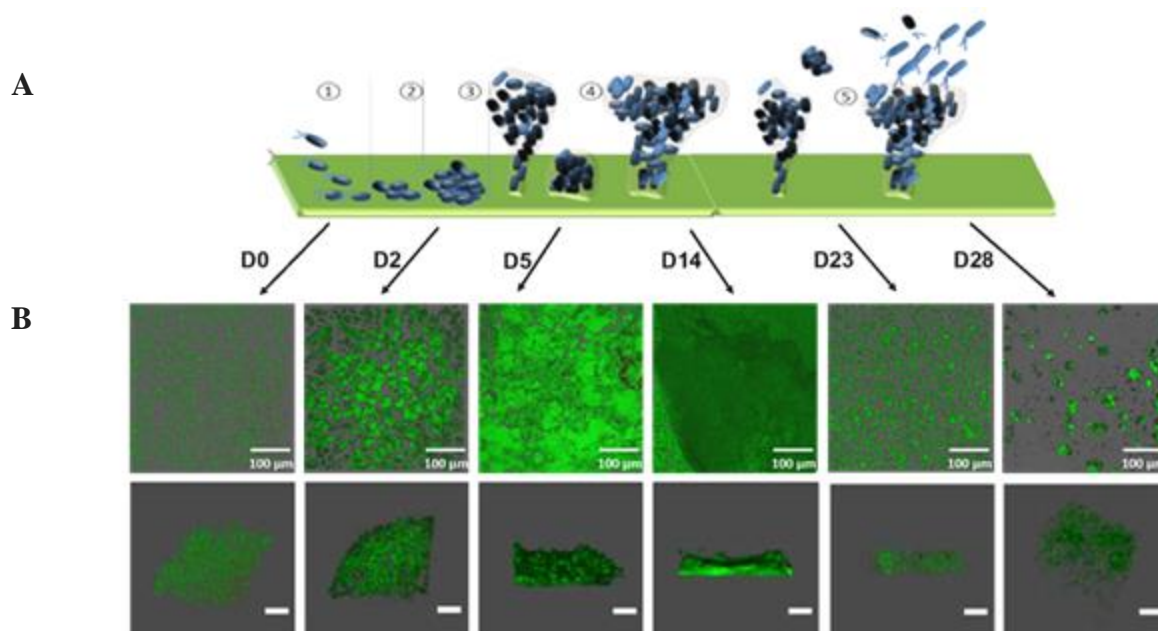
Figure 6.6 Capturing the in vitro life cycle of biofilm in 3D. **(A)** The five-step biofilm lifecycle. (1) Free swimming planktonic bacterial cells initially attach to a biological or inert surface. (2) Soon after, bacteria began to divide and aggregate together in small microcolonies and secrete quorum signals which initiate up-regulation of various genes and virulence factors on a community-wide basis. (3) Bacteria form an extracellular biofilm matrix through secretion of copious polymers including polysaccharides, proteins and oligonucleotides that (4) becomes increasingly mature. (5) Consumption of nutrients, increases in shear stress and other cell

signalling events lead to portions of biofilm detaching. Dispersed cells can quickly revert to their planktonic form to colonise other sites, whilst retaining properties such as AMR [62]. **(B)** The 5-step process of biofilm formation in 2D correlated with cross-sectional and side-on CLSM images of 3D bioprinted biofilm formation. Significant biofilm formation was evident after 5 days. Increasing biofilm formation and maturation is evident up to day 14 of imaging. At day 23 and beyond, the biofilm appears to begin the process of dispersion as some bacteria seek to leave the construct and colonise a new environment.

6.3.6 **Bioprinting of Thick, Anaerobic 3D Biofilm Constructs**

Whilst aerobic bacteria including MRSA and *E. coli* had limited growth in thicker bioprinted constructs (Fig. 6.4 B), presumably due to limited diffusion of nutrients and oxygen, anaerobic bacteria have greater potential to thrive in oxygen-deplete conditions. As an opportunistic, nosocomial pathogen of immunocompromised individuals, the anaerobic strain *Pseudomonas aeruginosa* (*P. aeruginosa)* is well known for infecting the thick, oxygen-depleted mucus in the airways of cystic fibrosis (CF) patients, producing robust *in vivo* biofilms [63]. It is also frequently implicated in chronic, polymicrobial wound infections, skin, soft tissue and bone infections; co-infection with *P. aeruginosa* is noted to be more virulent than infection with a single infection and a risk factor for development of AMR [64]. The culture conditions provided by the thick respiratory mucus in CF patients and chronic discharging wounds is somewhat analogous to those provided by our thick, non-porous hydrogel constructs. To investigate this, *in vitro* biofilm formation of *P. aeruginosa* was examined in non-porous, thick (2 mm and 4 mm) constructs (Fig. 6.7).

P.aeruginosa was observed to undergo extensive growth in 2 mm and 4 mm thick, non-porous structures, forming an extremely dense layer of biofilm (Fig. 6.7 B). In contrast, much more limited bacterial growth and biofilm formation was observed via CLSM in 2 mm and 4 mm constructs inoculated with the aerobic bacteria *E. coli* (Fig. 6.4 B). Strong blue-green pigmentation was also seen to form in 2 mm and 4 mm *P.aeruginosa* constructs over 14 days of culture (Fig. 6.7 A); this is likely related to the expression of two metabolites, pyocyanin (blue) and pyoverdine (green), which is known to occur in *P.aeruginosa* to facilitate anaerobic respiration [65]. To give wider context, the prevalence of multidrug-resistant (MDR) anaerobes including *P. aeruginosa* is increasing worldwide, with limited current therapeutic options [66, 67]. The extensive growth of *P.aeruginosa* and associated biofilm formation seen within our 3D bioprinted constructs therefore offers a novel and highly promising *in vitro* method of studying anaerobic bacterial biofilm infection.
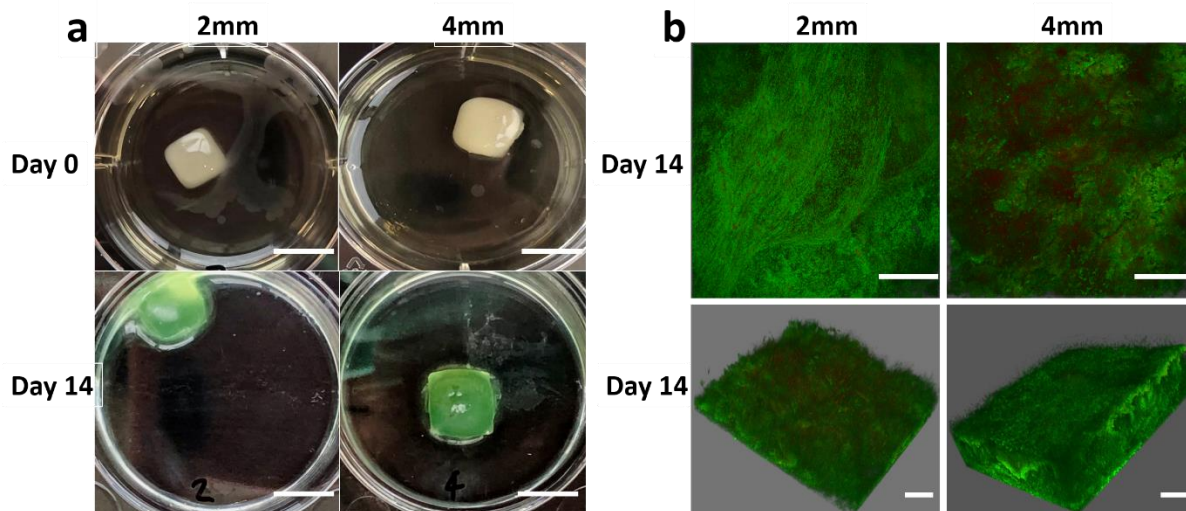
Figure 6.7 *Pseudomonas aeruginosa* (PAO1) formed anaerobic biofilms in thick constructs. (A) Photo images of 3D bioprinted PAO1 biofilm at day 0 (white colour) and matured biofilm at day 14 (blue-green colour). (B) 3D reconstructed CLSM Z-stack in 2D-projection and 3D reconstructed images (1:1 aspect ratio in x, y & z axes) of matured PAO1 biofilm formed at 2

mm and 4 mm thickness at day 14. The sizes of the scale bars in the photograph and fluorescence images are 1 centimetre and 100 microns.

6.3.7 3D Biofilms Require Greater Antibiotic Doses to Treat Than Traditional 2D Models

Biofilm formation is a significant defence mechanism by which bacteria can evade and resist eradication by the host immune system and antimicrobials. However, within the human body biofilm formation is a 3D process, in contrast to most currently available laboratory models that tend to involve 2D biofilm culture [68]. AST methods such as MIC calculation do not distinguish between bactericidal and bacteriostatic effects of antibitoics, and crucially do not provide information on the degree of antimicrobial biofilm penetration or eradicaiton [22, 30, 65, 69-73]. We therefore utilised our method of producing mature, 3D biofilm constructs to study antimicrobial penetration in 3D as compared to 2D bacterial cultures.

The MIC (defined as the lowest concentration of a chemical which prevents visible growth of a bacterium [74]) was calculated for MSSA and MRSA in 2D culture models; bacteria were cultured for 24 hours to allow maximum density of growth to occur, before exposure to increasing concentrations of methicillin via broth microdilution. The same method was then used to determine the MBEC in 3D bioprinted MRSA and MSSA biofilm culture models that had been allowed to grow for 5 days, allowing dense biofilm formation. The MIC and MBEC were determined by a visual inspection of culture wells and correlated with measurements of absorbance of light through treated culture wells in both cases (Figs. 6.8 B & 6.8 D). Due to resistance to methicillin, MRSA had a higher MIC than MSSA in 2D (Fig. 6.8 A) and a higher MBEC than MSSA in 3D culture as expected (Fig. 6.8 C). However, for both MRSA and

MSSA, the MBEC calculated in 3D culture was significantly higher than the MIC for 2D culture. Whilst 0.16 μg/mL methicillin prevented visible growth of 2D MSSA culture, the MBEC for MSSA in 3D culture appeared to be at least 15 times higher at 2.5 mg/ml. Similarly, although 1.25 μg/mL methicillin appeared to prevent 2D growth of MRSA, growth of MRSA in 3D culture still occurred with greater than 10 mg/ml methicillin. Therefore, for both MRSA and MSSA, a far higher dose of methicillin was required to treat 3D biofilms compared to 2D cultures inoculated with the same initial OD of bacteria. This result is in keeping with previous reports suggesting that biofilm formation can cause a 10 to 1,000-fold increase in bacterial tolerance to antimicrobial treatment compared to 2D, planktonic cultures [47, 75].
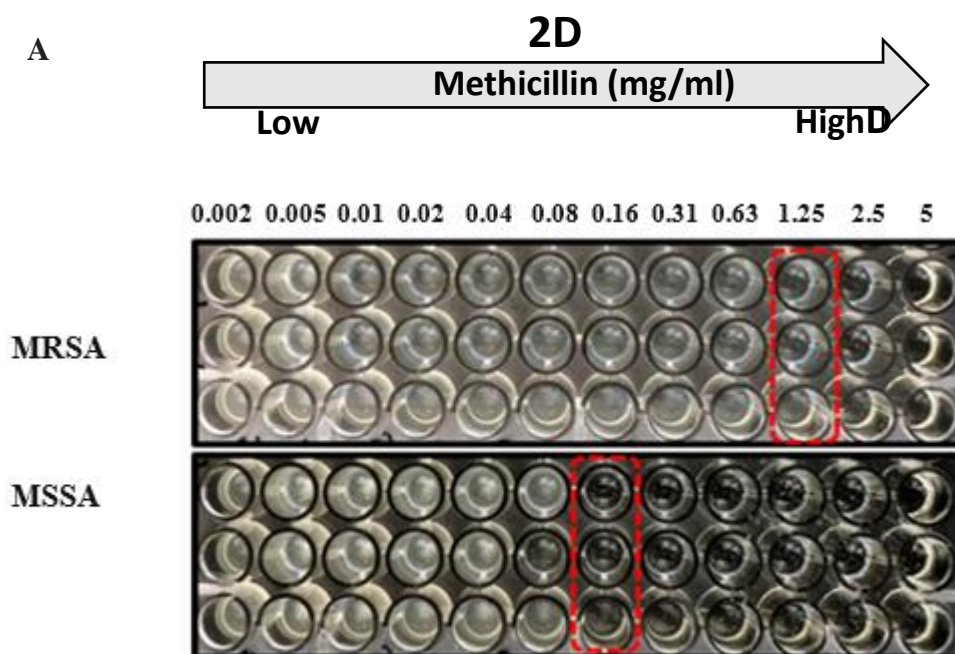
B
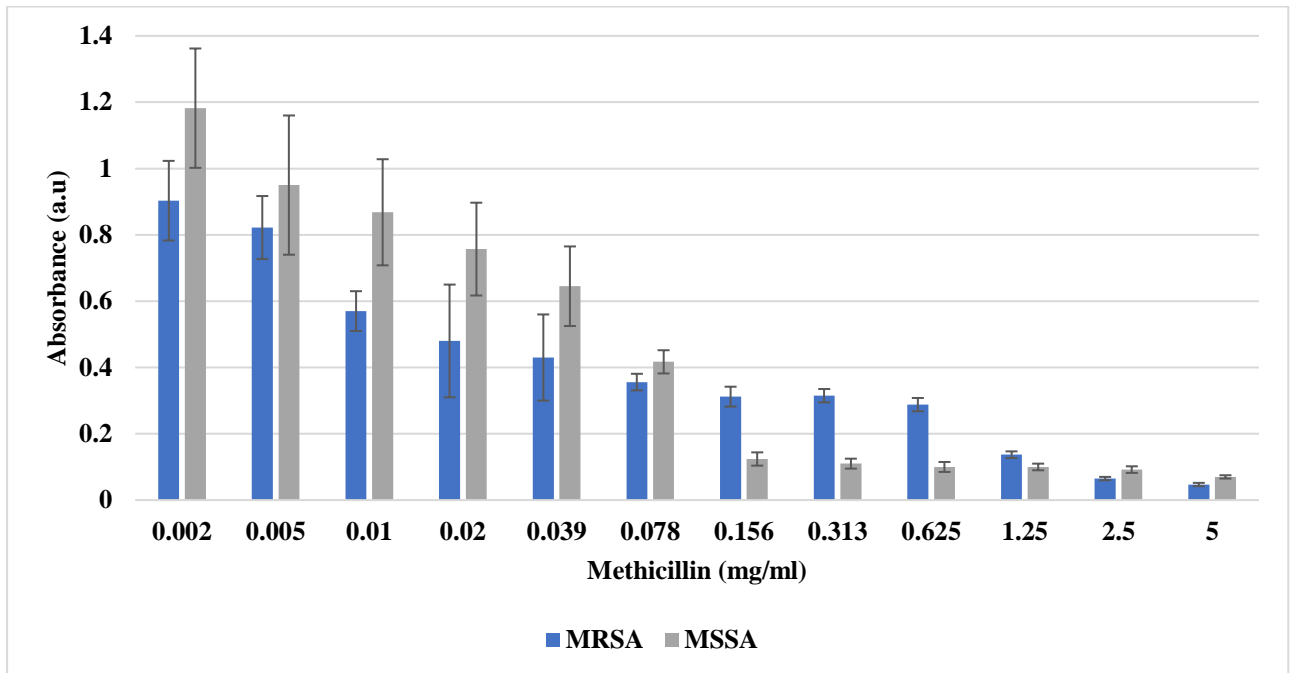
C
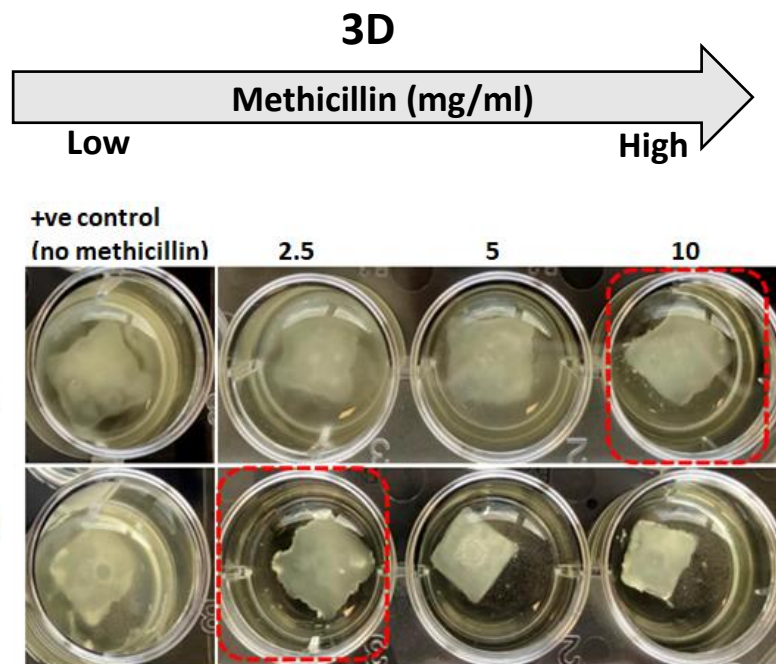
D
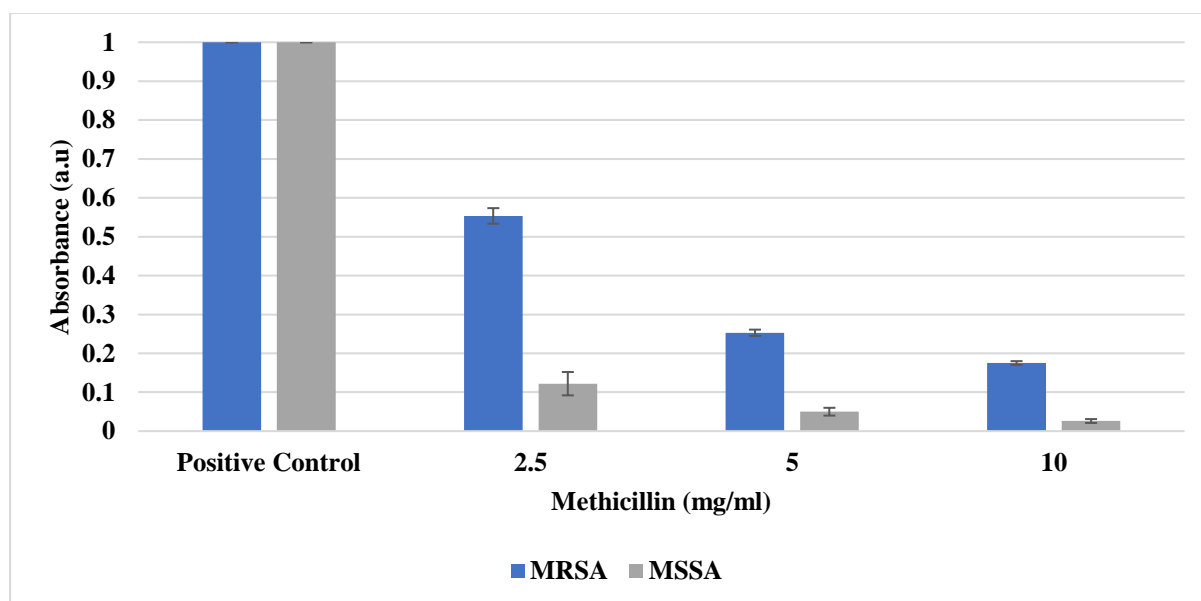
Figure 6.8 3D biofilms require greater antibiotic doses to treat than traditional 2D models. **(A)** The MIC of MRSA and MSSA cultured in 2D was calculated through exposure to increasing concentrations of methicillin for 24 hours. For MSSA, 0.16 μg/mL methicillin prevented visible growth, whilst for MRSA a concentration of 1.25 μg/mL methicillin was required. **(B)** Measurement of the absorbance of light through the methicillin-containing culture was used to verify these findings. No significant change in absorbance was seen when methicillin concentrations were increased beyond the MIC calculated for MRSA or MSSA. **(C)** 1mm thick constructs, inoculated with the same OD of MRSA and MSSA as the 2D culture plates prior to bioprinting, were then exposed to increasing concentrations of methicillin. The MIC appeared to be at least 2.5mg/ml for MSSA, and higher than 10mg/ml for MRSA on inspection. **(D)** Measurement of the light absorbance of the culture broth surrounding the MRSA and MSSA constructs supported these findings, with far higher doses of methicillin required to reduce bacteria growth and therefore the measured broth light absorbance. Mean plus SD displayed for all data. All experiments performed in triplicate.

6.3.8 Biofilm thickness influences response to antimicrobial treatment

The relationship between bacterial construct thickness and susceptibility to antimicrobial treatment was then investigated. Sensitivity of *E. coli* to tetracycline was first confirmed in 2D culture (6.9 A). Bioprinted *E.coli* constructs of 1 and 2mm thickness were grown for 7 days to allow biofilm maturation, and then exposed to oxytetracycline discs which were changed every 24 h (Fig. 6.9 B). It was apparent that 2mm constructs remained opaque whilst 1mm constructs became increasingly transparent in response to oxytetracycline exposure. CSLM imaging of the constructs after 7 days oxytetracycline exposure demonstrated that *E.coli* biofilm had greater viability in the 2mm constructs, whilst bacteria located below the oxytetracycline disc in 1mm constructs had largely been destroyed (Fig. 6.9 C).

C

E.Coli-2mm thick- after treatment   E.Coli-1mm thick- after Treatment
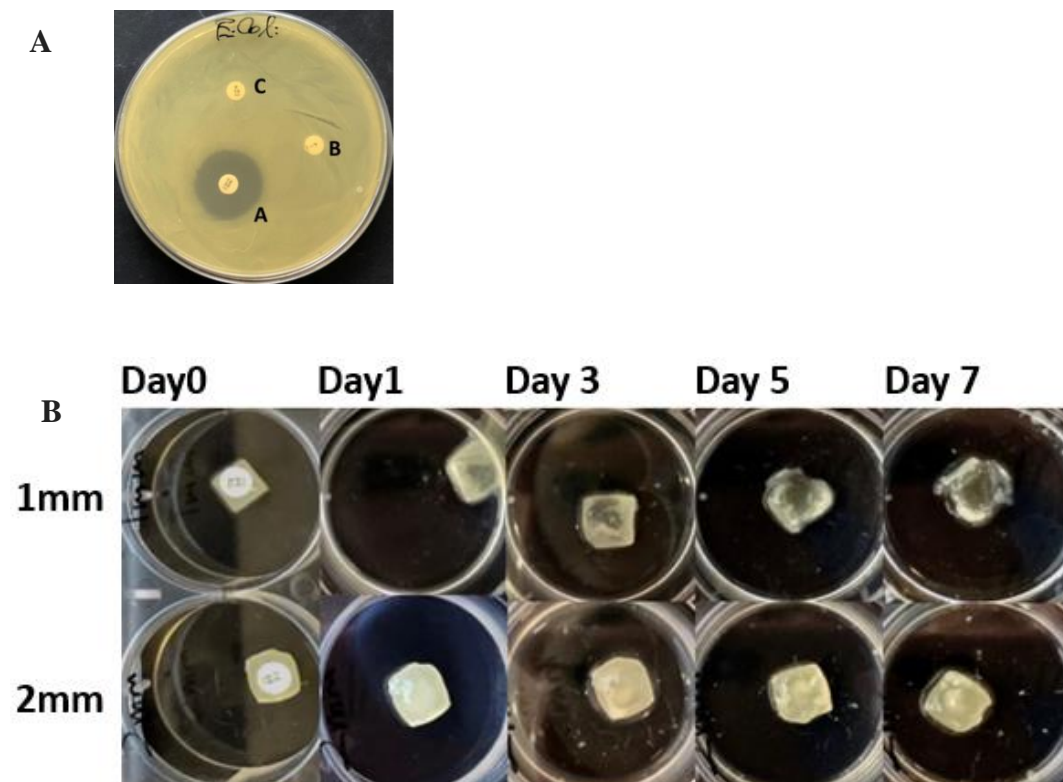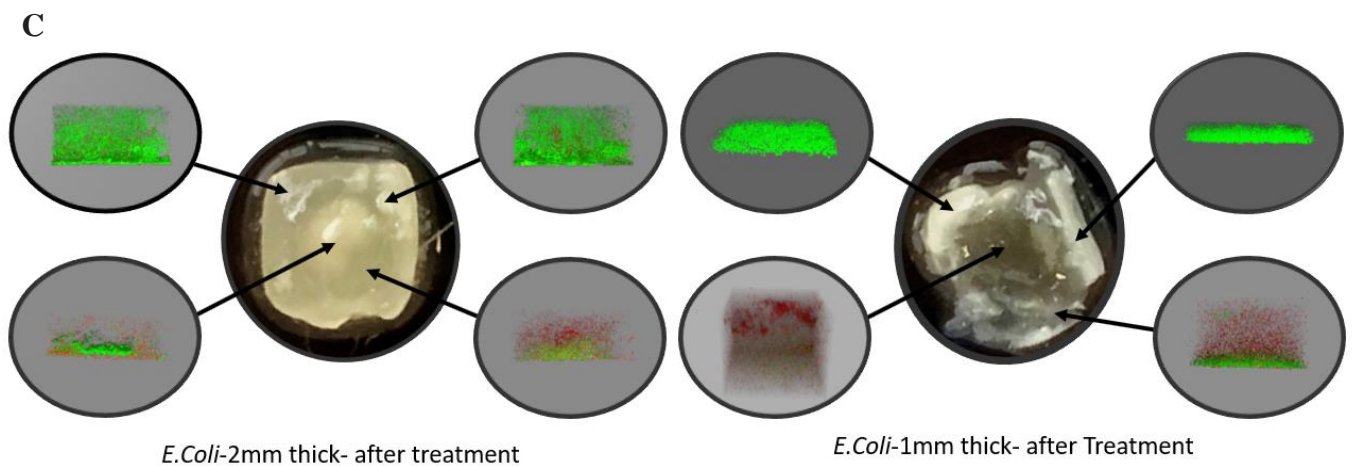
Figure 6.9 Biofilm thickness influences response to antimicrobial treatment. **(A)** Initial sensitivity of *E.coli* to oxytetracycline was confirmed using discs of A – oxytetracycline, B – low dose penicillin and C – higher dose penicillin. The death of surrounding E. coli on the culture plate confirmed the expected sensitivity to oxytetracycline and resistance to penicillin. **(B)** 1mm and 2mm thick constructs containing *E.coli* were bioprinted and allowed to mature for 7 days before oxytetracycline discs were placed directly on top of them. Discs were changed every 24 hours to maintain a high dose of oxytetracycline delivery to the constructs. Over a 7-day period, visible clearing of biofilm occurred within the 1mm construct below the area of oxytetracycline exposure. **(C)** CLSM imaging of the 1mm and 2mm constructs was performed after 7 days exposure to oxytetracycline discs. A commercial Film Tracer™ LIVE/DEAD™ biofilm viability kit (Thermo Fisher, UK) was used to assess biofilm viability using propidium iodide (PI) (490 nm excitation, red emission) and the nucleic acid stain SYTO-9 (488 nm excitation, green emission).Whilst the majority of bacteria were found to be dead (seen as red) below the area of oxytetracycline disc exposure in the 1mm construct, greater evidence of biofilm survival (green staining) in the 2mm construct was seen.

6.4 **Discussion**

This study presents a first-time bioprinting of bacterial biofilm, with sustained bacterial viability and biofilm formation demonstrated in 3D bioprinted constructs over several weeks of culture. The stability of the cross-linked, bacteria-friendly hydrogel developed allowed the whole process of biofilm formation to be observed in 3D, including the growth, maturation and final dispersion of biofilm. Clinically relevant gram-positive, gram-negative, aerobic and anaerobic bacteria were all successfully 3D bioprinted, producing biofilms in constructs with specified dimensions. The high degree of control over construct size and shape afforded by bioprinting also allowed investigation of the influence of construct size, shape and cross-linking conditions on biofilm formation. It was evident that thinner, porous structures formed biofilm quicker when aerobic bacteria were bioprinted, although sufficient cross-linking was required to achieve maximal biofilm formation. It was also observed that thicker biofilms had significantly greater tolerance to antimicrobial therapy, even over a prolonged period of treatment. Furthermore, 2D cultures required significantly less antimicrobial to inhibit growth of bacteria compared to 3D construct inoculated with same initial dose of bacteria.

As a fast-developing technology, 3D bioprinting has been widely utilised to produce 3D constructs for human tissue-engineering. However, few previous attempts have been made at 3D bioprinting bacteria. Lehner *et al.* used extrusion bioprinting to deposit alginate hydrogel containing *E.coli* onto agar plates coated with calcium chloride. This precipitated calcium cross-linking of bioprinted structures, allowing various shapes to be bioprinted with bacteria also shown to survive for at least 2 days post-bioprinting [6]. Schaffner *et al.* also used an extrusion bioprinting approach, developing a custom hydrogel to bioprint *Pseudomonas putida* and *Acetobacter xylinium* [5]. This approach allowed observation of in-situ formation of cellulose by *A. xylinum,* with bacterial viability up to 7 days also observed, demonstrating

biotechnological applications for bioprinted bacteria. Huang *et al*. developed a novel approach, whereby they used illumination and optogenetic manipulation to pattern *Pseudomonas aeruginosa* into controlled shapes with high resolution [7]. Exposure to two optogenetic modules allowed bacteria to be pattered onto 2D surfaces illuminated with red or blue light. Bacterial growth was demonstrated 10 hours after printing, although mature biofilm formation was not demonstrated. This approach was novel in that the requirement for a bioink to achieve 3D patterning of bacteria was removed. However, limitations included an inability to precisely control construct 3D structure, and the requirement for gene manipulation to be performed. Schmieden *et al. also* bioprinted *E.coli* within an alginate hydrogel [8]. Similar to the approach of Lehner *et al.* [6], printing was performed onto a calcium-impregnated surface to trigger alginate cross-linking. Bacteria were also induced to express the CsgA protein after bioprinting, increasing formation of biofilm. However, beyond 7-9 days, bacteria appeared to lose viability. Connell *et al.* adopted a micro-3D printing approach to create *Pseudomonas aeruginosa* aggregates in situ [76]. Micrometer-sized houses constructed using a biocompatible, multiphoton 3D lithography technique were used to confine seeded *P. aeruginosa* bacteria and trigger formation of aggregates of defined size. Scanning electrochemical microscopy (SECM) performed on the aggregates then provided a sensitive, quantitative technique to study the process of quorum sensing (QS) within biofilms.

Compared to previous attempts to bioprint bacteria in the literature, our work provides several potential advantages in relation to future ability to study 3D biofilms. The extended stability and viability of bacteria after bioprinting allowed observation of 3D biofilm formation for several weeks; this far exceeds previous bioprinting attempts where observation of bacterial growth was possible for a maximum of 7-9 days, in structures that did not facilitate the potential to perform antimicrobial testing on 3D biofilms [43, 45, 46]. The stability in culture of the

236

bacterial bioink in our study is therefore significant, as it allows for extended observation of bacterial growth as well as offering the potential to perform antimicrobial studies and further analysis of biofilm formation in 3D. Whilst alginate is amongst the polysaccharides present in the biofilms of *Pseudomonas* and *Azotobacter,* it is not thought to be significantly involved in *Staphylococcus* or *E coli* [77, 78]. This minimised potential for the alginate used as part of our bioink to give a false impression of dense biofilm formation in bacterial studies, particularly given that non-biofilm or alginate specific fluorescent stains were used to monitor bacterial growth and density. The methodology we developed also allowed a range of clinically relevant bacteria to be bioprinted, resulting in significant formation of mature biofilm in all cases. Clinical biofilm infections are most often chronic in nature, may be polymicrobial and develop over a period of weeks and even months; the stability and versatility of our bioprinted constructs may therefore facilitate greater potential to mirror clinical biofilms than currently available biofilm models [17, 37, 58, 79, 80].

By performing alginate hydrogel cross-linking prior to bioprinting, rather than extruding alginate onto a calcium-coated culture surface as performed elsewhere, homogenous hydrogel cross-linking was achieved. In turn, this allowed 3D bioprinting of constructs with larger vertical thicknesses than previously described, with further cross-linking in $BaCl_2$ a novel approach used to ensure enduring construct stability within bacterial culture conditions. A high level of precision was also achieved in relation to controlling biofilm thickness and dimensions, which proved to be a significant asset in studying depth of antimicrobial penetration. The optimised bioprintability of the bioink was also in part attributable to the use of Protanal alginate (Protanal LF 10/60 FT, 89.00 g/mol, FMC Biopolymers Girvan, UK) which has advantages compared to alginates used elsewhere to bioprint bacteria [5, 6, 48, 81]. Protanal has a high-G block content (over 70%) within its structure compared to other alginates, with G-

blocks thought to facilitate rapid crosslinking with cations following bioprinting [82]. Furthermore, it is recognised as having high purity following manufacture; other alginate preparations retain higher levels of potentially pro-inflammatory impurities such as endotoxin and polyphenols following extraction from seaweed [83].

There are some limitations to our findings. Our main method of monitoring bacterial growth and biofilm formation was confocal laser scanning microscopy (CLSM) combined with fluorescent dyes. Standard light microscopes often struggle to image biofilm of more than 3-4 μm thickness as biofilm material above and below the focal plane tend to scatter light and interfere with direct measurement [84]. Contrastingly, CLSM allows optical sectioning of biofilms and, with image analysis, 3D reconstruction is possible [85]. More detailed analysis of biofilm structure could however have been added by performing scanning electron microscopy, perhaps with biofilm specific dyes; this is recognised as being able to provide detailed information regarding biofilm structural characteristics, as well as spatial information regarding biofilm disruption following antimicrobial treatment [11, 22, 59, 65, 70, 86-88]. This would have allowed greater commentary to be provided on the comparative properties of biofilm developed in our experiments relative to that observed to develop in the native environment outwith our bacterial bioink. However, macroscopically there appeared to be a strong resemblance observed, with the biofilm lifecycle observed to occur on CSLM. Throughout experiments, a consistent optical density of bacterial solution was utilised to prepare bioinks. It would therefore be interesting to investigate the rate of biofilm formation that occurs when higher and lower inoculations of bacteria are used to prepare bioinks. Single species of bacteria were included in each bioprinted construct. However, clinical infections and biofilms often involve interaction between multiple bacterial species [11]. It would therefore be of interest to bioprint bioinks containing multiple bacteria and observe related biofilm formation. A degree

238

of hydrogel swelling was also noted to occur following bioprinting in other literature during bacterial culture [5]. It would therefore be of interest to measure construct dimensions during culture and compare this to post-printing results. However, hydrogel swelling did not appear to be a significant issue in terms of altering construct integrity or design, and so we elected not to directly measure constructs to reduce chances of bacterial contamination and construct damage. Measurement of construct dry mass may have helped clarify degradation rates, but biofilm production would also have potentially confounded results.

6.5 **Conclusions**

In summary, our methodology allows for the precise additive manufacturing of bacteria-laden, self-supporting 3D structures that survive extended bacterial culture, allowing formation of mature 3D biofilm. This was achieved by combining the development of a biocompatible hydrogel with optimised cross-linking conditions. This can be applied to bioprint a range of clinically relevant bacteria, which go on to form biofilm with pre-designed 3D dimensions. Furthermore, our methodology allows monitoring of response of 3D biofilms to antimicrobials to be performed. We envision that bioprinted biofilms will provide a versatile platform in future to study processes such a quorum sensing, antimicrobial activity and bacterial interaction in 3D. With rising worldwide antimicrobial resistance, 3D bioprinted biofilms could also become a key weapon to aid the discovery of novel therapeutics targets, as mankind battles to combat ever-evolving microbial defence mechanisms.

7 Chapter 7 –Applying 3D Bioprinted Biofilms to Develop a Novel Method for Identifying Orthopaedic Joint Infection

7.1 Acknowledgement of Collaboration

All aspects of bioprinting were performed by the author. Experimental design and data analysis was performed in collaboration with Evita Ning and Professor Karen Faulds (Centre for Molecular Nanometrology, Department of Pure and Applied Chemistry, Technology and Innovation Centre, University of Strathclyde). SESORRS Chemical functionalisation and instrumentation was performed by Evita Ning.

7.2 Introduction

Joint replacement surgery is considered amongst the most successful medical developments of the last century, with life-enhancing surgery performed on millions of people worldwide each year suffering from diseased or damaged joints [1-9]. The total number of patients with existing arthroplasties in place continues to increase with exponential growth of up to 637% predicted for primary procedures by 2030 [10, 11]. Whilst the majority of joint arthroplasties provide pain-free function, a minority of around 1-2 % of patients will experience the devastating complication of prosthetic joint infection (PJI), defined as infection involving the joint prosthesis and adjacent tissue. With an increasing number of joint replacements being performed worldwide, the number of PJIs continues to increase [12-14].

Management of PJI is directed at removing infection from within the joint and restoring function. This often requires complex treatment strategies including multiple surgical revisions with removal of implants and long-term antimicrobial treatment. This translates into significant morbidity for patients and even risk of mortality in cases where PJI results in systemic infection

or sepsis developing. The economic impact of PJI is also significant, with the cost to treat a single PJI up to 6-fold the cost of the primary implantation [15, 16].

Central to the pathogenesis of PJI is the formation of bacterial biofilm. Biofilms can be defined as 3D structured communities of bacterial cells enclosed in a self- produced polymeric matrix, attached to a solid surface or substratum [17]. Within the protective environment of a biofilm, bacteria increase their resistance to host immune defences and antibiotics up to 1000%, whilst their ability to exchange genetic information is also greatly increased [18, 19]. Bacteria in established biofilms also have low growth rate and can develop resistant subpopulations (so-called "persisters"). Eradication of infection once biofilm has formed is therefore hugely challenging, and often leads to chronic infection, requiring surgical removal of implants, prolonged antimicrobial therapy and can even lead to mortality [20]. A key clinical challenge in manging PJI is therefore identifying infecting bacterial organisms early in the disease process. This allows targeted treatment to begin with appropriate antimicrobials and increases the chances of disrupting mature biofilm formation and thus eradication of infection [21-23].

Rapid diagnosis of infecting organisms within PJI can unfortunately prove challenging in the clinical environment, forcing clinicians to take a "best guess" approach with antibiotics, potentially leading to an increase in antimicrobial tolerance, resistance and treatment failure [24]. Routine blood tests can show signs of infection, however, all lack sufficient sensitivity or specificity to diagnose or exclude PJI, and in the context of recent surgery are often raised due to post-surgery inflammation [21, 25, 26]. Joint aspiration is a more targeted and invasive investigation and allows synovial fluid culture to be performed. However, it can require up to 14 days incubation to detect some low-virulent and difficult-to-detect pathogens [27, 28]. Further techniques such as PCR [29], culture of sonication fluid, radionucleotide imaging [24]

and positron emission tomography (PET) scans [30] have also been utilised; however, limitations include high costs, susceptibility to contamination and exposure to radiation [21, 31, 32]. Furthermore, up to 20% of patients develop culture-negative PJI, even with synovial fluid culture and sampling of periprosthetic tissue, with no bacterial diagnosis reached. This makes elimination of infection and use of appropriate antimicrobials more challenging, and can lead to increased morbidity and mortality for patients [21-23, 33, 34]. Demand for a novel technique to diagnose PJI therefore exists; a cost-effective test that could non-invasively diagnose PJI due to specific bacteria in a rapid and reproducible manner at the bedside or in clinic would represent a major step forward in PJI diagnostics.

One potential novel approach to the diagnosis of PJI is offered by Raman spectroscopy. Raman is capable of probing the chemical composition of materials through barriers and can detect vibrational, rotational, and other states in a molecular system. Raman spectroscopy works by shining a monochromatic light source onto a sample and detecting the scattered light. Most scattered light is at the same frequency as the excitation source; however, a small amount of the scattered light shifts in energy from the laser frequency because of interactions between the incident electromagnetic waves and the vibrational energy levels of the molecules in the sample (Fig. 7.1 A). Plotting the intensity of the shifted light against the frequency produces a Raman spectrum of the sample [35-37]. Unfortunately, very weak signal is generated using conventional Raman spectroscopy as very few incident electromagnetic waves, or photons, undergo a Raman shift. Alternative techniques have been developed to enhance signal, including Surface enhanced Raman spectroscopy (SERS) (Fig. 7.1 B). SERS can generate signal intensities 10^{10} to 10^{11} magnitude greater than conventional Raman, thought to be due to an enhancement in the electrical field that occurs in the presence of roughened and metallic

surfaces, which in turn enhances Raman scattering [38]. SERS has already been applied by by Haisch *et,al.* to perform chemical analysis of a biofilm matrix using SERS-active silver nanoparticles [39]. Spatially offset Raman spectroscopy (SORS) is a technique that allows Raman signals to be obtained at depth by offsetting the point of collection of the scattered light from the laser-illumination (Fig. 7.1 C). SORS relies on the fact that deeper penetrating photons tend to scatter laterally from the illumination zone on the sample surface, whereas photons scattered back to the surface from shallower samples depths have less opportunity to travel laterally. Collecting Raman photons at the sample surface away from the laser illumination zone therefore allows greater detection of signal from deeper zones within a sample [40, 41]. This allows subsurface and surface spectra to be subtracted, which strengthens signal and facilitates highly accurate chemical analysis beneath obscuring barriers [42]. SORS has already been applied to allow penetration depths through 4 mm of soft tissue, allowing transcutaneous characterisation of bone in animal and human cadavers [43, 44]. However, depth penetration capabilities of SORS are limited by the weak Raman scattering signal that comes from measuring at depth, which hampers analysis through tissue in clinical studies.

(A) Raman scattering
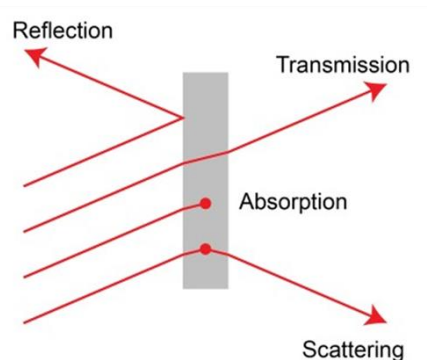
(B) SERS
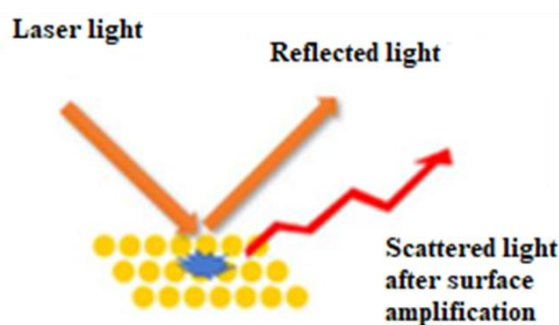
(C) SORs
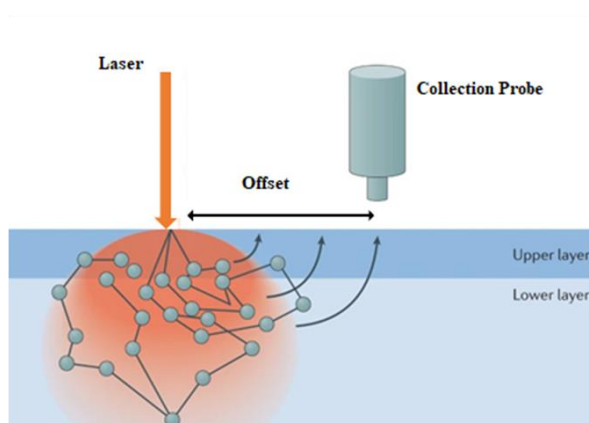
Figure 7.1 Methods of Raman spectroscopy. **(A)** Raman spectroscopy works by shining a monochromatic light source onto a sample and detecting the scattered light. A small amount of scattered light shifts in energy from the laser frequency because of interactions between the incident electromagnetic waves and the vibrational energy levels of the molecules in the sample, undergoing Raman shift. **(B)** Surface enhanced Raman spectroscopy (SERS) can generate signal intensities 10^{10} to 10^{11} magnitude greater than conventional Raman, thought to be due to an enhancement in the electrical field that occurs in the presence of roughened and metallic surfaces, which in turn enhances Raman scattering. **(C)** Spatially offset Raman spectroscopy (SORS) is a technique that allows Raman signals to be obtained at depth by offsetting the point

of collection of the scattered light from the laser-illumination. Deeper penetrating photons tend to scatter laterally from the illumination zone on the sample surface.

In order to maximise Raman capabilities, the combination of surface enhanced Raman scattering with spatially offset Raman spectroscopy (SESORS) has emerged, offering potential to detect clinical infection at depth. Stone *et al*. first applied SESORS to detect gold nanoparticles through depths of up to 50 mm of tissue [42]. Subsequent work demonstrated the use of SESORS for *in vivo* glucose sensing through up to 8 mm of bone [45]. Recent work has also demonstrated SESORS detection of neurochemicals through 3 mm of cat skull [36]. In a further advancement, the technique of spatially offset resonance Raman scattering (SESORRS) has been developed by combining SESORS with resonant reporters; this allowed detection of gold nanoparticles functionalised with resonant Raman reporters through 25 mm of porcine tissue using a handheld SORS instrument [41, 42, 46, 47].

In the following section we combine 3D bioprinted biofilms with animal tissue to create a joint infection model. The potential for gold nanoparticles functionalised with resonant Raman reporters and bacteria-specific DNA-aptamers to detect 3D bioprinted biofilms under depths of tissue using SESORRS is then investigated. To the best of our knowledge, this is the first application of SESORRS to allow the correct identification of specific bacterial species at depths down to 2.1 cm.

7.3 **Results**

7.3.1 **Creation of Aptamer Functionalised Nanoparticles**

To allow SESORRS detection of specific 3D bacterial biofilms at depth, SERS active gold nanoparticles functionalised with resonant chalcogenpyrylium Raman reporter dyes and

bacteria-specific DNA aptamers were first produced by collaborators (Fig. 3.11). Specifically, dye823 and dye815 with absorbance maxima at 823 and 815 nm respectively were chosen, as both dyes can be detected by the handheld SORS instrument (Fig. 3.10). Dye823 was conjugated to MRSA aptamer-functionalised AuNPs (AuNP@MRSA-Apt@dye823), and dye815 conjugated to *E.coli* aptamer-functionalised AuNPs (AuNP@*E.coli*-Apt@dye815).

7.3.2 3D Biofilm Creation

MRSA and E.coli were initially chosen for inclusion in a joint infection model as clinically relevant gram-positive and gram-negative bacteria recognised to frequently cause PJI [48]. Given *in vivo* biofilm formation is 3D in nature, we attempted to replicate this by 3D bioprinting bacteria within a custom bacterial bioink using the methodology initially developed within chapter 5. Briefly, this involved initial creation of a partially cross-linked Protanal alginate hydrogel by mixing Protanal and $CaCl_2$ solution together. Inoculations of selected bacteria were then mixed into the hydrogel to produce a bioink with homogenously distributed bacteria. 3D bioprinting of the bacterial bioink was then performed (Fig. 7.2), with subsequent immersion of constructs in $BaCl_2$ performed to allow secondary ionic cross-linking following bioprinting that increases stability during bacterial culture (Fig. 6.3). This allowed creation of a 10 mm x 10 mm biofilm model that was 1 mm thick, with mature biofilm formation observed on CSLM imaging prior to inclusion in experimental work (Fig. 6.5). The mechanical integrity of the 3D biofilm also allowed for ease of physical movement and manipulation of the biofilm during experiments, which would have been otherwise challenging if using biofilms produced via traditional 2D culture methods. A further finding of crucial importance was that that the bacterial bioink did not overlap with any of the Raman dye spectra and thus interfere with results, or indeed block Raman detection by their presence (Fig. 7.3).
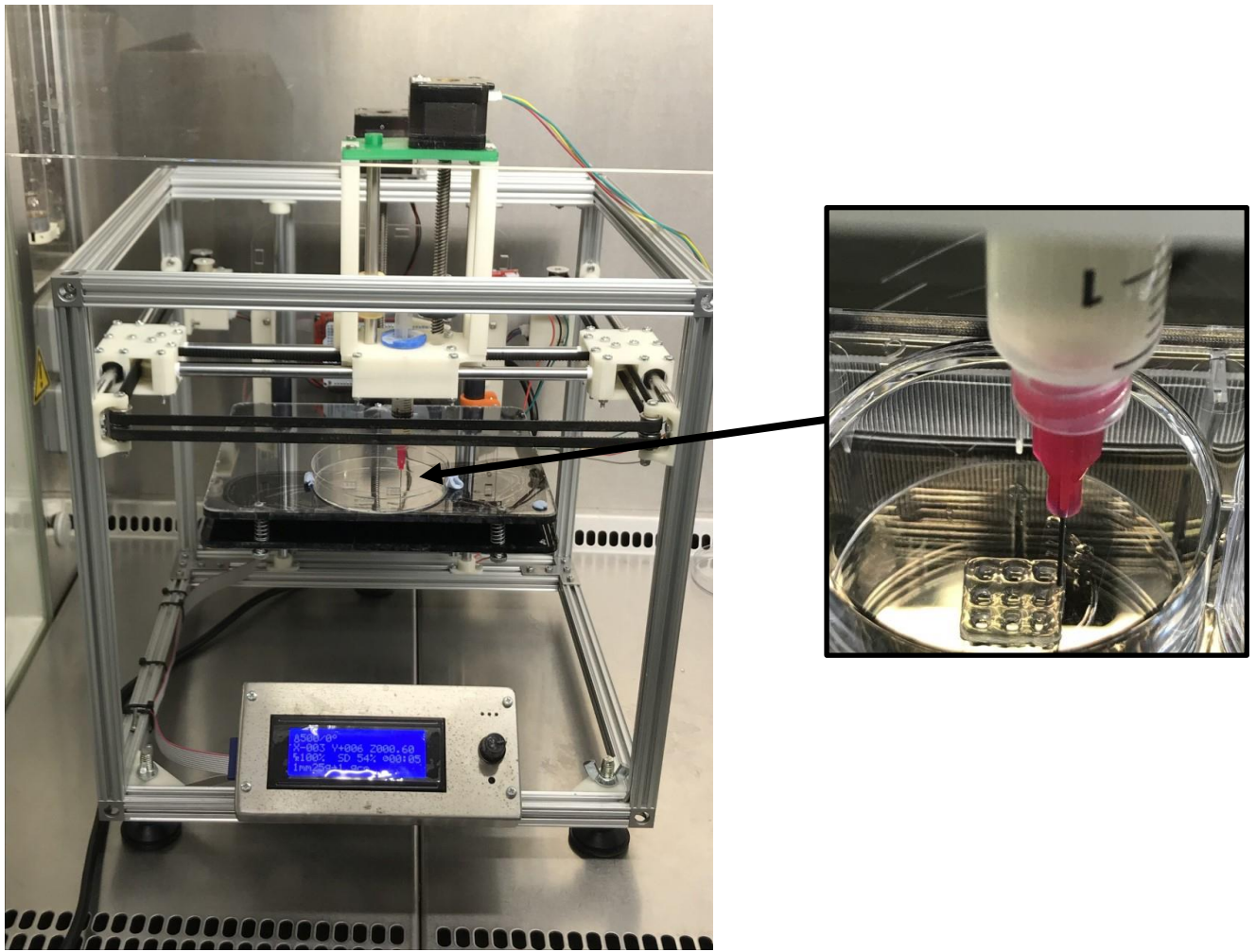
Figure 7.2 3D extrusion bioprinter depositing bacterial bioink to create 3D bacterial scaffolds.

7.3.3 Creation of Joint Infection Model

To replicate the soft and hard tissues found within a native joint, porcine tissues were utilised to create a layered PJI model. 3D bacterial biofilm was placed between porcine bone in the deepest layer and porcine soft tissue in the most superficial layer, thus creating a sandwich-type PJI model (Fig. 3.12).

7.3.4 Sampling Reference Spectra from PJI Model Components and Bacterial Bioink

Initial reference spectra were acquired for each component of the PJI model. It was notable that no overlap occurred between spectra obtained from bone, soft tissue, *E.coli* biofilm or "reference" bioink containing no bacteria. Some overlap was seen to occur between dye815 used in the *E.coli* aptamer conjugates (yellow) and dye823 from MRSA aptamer conjugates (purple) due to the similar structure of both dyes. However, dye815 was seen to exhibit a unique peak at 550 cm^{-1} whilst dye823 had a unique peak at 710 cm^{-1}, allowing for discrimination between the two dyes (Fig. 7.3). The fact that our bioink did not display significant overlap with either dye was crucial, whilst the bioink also did not block Raman spectra from being obtained.
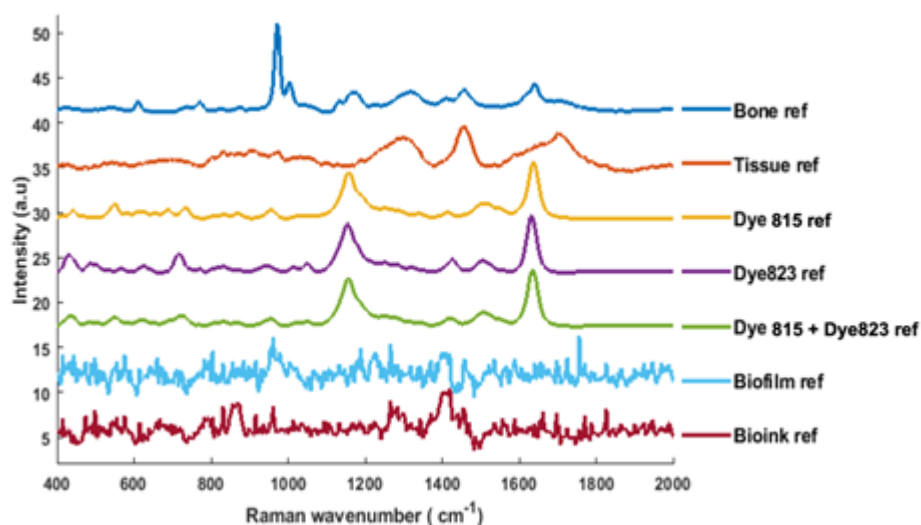
Figure 7.3 Reference spectra of the PJI model components obtained using SORS. Pork bone (dark blue), porcine loin tissue (orange), dye815 (yellow), dye 823 (purple), mixture of dye815 & dye823 (green), 3D bioprinted *E. Coli* biofilm with no aptamers present (light blue) and reference bioink containing no bacteria (red). All measurements were carried out using a 2 s integration time, 5 accumulations and an 830 nm laser excitation wavelength.

7.3.5 Confirming Specificity of Aptamer Functionalised Nanoparticles to Respective Bacterial Species

The binding specificity of aptamer functionalised nanoparticles towards respective bacterial species was then examined by incubating anti-*E.coli* and anti-MRSA aptamer AuNP conjugates with *E.coli* and MRSA biofilm samples overnight. After overnight incubation, unbounded conjugates were removed by washing three times in Hank's balanced salt solution (HBSS) prior to SESORRS measurement. SESORRS spectra were then obtained from each of the biofilm-conjugate combinations. Peaks at 710 cm^{-1}, 1178 cm^{-1} and 1640 cm^{-1} from AuNP@MRSA-Apt@dye823 were only detected when AuNP@MRSA-Apt@dye823 was incubated with MRSA biofilms (Fig. 7.4 A), with no significant peaks evident when incubation was performed with *E.coli* biofilms (Fig 7.4 C), indicating specific binding having occurred between the MRSA biofilm and AuNPs functionalised with MRSA aptamer. Similarly, when AuNP@*E.coli*-Apt@dye815 was incubated with *E.coli* biofilms, a 550 cm^{-1} peak from dye 815 was observed (Fig. 7.4 B), that did not occur when AuNP@*E.coli*-Apt@dye815 was incubated with MRSA biofilms (Fig. 7.4 D). This again suggested specific binding of the *E.coli* aptamers towards *E.coli* biofilm.
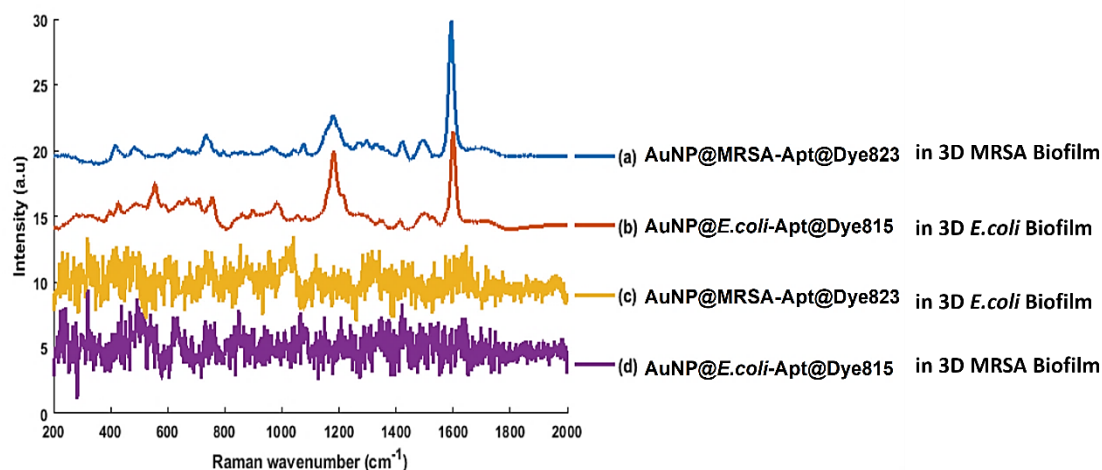
Figure 7.4 SESORRS spectra obtained from an aptamer functionalised gold nanoparticle specificity binding assay against 3D bioprinted biofilms. SESORRS spectra of (a) MRSA aptamer conjugates (AuNP@MRSA-Apt@dye823) added to MRSA biofilm (blue), (b) *E. coli* aptamers conjugates (AuNP@*E.coli*-Apt@dye815) added to *E. coli* biofilm (red), (c) MRSA aptamer conjugates added to *E. coli* biofilm (yellow) and (c) *E. coli* aptamers conjugates added to MRSA biofilm (purple) as control. Peaks at 710 cm^{-1}, 1178 cm^{-1} and 1640 cm^{-1} from AuNP@MRSA-Apt@dye823 were only detected when AuNP@MRSA-Apt@dye823 was incubated with MRSA biofilms (Fig. 6.6 A). Similarly, when AuNP@*E.coli*-Apt@dye815 was incubated with *E.coli* biofilms, a 550 cm^{-1} peak from dye 815 was observed (Fig. 6.6 B), that did not occur when AuNP@*E.coli*-Apt@dye815 was incubated with MRSA biofilms (Fig. 6.6 D). This again suggested specific binding of the *E.coli* aptamers towards *E.coli* biofilm.

7.3.6 **SESORRS Detection of Functionalised Nanoparticle Binding to Biofilms Within PJI Model**

Following successful demonstration of the binding specificity of functionalised nanoparticles against MRSA and *E. coli*, the potential for SESORRS detection of biofilms using

251

functionalised nanoparticles within our PJI model (Fig. 6.4) was examined. Initially *E.coli*-targeting conjugates (AuNP@*E.coli*-Apt@dye815) and MRSA-targeting conjugates (AuNP@MRSA-Apt@dye823) were incubated with *E.coli* biofilms and MRSA biofilms respectively overnight. Unbounded conjugates were again washed away via washing x 3 in HBSS prior to experimentation. MRSA and *E. coli* biofilms exposed to functionalised nanoparticles were then placed in the PJI model. SESORRS spectra from AuNP@MRSA-Apt@dye823 conjugates incubated with MRSA biofilms could be obtained through 18 mm of porcine tissue (Fig. 7.5 A). Intensity of spectra decreased as overlying soft tissue thickness increased, for both peaks at 1178 cm^{-1} (Fig. 7.5 B) and 1640 cm^{-1} (Fig. 7.5 C) associated with AuNP@MRSA-Apt@dye823. SESORRS spectra of AuNP@*E.coli*-Apt@dye815 conjugates incubated with *E.coli* biofilms could be observed through 21 mm of porcine tissue (Figure 7.5 D). Again, spectral intensity declined as overlying soft tissue depth increased (Fig. 7.5 E). Spectra obtained for MRSA and *E.coli* were significantly different to the control bioink constructs, that contained no bacteria, following exposure to the conjugates. This demonstrates that nanoparticles functionalised with specific biorecognition aptamers have the potential to target and detect specific bacterial biofilms at depths of 18-21 mm by SESORRS using a portable handheld SORS instrument.

7.3.7 Relationship Between Biofilm/Nanoparticle Depth and Raman Signal

The relationship between biofilm/nanoparticle depth and detected Raman spectral intensity was examined by comparing the intensity of nanoparticle signal with surface tissue signal. Initial reference spectra collected from soft tissue identified a Raman band at 1460 cm^{-1} (Fig. 7.5 A), the intensity of which should remain the same in our PJI model given the consistent distance maintained between soft tissue surface and SORS device. However, intensity of functionalised

nanoparticle signal was expected to decrease as thickness of soft tissue overlying the biofilm increased. For functionalised nanoparticle AuNP@MRSA-Apt@dye823, the intensity of the most prominent spectral peaks at 1178 cm^{-1} (Fig. 7.5 B) and 1640 cm^{-1} (Fig. 7.5 C) were compared to the soft tissue surface peak at 1460 cm^{-1}. The ratio of Raman band intensities demonstrated an inverse relationship, decreasing significantly as overlying soft tissue thickness increased, until minimal signal from AuNP@MRSA-Apt@dye823 could be detected beyond 18 mm tissue thickness. Similarly, for AuNP@*E.coli*-Apt@dye815dye intensity of the spectral peak at 550 cm^{-1} was compared to the 1460 cm^{-1} tissue peak. An inverse relationship was again found, with decreasing signal detected as overlying soft tissue thickness increased, with signal beyond 21 mm difficult to detect (Fig. 7.5 E). Again, spectra obtained for MRSA and *E.coli* were significantly different to the control bioink constructs, that contained no bacteria, following exposure to the conjugates. Overall, there appeared to be a clear correlation between Raman signal intensity, with signal significantly weakening as depth of tissue increased. However, functionalised nanoparticles were able to facilitate positive detection of MRSA biofilms under up to 18 mm tissue and E. coli biofilms under 21 mm of soft tissue.
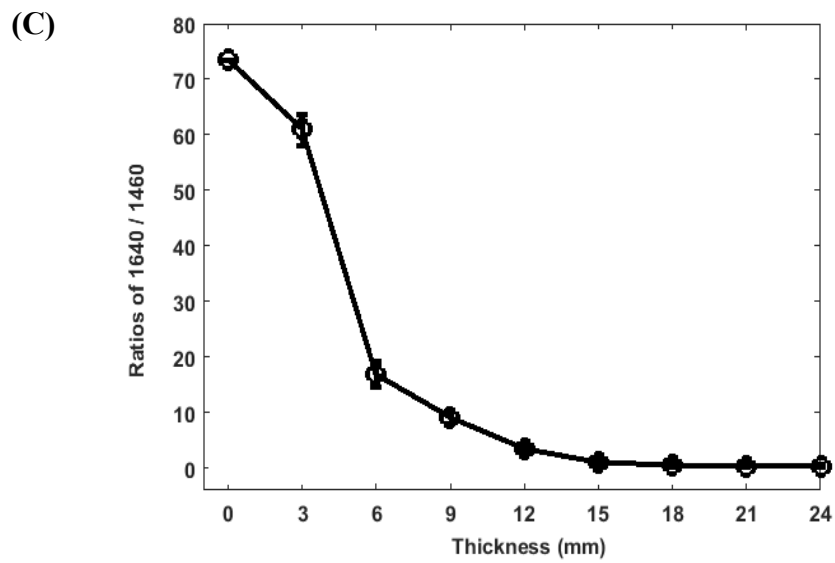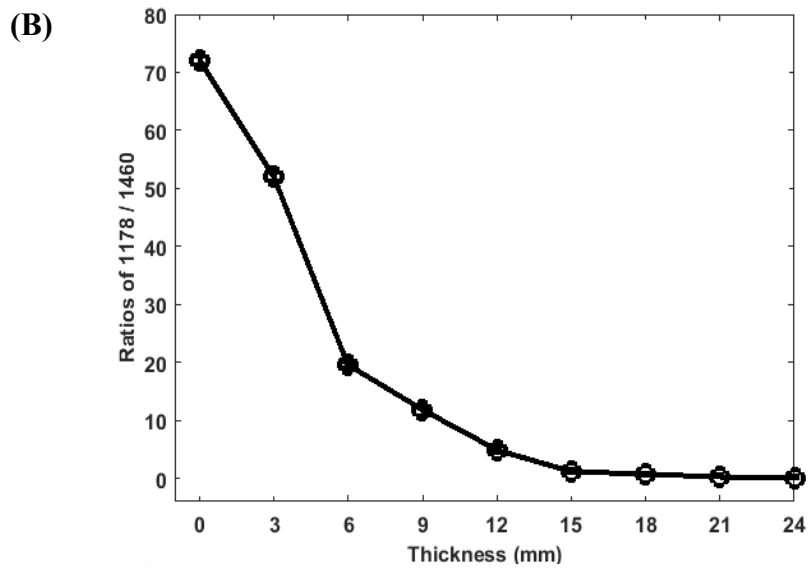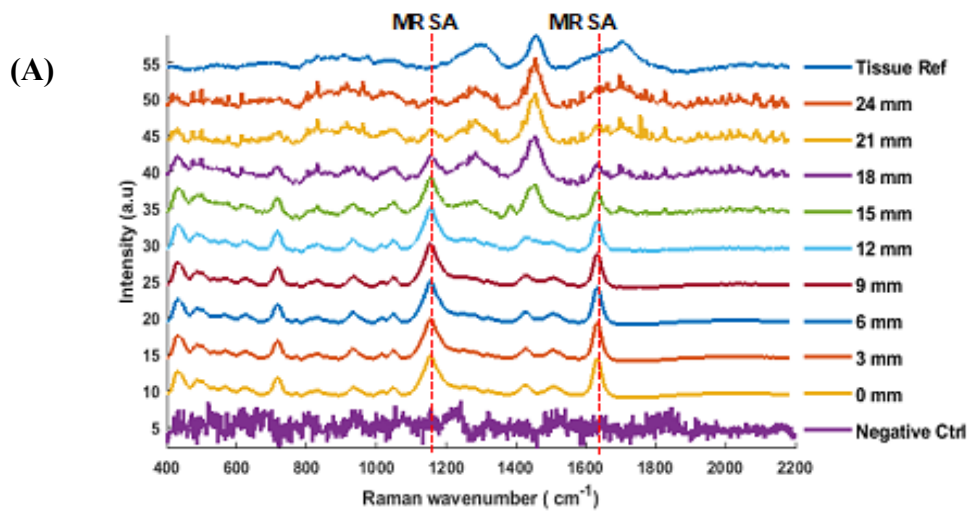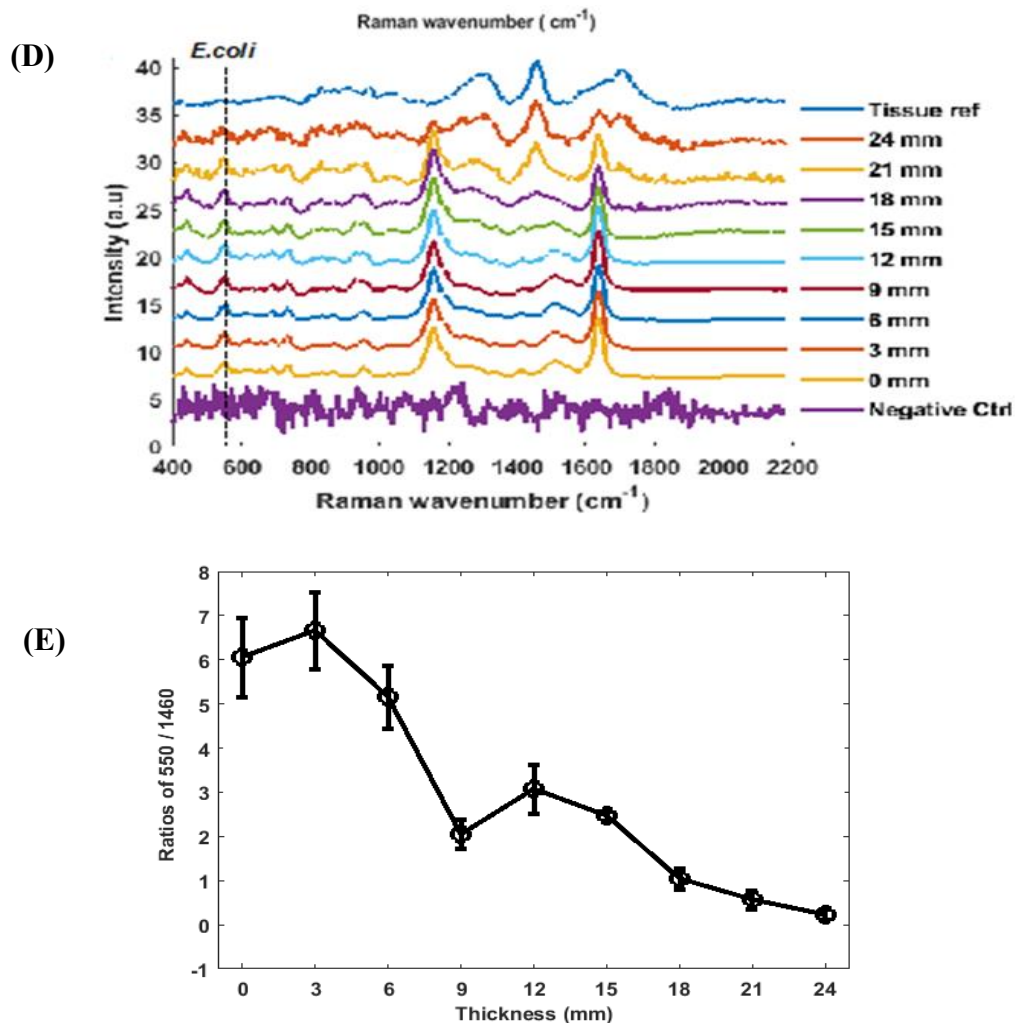
Figure 7.5 SESORRS detection of functionalised nanoparticle binding to biofilms within PJI model. (A) For the functionalised nanoparticle AuNP@MRSA-Apt@dye823, dye peaks at 1178 cm^{-1} and 1640 cm^{-1} (red dotted lines) could be detected through 18 mm of overlying soft tissue. (B) The Raman band intensities ratio of AuNP@MRSA-Apt@dye823 at 1178 cm^{-1} to 1460 cm^{-1} (1178/1460) and (C) 1640 cm^{-1} to 1460 cm^{-1} (1640/1460) decreased as overlying soft tissue thickness increased. (D) The functionalised nanoparticle AuNP@*E.coli*-Apt@dye815 had a dye peak at 550 cm^{-1} that could be detected through 21 mm of porcine tissue. (F) The Raman band intensities ratio of AuNP@*E.coli*-Apt@dye815 at 550 cm^{-1} to 1460 cm^{-1}

255

(550/1460) again decreased as overlying soft tissue thickness increased. Peak intensities were obtained by scanning 3 replicate samples. All measurements were carried out using the same instrument settings.

7.3.8 Detection of Polymicrobial Biofilms

Biofilm infections are often composed of multiple, interacting microbial species. We therefore investigated the detection of 3D bioprinted 1mm thick multi-strain biofilms containing both MRSA and *E. coli*. A mixture of functionalised nanoparticles, AuNP@MRSA-Apt@dye823 (*E.coli*-targeting) and AuNP@*E.coli*-Apt@dye815 (MRSA-targeting) were incubated with the multi-strain biofilm overnight and unbound nanoparticles washed away using HBSS solution. The multi-strain biofilm was then placed on top of bone and buried beneath increasing layers of porcine soft tissue to recreate the PJI model. SESORRS spectra corresponding to functionalised nanoparticles targeted against both MRSA and *E. coli* could be identified through a depth of 15 mm of porcine tissue, with peaks at 1178 cm^{-1} and 1640 cm^{-1} having a greater intensity due to spectral overlap from both dyes (Fig. 7.6 A, blue dotted box). The unique peak from AuNP@MRSA-Apt@dye823 at 710 cm^{-1} (Fig 7.6 A, red dotted line) confirmed the presence of MRSA within the biofilm. The presence of *E.coli* was also detected via the 550 cm^{-1} peak from AuNP@*E.coli*-Apt@dye815 (Fig. 7.6 A, black dotted line).

The relationship between biofilm/nanoparticle depth and detected Raman spectral intensity was again examined by comparing the intensity of nanoparticle signal with surface soft tissue signal. Once again an inverse relationship was found, with decreasing signal detected as overlying soft tissue thickness increased, with signal beyond 15 mm difficult to detect (Fig. 7.6 A). Overall, it appeared that use of SESORRS and targeted AuNPs allowed successful detection of both

E.coli and MRSA strains in a polymicrobial biofilm under a depth of 15 mm of porcine soft tissue.

(B)

(C)
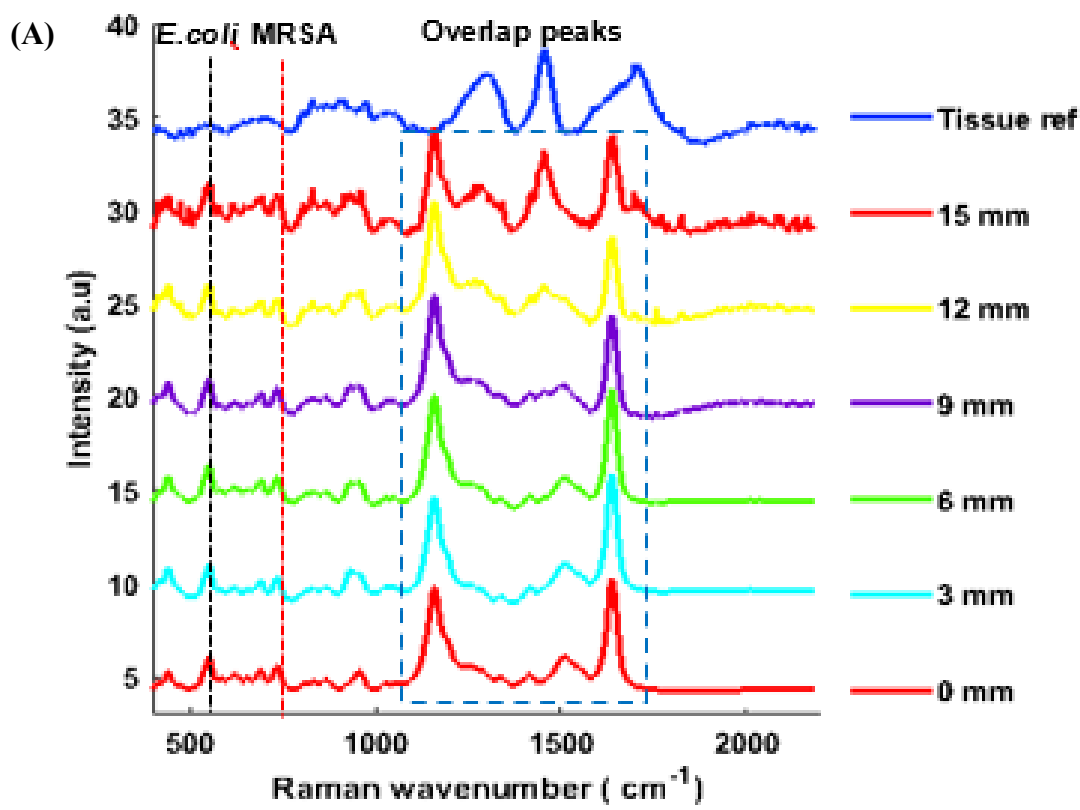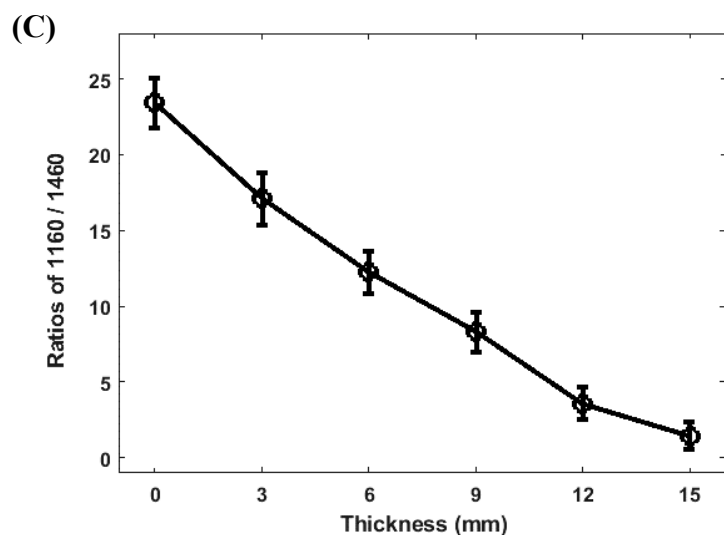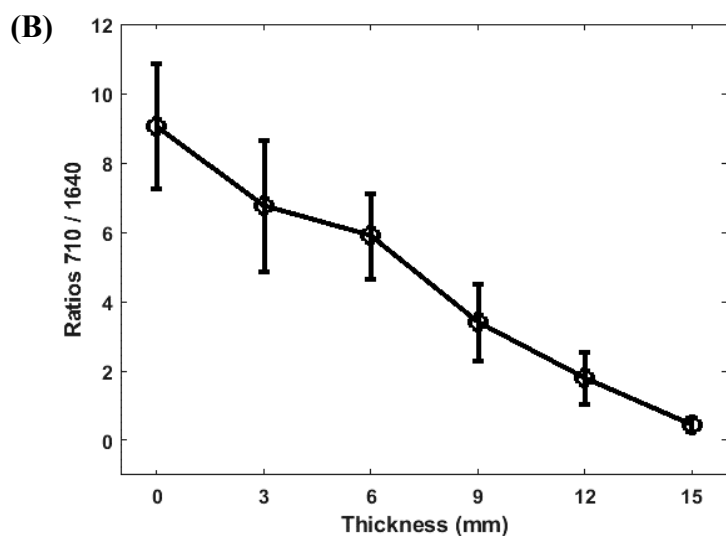
Figure 7.6 Detection of a polymicrobial 3D bioprinted bacterial biofilm using functionalised nanoparticles and SESORRS. (A) A mixture of MRSA and *E.coli* strains were 3D bioprinted to form a multi-strain biofilm and incubated with both AuNP@MRSA-Apt@dye823 and AuNP@*E.coli*-Apt@dye815 overnight prior to SESORRS measurement. A tissue reference spectrum is displayed at the top of the spectra (dark blue). The black dotted line denotes a peak at 550 cm^{-1} corresponding to *E.coli* biofilms bound by AuNP@*E.coli*-Apt@dye815, whilst the

red dotted line corresponds to a 710 cm^{-1} peak unique to MRSA biofilms bound by AuNP@MRSA-Apt@dye823. The blue dotted box shows spectral overlap at 1178 cm^{-1} and 1640 cm^{-1} from detection of both AuNP@MRSA-Apt@dye823 and AuNP@*E.coli*-Apt@dye815 conjugates. The relationship between biofilm/nanoparticle depth under tissue and detected Raman spectral intensity was then examined by comparing the intensity of nanoparticle signal with surface soft tissue signal. The Raman band intensity ratios of anti-MRSA at 710 cm^{-1} (Fig. 7.6 B) and anti-*E. coli* at 550 cm^{-1} (Fig. 7.6 C) against tissue Raman band 1460 cm^{-1} were calculated as thickness of soft tissue overlying the multi-strain biofilm increased. An inverse relationship was found, with decreasing signal detected as overlying soft tissue thickness increased, with signal beyond 15 mm difficult to detect.

7.4 **Discussion**

By utilising 3D biofilms within a joint infection model, we were able to test the application of a novel approach to diagnosing joint infection *in vitro*. To the best of our knowledge, we have successfully demonstrated for the first time the targeted detection of specific bacterial biofilm joint infections under depth of tissue using SESORRS Raman technology. As a potentially non-invasive technology that can generate rapid results, this shows promise for a point of care test that could allow rapid diagnosis at the bedside or in clinic. Early diagnosis of infecting organisms within PJI can be challenging in the current clinical environment, in cases forcing clinicians to take a "best guess" approach with antibiotics until a bacteriological diagnosis is made following extended culture. In the 20% of patients that develop culture-negative PJI, elimination of infection and use of appropriate antimicrobials is even more challenging and can lead to increased morbidity and mortality for patients [21-23, 33, 34]. Furthermore, worldwide

levels of antimicrobial resistance continue to increase, making early use of correct antimicrobial treatment even more critical [49-52]. Demand for a novel and cost-effective test that could non-invasively diagnose PJI due to specific bacteria in a rapid and reproducible manner at the bedside or in clinic would therefore represent a major step forward in PJI diagnostics and allow earlier targeted antimicrobial treatment to begin in patients with infeciton.

The successful development and investigation of SESORRS was aided significantly by the use of 3D bioprinted biofilms. From a practical perspective, having robust 1mm thick biofilms with controlled dimensions (due to bioprinting precision) and stability in culture allowed for much easier physical manipulation of biofilms and also allowed creation of 3D models with precise dimension; using traditional biofilm culture methods to produce much thinner, essentially 2D biofilm structures with limited physical robustness and stability would have limited the scale, repeatability and reliability of our physical model whilst accuracy of biofilm thickness may also have been less certain and harder to control. 3D biofilms may also more closely replicate *in vivo* biofilm infection as embedded bacteria have been shown to have increased metabolic activity, AMR and plasmid stability, more in keeping with that found within the *in vivo* environment compared to bacteria grown in 2D [53, 54].

Despite the promise of our results, there are some areas for development to allow SESORRS to be more widely adopted. Increasing the scalability of the technology is limited in part by the cost and expertise required to develop the functionalised nanoparticles we deployed. One potential solution could be to incorporate the nanoparticles directly into joint implants, so that they are present from the time of joint replacement in the patient. This would require optimisation of the stability of the nanoparticles, and investigation of their impact on implant

performance and longevity. However, it would allow for the non-invasive diagnosis of PJI to be performed at the bedside or in clinic without requirement for further injection or aspiration. This approach could have dual benefits for patients, as functionalised nanoparticles have significant antimicrobial properties, so their inclusion in joint replacement constructs could aid both the prevention and diagnosis of PJI. However, a significant step would have to be overcome in terms of achieving approval for usage of the nanoparticles in humans. Current research in the field of cancer diagnostics using SEOSRS is moving towards human trails, however further work is needed to progress to this stage in musculoskeletal applications [40, 41, 47, 55].

To increase the validity of our results, performing SESORRS in the presence of joint implants instead of just porcine bone would be a logical next step. *In vivo* analysis would also increase the implications of our results. Whilst we were able to detect spectral signal under 2cm of tissue for single bacteria and 1.5cm for polymicrobial biofilms, optimising the technology to allow probing of greater depths of tissue would also make results applicable to a wider range of patients, especially given the rising numbers of patients with obesity and therefore thicker overlying soft tissues worldwide [56]. Making the functionalised nanoparticles less specific to different bacteria could also be of benefit. For example, being able to simply determine whether or not infection in general is present can initially be just as important as determining the presence of specific bacteria, especially in patients presenting with painful loosening of a joint replacement, which may be aseptic or septic in nature [33]. Being able to detect presence of low-level infection, rather than presence of mature biofilm as we have demonstrated, would also be of benefit in patients presenting early in the PJI process. Despite these areas for development, the potential of SESORRS and SORS technology has been

demonstrated for other clinical indications including diagnosis of breast cancer, osteoporosis and analysis of blood content [40, 41, 46, 47, 57]. By combining 3D bioprinted biofilms with animal tissue, we have demonstrated that SESORRS appears to offer great potential for a point-of-care test for PJI that could rapidly diagnose specific bacterial infections, allowing clinicians to begin targeted antimicrobial treatment in patients at an earlier stage.

8 Overall Conclusions and Recommendations for Future Work

The overall aim of this thesis was to utilise a 3D biofabrication approach to study two pressing and interrelated areas within clinical orthopaedics; the regeneration and reconstruction of osteochondral tissue, and the study and treatment of bacterial biofilms that cause infection of joint replacements and native joint destruction.

To attempt the regeneration of osteochondral tissue, key challenges included the identification and optimisation of successful biofabrication techniques, biomaterials and cell sources that could be applied to osteochondral regeneration. Novel composite AlgMA/GelMA and AlgMA/Col bioinks that can be triple-crosslinked, extrusion bioprinted or manually injected into defects were developed. Compared to previously produced bioinks, the novel AlgMA/GelMA composite bioink has some key advantages. The ability to perform rapid, step-wise triple crosslinking allows for high fidelity bioprinting to be achieved, mediated by Ca^{2+} crosslinking and supported by using a FRESH bioprinting approach. A key success was to combine bioprintabiltiy with extended longevity of constructs in culture. This was achieved by fine-tuning AlgMA content, and by combining initial Ca^{2+} crosslinking with both Ba^{2+} ionic crosslinking and UV-mediated covalent crosslinking. This allowed observation of cell growth to be performed for several weeks in intact constructs, which is difficult to achieve and less often combined with the biocompatibility demonstrated using both chondrocytes and MSCs *in vitro* in this research [1-8].

Overall, the composite AlgMA/GelMA bioink appeared to be highly biocompatible and capable of supporting excellent chondrocyte and MSC growth in 3D extrusion-bioprinted scaffolds whilst maintained macroscopic patch-repair of an *in vitro* osteochondral defect model was also

observed, with growth expedited by inclusion of cell spheroids. This is in keeping with a range of studies where excellent growth of MSCs, chondrocytes and other cells has been supported by use of alginate/GelMA bioinks, demonstrating the versatility and biocompatibility of this composite bioink [1, 2, 4-6, 9].

In terms of clinical applications, it is hoped that similar technology could be applied in due course to patch-repair OCDs in patients with biofabricated biological tissue, perhaps delaying or circumventing entirely the need to undergo more extensive joint replacement surgery, particularly in younger patients. The ability to perform 3D bioprinting with high resolution potentially allows biofabricated constructs to be tailored to individual patients and individual defects. The additional option to inject and crosslink the bioink in situ also adds greater flexibility, and could be readily adapted to arthroscopic "key-hole" surgery attempts to repair OCDs. It also offers the potential to treat previously unidentified defects in situ without waiting for bioprinting to be performed during surgery. Whilst this research may offer further evidence for a new approach to treating osteochondral defects in the future, barriers to clinical translation remain. Scaling up bespoke, novel biofabrication platforms such as those used in this thesis to allow treatment of high volumes of patients and large tissue defects remains a challenge. Mironov *et al.* suggest that "It is not sufficient to develop just one robotic device—a bioprinter … [it] will require the development of series of integrated automated robotic devices, or an organ biofabrication line" [10]. To increase the scalability of biofabrication platforms, the bespoke systems often used in current research must therefore be developed towards standardized and integrated systems capable of the high throughput performance required in clinical practice. Ease of deployment of the technology in major teaching hospitals and more rural or local hospitals alike would allow maximum impact in worldwide healthcare systems.

Such systems would allow the sequential development of printed constructs into vascularized living tissue or organs suitable for patient use.

A lack of long-term i*n vivo* studies following implantation of bioprinted cells and constructs into the human body represents a further challenge. It is therefore difficult to properly characterise the risk of implanting biomaterials or cells into a patient; breakdown products could trigger unforeseen immune reactions, as has occurred following some modern hip replacements [11]; furthermore, implanted cells could migrate or dislodge from constructs, causing ectopic tissue growth or teratoma formation depending on cell types used [12]. The long-term *in vivo* performance of many novel biomaterials, assessed by their degradation profiles, tissue integration and biocompatibility remains uncertain [13-15]. An ethical challenge may also arise in future from the cost of implementing biofabrication technology, as wealthy patients could have greater access to the technology, bypassing transplant waiting lists by paying for their 'own' tissue or organs, whilst patients with less resources are forced to wait for donor tissue or undergo alternative procedures such as amputation or dialysis. However, as scalability of the technology is improved, the ethical dilemma of having a "two-tiered" level of access to new tissue and organs may reduce. Furthermore, biomaterials are often animal-derived, which some patients may find disagreeable.

Turning attention to the second aim of this thesis, we sought to biofabricate clinically relevant 3D bacterial biofilms that would allow would further investigation of biofilm growth, biofilm antimicrobial treatment, and testing of a novel method of detection of joint infection to occur. Initially we were able to combine our biofabrication methodology with bacteria to allow extrusion bioprinting of thick structures that formed clinically relevant biofilms with controlled dimensions. This allowed the biofilm life cycle in 3D to be captured and AST in 3D to be

265

performed, with significant differences to AST on corresponding 2D cultures found. To the best of our knowledge, this is the first time the processes involved in mature 3D biofilm formation have been observed *in vitro* in true 3D and following bioprinting [16-19]. Future work could hopefully expand upon this by investigating a wider range of bacterial biofilms. In terms of clinical translation, this potentially would allow investigation of 3D biofilm penetration by antimicrobials in a model that more closely replicates the *in vivo* environment where complex factors such as local immune responses also influence treatment. Analysing the biofilm formation process in 3D in more detail may also allow novel targets to be identified with therapeutic potential for halting biofilm formation. Compared to currently available biofilm models, the physical robustness of our biofilm model in culture also allowed it to be easily applied to create a 3D PJI model. As a result, we were able to use our biofilms to demonstrate the novel application and potential of SESORRS as a point-of-care test that could rapidly diagnose specific bacterial infections, hopefully allowing clinicians to diagnose PJI non-invasively and begin targeted antimicrobial treatment in patients at an earlier stage.

Overall, the field of 3D biofabrication offers an increasingly large number of potential solutions to help ease the treatment burden of cartilage defects, arthritis and PJI thanks to the increasing range of available bioinks, bioprinting techniques, biomaterials and anatomical scaffold designs. As biofabrication platforms become more standardised and increase in scale, it is hoped that increasingly cost effective and reproducible treatment tailored to the individual patient will become possible in future, whilst more solutions to AMR may be offered through the study of 3D biofilms.

9 References

9.1 Chapter 1

[1] Walker-Bone K, Javaid K, Arden N, Cooper C. Regular review: medical management of osteoarthritis. BMJ (Clinical research ed). 2000;321:936-40.

[2] Yu SP, Hunter DJ. Managing osteoarthritis. Australian prescriber. 2015;38:115-9.

[3] 3D Bioprinting: New directions in articular cartilage tissue engineering. ACS Biomaterials Science & Engineering. 2017.

[4] Bae DK, Yoon KH, Song SJ. Cartilage healing after microfracture in osteoarthritic knees. Arthroscopy. 2006;22:367-74.

[5] Bhosale AM, Richardson JB. Articular cartilage: structure, injuries and review of management. British Medical Bulletin. 2008;87:77-95.

[6] Curl WW, Krome J, Gordon ES, Rushing J, Smith BP, Poehling GG. Cartilage injuries: A review of 31,516 knee arthroscopies. Arthroscopy: The Journal of Arthroscopic & Related Surgery. 1997;13:456-60.

[7] van den Borne MPJ, Raijmakers NJH, Vanlauwe J, Victor J, de Jong SN, Bellemans J, et al. International Cartilage Repair Society (ICRS) and Oswestry macroscopic cartilage evaluation scores validated for use in Autologous Chondrocyte Implantation (ACI) and microfracture. Osteoarthritis and Cartilage. 2007;15:1397-402.

[8] Southwood RT, Rice JL, McDonald PJ, Hakendorf PH, Rozenbilds MA. Infection in experimental hip arthroplasties. J Bone Joint Surg Br. 1985;67:229-31.

[9] Tande AJ, Patel R. Prosthetic joint infection. Clinical microbiology reviews. 2014;27:302-45.

[10] Association AO. Australian Orthopaedic Association National Joint Registry Annual Report. Adelaide, Australia: AOA; 2017.

[11] Springer BD, Cahue S, Etkin CD, Lewallen DG, McGrory BJ. Infection burden in total hip and knee arthroplasties: an international registry-based perspective. Arthroplasty Today. 2017;3:137-40.

[12] Bjarnsholt T. The role of bacterial biofilms in chronic infections. APMIS Supplementum. 2013:1-51.

[13] Hengzhuang W, Wu H, Ciofu O, Song Z, Hoiby N. Pharmacokinetics/pharmacodynamics of colistin and imipenem on mucoid and nonmucoid Pseudomonas aeruginosa biofilms. Antimicrobial agents and chemotherapy. 2011;55:4469-74.

[14] Wu H, Moser C, Wang H-Z, Høiby N, Song Z-J. Strategies for combating bacterial biofilm infections. International Journal Of Oral Science. 2014;7:1.

[15] Garrett TR, Bhakoo M, Zhang Z. Bacterial adhesion and biofilms on surfaces. Progress in Natural Science. 2008;18:1049-56.

[16] Wieringa PA, Gonçalves de Pinho AR, Micera S, van Wezel RJA, Moroni L. Biomimetic Architectures for Peripheral Nerve Repair: A Review of Biofabrication Strategies. Advanced Healthcare Materials. 2018;7:1701164.

[17] Sun W, Starly B, Daly AC, Burdick JA, Groll J, Skeldon G, et al. The bioprinting roadmap. Biofabrication. 2020;12:022002.

[18] Willyard C. The drug-resistant bacteria that pose the greatest health threats. Nature. 2017;543:15.

[19] Roberts AE, Kragh KN, Bjarnsholt T, Diggle SP. The Limitations of In Vitro Experimentation in Understanding Biofilms and Chronic Infection. J Mol Biol. 2015;427:3646-61.

[20] Olsen I. Biofilm-specific antibiotic tolerance and resistance. Eur J Clin Microbiol Infect Dis. 2015;34:877-86.

[21] Macia MD, Rojo-Molinero E, Oliver A. Antimicrobial susceptibility testing in biofilm-growing bacteria. Clin Microbiol Infect. 2014;20:981-90.

9.2 **Chapter 2**

[1] Kessler JI, Nikizad H, Shea KG, Jacobs JC, Jr., Bebchuk JD, Weiss JM. The demographics and epidemiology of osteochondritis dissecans of the knee in children and adolescents. Am J Sports Med. 2014;42:320-6.

[2] Sophia Fox AJ, Bedi A, Rodeo SA. The basic science of articular cartilage: structure, composition, and function. Sports Health. 2009;1:461-8.

[3] Ayhan E, Kesmezacar H, Akgun I. Intraarticular injections (corticosteroid, hyaluronic acid, platelet rich plasma) for the knee osteoarthritis. World journal of orthopedics. 2014;5:351-61.

[4] Strauss EJ, Goodrich LR, Chen CT, Hidaka C, Nixon AJ. Biochemical and biomechanical properties of lesion and adjacent articular cartilage after chondral defect repair in an equine model. The American journal of sports medicine. 2005;33:1647-53.

[5] Merkely G, Ackermann J, Lattermann C. Articular Cartilage Defects: Incidence, Diagnosis, and Natural History. Operative Techniques in Sports Medicine. 2018;26:156-61.

[6] Hamilton DF, Howie CR. Knee arthroscopy: influence of systems for delivering healthcare on procedure rates. BMJ : British Medical Journal. 2015;351.

[7] Parvizi J, Nunley RM, Berend KR, Lombardi AV, Jr., Ruh EL, Clohisy JC, et al. High level of residual symptoms in young patients after total knee arthroplasty. Clin Orthop Relat Res. 2014;472:133-7.

[8] Scott CE, Howie CR, MacDonald D, Biant LC. Predicting dissatisfaction following total knee replacement: a prospective study of 1217 patients. J Bone Joint Surg Br. 2010;92:1253-8.

[9] Scott CE, Oliver WM, MacDonald D, Wade FA, Moran M, Breusch SJ. Predicting dissatisfaction following total knee arthroplasty in patients under 55 years of age. The bone & joint journal. 2016;98-b:1625-34.

[10] Registry. NJ. National Joint Registry 14th Annual Report, 2016. .

[11] Burn E, Edwards CJ, Murray DW, Silman A, Cooper C, Arden NK, et al. Trends and determinants of length of stay and hospital reimbursement following knee and hip replacement: evidence from linked primary care and NHS hospital records from 1997 to 2014. BMJ Open. 2018;8.

[12] Haddad FS, Garbuz DS, Chambers GK, Jagpal TJ, Masri BA, Duncan CP. The expectations of patients undergoing revision hip arthroplasty. The Journal of Arthroplasty.16:87-91.

[13] Patel A, Pavlou G, Mujica-Mota RE, Toms AD. The epidemiology of revision total knee and hip arthroplasty in England and Wales: a comparative analysis with projections for the United States. A study using the National Joint Registry dataset. Bone Joint J. 2015;97-b:1076-81.

[14] Postler AE, Beyer F, Wegner T, Lützner J, Hartmann A, Ojodu I, et al. Patient-reported outcomes after revision surgery compared to primary total hip arthroplasty. Hip International. 2017;27:180-6.

[15] Turnbull GS, Scott CEH, MacDonald DJ, Breusch SJ. Gender and Preoperative Function Predict Physical Activity Levels After Revision Total Knee Arthroplasty. J Arthroplasty. 2019;34:939-46.

[16] Turnbull GS, Scott CEH, MacDonald DJ, Breusch SJ. Return to activity following revision total hip arthroplasty. Arch Orthop Trauma Surg. 2019;139:411-21.

[17] Makris EA, Gomoll AH, Malizos KN, Hu JC, Athanasiou KA. Repair and tissue engineering techniques for articular cartilage. Nat Rev Rheumatol. 2015;11:21-34.

[18] Sanchez-Adams J, Leddy HA, McNulty AL, O'Conor CJ, Guilak F. The mechanobiology of articular cartilage: bearing the burden of osteoarthritis. Curr Rheumatol Rep. 2014;16:451.

[19] Chen FH, Rousche KT, Tuan RS. Technology Insight: adult stem cells in cartilage regeneration and tissue engineering. Nat Clin Pract Rheumatol. 2006;2:373-82.

[20] Roughley PJ, Rodriguez E, Lee ER. The interactions of 'non-aggregating' proteoglycans. Osteoarthritis and Cartilage. 1995;3:239-48.

[21] Heinegard DK, Hascall VC. Characteristics of the nonaggregating proteoglycans isolated from bovine nasal cartilage. J Biol Chem. 1979;254:927-34.

[22] Akkiraju H, Nohe A. Role of Chondrocytes in Cartilage Formation, Progression of Osteoarthritis and Cartilage Regeneration. J Dev Biol. 2015;3:177-92.

[23] Muir H. The chondrocyte, architect of cartilage. Biomechanics, structure, function and molecular biology of cartilage matrix macromolecules. Bioessays. 1995;17:1039-48.

[24] Bhosale AM, Richardson JB. Articular cartilage: structure, injuries and review of management. British Medical Bulletin. 2008;87:77-95.

[25] Havelka S, Horn V, Spohrova D, Valouch P. The calcified-noncalcified cartilage interface: the tidemark. Acta Biol Hung. 1984;35:271-9.

[26] Di Bella C, Fosang A, Donati D, Wallace G, Choong P. 3D Bioprinting of Cartilage for Orthopedic Surgeons: Reading between the Lines2015.

[27] von Engelhardt LV, Schmitz A, Burian B, Pennekamp PH, Schild HH, Kraft CN, et al. [3-Tesla MRI vs. arthroscopy for diagnostics of degenerative knee cartilage diseases: preliminary clinical results]. Orthopade. 2008;37:914, 6-22.

[28] Potter HG, Chong le R, Sneag DB. Magnetic resonance imaging of cartilage repair. Sports Med Arthrosc Rev. 2008;16:236-45.

[29] Barber FA. What is the terrible triad? Arthroscopy. 1992;8:19-22.

[30] van den Borne MPJ, Raijmakers NJH, Vanlauwe J, Victor J, de Jong SN, Bellemans J, et al. International Cartilage Repair Society (ICRS) and Oswestry macroscopic cartilage evaluation scores validated for use in Autologous Chondrocyte Implantation (ACI) and microfracture. Osteoarthritis and Cartilage. 2007;15:1397-402.

[31] Steadman JR, Rodkey WG, Singleton SB, Briggs KK. Microfracture technique forfull-thickness chondral defects: Technique and clinical results. Operative Techniques in Orthopaedics. 1997;7:300-4.

[32] Bae DK, Yoon KH, Song SJ. Cartilage healing after microfracture in osteoarthritic knees. Arthroscopy. 2006;22:367-74.

[33] Kreuz PC, Steinwachs MR, Erggelet C, Krause SJ, Konrad G, Uhl M, et al. Results after microfracture of full-thickness chondral defects in different compartments in the knee. Osteoarthritis Cartilage. 2006;14:1119-25.

[34] Goyal D, Keyhani S, Lee EH, Hui JH. Evidence-based status of microfracture technique: a systematic review of level I and II studies. Arthroscopy. 2013;29:1579-88.

[35] Hangody L, Fules P. Autologous osteochondral mosaicplasty for the treatment of full-thickness defects of weight-bearing joints: ten years of experimental and clinical experience. J Bone Joint Surg Am. 2003;85-A Suppl 2:25-32.

[36] Marcacci M, Kon E, Zaffagnini S, Iacono F, Neri MP, Vascellari A, et al. Multiple osteochondral arthroscopic grafting (mosaicplasty) for cartilage defects of the knee: prospective study results at 2-year follow-up. Arthroscopy. 2005;21:462-70.

[37] Robert H. Chondral repair of the knee joint using mosaicplasty. Orthopaedics & Traumatology: Surgery & Research. 2011;97:418-29.

[38] Solheim E, Hegna J, Oyen J, Austgulen OK, Harlem T, Strand T. Osteochondral autografting (mosaicplasty) in articular cartilage defects in the knee: results at 5 to 9 years. Knee. 2010;17:84-7.

[39] Bentley G, Biant LC, Carrington RW, Akmal M, Goldberg A, Williams AM, et al. A prospective, randomised comparison of autologous chondrocyte implantation versus mosaicplasty for osteochondral defects in the knee. J Bone Joint Surg Br. 2003;85:223-30.

[40] Gortz S, Bugbee WD. Allografts in articular cartilage repair. J Bone Joint Surg Am. 2006;88:1374-84.

[41] Saris DB, Vanlauwe J, Victor J, Haspl M, Bohnsack M, Fortems Y, et al. Characterized chondrocyte implantation results in better structural repair when treating symptomatic cartilage defects of the knee in a randomized controlled trial versus microfracture. Am J Sports Med. 2008;36:235-46.

[42] Gooding CR, Bartlett W, Bentley G, Skinner JA, Carrington R, Flanagan A. A prospective, randomised study comparing two techniques of autologous chondrocyte implantation for osteochondral defects in the knee: Periosteum covered versus type I/III collagen covered. Knee. 2006;13:203-10.

[43] Peterson L, Minas T, Brittberg M, Nilsson A, Sjogren-Jansson E, Lindahl A. Two- to 9-year outcome after autologous chondrocyte transplantation of the knee. Clin Orthop Relat Res. 2000:212-34.

[44] Behery OA, Harris JD, Karnes JM, Siston RA, Flanigan DC. Factors influencing the outcome of autologous chondrocyte implantation: a systematic review. J Knee Surg. 2013;26:203-11.

[45] Filardo G, Kon E, Di Martino A, Iacono F, Marcacci M. Arthroscopic second-generation autologous chondrocyte implantation: a prospective 7-year follow-up study. Am J Sports Med. 2011;39:2153-60.

[46] Mistry H, Connock M, Pink J, Shyangdan D, Clar C, Royle P, et al. Autologous chondrocyte implantation in the knee: systematic review and economic evaluation. Health Technol Assess. 2017;21:1-294.

[47] Zeifang F, Oberle D, Nierhoff C, Richter W, Moradi B, Schmitt H. Autologous chondrocyte implantation using the original periosteum-cover technique versus matrix-associated autologous chondrocyte implantation: a randomized clinical trial. Am J Sports Med. 2010;38:924-33.

[48] Brittberg M, Recker D, Ilgenfritz J, Saris DBF. Matrix-Applied Characterized Autologous Cultured Chondrocytes Versus Microfracture: Five-Year Follow-up of a Prospective Randomized Trial. Am J Sports Med. 2018:363546518756976.

[49] Marcacci M, Berruto M, Brocchetta D, Delcogliano A, Ghinelli D, Gobbi A, et al. Articular cartilage engineering with Hyalograft C: 3-year clinical results. Clin Orthop Relat Res. 2005:96-105.

[50] Kon E, Filardo G, Berruto M, Benazzo F, Zanon G, Della Villa S, et al. Articular cartilage treatment in high-level male soccer players: a prospective comparative study of arthroscopic second-generation autologous chondrocyte implantation versus microfracture. Am J Sports Med. 2011;39:2549-57.

[51] Buckwalter JA. Chondral and osteochondral injuries: mechanisms of injury and repair responses. Operative Techniques in Orthopaedics. 1997;7:263-9.

[52] Walker-Bone K, Javaid K, Arden N, Cooper C. Regular review: medical management of osteoarthritis. BMJ (Clinical research ed). 2000;321:936-40.

[53] Yu SP, Hunter DJ. Managing osteoarthritis. Australian prescriber. 2015;38:115-9.

[54] Charnley J. ARTHROPLASTY OF THE HIP: A New Operation. The Lancet. 1961;277:1129-32.

[55] Gunston FH. Polycentric knee arthroplasty. Prosthetic simulation of normal knee movement. J Bone Joint Surg Br. 1971;53:272-7.

[56] Santavirta S, Konttinen YT, Lappalainen R, Anttila A, Goodman SB, Lind M, et al. Materials in total joint replacement. Current Orthopaedics. 1998;12:51-7.

[57] López-López JA, Humphriss RL, Beswick AD, Thom HHZ, Hunt LP, Burston A, et al. Choice of implant combinations in total hip replacement: systematic review and network meta-analysis. BMJ. 2017;359:j4651.

[58] Turnbull GS, Scott CEH, MacDonald DJ, Breusch SJ. Return to activity following revision total hip arthroplasty. Archives of Orthopaedic and Trauma Surgery. 2018.

[59] Scott CE, Bugler KE, Clement ND, MacDonald D, Howie CR, Biant LC. Patient expectations of arthroplasty of the hip and knee. J Bone Joint Surg Br. 2012;94:974-81.

[60] Association AO. Australian Orthopaedic Association National Joint Registry Annual Report. Adelaide, Australia: AOA; 2017.

[61] Kurtz S, Ong K, Lau E, Mowat F, Halpern M. Projections of primary and revision hip and knee arthroplasty in the United States from 2005–2030. J Bone Joint Surg Am. 2007;89.

[62] Zhan C, Kaczmarek R, Loyo-Berrios N, Sangl J, Bright RA. Incidence and short-term outcomes of primary and revision hip replacement in the United States. J Bone Joint Surg Am. 2007;89.

[63] Williams DP, Price AJ, Beard DJ, Hadfield SG, Arden NK, Murray DW, et al. The effects of age on patient-reported outcome measures in total knee replacements. Bone Joint J. 2013;95-b:38-44.

[64] Villanueva-Martınez M, Hernandez-Barrera V, Chana-Rodríguez F, Rojo-Manaute J, Rıos-Luna A, San Roman Montero J, et al. Trends in incidence and outcomes of revision total hip arthroplasty in Spain: A population based study. BMC Musculoskeletal Disorders. 2012;13:37.

[65] Pivec R, Issa K, Kapadia BH, Cherian JJ, Maheshwari AV, Bonutti PM, et al. Incidence and Future Projections of Periprosthetic Femoral Fracture Following Primary Total Hip

Arthroplasty: An Analysis of International Registry Data. J Long Term Eff Med Implants. 2015;25:269-75.

[66] Pedersen AB, Mehnert F, Johnsen SP, Sørensen HT. Risk of revision of a total hip replacement in patients with diabetes mellitus: a population-based follow up study. J Bone Joint Surg Br. 2010;92.

[67] Nichols CI, Vose JG. Clinical Outcomes and Costs Within 90 Days of Primary or Revision Total Joint Arthroplasty. The Journal of Arthroplasty. 2016;31:1400-6.e3.

[68] Jeuken R, Roth A, Peters R, van Donkelaar C, Thies J, van Rhijn L, et al. Polymers in Cartilage Defect Repair of the Knee: Current Status and Future Prospects. Polymers. 2016;8:219.

[69] Siemieniuk RAC, Harris IA, Agoritsas T, Poolman RW, Brignardello-Petersen R, Van de Velde S, et al. Arthroscopic surgery for degenerative knee arthritis and meniscal tears: a clinical practice guideline. BMJ. 2017;357.

[70] Räsänen P, Paavolainen P, Sintonen H, Koivisto AM, Blom M, Ryynänen OP, et al. Effectiveness of hip or knee replacement surgery in terms of quality-adjusted life years and costs. Acta Orthop. 2007;78.

[71] Moroni L, Boland T, Burdick JA, De Maria C, Derby B, Forgacs G, et al. Biofabrication: A Guide to Technology and Terminology. Trends Biotechnol. 2018;36:384-402.

[72] Groll J, Yoo JJ. Special issue on bioinks. Biofabrication. 2018;11:010201.

[73] Groll J, Burdick JA, Cho DW, Derby B, Gelinsky M, Heilshorn SC, et al. A definition of bioinks and their distinction from biomaterial inks. Biofabrication. 2019;11:013001.

[74] Groll J, Boland T, Blunk T, Burdick JA, Cho DW, Dalton PD, et al. Biofabrication: reappraising the definition of an evolving field. Biofabrication. 2016;8:013001.

[75] Zhu N, Chen X. Biofabrication of Tissue Scaffolds. In: Pignatello R, editor. Advances in Biomaterials Science and Biomedical Applications. Rijeka: InTech; 2013. p. Ch. 12.

[76] Hutmacher DW. Scaffolds in tissue engineering bone and cartilage. Biomaterials. 2000;21:2529-43.

[77] Gao C, Deng Y, Feng P, Mao Z, Li P, Yang B, et al. Current progress in bioactive ceramic scaffolds for bone repair and regeneration. Int J Mol Sci. 2014;15:4714-32.

[78] Webber MJ, Khan OF, Sydlik SA, Tang BC, Langer R. A Perspective on the Clinical Translation of Scaffolds for Tissue Engineering. Annals of biomedical engineering. 2015;43:641-56.

[79] Loh QL, Choong C. Three-Dimensional Scaffolds for Tissue Engineering Applications: Role of Porosity and Pore Size. Tissue engineering Part B, Reviews. 2013;19:485-502.

[80] Bose S, Roy M, Bandyopadhyay A. Recent advances in bone tissue engineering scaffolds. Trends in biotechnology. 2012;30:546-54.

[81] Lloyd AW. Interfacial bioengineering to enhance surface biocompatibility. Medical device technology. 2001;13:18-21.

[82] Dong Z, Li Y, Zou Q. Degradation and biocompatibility of porous nano-hydroxyapatite/polyurethane composite scaffold for bone tissue engineering. Applied Surface Science. 2009;255:6087-91.

[83] Mountziaris PM, Mikos AG. Modulation of the Inflammatory Response for Enhanced Bone Tissue Regeneration. Tissue Engineering Part B, Reviews. 2008;14:179-86.

[84] Zhang C, Hu YY, Cui FZ, Zhang SM, Ruan DK. A study on a tissue-engineered bone using rhBMP-2 induced periosteal cells with a porous nano-hydroxyapatite/collagen/poly(L-lactic acid) scaffold. Biomed Mater. 2006;1:56-62.

[85] Hing KA, Best SM, Tanner KE, Bonfield W, Revell PA. Mediation of bone ingrowth in porous hydroxyapatite bone graft substitutes. J Biomed Mater Res A. 2004;68:187-200.

[86] Barrere F, Mahmood T, De Groot K, Van Blitterswijk C. Advanced biomaterials for skeletal tissue regeneration: Instructive and smart functions. Materials Science and Engineering: R: Reports. 2008;59:38-71.

[87] Zeltinger J, Sherwood JK, Graham DA, Mueller R, Griffith LG. Effect of pore size and void fraction on cellular adhesion, proliferation, and matrix deposition. Tissue Eng. 2001;7:557-72.

[88] O'Brien FJ, Harley BA, Yannas IV, Gibson LJ. The effect of pore size on cell adhesion in collagen-GAG scaffolds. Biomaterials. 2005;26:433-41.

[89] Hulbert S, Young F, Mathews R, Klawitter J, Talbert C, Stelling F. Potential of ceramic materials as permanently implantable skeletal prostheses. Journal of biomedical materials research. 1970;4:433-56.

[90] Kuboki Y, Jin Q, Takita H. Geometry of carriers controlling phenotypic expression in BMP-induced osteogenesis and chondrogenesis. J Bone Joint Surg Am. 2001;83-A Suppl 1:S105-15.

[91] Tsuruga E, Takita H, Itoh H, Wakisaka Y, Kuboki Y. Pore size of porous hydroxyapatite as the cell-substratum controls BMP-induced osteogenesis. J Biochem. 1997;121:317-24.

[92] Walthers CM, Nazemi AK, Patel SL, Wu BM, Dunn JC. The effect of scaffold macroporosity on angiogenesis and cell survival in tissue-engineered smooth muscle. Biomaterials. 2014;35:5129-37.

[93] Rouahi M, Gallet O, Champion E, Dentzer J, Hardouin P, Anselme K. Influence of hydroxyapatite microstructure on human bone cell response. J Biomed Mater Res A. 2006;78:222-35.

[94] Rosa AL, Beloti MM, van Noort R. Osteoblastic differentiation of cultured rat bone marrow cells on hydroxyapatite with different surface topography. Dent Mater. 2003;19:768-72.

[95] Habibovic P, Yuan H, van der Valk CM, Meijer G, van Blitterswijk CA, de Groot K. 3D microenvironment as essential element for osteoinduction by biomaterials. Biomaterials. 2005;26:3565-75.

[96] Whang K, Healy KE, Elenz DR, Nam EK, Tsai DC, Thomas CH, et al. Engineering bone regeneration with bioabsorbable scaffolds with novel microarchitecture. Tissue Eng. 1999;5:35-51.

[97] Boccaccio A, Ballini A, Pappalettere C, Tullo D, Cantore S, Desiate A. Finite element method (FEM), mechanobiology and biomimetic scaffolds in bone tissue engineering. Int J Biol Sci. 2011;7:112-32.

[98] Kelly DJ, Prendergast PJ. Prediction of the optimal mechanical properties for a scaffold used in osteochondral defect repair. Tissue Eng. 2006;12:2509-19.

[99] Sandino C, Lacroix D. A dynamical study of the mechanical stimuli and tissue differentiation within a CaP scaffold based on micro-CT finite element models. Biomech Model Mechanobiol. 2011;10:565-76.

[100] Chen G, Dong C, Yang L, Lv Y. 3D Scaffolds with Different Stiffness but the Same Microstructure for Bone Tissue Engineering. ACS Appl Mater Interfaces. 2015;7:15790-802.

[101] Breuls RGM, Jiya TU, Smit TH. Scaffold Stiffness Influences Cell Behavior: Opportunities for Skeletal Tissue Engineering. The Open Orthopaedics Journal. 2008;2:103-9.

[102] Polo-Corrales L, Latorre-Esteves M, Ramirez-Vick JE. Scaffold Design for Bone Regeneration. Journal of nanoscience and nanotechnology. 2014;14:15-56.

[103] Howk D, Chu TM. Design variables for mechanical properties of bone tissue scaffolds. Biomed Sci Instrum. 2006;42:278-83.

[104] Stanton MM, Samitier J, Sanchez S. Bioprinting of 3D hydrogels. Lab Chip. 2015;15:3111-5.

[105] Zhang H-B, Xing T-L, Yin R-X, Shi Y, Yang S-M, Zhang W-J. Three-dimensional bioprinting is not only about cell-laden structures. Chinese Journal of Traumatology. 2016;19:187-92.

[106] Guvendiren M, Molde J, Soares RMD, Kohn J. Designing Biomaterials for 3D Printing. ACS Biomaterials Science & Engineering. 2016;2:1679-93.

[107] Hersel U, Dahmen C, Kessler H. RGD modified polymers: biomaterials for stimulated cell adhesion and beyond. Biomaterials. 2003;24:4385-415.

[108] Baldwin AD, Kiick KL. Polysaccharide-Modified Synthetic Polymeric Biomaterials. Biopolymers. 2010;94:128-40.

[109] Nie T, Baldwin A, Yamaguchi N, Kiick KL. Production of heparin-functionalized hydrogels for the development of responsive and controlled growth factor delivery systems. Journal of Controlled Release. 2007;122:287-96.

[110] Liang Y, Kiick KL. Heparin-functionalized polymeric biomaterials in tissue engineering and drug delivery applications. Acta biomaterialia. 2014;10:1588-600.

[111] Ossipov DA. Bisphosphonate-modified biomaterials for drug delivery and bone tissue engineering. Expert Opin Drug Deliv. 2015;12:1443-58.

[112] Fortier LA, Barker JU, Strauss EJ, McCarrel TM, Cole BJ. The role of growth factors in cartilage repair. Clinical orthopaedics and related research. 2011;469:2706-15.

[113] Wang W, Rigueur D, Lyons KM. TGFβ signaling in cartilage development and maintenance. Birth defects research Part C, Embryo today : reviews. 2014;102:37-51.

[114] Diao H, Wang J, Shen C, Xia S, Guo T, Dong L, et al. Improved cartilage regeneration utilizing mesenchymal stem cells in TGF-beta1 gene-activated scaffolds. Tissue Eng Part A. 2009;15:2687-98.

[115] Finnson KW, Chi Y, Bou-Gharios G, Leask A, Philip A. TGF-b signaling in cartilage homeostasis and osteoarthritis. Front Biosci (Schol Ed). 2012;4:251-68.

[116] Tekari A, Luginbuehl R, Hofstetter W, Egli RJ. Transforming Growth Factor Beta Signaling Is Essential for the Autonomous Formation of Cartilage-Like Tissue by Expanded Chondrocytes. PLOS ONE. 2015;10:e0120857.

[117] Cherian JJ, Parvizi J, Bramlet D, Lee KH, Romness DW, Mont MA. Preliminary results of a phase II randomized study to determine the efficacy and safety of genetically engineered allogeneic human chondrocytes expressing TGF-beta1 in patients with grade 3 chronic degenerative joint disease of the knee. Osteoarthritis Cartilage. 2015;23:2109-18.

[118] Lee MC, Ha CW, Elmallah RK, Cherian JJ, Cho JJ, Kim TW, et al. A placebo-controlled randomised trial to assess the effect of TGF-ss1-expressing chondrocytes in patients with arthritis of the knee. Bone Joint J. 2015;97-b:924-32.

[119] Cao X, Chen D. The BMP signaling and in vivo bone formation. Gene. 2005;357:1-8.

[120] Nishida Y, Knudson CB, Eger W, Kuettner KE, Knudson W. Osteogenic protein 1 stimulates cells-associated matrix assembly by normal human articular chondrocytes: up-regulation of hyaluronan synthase, CD44, and aggrecan. Arthritis Rheum. 2000;43:206-14.

[121] Chubinskaya S, Hakimiyan A, Pacione C, Yanke A, Rappoport L, Aigner T, et al. Synergistic effect of IGF-1 and OP-1 on matrix formation by normal and OA chondrocytes cultured in alginate beads. Osteoarthritis Cartilage. 2007;15:421-30.

[122] Im HJ, Pacione C, Chubinskaya S, Van Wijnen AJ, Sun Y, Loeser RF. Inhibitory effects of insulin-like growth factor-1 and osteogenic protein-1 on fibronectin fragment- and interleukin-1beta-stimulated matrix metalloproteinase-13 expression in human chondrocytes. J Biol Chem. 2003;278:25386-94.

[123] Schmidt MB, Chen EH, Lynch SE. A review of the effects of insulin-like growth factor and platelet derived growth factor on in vivo cartilage healing and repair. Osteoarthritis and Cartilage. 2006;14:403-12.

[124] Jelic M, Pecina M, Haspl M, Kos J, Taylor K, Maticic D, et al. Regeneration of articular cartilage chondral defects by osteogenic protein-1 (bone morphogenetic protein-7) in sheep. Growth Factors. 2001;19:101-13.

[125] Ko EC, Fujihara Y, Ogasawara T, Asawa Y, Nishizawa S, Nagata S, et al. BMP-2 Embedded Atelocollagen Scaffold for Tissue-Engineered Cartilage Cultured in the Medium Containing Insulin and Triiodothyronine—A New Protocol for Three-Dimensional In Vitro Culture of Human Chondrocytes. Tissue Engineering Part C: Methods. 2011;18:374-86.

[126] Reyes R, Delgado A, Solis R, Sanchez E, Hernandez A, San Roman J, et al. Cartilage repair by local delivery of transforming growth factor-beta1 or bone morphogenetic protein-2 from a novel, segmented polyurethane/polylactic-co-glycolic bilayered scaffold. J Biomed Mater Res A. 2014;102:1110-20.

[127] Leblanc E, Trensz F, Haroun S, Drouin G, Bergeron E, Penton CM, et al. BMP-9-induced muscle heterotopic ossification requires changes to the skeletal muscle microenvironment. J Bone Miner Res. 2011;26:1166-77.

[128] Li C, Vepari C, Jin HJ, Kim HJ, Kaplan DL. Electrospun silk-BMP-2 scaffolds for bone tissue engineering. Biomaterials. 2006;27:3115-24.

[129] Nie H, Wang CH. Fabrication and characterization of PLGA/HAp composite scaffolds for delivery of BMP-2 plasmid DNA. J Control Release. 2007;120:111-21.

[130] Shi S, Cheng X, Wang J, Zhang W, Peng L, Zhang Y. RhBMP-2 microspheres-loaded chitosan/collagen scaffold enhanced osseointegration: an experiment in dog. J Biomater Appl. 2009;23:331-46.

[131] Cipitria A, Wagermaier W, Zaslansky P, Schell H, Reichert JC, Fratzl P, et al. BMP delivery complements the guiding effect of scaffold architecture without altering bone microstructure in critical-sized long bone defects: A multiscale analysis. Acta Biomater. 2015;23:282-94.

[132] Schantz JT, Chim H, Whiteman M. Cell guidance in tissue engineering: SDF-1 mediates site-directed homing of mesenchymal stem cells within three-dimensional polycaprolactone scaffolds. Tissue Eng. 2007;13:2615-24.

[133] Wernike E, Montjovent MO, Liu Y, Wismeijer D, Hunziker EB, Siebenrock KA, et al. VEGF incorporated into calcium phosphate ceramics promotes vascularisation and bone formation in vivo. Eur Cell Mater. 2010;19:30-40.

[134] Kaigler D, Wang Z, Horger K, Mooney DJ, Krebsbach PH. VEGF scaffolds enhance angiogenesis and bone regeneration in irradiated osseous defects. J Bone Miner Res. 2006;21:735-44.

[135] Dimitriou R, Tsiridis E, Giannoudis PV. Current concepts of molecular aspects of bone healing. Injury. 2005;36:1392-404.

[136] Salgado AJ, Coutinho OP, Reis RL. Bone tissue engineering: state of the art and future trends. Macromol Biosci. 2004;4:743-65.

[137] Chan BP, Leong KW. Scaffolding in tissue engineering: general approaches and tissue-specific considerations. European Spine Journal. 2008;17:467-79.

[138] Hollister SJ, Maddox RD, Taboas JM. Optimal design and fabrication of scaffolds to mimic tissue properties and satisfy biological constraints. Biomaterials. 2002;23:4095-103.

[139] Johnson T, Bahrampourian R, Patel A, Mequanint K. Fabrication of highly porous tissue-engineering scaffolds using selective spherical porogens. Biomed Mater Eng. 2010;20:107-18.

[140] Liao C-J, Chen C-F, Chen J-H, Chiang S-F, Lin Y-J, Chang K-Y. Fabrication of porous biodegradable polymer scaffolds using a solvent merging/particulate leaching method. Journal of biomedical materials research. 2002;59:676-81.

[141] Mooney DJ, Baldwin DF, Suh NP, Vacanti JP, Langer R. Novel approach to fabricate porous sponges of poly(d,l-lactic-co-glycolic acid) without the use of organic solvents. Biomaterials. 1996;17:1417-22.

[142] Hollister SJ. Porous scaffold design for tissue engineering. Nat Mater. 2005;4:518-24.

[143] Dehghani F, Annabi N. Engineering porous scaffolds using gas-based techniques. Current Opinion in Biotechnology. 2011;22:661-6.

[144] Puppi D, Chiellini F, Piras AM, Chiellini E. Polymeric materials for bone and cartilage repair. Progress in polymer science. 2010;35:403-40.

[145] Whang K, Thomas CH, Healy KE, Nuber G. A novel method to fabricate bioabsorbable scaffolds. Polymer. 1995;36:837-42.

[146] Matthews JA, Wnek GE, Simpson DG, Bowlin GL. Electrospinning of collagen nanofibers. Biomacromolecules. 2002;3:232-8.

[147] Li WJ, Laurencin CT, Caterson EJ, Tuan RS, Ko FK. Electrospun nanofibrous structure: a novel scaffold for tissue engineering. J Biomed Mater Res. 2002;60:613-21.

[148] Huang Y, Han S, Pang X, Ding Q, Yan Y. Electrodeposition of porous hydroxyapatite/calcium silicate composite coating on titanium for biomedical applications. Applied Surface Science. 2013;271:299-302.

[149] Huang Z-M, Zhang YZ, Kotaki M, Ramakrishna S. A review on polymer nanofibers by electrospinning and their applications in nanocomposites. Composites Science and Technology. 2003;63:2223-53.

[150] L J. Primary 3D Printing Processes.

[151] Kim K, Yeatts A, Dean D, Fisher JP. Stereolithographic Bone Scaffold Design Parameters: Osteogenic Differentiation and Signal Expression. Tissue Eng Part B Rev. 2010;16:523-39.

[152] Zein I, Hutmacher DW, Tan KC, Teoh SH. Fused deposition modeling of novel scaffold architectures for tissue engineering applications. Biomaterials. 2002;23:1169-85.

[153] Do A-V, Khorsand B, Geary SM, Salem AK. 3D Printing of Scaffolds for Tissue Regeneration Applications. Advanced healthcare materials. 2015;4:1742-62.

[154] Williams JM, Adewunmi A, Schek RM, Flanagan CL, Krebsbach PH, Feinberg SE, et al. Bone tissue engineering using polycaprolactone scaffolds fabricated via selective laser sintering. Biomaterials. 2005;26:4817-27.

[155] Xia Y, Zhou P, Cheng X, Xie Y, Liang C, Li C, et al. Selective laser sintering fabrication of nano-hydroxyapatite/poly-ε-caprolactone scaffolds for bone tissue engineering applications. International Journal of Nanomedicine. 2013;8:4197-213.

[156] Murphy SV, Atala A. 3D bioprinting of tissues and organs. Nat Biotech. 2014;32:773-85.

[157] Guillemot F, Mironov V, Nakamura M. Bioprinting is coming of age: Report from the International Conference on Bioprinting and Biofabrication in Bordeaux (3B'09). Biofabrication. 2010;2:010201.

[158] Orciani M, Fini M, Di Primio R, Mattioli-Belmonte M. Biofabrication and Bone Tissue Regeneration: Cell Source, Approaches, and Challenges. Frontiers in Bioengineering and Biotechnology. 2017;5.

[159] Frese L, Dijkman PE, Hoerstrup SP. Adipose Tissue-Derived Stem Cells in Regenerative Medicine. Transfusion Medicine and Hemotherapy. 2016;43:268-74.

[160] Hospodiuk M, Dey M, Sosnoski D, Ozbolat IT. The bioink: A comprehensive review on bioprintable materials. Biotechnology Advances. 2017;35:217-39.

[161] Ozbolat IT, Hospodiuk M. Current advances and future perspectives in extrusion-based bioprinting. Biomaterials. 2016;76:321-43.

[162] Petcu EB, Midha R, McColl E, Popa-Wagner A, Chirila TV, Dalton PD. 3D printing strategies for peripheral nerve regeneration. Biofabrication. 2018;10:032001.

[163] Cornelissen D-J, Faulkner-Jones A, Shu W. Current developments in 3D bioprinting for tissue engineering. Current Opinion in Biomedical Engineering. 2017;2:76-82.

[164] Turnbull G, Clarke J, Picard F, Riches P, Jia L, Han F, et al. 3D bioactive composite scaffolds for bone tissue engineering. Bioactive Materials. 2017.

[165] Datta P, Ayan B, Ozbolat IT. Bioprinting for vascular and vascularized tissue biofabrication. Acta Biomater. 2017;51:1-20.

[166] Ventola CL. Medical Applications for 3D Printing: Current and Projected Uses. Pharmacy and Therapeutics. 2014;39:704-11.

[167] Li J, Chen M, Fan X, Zhou H. Recent advances in bioprinting techniques: approaches, applications and future prospects. Journal of Translational Medicine. 2016;14:271.

[168] Tsimbouri PM, Childs PG, Pemberton GD, Yang J, Jayawarna V, Orapiriyakul W, et al. Stimulation of 3D osteogenesis by mesenchymal stem cells using a nanovibrational bioreactor. Nature Biomedical Engineering. 2017;1:758-70.

[169] Murphy SV, Atala A. 3D bioprinting of tissues and organs. Nat Biotechnol. 2014;32:773-85.

[170] Kang H-W, Lee SJ, Ko IK, Kengla C, Yoo JJ, Atala A. A 3D bioprinting system to produce human-scale tissue constructs with structural integrity. Nat Biotech. 2016;34:312-9.

[171] Shafiee A, Atala A. Printing Technologies for Medical Applications. Trends Mol Med. 2016;22:254-65.

[172] Koch L, Deiwick A, Franke A, Schwanke K, Haverich A, Zweigerdt R, et al. Laser bioprinting of human induced pluripotent stem cells—the effect of printing and biomaterials on cell survival, pluripotency, and differentiation. Biofabrication. 2018;10:035005.

[173] Li Q, Lin H, Du Q, Liu K, Wang O, Evans C, et al. Scalable and physiologically relevant microenvironments for human pluripotent stem cell expansion and differentiation. Biofabrication. 2018;10:025006.

[174] Hoffman LM, Carpenter MK. Characterization and culture of human embryonic stem cells. Nat Biotechnol. 2005;23:699-708.

[175] Colnot C. Cell sources for bone tissue engineering: insights from basic science. Tissue Eng Part B Rev. 2011;17:449-57.

[176] Singh VK, Kalsan M, Kumar N, Saini A, Chandra R. Induced pluripotent stem cells: applications in regenerative medicine, disease modeling, and drug discovery. Frontiers in Cell and Developmental Biology. 2015;3.

[177] Bioprinting and Differentiation of Stem Cells. Molecules. 2016;21:1188.

[178] Leeper NJ, Hunter AL, Cooke JP. Stem cell therapy for vascular regeneration: Adult, Embryonic, and Induced Pluripotent Stem Cells. Circulation. 2010;122:517-26.

[179] Ratajczak J, Zuba-Surma E, Paczkowska E, Kucia M, Nowacki P, Ratajczak MZ. Stem cells for neural regeneration--a potential application of very small embryonic-like stem cells. J Physiol Pharmacol. 2011;62:3-12.

[180] Ji H, Kim HS, Kim H-W, Leong KW. Application of induced pluripotent stem cells to model smooth muscle cell function in vascular diseases. Current Opinion in Biomedical Engineering.

[181] Illich DJ, Demir N, Stojkovic M, Scheer M, Rothamel D, Neugebauer J, et al. Concise review: induced pluripotent stem cells and lineage reprogramming: prospects for bone regeneration. Stem Cells. 2011;29:555-63.

[182] Ciuffreda MC, Malpasso G, Musaro P, Turco V, Gnecchi M. Protocols for in vitro Differentiation of Human Mesenchymal Stem Cells into Osteogenic, Chondrogenic and Adipogenic Lineages. Methods Mol Biol. 2016;1416:149-58.

[183] Pittenger MF. Mesenchymal stem cells from adult bone marrow. Methods Mol Biol. 2008;449.

[184] Pittenger MF, Mackay AM, Beck SC, Jaiswal RK, Douglas R, Mosca JD, et al. Multilineage potential of adult human mesenchymal stem cells. Science (New York, NY). 1999;284.

[185] Bertani N, Malatesta P, Volpi G, Sonego P, Perris R. Neurogenic potential of human mesenchymal stem cells revisited: analysis by immunostaining, time-lapse video and microarray. Journal of Cell Science. 2005;118:3925-36.

[186] Huang NF, Li S. Mesenchymal stem cells for vascular regeneration. Regenerative medicine. 2008;3:877-92.

[187] Bunnell BA, Flaat M, Gagliardi C, Patel B, Ripoll C. Adipose-derived Stem Cells: Isolation, Expansion and Differentiation. Methods (San Diego, Calif). 2008;45:115-20.

[188] Gao G, Yonezawa T, Hubbell K, Dai G, Cui X. Inkjet-bioprinted acrylated peptides and PEG hydrogel with human mesenchymal stem cells promote robust bone and cartilage formation with minimal printhead clogging. Biotechnol J. 2015;10:1568-77.

[189] Marco C, Joanna I, Krisztina S, Jakub J, Mariella D, Andrea B, et al. 3D bioprinting of BM-MSCs-loaded ECM biomimetic hydrogels for in vitro neocartilage formation. Biofabrication. 2016;8:035002.

[190] Haishuang L, Qiang L, Yuguo L. Three-dimensional tissues using human pluripotent stem cell spheroids as biofabrication building blocks. Biofabrication. 2017;9:025007.

[191] Otto IA, Levato R, Webb WR, Khan IM, Breugem CC, Malda J. Progenitor cells in auricular cartilage demonstrate cartilage-forming capacity in 3D hydrogel culture. European cells & materials. 2018;35:132-50.

[192] Zhang Y, Khan D, Delling J, Tobiasch E. Mechanisms Underlying the Osteo- and Adipo-Differentiation of Human Mesenchymal Stem Cells. The Scientific World Journal. 2012;2012:793823.

[193] Steinert AF, Ghivizzani SC, Rethwilm A, Tuan RS, Evans CH, Nöth U. Major biological obstacles for persistent cell-based regeneration of articular cartilage. Arthritis Research & Therapy. 2007;9:213.

[194] Roobrouck VD, Ulloa-Montoya F, Verfaillie CM. Self-renewal and differentiation capacity of young and aged stem cells. Experimental Cell Research. 2008;314:1937-44.

[195] Peng L, Jia Z, Yin X, Zhang X, Liu Y, Chen P, et al. Comparative analysis of mesenchymal stem cells from bone marrow, cartilage, and adipose tissue. Stem Cells Dev. 2008;17:761-73.

[196] Lee RH, Kim B, Choi I, Kim H, Choi HS, Suh K, et al. Characterization and expression analysis of mesenchymal stem cells from human bone marrow and adipose tissue. Cell Physiol Biochem. 2004;14:311-24.

[197] Fennema E, Rivron N, Rouwkema J, van Blitterswijk C, de Boer J. Spheroid culture as a tool for creating 3D complex tissues. Trends Biotechnol. 2013;31:108-15.

[198] Lee GH, Lee JS, Lee G-H, Joung WY, Kim SH, Lee SH, et al. Networked concave microwell arrays for constructing 3D cell spheroids. Biofabrication. 2017;10:015001.

[199] Mironov V, Visconti RP, Kasyanov V, Forgacs G, Drake CJ, Markwald RR. Organ printing: tissue spheroids as building blocks. Biomaterials. 2009;30:2164-74.

[200] Zhang K, Yan S, Cui L, Yin J. ASC spheroids formed in poly(L-glutamic acid)/chitosan scaffold to enhance hyaline-like cartilage regeneration. Frontiers in Bioengineering and Biotechnology.

[201] Zhuang P, Sun AX, An J, Chua CK, Chew SY. 3D neural tissue models: From spheroids to bioprinting. Biomaterials. 2018;154:113-33.

[202] Yu Y, Moncal KK, Li J, Peng W, Rivero I, Martin JA, et al. Three-dimensional bioprinting using self-assembling scalable scaffold-free "tissue strands" as a new bioink. Scientific Reports. 2016;6:28714.

[203] Fleming PA, Argraves WS, Gentile C, Neagu A, Forgacs G, Drake CJ. Fusion of uniluminal vascular spheroids: A model for assembly of blood vessels. Developmental Dynamics. 2010;239:spcone-spcone.

[204] Mekhileri NV, Lim KS, Brown GCJ, Mutreja I, Schon BS, Hooper GJ, et al. Automated 3D bioassembly of micro-tissues for biofabrication of hybrid tissue engineered constructs. Biofabrication. 2018;10:024103.

[205] Ahmed EM. Hydrogel: Preparation, characterization, and applications: A review. Journal of Advanced Research. 2015;6:105-21.

[206] Fellah BH, Weiss P, Gauthier O, Rouillon T, Pilet P, Daculsi G, et al. Bone repair using a new injectable self-crosslinkable bone substitute. J Orthop Res. 2006;24:628-35.

[207] Kim J, Kim IS, Cho TH, Lee KB, Hwang SJ, Tae G, et al. Bone regeneration using hyaluronic acid-based hydrogel with bone morphogenic protein-2 and human mesenchymal stem cells. Biomaterials. 2007;28:1830-7.

[208] Chimene D, Lennox KK, Kaunas RR, Gaharwar AK. Advanced Bioinks for 3D Printing: A Materials Science Perspective. Annals of Biomedical Engineering. 2016;44:2090-102.

[209] Tabriz AG, Hermida MA, Leslie NR, Shu W. Three-dimensional bioprinting of complex cell laden alginate hydrogel structures. Biofabrication. 2015;7:045012.

[210] Elise D, Kristin S, Alexandra P, Thomas S. Recombinant spider silk-based bioinks. Biofabrication. 2017;9:044104.

[211] Zongjie W, Zhenlin T, Fredric M, Keekyoung K. Comparative study of gelatin methacrylate hydrogels from different sources for biofabrication applications. Biofabrication. 2017;9:044101.

[212] Nicole D, Louis W, Tylar P, Joseph S, Caroline D, Sonya S, et al. Correlating rheological properties and printability of collagen bioinks: the effects of riboflavin photocrosslinking and pH. Biofabrication. 2017;9:034102.

[213] DeSimone E, Schacht K, Pellert A, Scheibel T. Recombinant spider silk-based bioinks. Biofabrication. 2017;9:044104.

[214] Teng G, Gregory JG, Joshua SC, Anil Kumar PR, Young-Joon S, Anthony A, et al. Optimization of gelatin–alginate composite bioink printability using rheological parameters: a systematic approach. Biofabrication. 2018;10:034106.

[215] Byoung Soo K, Hyeonji K, Ge G, Jinah J, Dong-Woo C. Decellularized extracellular matrix: a step towards the next generation source for bioink manufacturing. Biofabrication. 2017;9:034104.

[216] Onur B, Elena MD-J-P, Christoph M, Davide DA, Jeremy GB, Laura JB, et al. Biofabricated soft network composites for cartilage tissue engineering. Biofabrication. 2017;9:025014.

[217] Elke K, Anne-Kathrin K, Eliane H, Uwe F, Carsten W, Friederike B, et al. StarPEG/heparin-hydrogel based in vivo engineering of stable bizonal cartilage with a calcified bottom layer. Biofabrication. 2019;11:015001.

[218] Liliang O, Rui Y, Yu Z, Wei S. Effect of bioink properties on printability and cell viability for 3D bioplotting of embryonic stem cells. Biofabrication. 2016;8:035020.

[219] Houzhu D, Filippos T, Robert CC. Bioprinting multidimensional constructs: a quantitative approach to understanding printed cell density and redistribution phenomena. Biomedical Physics & Engineering Express. 2017;3:035016.

[220] Cornelissen D-J, Faulkner-Jones A, Shu W. Current developments in 3D bioprinting for tissue engineering. Current Opinion in Biomedical Engineering.

[221] Alakpa Enateri V, Jayawarna V, Lampel A, Burgess Karl V, West Christopher C, Bakker Sanne CJ, et al. Tunable Supramolecular Hydrogels for Selection of Lineage-Guiding Metabolites in Stem Cell Cultures. Chem.1:298-319.

[222] Zhu J, Marchant RE. Design properties of hydrogel tissue-engineering scaffolds. Expert review of medical devices. 2011;8:607-26.

[223] Chen F, Ni Y, Liu B, Zhou T, Yu C, Su Y, et al. Self-crosslinking and injectable hyaluronic acid/RGD-functionalized pectin hydrogel for cartilage tissue engineering. Carbohydrate Polymers. 2017;166:31-44.

[224] Khoon SL, Riccardo L, Pedro FC, Miguel DC, Cesar RA-O, Kim MAvD, et al. Bio-resin for high resolution lithography-based biofabrication of complex cell-laden constructs. Biofabrication. 2018;10:034101.

[225] Ahlfeld T, Cidonio G, Kilian D, Duin S, Akkineni AR, Dawson JI, et al. Development of a clay based bioink for 3D cell printing for skeletal application. Biofabrication. 2017;9:034103.

[226] Annika W, Kirsten B, Günter EMT, Petra JK. Bone matrix production in hydroxyapatite-modified hydrogels suitable for bone bioprinting. Biofabrication. 2017;9:044103.

[227] Yang L, Xulin J, Ling L, Zhi-Nan C, Ge G, Rui Y, et al. 3D printing human induced pluripotent stem cells with novel hydroxypropyl chitin bioink: scalable expansion and uniform aggregation. Biofabrication. 2018;10:044101.

[228] Kim IL, Mauck RL, Burdick JA. Hydrogel design for cartilage tissue engineering: A case study with hyaluronic acid. Biomaterials. 2011;32:8771-82.

[229] Costa RM, Rauf S, Hauser CAE. Towards biologically relevant synthetic designer matrices in 3D bioprinting for tissue engineering and regenerative medicine. Current Opinion in Biomedical Engineering.

[230] Cicha I, Detsch R, Singh R, Reakasame S, Alexiou C, Boccaccini AR. Biofabrication of vessel grafts based on natural hydrogels. Current Opinion in Biomedical Engineering.

[231] Bioprinting of Thermoresponsive Hydrogels for Next Generation Tissue Engineering: A Review. Macromolecular Materials and Engineering. 2017;302:1600266.

[232] Park H, Lee HJ, An H, Lee KY. Alginate hydrogels modified with low molecular weight hyaluronate for cartilage regeneration. Carbohydr Polym. 2017;162:100-7.

[233] Shin J, Choi EJ, Cho JH, Cho AN, Jin Y, Yang K, et al. Three-Dimensional Electroconductive Hyaluronic Acid Hydrogels Incorporated with Carbon Nanotubes and Polypyrrole by Catechol-Mediated Dispersion Enhance Neurogenesis of Human Neural Stem Cells. Biomacromolecules. 2017;18:3060-72.

[234] Holmes AM, Charlton A, Derby B, Ewart L, Scott A, Shu W. Rising to the challenge: applying biofabrication approaches for better drug and chemical product development. Biofabrication. 2017;9:033001.

[235] Alan F-J, Catherine F, Dirk-Jan C, John G, Jason K, Aidan C, et al. Bioprinting of human pluripotent stem cells and their directed differentiation into hepatocyte-like cells for the generation of mini-livers in 3D. Biofabrication. 2015;7:044102.

[236] Faulkner-Jones A, Greenhough S, King JA, Gardner J, Courtney A, Shu W. Development of a valve-based cell printer for the formation of human embryonic stem cell spheroid aggregates. Biofabrication. 2013;5:015013.

[237] Cui X, Boland T, D'Lima DD, Lotz MK. Thermal Inkjet Printing in Tissue Engineering and Regenerative Medicine. Recent patents on drug delivery & formulation. 2012;6:149-55.

[238] Saunders RE, Derby B. Inkjet printing biomaterials for tissue engineering: bioprinting. International Materials Reviews. 2014;59:430-48.

[239] Bose S, Vahabzadeh S, Bandyopadhyay A. Bone tissue engineering using 3D printing. Materials Today. 2013;16:496-504.

[240] Michael S, Sorg H, Peck C-T, Koch L, Deiwick A, Chichkov B, et al. Tissue Engineered Skin Substitutes Created by Laser-Assisted Bioprinting Form Skin-Like Structures in the Dorsal Skin Fold Chamber in Mice. PLOS ONE. 2013;8:e57741.

[241] Koch L, Gruene M, Unger C, Chichkov B. Laser assisted cell printing. Curr Pharm Biotechnol. 2013;14:91-7.

[242] Gurkan UA, El Assal R, Yildiz SE, Sung Y, Trachtenberg AJ, Kuo WP, et al. Engineering Anisotropic Biomimetic Fibrocartilage Microenvironment by Bioprinting

Mesenchymal Stem Cells in Nanoliter Gel Droplets. Molecular Pharmaceutics. 2014;11:2151-9.

[243] Yu Y, Moncal KK, Li J, Peng W, Rivero I, Martin JA, et al. Three-dimensional bioprinting using self-assembling scalable scaffold-free "tissue strands" as a new bioink. 2016;6:28714.

[244] Moroni L, Burdick JA, Highley C, Lee SJ, Morimoto Y, Takeuchi S, et al. Biofabrication strategies for 3D in vitro models and regenerative medicine. Nature Reviews Materials. 2018;3:21-37.

[245] Holzl K, Lin S, Tytgat L, Van Vlierberghe S, Gu L, Ovsianikov A. Bioink properties before, during and after 3D bioprinting. Biofabrication. 2016;8:032002.

[246] Ouyang L, Highley CB, Sun W, Burdick JA. A Generalizable Strategy for the 3D Bioprinting of Hydrogels from Nonviscous Photo-crosslinkable Inks. Advanced Materials. 2017;29:1604983.

[247] Seol Y-J, Lee H, Copus JS, Kang H-W, Cho D-W, Atala A, et al. 3D bioprinted biomask for facial skin reconstruction. Bioprinting. 2018;10:e00028.

[248] Kolesky DB, Homan KA, Skylar-Scott MA, Lewis JA. Three-dimensional bioprinting of thick vascularized tissues. Proceedings of the National Academy of Sciences. 2016;113:3179-84.

[249] Lee JS, Hong JM, Jung JW, Shim JH, Oh JH, Cho DW. 3D printing of composite tissue with complex shape applied to ear regeneration. Biofabrication. 2014;6:024103.

[250] Armstrong JPK, Burke M, Carter BM, Davis SA, Perriman AW. 3D Bioprinting Using a Templated Porous Bioink. Advanced Healthcare Materials. 2016;5:1724-30.

[251] Hinton TJ, Jallerat Q, Palchesko RN, Park JH, Grodzicki MS, Shue H-J, et al. Three-dimensional printing of complex biological structures by freeform reversible embedding of suspended hydrogels. Science Advances. 2015;1.

[252] Yang GH, Lee J, Kim G. The fabrication of uniaxially aligned micro-textured polycaprolactone struts and application for skeletal muscle tissue regeneration. Biofabrication. 2019;11:025005.

[253] Wu S, Peng H, Li X, Streubel PN, Liu Y, Duan B. Effect of scaffold morphology and cell co-culture on tenogenic differentiation of HADMSC on centrifugal melt electrospun poly (L-lactic acid) fibrous meshes. Biofabrication. 2017;9:044106.

[254] Polk S, Sori N, Thayer N, Kemper N, Maghdouri-White Y, Bulysheva AA, et al. Pneumatospinning of collagen microfibers from benign solvents. Biofabrication. 2018;10:045004.

[255] Itoh M, Nakayama K, Noguchi R, Kamohara K, Furukawa K, Uchihashi K, et al. Scaffold-Free Tubular Tissues Created by a Bio-3D Printer Undergo Remodeling and Endothelialization when Implanted in Rat Aortae. PLoS One. 2015;10:e0136681.

[256] Moldovan NI, Hibino N, Nakayama K. Principles of the Kenzan Method for Robotic Cell Spheroid-Based Three-Dimensional Bioprinting. Tissue Engineering Part B: Reviews. 2016;23:237-44.

[257] Norotte C, Marga FS, Niklason LE, Forgacs G. Scaffold-free vascular tissue engineering using bioprinting. Biomaterials. 2009;30:5910-7.

[258] Choi JS, Lee SJ, Christ GJ, Atala A, Yoo JJ. The influence of electrospun aligned poly(epsilon-caprolactone)/collagen nanofiber meshes on the formation of self-aligned skeletal muscle myotubes. Biomaterials. 2008;29:2899-906.

[259] Criscenti G, De Maria C, Longoni A, van Blitterswijk CA, Fernandes HAM, Vozzi G, et al. Soft-molecular imprinted electrospun scaffolds to mimic specific biological tissues. Biofabrication. 2018;10:045005.

[260] Costantini M, Colosi C, Święszkowski W, Barbetta A. Co-axial wet-spinning in 3D bioprinting: state of the art and future perspective of microfluidic integration. Biofabrication. 2018;11:012001.

[261] Liu W, Zhong Z, Hu N, Zhou Y, Maggio L, Miri AK, et al. Coaxial extrusion bioprinting of 3D microfibrous constructs with cell-favorable gelatin methacryloyl microenvironments. Biofabrication. 2018;10:024102.

[262] Zhang Y, Yu Y, Ozbolat IT. Direct Bioprinting of Vessel-Like Tubular Microfluidic Channels. Journal of Nanotechnology in Engineering and Medicine. 2013;4:0210011-7.

[263] Gao Q, He Y, Fu JZ, Liu A, Ma L. Coaxial nozzle-assisted 3D bioprinting with built-in microchannels for nutrients delivery. Biomaterials. 2015;61:203-15.

[264] Jia W, Gungor-Ozkerim PS, Zhang YS, Yue K, Zhu K, Liu W, et al. Direct 3D bioprinting of perfusable vascular constructs using a blend bioink. Biomaterials. 2016;106:58-68.

[265] Lee YB, Lee J-y, Byun H, Ahmad T, Akashi M, Matsusaki M, et al. One-step delivery of a functional multi-layered cell sheet using a thermally expandable hydrogel with controlled presentation of cell adhesive proteins. Biofabrication. 2018;10:025001.

[266] L'heureux N, Pâquet S, Labbé R, Germain L, Auger FA. A completely biological tissue-engineered human blood vessel. The FASEB Journal. 1998;12:47-56.

[267] Egami M, Haraguchi Y, Shimizu T, Yamato M, Okano T. Latest status of the clinical and industrial applications of cell sheet engineering and regenerative medicine. Arch Pharm Res. 2014;37:96-106.

[268] Yang J, Yamato M, Kohno C, Nishimoto A, Sekine H, Fukai F, et al. Cell sheet engineering: recreating tissues without biodegradable scaffolds. Biomaterials. 2005;26:6415-22.

[269] J. HM, Fumiki Y, Yun-Ho J, Jiankang H, N. KN, Hirokazu K, et al. Designer Hydrophilic Regions Regulate Droplet Shape for Controlled Surface Patterning and 3D Microgel Synthesis. Small. 2012;8:393-403.

[270] Fernandez Javier G, Khademhosseini A. Micro-Masonry: Construction of 3D Structures by Microscale Self-Assembly. Advanced Materials. 2010;22:2538-41.

[271] Tasoglu S, Diller E, Guven S, Sitti M, Demirci U. Untethered micro-robotic coding of three-dimensional material composition. Nature Communications. 2014;5:3124.

[272] Baraniak PR, McDevitt TC. Scaffold-free culture of mesenchymal stem cell spheroids in suspension preserves multilineage potential. Cell Tissue Res. 2012;347.

[273] Cheng NC, Wang S, Young TH. The influence of spheroid formation of human adipose-derived stem cells on chitosan films on stemness and differentiation capabilities. Biomaterials. 2012;33.

[274] Mironov V, Kasyanov V, Markwald RR. Organ printing: from bioprinter to organ biofabrication line. Curr Opin Biotechnol. 2011;22:667-73.

[275] Elena AB, Elizaveta VK, Jonathan D, Charlotte H, Frederico DASP, Vladislav AP, et al. Bioprinting of a functional vascularized mouse thyroid gland construct. Biofabrication. 2017;9:034105.

[276] Morimoto Y, Hsiao AY, Takeuchi S. Point-, line-, and plane-shaped cellular constructs for 3D tissue assembly. Advanced Drug Delivery Reviews. 2015;95:29-39.

[277] Pacak CA, Cowan DB. Fabrication of Myogenic Engineered Tissue Constructs. Journal of Visualized Experiments : JoVE. 2009:1137.

[278] Ghanizadeh Tabriz A, Mills CG, Mullins JJ, Davies JA, Shu W. Rapid Fabrication of Cell-Laden Alginate Hydrogel 3D Structures by Micro Dip-Coating. Front Bioeng Biotechnol. 2017;5:13.

[279] Wilkens CA, Rivet CJ, Akentjew TL, Alverio J, Khoury M, Acevedo JP. Layer-by-layer approach for a uniformed fabrication of a cell patterned vessel-like construct. Biofabrication. 2016;9:015001.

[280] Holland I, Logan J, Shi J, McCormick C, Liu D, Shu W. 3D biofabrication for tubular tissue engineering. Bio-Design and Manufacturing. 2018;1:89-100.

[281] Rhee S, Puetzer JL, Mason BN, Reinhart-King CA, Bonassar LJ. 3D Bioprinting of Spatially Heterogeneous Collagen Constructs for Cartilage Tissue Engineering. ACS Biomaterials Science & Engineering. 2016;2:1800-5.

[282] Current Status of Bioinks for Micro-Extrusion-Based 3D Bioprinting. Molecules. 2016;21:685.

[283] Bahcecioglu G, Hasirci N, Bilgen B, Hasirci V. A 3D printed PCL/hydrogel construct with zone-specific biochemical composition mimicking that of the meniscus. Biofabrication. 2019;11:025002.

[284] Kunisch E, Knauf A-K, Hesse E, Freudenberg U, Werner C, Bothe F, et al. StarPEG/heparin-hydrogel based in vivo engineering of stable bizonal cartilage with a calcified bottom layer. Biofabrication. 2018;11:015001.

[285] You F, Chen X, Cooper DML, Chang T, Eames BF. Homogeneous hydroxyapatite/alginate composite hydrogel promotes calcified cartilage matrix deposition with potential for three-dimensional bioprinting. Biofabrication. 2018;11:015015.

[286] Onofrillo C, Duchi S, O'Connell CD, Blanchard R, O'Connor AJ, Scott M, et al. Biofabrication of human articular cartilage: a path towards the development of a clinical treatment. Biofabrication. 2018;10:045006.

[287] Alginate Sulfate–Nanocellulose Bioinks for Cartilage Bioprinting Applications. Annals of Biomedical Engineering. 2017;45:210.

[288] Lee KY, Mooney DJ. Alginate: properties and biomedical applications. Prog Polym Sci. 2012;37:106-26.

[289] Morch YA, Donati I, Strand BL, Skjak-Braek G. Effect of Ca2+, Ba2+, and Sr2+ on alginate microbeads. Biomacromolecules. 2006;7:1471-80.

[290] Moshaverinia A, Chen C, Akiyama K, Ansari S, Xu X, Chee WW, et al. Alginate hydrogel as a promising scaffold for dental-derived stem cells: an in vitro study. Journal of materials science Materials in medicine. 2012;23:3041-51.

[291] Alsberg E, Anderson KW, Albeiruti A, Franceschi RT, Mooney DJ. Cell-interactive alginate hydrogels for bone tissue engineering. Journal of dental research. 2001;80:2025-9.

[292] Lee KY, Mooney DJ. Alginate: properties and biomedical applications. Prog Polym Sci. 2012;37:106-26.

[293] Markstedt K, Mantas A, Tournier I, Martínez Ávila H, Hägg D, Gatenholm P. 3D Bioprinting Human Chondrocytes with Nanocellulose–Alginate Bioink for Cartilage Tissue Engineering Applications. Biomacromolecules. 2015;16:1489-96.

[294] Lou YR, Kanninen L, Kuisma T, Niklander J, Noon LA, Burks D, et al. The use of nanofibrillar cellulose hydrogel as a flexible three-dimensional model to culture human pluripotent stem cells. Stem Cells Dev. 2014;23:380-92.

[295] Park H, Lee KY. Cartilage regeneration using biodegradable oxidized alginate/hyaluronate hydrogels. J Biomed Mater Res A. 2014;102:4519-25.

[296] Davies RL, Kuiper NJ. Regenerative Medicine: A Review of the Evolution of Autologous Chondrocyte Implantation (ACI) Therapy. Bioengineering (Basel). 2019;6.

[297] Bernhardt A, Paul B, Gelinsky M. Biphasic Scaffolds from Marine Collagens for Regeneration of Osteochondral Defects. Marine Drugs. 2018;16:91.

[298] Nguyen T-U, Shojaee M, Bashur CA, Kishore V. Electrochemical fabrication of a biomimetic elastin-containing bi-layered scaffold for vascular tissue engineering. Biofabrication. 2018;11:015007.

[299] Yang X, Lu Z, Wu H, Li W, Zheng L, Zhao J. Collagen-alginate as bioink for three-dimensional (3D) cell printing based cartilage tissue engineering. Mater Sci Eng C Mater Biol Appl. 2018;83:195-201.

[300] Turnbull G, Clarke J, Picard F, Zhang W, Riches P, Li B, et al. 3D biofabrication for soft tissue and cartilage engineering. Medical Engineering & Physics. 2020;82:13-39.

[301] Perdisa F, Filardo G, Sessa A, Busacca M, Zaffagnini S, Marcacci M, et al. One-Step Treatment for Patellar Cartilage Defects With a Cell-Free Osteochondral Scaffold. The American Journal of Sports Medicine.0:0363546517694159.

[302] Grigolo B, Cavallo C, Desando G, Manferdini C, Lisignoli G, Ferrari A, et al. Novel nano-composite biomimetic biomaterial allows chondrogenic and osteogenic differentiation of bone marrow concentrate derived cells. Journal of Materials Science: Materials in Medicine. 2015;26:173.

[303] Choi B, Kim S, Lin B, Wu BM, Lee M. Cartilaginous extracellular matrix-modified chitosan hydrogels for cartilage tissue engineering. ACS Appl Mater Interfaces. 2014;6:20110-21.

[304] Lee JC, Lee SY, Min HJ, Han SA, Jang J, Lee S, et al. Synovium-derived mesenchymal stem cells encapsulated in a novel injectable gel can repair osteochondral defects in a rabbit model. Tissue Eng Part A. 2012;18:2173-86.

[305] Aldana AA, Valente F, Dilley R, Doyle B. Development of 3D bioprinted GelMA-alginate hydrogels with tunable mechanical properties. Bioprinting. 2021;21:e00105.

[306] Yin J, Yan M, Wang Y, Fu J, Suo H. 3D bioprinting of low-concentration cell-laden gelatin methacrylate (GelMA) bioinks with a two-step cross-linking strategy. ACS applied materials & interfaces. 2018;10:6849-57.

[307] Ying G, Jiang N, Yu C, Zhang YS. Three-dimensional bioprinting of gelatin methacryloyl (GelMA). Bio-design and Manufacturing. 2018;1:215-24.

[308] Yue K, Trujillo-de Santiago G, Alvarez MM, Tamayol A, Annabi N, Khademhosseini A. Synthesis, properties, and biomedical applications of gelatin methacryloyl (GelMA) hydrogels. Biomaterials. 2015;73:254-71.

[309] Daly AC, Critchley SE, Rencsok EM, Kelly DJ. A comparison of different bioinks for 3D bioprinting of fibrocartilage and hyaline cartilage. Biofabrication. 2016;8:045002.

[310] Costantini M, Idaszek J, Szöke K, Jaroszewicz J, Dentini M, Barbetta A, et al. 3D bioprinting of BM-MSCs-loaded ECM biomimetic hydrogels forin vitroneocartilage formation. Biofabrication. 2016;8:035002.

[311] Ansari S, Pouraghaei Sevari S, Chen C, Sarrion P, Moshaverinia A. RGD-Modified Alginate–GelMA Hydrogel Sheet Containing Gingival Mesenchymal Stem Cells: A Unique Platform for Wound Healing and Soft Tissue Regeneration. ACS Biomaterials Science & Engineering. 2021.

[312] Seyedmahmoud R, Çelebi-Saltik B, Barros N, Nasiri R, Banton E, Shamloo A, et al. Three-Dimensional Bioprinting of Functional Skeletal Muscle Tissue Using GelatinMethacryloyl-Alginate Bioinks. Micromachines. 2019;10.

[313] Levato R, Webb WR, Otto IA, Mensinga A, Zhang Y, van Rijen M, et al. The bio in the ink: cartilage regeneration with bioprintable hydrogels and articular cartilage-derived progenitor cells. Acta biomaterialia. 2017;61:41-53.

[314] Vijayavenkataraman S, Thaharah S, Zhang S, Lu WF, Fuh JYH. Electrohydrodynamic jet 3D-printed PCL/PAA conductive scaffolds with tunable biodegradability as nerve guide conduits (NGCs) for peripheral nerve injury repair. Materials & Design. 2019;162:171-84.

[315] Simone S, Thomas B, Naomi P, Sarah B, Riccardo L, Verena S, et al. Double printing of hyaluronic acid/poly(glycidol) hybrid hydrogels with poly(ε -caprolactone) for MSC chondrogenesis. Biofabrication. 2017;9:044108.

[316] Tyler KM, Morgan B, Young-Joon S, Hyun-Wook K, Sang Jin L, James JY, et al. A 3D bioprinted complex structure for engineering the muscle–tendon unit. Biofabrication. 2015;7:035003.

[317] Kim MS, Kim G. Three-dimensional electrospun polycaprolactone (PCL)/alginate hybrid composite scaffolds. Carbohydr Polym. 2014;114:213-21.

[318] Woodruff MA, Hutmacher DW. The return of a forgotten polymer—Polycaprolactone in the 21st century. Progress in Polymer Science. 2010;35:1217-56.

[319] Yao Q, Cosme JG, Xu T, Miszuk JM, Picciani PH, Fong H, et al. Three dimensional electrospun PCL/PLA blend nanofibrous scaffolds with significantly improved stem cells osteogenic differentiation and cranial bone formation. Biomaterials. 2017;115:115-27.

[320] Gonçalves EM, Oliveira FJ, Silva RF, Neto MA, Fernandes MH, Amaral M, et al. Three-dimensional printed PCL-hydroxyapatite scaffolds filled with CNTs for bone cell growth stimulation. Journal of Biomedical Materials Research Part B: Applied Biomaterials. 2016;104:1210-9.

[321] Kim YB, Kim GH. PCL/Alginate Composite Scaffolds for Hard Tissue Engineering: Fabrication, Characterization, and Cellular Activities. ACS Combinatorial Science. 2015;17:87-99.

[322] Cheng Y-L, Chen Y-W, Wang K, Shie M-Y. Enhanced adhesion and differentiation of human mesenchymal stem cell inside apatite-mineralized/poly(dopamine)-coated poly(?-caprolactone) scaffolds by stereolithography. Journal of Materials Chemistry B. 2016;4:6307-15.

[323] Wang W, Caetano G, Ambler WS, Blaker JJ, Frade MA, Mandal P, et al. Enhancing the Hydrophilicity and Cell Attachment of 3D Printed PCL/Graphene Scaffolds for Bone Tissue Engineering. Materials. 2016;9:992.

[324] Fu S, Ni P, Wang B, Chu B, Zheng L, Luo F, et al. Injectable and thermo-sensitive PEG-PCL-PEG copolymer/collagen/n-HA hydrogel composite for guided bone regeneration. Biomaterials. 2012;33:4801-9.

[325] Park JS, Kim J-M, Lee SJ, Lee SG, Jeong Y-K, Kim SE, et al. Surface hydrolysis of fibrous poly(ε-caprolactone) scaffolds for enhanced osteoblast adhesion and proliferation. Macromolecular Research. 2007;15:424-9.

[326] Shim JH, Jang KM, Hahn SK, Park JY, Jung H, Oh K, et al. Three-dimensional bioprinting of multilayered constructs containing human mesenchymal stromal cells for osteochondral tissue regeneration in the rabbit knee joint. Biofabrication. 2016;8:014102.

[327] Visser J, Melchels FPW, Jeon JE, van Bussel EM, Kimpton LS, Byrne HM, et al. Reinforcement of hydrogels using three-dimensionally printed microfibres. Nature Communications. 2015;6:6933.

[328] Castro NJ, O'Brien J, Zhang LG. Integrating biologically inspired nanomaterials and table-top stereolithography for 3D printed biomimetic osteochondral scaffolds. Nanoscale. 2015;7:14010-22.

[329] Khanarian NT, Jiang J, Wan LQ, Mow VC, Lu HH. A Hydrogel-Mineral Composite Scaffold for Osteochondral Interface Tissue Engineering. Tissue Engineering Part A. 2012;18:533-45.

[330] Spalazzi JP, Dagher E, Doty SB, Guo XE, Rodeo SA, Lu HH. In vivo evaluation of a multiphased scaffold designed for orthopaedic interface tissue engineering and soft tissue-to-bone integration. Journal of biomedical materials research Part A. 2008;86:1-12.

[331] Vladislav AP, Elizaveta VK, Elena AB, Pavel AK, Frederico DASP, Nikita EN, et al. Scaffold-free, label-free and nozzle-free biofabrication technology using magnetic levitational assembly. Biofabrication. 2018;10:034104.

[332] Jin R, Moreira Teixeira LS, Dijkstra PJ, Karperien M, van Blitterswijk CA, Zhong ZY, et al. Injectable chitosan-based hydrogels for cartilage tissue engineering. Biomaterials. 2009;30:2544-51.

[333] Tan H, Li H, Rubin JP, Marra KG. Controlled Gelation and Degradation Rates of Injectable Hyaluronic Acid-based Hydrogels through a Double Crosslinking Strategy. Journal of tissue engineering and regenerative medicine. 2011;5:790-7.

[334] Wei Y, Hu Y, Hao W, Han Y, Meng G, Zhang D, et al. A novel injectable scaffold for cartilage tissue engineering using adipose-derived adult stem cells. J Orthop Res. 2008;26:27-33.

[335] Li Y, Tian H, Chen X. Hyaluronic acid based injectable hydrogels for localized and sustained gene delivery. J Control Release. 2015;213:e140-1.

[336] Ji X, Yang W, Wang T, Mao C, Guo L, Xiao J, et al. Coaxially electrospun core/shell structured poly(L-lactide) acid/chitosan nanofibers for potential drug carrier in tissue engineering. J Biomed Nanotechnol. 2013;9:1672-8.

[337] Sargeant TD, Desai AP, Banerjee S, Agawu A, Stopek JB. An in situ forming collagen-PEG hydrogel for tissue regeneration. Acta Biomater. 2012;8:124-32.

[338] Fathi A, Mithieux SM, Wei H, Chrzanowski W, Valtchev P, Weiss AS, et al. Elastin based cell-laden injectable hydrogels with tunable gelation, mechanical and biodegradation properties. Biomaterials. 2014;35:5425-35.

[339] Bidarra SJ, Barrias CC, Granja PL. Injectable alginate hydrogels for cell delivery in tissue engineering. Acta Biomater. 2014;10:1646-62.

[340] Ren K, He C, Xiao C, Li G, Chen X. Injectable glycopolypeptide hydrogels as biomimetic scaffolds for cartilage tissue engineering. Biomaterials. 2015;51:238-49.

[341] Radhakrishnan J, Subramanian A, Krishnan UM, Sethuraman S. Injectable and 3D Bioprinted Polysaccharide Hydrogels: From Cartilage to Osteochondral Tissue Engineering. Biomacromolecules. 2017;18:1-26.

[342] Jin R, Moreira Teixeira LS, Krouwels A, Dijkstra PJ, van Blitterswijk CA, Karperien M, et al. Synthesis and characterization of hyaluronic acid-poly(ethylene glycol) hydrogels via Michael addition: An injectable biomaterial for cartilage repair. Acta Biomater. 2010;6:1968-77.

[343] Yan S, Wang T, Feng L, Zhu J, Zhang K, Chen X, et al. Injectable in situ self-cross-linking hydrogels based on poly(L-glutamic acid) and alginate for cartilage tissue engineering. Biomacromolecules. 2014;15:4495-508.

[344] Ehlers EM, Behrens P, Wunsch L, Kuhnel W, Russlies M. Effects of hyaluronic acid on the morphology and proliferation of human chondrocytes in primary cell culture. Ann Anat. 2001;183:13-7.

[345] Aibe K, Ryu J, Sano S. Effects of hyaluronic acid on cartilage metabolism in free chondrocytes. Journal of Orthopaedic Science. 1996;1:268-76.

[346] Patti AM, Gabriele A, Vulcano A, Ramieri MT, Della Rocca C. Effect of hyaluronic acid on human chondrocyte cell lines from articular cartilage. Tissue Cell. 2001;33:294-300.

[347] Akmal M, Singh A, Anand A, Kesani A, Aslam N, Goodship A, et al. The effects of hyaluronic acid on articular chondrocytes. Journal of Bone & Joint Surgery, British Volume. 2005;87-B:1143-9.

[348] Petta D, Armiento AR, Grijpma D, Alini M, Eglin D, D'Este M. 3D bioprinting of a hyaluronan bioink through enzymatic-and visible light-crosslinking. Biofabrication. 2018;10:044104.

[349] Hua Q, Knudson CB, Knudson W. Internalization of hyaluronan by chondrocytes occurs via receptor-mediated endocytosis. J Cell Sci. 1993;106 (Pt 1):365-75.

[350] Ishida O, Tanaka Y, Morimoto I, Takigawa M, Eto S. Chondrocytes are regulated by cellular adhesion through CD44 and hyaluronic acid pathway. J Bone Miner Res. 1997;12:1657-63.

[351] Hyaluronan receptor-directed assembly of chondrocyte pericellular matrix. The Journal of Cell Biology. 1993;120:825-34.

[352] Park H, Choi B, Hu J, Lee M. Injectable chitosan hyaluronic acid hydrogels for cartilage tissue engineering. Acta Biomater. 2013;9:4779-86.

[353] Bacakova L, Novotna K, Parizek M. Polysaccharides as cell carriers for tissue engineering: the use of cellulose in vascular wall reconstruction. Physiol Res. 2014;63 Suppl 1:S29-47.

[354] Munarin F, Guerreiro SG, Grellier MA, Tanzi MC, Barbosa MA, Petrini P, et al. Pectin-based injectable biomaterials for bone tissue engineering. Biomacromolecules. 2011;12:568-77.

[355] Yu F, Cao X, Li Y, Zeng L, Yuan B, Chen X. An injectable hyaluronic acid/PEG hydrogel for cartilage tissue engineering formed by integrating enzymatic crosslinking and Diels-Alder "click chemistry". Polymer Chemistry. 2014;5:1082-90.

[356] Guo Y, Yuan T, Xiao Z, Tang P, Xiao Y, Fan Y, et al. Hydrogels of collagen/chondroitin sulfate/hyaluronan interpenetrating polymer network for cartilage tissue engineering. J Mater Sci Mater Med. 2012;23:2267-79.

[357] Fan C, Wang D-A. A biodegradable PEG-based micro-cavitary hydrogel as scaffold for cartilage tissue engineering. European Polymer Journal. 2015;72:651-60.

[358] Hwang Y, Sangaj N, Varghese S. Interconnected macroporous poly(ethylene glycol) cryogels as a cell scaffold for cartilage tissue engineering. Tissue Eng Part A. 2010;16:3033-41.

[359] Lee WK, Ichi T, Ooya T, Yamamoto T, Katoh M, Yui N. Novel poly(ethylene glycol) scaffolds crosslinked by hydrolyzable polyrotaxane for cartilage tissue engineering. J Biomed Mater Res A. 2003;67:1087-92.

[360] Dubbini A, Censi R, Butini ME, Sabbieti MG, Agas D, Vermonden T, et al. Injectable hyaluronic acid/PEG-p(HPMAm-lac)-based hydrogels dually cross-linked by thermal gelling and Michael addition. European Polymer Journal. 2015;72:423-37.

[361] Delanois RE, Mistry JB, Gwam CU, Mohamed NS, Choksi US, Mont MA. Current Epidemiology of Revision Total Knee Arthroplasty in the United States. The Journal of Arthroplasty. 2017;32:2663-8.

[362] Welsink CL, Lambers KTA, van Deurzen DFP, Eygendaal D, van den Bekerom MPJ. Total Elbow Arthroplasty: A Systematic Review. JBJS Rev. 2017;5:e4.

[363] Adkinson JM, Chung KC. Advances in small joint arthroplasty of the hand. Plastic and reconstructive surgery. 2014;134:1260-8.

[364] Cowie JG, Turnbull GS, Ker AM, Breusch SJ. Return to work and sports after total hip replacement. Arch Orthop Trauma Surg. 2013;133:695-700.

[365] Kurtz S, Ong K, Lau E, Mowat F, Halpern M. Projections of primary and revision hip and knee arthroplasty in the United States from 2005 to 2030. The Journal of bone and joint surgery American volume. 2007;89:780-5.

[366] Kurtz S, Mowat F, Ong K, Chan N, Lau E, Halpern M. Prevalence of primary and revision total hip and knee arthroplasty in the United States from 1990 through 2002. J Bone Joint Surg Am. 2005;87.

[367] Shahi N, Arosemena M, Kwon J, DiMuzio P, Abai B, Salvatore DM. A rare case of Clostridium septicum aortitis with colon adenocarcinoma. J Vasc Surg Cases Innov Tech. 2018;4:87-90.

[368] Aggarwal VK, Rasouli MR, Parvizi J. Periprosthetic joint infection: Current concept. Indian J Orthop. 2013;47:10-7.

[369] Zmistowski B, Karam JA, Durinka JB, Casper DS, Parvizi J. Periprosthetic joint infection increases the risk of one-year mortality. J Bone Joint Surg Am. 2013;95:2177-84.

[370] Peel TN, Dowsey MM, Buising KL, Liew D, Choong PF. Cost analysis of debridement and retention for management of prosthetic joint infection. Clin Microbiol Infect. 2013;19:181-6.

[371] Klouche S, Sariali E, Mamoudy P. Total hip arthroplasty revision due to infection: a cost analysis approach. Orthop Traumatol Surg Res. 2010;96.

[372] Tande AJ, Patel R. Prosthetic joint infection. Clinical microbiology reviews. 2014;27:302-45.

[373] Murdoch DR, Roberts SA, Fowler VG, Jr., Shah MA, Taylor SL, Morris AJ, et al. Infection of orthopedic prostheses after Staphylococcus aureus bacteremia. Clin Infect Dis. 2001;32:647-9.

[374] Fowler VG, Jr., Olsen MK, Corey GR, Woods CW, Cabell CH, Reller LB, et al. Clinical identifiers of complicated Staphylococcus aureus bacteremia. Arch Intern Med. 2003;163:2066-72.

[375] Ghanem GA, Boktour M, Warneke C, Pham-Williams T, Kassis C, Bahna P, et al. Catheter-related Staphylococcus aureus bacteremia in cancer patients: high rate of complications with therapeutic implications. Medicine (Baltimore). 2007;86:54-60.

[376] Lautenschlager S, Herzog C, Zimmerli W. Course and outcome of bacteremia due to Staphylococcus aureus: evaluation of different clinical case definitions. Clin Infect Dis. 1993;16:567-73.

[377] Azeredo J, Azevedo NF, Briandet R, Cerca N, Coenye T, Costa AR, et al. Critical review on biofilm methods. Critical Reviews in Microbiology. 2017;43:313-51.

[378] Bjarnsholt T. The role of bacterial biofilms in chronic infections. APMIS Supplementum. 2013:1-51.

[379] Bjarnsholt T, Alhede M, Alhede M, Eickhardt-Sorensen SR, Moser C, Kuhl M, et al. The in vivo biofilm. Trends Microbiol. 2013;21:466-74.

[380] Jamal M, Ahmad W, Andleeb S, Jalil F, Imran M, Nawaz MA, et al. Bacterial biofilm and associated infections. Journal of the Chinese Medical Association. 2018;81:7-11.

[381] Hoiby N, Ciofu O, Bjarnsholt T. Pseudomonas aeruginosa biofilms in cystic fibrosis. Future microbiology. 2010;5:1663-74.

[382] Hengzhuang W, Wu H, Ciofu O, Song Z, Hoiby N. Pharmacokinetics/pharmacodynamics of colistin and imipenem on mucoid and nonmucoid Pseudomonas aeruginosa biofilms. Antimicrobial agents and chemotherapy. 2011;55:4469-74.

[383] Wu H, Moser C, Wang H-Z, Høiby N, Song Z-J. Strategies for combating bacterial biofilm infections. International Journal Of Oral Science. 2014;7:1.

[384] Garrett TR, Bhakoo M, Zhang Z. Bacterial adhesion and biofilms on surfaces. Progress in Natural Science. 2008;18:1049-56.

[385] Izakovicova P, Borens O, Trampuz A. Periprosthetic joint infection: current concepts and outlook. EFORT Open Reviews. 2019;4:482-94.

[386] Parsek MR, Singh PK. Bacterial biofilms: an emerging link to disease pathogenesis. Annual review of microbiology. 2003;57:677-701.

[387] Bodelon G, Montes-Garcia V, Lopez-Puente V, Hill EH, Hamon C, Sanz-Ortiz MN, et al. Detection and imaging of quorum sensing in Pseudomonas aeruginosa biofilm communities by surface-enhanced resonance Raman scattering. Nature materials. 2016;15:1203-11.

[388] Rutherford ST, Bassler BL. Bacterial Quorum Sensing: Its Role in Virulence and Possibilities for Its Control. Cold Spring Harbor Perspectives in Medicine. 2012;2:a012427.

[389] Baselga R, Albizu I, Amorena B. Staphylococcus aureus capsule and slime as virulence factors in ruminant mastitis. A review. Veterinary Microbiology. 1994;39:195-204.

[390] Stoodley P, Ehrlich GD, Sedghizadeh PP, Hall-Stoodley L, Baratz ME, Altman DT, et al. Orthopaedic biofilm infections. Current orthopaedic practice. 2011;22:558-63.

[391] Berbari E, Mabry T, Tsaras G, Spangehl M, Erwin PJ, Murad MH, et al. Inflammatory blood laboratory levels as markers of prosthetic joint infection: a systematic review and meta-analysis. J Bone Joint Surg Am. 2010;92:2102-9.

[392] Shahi A, Tan TL, Kheir MM, Tan DD, Parvizi J. Diagnosing Periprosthetic Joint Infection: And the Winner Is? J Arthroplasty. 2017;32:S232-s5.

[393] Trampuz A, Hanssen AD, Osmon DR, Mandrekar J, Steckelberg JM, Patel R. Synovial fluid leukocyte count and differential for the diagnosis of prosthetic knee infection. Am J Med. 2004;117:556-62.

[394] Morgenstern C, Cabric S, Perka C, Trampuz A, Renz N. Synovial fluid multiplex PCR is superior to culture for detection of low-virulent pathogens causing periprosthetic joint infection. Diagnostic microbiology and infectious disease. 2018;90:115-9.

[395] Stirling P, Tahir M, Atkinson HD. The Limitations of Gram-stain Microscopy of Synovial Fluid in Concomitant Septic and Crystal Arthritis. Curr Rheumatol Rev. 2018;14:255-7.

[396] Goswami K, Parvizi J, Maxwell Courtney P. Current Recommendations for the Diagnosis of Acute and Chronic PJI for Hip and Knee-Cell Counts, Alpha-Defensin, Leukocyte Esterase, Next-generation Sequencing. Current reviews in musculoskeletal medicine. 2018;11:428-38.

[397] Nodzo SR, Bauer T, Pottinger PS, Garrigues GE, Bedair H, Deirmengian CA, et al. Conventional diagnostic challenges in periprosthetic joint infection. J Am Acad Orthop Surg. 2015;23 Suppl:S18-25.

[398] Parvizi J, Zmistowski B, Berbari EF, Bauer TW, Springer BD, Della Valle CJ, et al. New definition for periprosthetic joint infection: from the Workgroup of the Musculoskeletal Infection Society. Clin Orthop Relat Res. 2011;469:2992-4.

[399] Portillo ME, Salvado M, Trampuz A, Siverio A, Alier A, Sorli L, et al. Improved diagnosis of orthopedic implant-associated infection by inoculation of sonication fluid into blood culture bottles. J Clin Microbiol. 2015;53:1622-7.

[400] Trampuz A, Piper KE, Jacobson MJ, Hanssen AD, Unni KK, Osmon DR, et al. Sonication of removed hip and knee prostheses for diagnosis of infection. N Engl J Med. 2007;357:654-63.

[401] Parvizi J, Jacovides C, Antoci V, Ghanem E. Diagnosis of periprosthetic joint infection: the utility of a simple yet unappreciated enzyme. J Bone Joint Surg Am. 2011;93:2242-8.

[402] Wetters NG, Berend KR, Lombardi AV, Morris MJ, Tucker TL, Della Valle CJ. Leukocyte esterase reagent strips for the rapid diagnosis of periprosthetic joint infection. J Arthroplasty. 2012;27:8-11.

[403] Tigges S, Stiles RG, Roberson JR. Appearance of septic hip prostheses on plain radiographs. AJR American journal of roentgenology. 1994;163:377-80.

[404] Rosenthall L, Lepanto L, Raymond F. Radiophosphate uptake in asymptomatic knee arthroplasty. J Nucl Med. 1987;28:1546-9.

[405] Abad CL, Haleem A. Prosthetic Joint Infections: an Update. Current Infectious Disease Reports. 2018;20:15.

[406] Li C, Renz N, Trampuz A. Management of Periprosthetic Joint Infection. Hip & pelvis. 2018;30:138-46.

[407] Springer BD, Cahue S, Etkin CD, Lewallen DG, McGrory BJ. Infection burden in total hip and knee arthroplasties: an international registry-based perspective. Arthroplasty Today. 2017;3:137-40.

[408] Bodelón G, Montes-García V, López-Puente V, Hill EH, Hamon C, Sanz-Ortiz MN, et al. Detection and imaging of quorum sensing in Pseudomonas aeruginosa biofilm communities by surface-enhanced resonance Raman scattering. Nature Materials. 2016;15:1203.

[409] Gieroba B, Krysa M, Wojtowicz K, Wiater A, Pleszczyńska M, Tomczyk M, et al. The FT-IR and Raman Spectroscopies as Tools for Biofilm Characterization Created by Cariogenic Streptococci. Int J Mol Sci. 2020;21.

[410] Kusić D, Rösch P, Popp J. Fast label-free detection of Legionella spp. in biofilms by applying immunomagnetic beads and Raman spectroscopy. Systematic and applied microbiology. 2016;39:132-40.

[411] Olubiyi OI, Lu F-K, Calligaris D, Jolesz FA, Agar NY. Chapter 17 - Advances in Molecular Imaging for Surgery. In: Golby AJ, editor. Image-Guided Neurosurgery. Boston: Academic Press; 2015. p. 407-39.

[412] Moody AS, Baghernejad PC, Webb KR, Sharma B. Surface Enhanced Spatially Offset Raman Spectroscopy Detection of Neurochemicals Through the Skull. Analytical Chemistry. 2017;89:5689-93.

[413] Huang Z, McWilliams A, Lui H, McLean DI, Lam S, Zeng H. Near-infrared Raman spectroscopy for optical diagnosis of lung cancer. International journal of cancer. 2003;107:1047-52.

[414] McMahon JM, Henry AI, Wustholz KL, Natan MJ, Freeman RG, Van Duyne RP, et al. Gold nanoparticle dimer plasmonics: finite element method calculations of the electromagnetic enhancement to surface-enhanced Raman spectroscopy. Analytical and Bioanalytical Chemistry. 2009;394:1819-25.

[415] Nicolson F, Jamieson LE, Mabbott S, Shand NC, Graham D, Faulds K. Through barrier detection of ethanol using handheld Raman spectroscopy—Conventional Raman versus spatially offset Raman spectroscopy (SORS). Journal of Raman Spectroscopy. 2017;48:1828-38.

[416] Matousek P. Deep non-invasive Raman spectroscopy of living tissue and powders. Chemical Society Reviews. 2007;36:1292-304.

[417] Nicolson F, Jamieson LE, Mabbott S, Plakas K, Shand NC, Detty MR, et al. Through tissue imaging of a live breast cancer tumour model using handheld surface enhanced spatially offset resonance Raman spectroscopy (SESORRS). Chemical Science. 2018;9:3788-92.

[418] Ivleva NP, Wagner M, Horn H, Niessner R, Haisch C. In Situ Surface-Enhanced Raman Scattering Analysis of Biofilm. Analytical Chemistry. 2008;80:8538-44.

[419] Stone N, Kerssens M, Lloyd GR, Faulds K, Graham D, Matousek P. Surface enhanced spatially offset Raman spectroscopic (SESORS) imaging – the next dimension. Chemical Science. 2011;2:776-80.

9.3 **Chapter 3**

[1] Dahlmann J, Kensah G, Kempf H, Skvorc D, Gawol A, Elliott DA, et al. The use of agarose microwells for scalable embryoid body formation and cardiac differentiation of human and murine pluripotent stem cells. Biomaterials. 2013;34:2463-71.

[2] Hinton TJ, Jallerat Q, Palchesko RN, Park JH, Grodzicki MS, Shue H-J, et al. Three-dimensional printing of complex biological structures by freeform reversible embedding of suspended hydrogels. Science Advances. 2015;1.

[3] Armstrong JPK, Burke M, Carter BM, Davis SA, Perriman AW. 3D Bioprinting Using a Templated Porous Bioink. Advanced Healthcare Materials. 2016;5:1724-30.

[4] Khattak SF, Bhatia SR, Roberts SC. Pluronic F127 as a cell encapsulation material: utilization of membrane-stabilizing agents. Tissue Eng. 2005;11:974-83.

[5] Lee SY, Tae G, Kim YH. Thermal gellation and photo-polymerization of di-acrylated Pluronic F 127. J Biomater Sci Polym Ed. 2007;18:1335-53.

[6] Kolesky DB, Homan KA, Skylar-Scott MA, Lewis JA. Three-dimensional bioprinting of thick vascularized tissues. Proceedings of the National Academy of Sciences. 2016;113:3179-84.

[7] Smeds KA, Pfister-Serres A, Miki D, Dastgheib K, Inoue M, Hatchell DL, et al. Photocrosslinkable polysaccharides for in situ hydrogel formation. J Biomed Mater Res. 2001;54:115-21.

[8] Li Q, Williams CG, Sun DDN, Wang J, Leong K, Elisseeff JH. Photocrosslinkable polysaccharides based on chondroitin sulfate. Journal of Biomedical Materials Research Part A. 2004;68A:28-33.

[9] Jeon O, Bouhadir KH, Mansour JM, Alsberg E. Photocrosslinked alginate hydrogels with tunable biodegradation rates and mechanical properties. Biomaterials. 2009;30:2724-34.

[10] Kloxin AM, Benton JA, Anseth KS. In situ elasticity modulation with dynamic substrates to direct cell phenotype. Biomaterials. 2010;31:1-8.

[11] Marco C, Joanna I, Krisztina S, Jakub J, Mariella D, Andrea B, et al. 3D bioprinting of BM-MSCs-loaded ECM biomimetic hydrogels for in vitro neocartilage formation. Biofabrication. 2016;8:035002.

[12] Paul A, Manoharan V, Krafft D, Assmann A, Uquillas JA, Shin SR, et al. Nanoengineered biomimetic hydrogels for guiding human stem cell osteogenesis in three dimensional microenvironments. J Mater Chem B Mater Biol Med. 2016;4:3544-54.

[13] Yue K, Trujillo-de Santiago G, Alvarez MM, Tamayol A, Annabi N, Khademhosseini A. Synthesis, properties, and biomedical applications of gelatin methacryloyl (GelMA) hydrogels. Biomaterials. 2015;73:254-71.

[14] Zongjie W, Zhenlin T, Fredric M, Keekyoung K. Comparative study of gelatin methacrylate hydrogels from different sources for biofabrication applications. Biofabrication. 2017;9:044101.

[15] Schneider CA, Rasband WS, Eliceiri KW. NIH Image to ImageJ: 25 years of image analysis. Nature Methods. 2012;9:671-5.

[16] Azeredo J, Azevedo NF, Briandet R, Cerca N, Coenye T, Costa AR, et al. Critical review on biofilm methods. Critical Reviews in Microbiology. 2017;43:313-51.

[17] Dhanachandra N, Manglem K, Chanu YJ. Image Segmentation Using K -means Clustering Algorithm and Subtractive Clustering Algorithm. Procedia Computer Science. 2015;54:764-71.

[18] He L, Ren X, Gao Q, Zhao X, Yao B, Chao Y. The connected-component labeling problem: A review of state-of-the-art algorithms. Pattern Recognition. 2017;70:25-43.

[19] Stone N, Kerssens M, Lloyd GR, Faulds K, Graham D, Matousek P. Surface enhanced spatially offset Raman spectroscopic (SESORS) imaging – the next dimension. Chemical Science. 2011;2:776-80.

[20] Frens G. CONTROLLED NUCLEATION FOR REGULATION OF PARTICLE-SIZE IN MONODISPERSE GOLD SUSPENSIONS. Nature-Physical Science. 1973;241:20-2.

[21] Lee PC, Meisel D. ADSORPTION AND SURFACE-ENHANCED RAMAN OF DYES ON SILVER AND GOLD SOLS. Journal of Physical Chemistry. 1982;86:3391-5.

[22] Nicolson F, Jamieson LE, Mabbott S, Plakas K, Shand NC, Detty MR, et al. Through tissue imaging of a live breast cancer tumour model using handheld surface enhanced spatially offset resonance Raman spectroscopy (SESORRS). Chemical Science. 2018;9:3788-92.

[23] Harmsen S, Bedics MA, Wall MA, Huang R, Detty MR, Kircher MF. Rational design of a chalcogenopyrylium-based surface-enhanced resonance Raman scattering nanoprobe with attomolar sensitivity. Nat Commun. 2015;6:6570.

[24] Nicolson F, Jamieson LE, Mabbott S, Shand NC, Graham D, Faulds K. Through barrier detection of ethanol using handheld Raman spectroscopy—Conventional Raman versus spatially offset Raman spectroscopy (SORS). Journal of Raman Spectroscopy. 2017;48:1828-38.

9.4 **Chapter 4**

[1] Ayhan E, Kesmezacar H, Akgun I. Intraarticular injections (corticosteroid, hyaluronic acid, platelet rich plasma) for the knee osteoarthritis. World journal of orthopedics. 2014;5:351-61.

[2] Turnbull G, Clarke J, Picard F, Riches P, Jia L, Han F, et al. 3D bioactive composite scaffolds for bone tissue engineering. Bioactive Materials. 2017.

[3] Turnbull G, Clarke J, Picard F, Zhang W, Riches P, Li B, et al. 3D biofabrication for soft tissue and cartilage engineering. Medical Engineering & Physics. 2020;82:13-39.

[4] Cowie JG, Turnbull GS, Ker AM, Breusch SJ. Return to work and sports after total hip replacement. Arch Orthop Trauma Surg. 2013;133:695-700.

[5] Turnbull GS, Scott CEH, MacDonald DJ, Breusch SJ. Return to activity following revision total hip arthroplasty. Archives of Orthopaedic and Trauma Surgery. 2018.

[6] Turnbull GS, Scott CEH, MacDonald DJ, Breusch SJ. Gender and Preoperative Function Predict Physical Activity Levels After Revision Total Knee Arthroplasty. J Arthroplasty. 2019;34:939-46.

[7] Turnbull GS, Scott CEH, MacDonald DJ, Breusch SJ. Return to activity following revision total hip arthroplasty. Arch Orthop Trauma Surg. 2019;139:411-21.

[8] Scott CE, Howie CR, MacDonald D, Biant LC. Predicting dissatisfaction following total knee replacement: a prospective study of 1217 patients. J Bone Joint Surg Br. 2010;92:1253-8.

[9] Scott CE, Oliver WM, MacDonald D, Wade FA, Moran M, Breusch SJ. Predicting dissatisfaction following total knee arthroplasty in patients under 55 years of age. The bone & joint journal. 2016;98-b:1625-34.

[10] Simone S, Thomas B, Naomi P, Sarah B, Riccardo L, Verena S, et al. Double printing of hyaluronic acid/poly(glycidol) hybrid hydrogels with poly(ε -caprolactone) for MSC chondrogenesis. Biofabrication. 2017;9:044108.

[11] Onur B, Elena MD-J-P, Christoph M, Davide DA, Jeremy GB, Laura JB, et al. Biofabricated soft network composites for cartilage tissue engineering. Biofabrication. 2017;9:025014.

[12] Gonçalves EM, Oliveira FJ, Silva RF, Neto MA, Fernandes MH, Amaral M, et al. Three-dimensional printed PCL-hydroxyapatite scaffolds filled with CNTs for bone cell growth stimulation. Journal of Biomedical Materials Research Part B: Applied Biomaterials. 2016;104:1210-9.

[13] Cheng Y-L, Chen Y-W, Wang K, Shie M-Y. Enhanced adhesion and differentiation of human mesenchymal stem cell inside apatite-mineralized/poly(dopamine)-coated poly(?-caprolactone) scaffolds by stereolithography. Journal of Materials Chemistry B. 2016;4:6307-15.

[14] Mozetic P, Giannitelli SM, Gori M, Trombetta M, Rainer A. Engineering muscle cell alignment through 3D bioprinting. Journal of Biomedical Materials Research Part A. 2017;105:2582-8.

[15] Armstrong JPK, Burke M, Carter BM, Davis SA, Perriman AW. 3D Bioprinting Using a Templated Porous Bioink. Advanced Healthcare Materials. 2016;5:1724-30.

[16] Michael M, Jana B, Matthias S, Marcy Z-W. Nanostructured Pluronic hydrogels as bioinks for 3D bioprinting. Biofabrication. 2015;7:035006.

[17] Lippens E, Swennen I, Girones J, Declercq H, Vertenten G, Vlaminck L, et al. Cell survival and proliferation after encapsulation in a chemically modified Pluronic(R) F127 hydrogel. J Biomater Appl. 2013;27:828-39.

[18] Han Y, Zeng Q, Li H, Chang J. The calcium silicate/alginate composite: preparation and evaluation of its behavior as bioactive injectable hydrogels. Acta Biomater. 2013;9:9107-17.

[19] D'Souza SE, Ginsberg MH, Plow EF. Arginyl-glycyl-aspartic acid (RGD): a cell adhesion motif. Trends Biochem Sci. 1991;16:246-50.

[20] Hiraoka Y, Kimura Y, Ueda H, Tabata Y. Fabrication and biocompatibility of collagen sponge reinforced with poly(glycolic acid) fiber. Tissue Eng. 2003;9:1101-12.

[21] Sophia Fox AJ, Bedi A, Rodeo SA. The basic science of articular cartilage: structure, composition, and function. Sports Health. 2009;1:461-8.

[22] Bernhardt A, Paul B, Gelinsky M. Biphasic Scaffolds from Marine Collagens for Regeneration of Osteochondral Defects. Marine Drugs. 2018;16:91.

[23] Yang X, Lu Z, Wu H, Li W, Zheng L, Zhao J. Collagen-alginate as bioink for three-dimensional (3D) cell printing based cartilage tissue engineering. Mater Sci Eng C Mater Biol Appl. 2018;83:195-201.

[24] Yunoki S, Ohyabu Y, Hatayama H. Temperature-Responsive Gelation of Type I Collagen Solutions Involving Fibril Formation and Genipin Crosslinking as a Potential Injectable Hydrogel. International Journal of Biomaterials. 2013;2013:620765.

[25] Lee RH, Kim B, Choi I, Kim H, Choi HS, Suh K, et al. Characterization and expression analysis of mesenchymal stem cells from human bone marrow and adipose tissue. Cell Physiol Biochem. 2004;14:311-24.

[26] Zhang Y, Khan D, Delling J, Tobiasch E. Mechanisms Underlying the Osteo- and Adipo-Differentiation of Human Mesenchymal Stem Cells. The Scientific World Journal. 2012;2012:793823.

[27] Frese L, Dijkman PE, Hoerstrup SP. Adipose Tissue-Derived Stem Cells in Regenerative Medicine. Transfusion Medicine and Hemotherapy. 2016;43:268-74.

[28] Peng L, Jia Z, Yin X, Zhang X, Liu Y, Chen P, et al. Comparative analysis of mesenchymal stem cells from bone marrow, cartilage, and adipose tissue. Stem Cells Dev. 2008;17:761-73.

[29] Somoza RA, Welter JF, Correa D, Caplan AI. Chondrogenic differentiation of mesenchymal stem cells: challenges and unfulfilled expectations. Tissue Eng Part B Rev. 2014;20:596-608.

[30] Levengood SL, Zhang M. Chitosan-based scaffolds for bone tissue engineering. Journal of materials chemistry B, Materials for biology and medicine. 2014;2:3161-84.

[31] Li Q, Lin H, Du Q, Liu K, Wang O, Evans C, et al. Scalable and physiologically relevant microenvironments for human pluripotent stem cell expansion and differentiation. Biofabrication. 2018;10:025006.

[32] Shi S, Cheng X, Wang J, Zhang W, Peng L, Zhang Y. RhBMP-2 microspheres-loaded chitosan/collagen scaffold enhanced osseointegration: an experiment in dog. J Biomater Appl. 2009;23:331-46.

[33] Zhang R, Ma J, Han J, Zhang W, Ma J. Mesenchymal stem cell related therapies for cartilage lesions and osteoarthritis. Am J Transl Res. 2019;11:6275-89.

[34] Bahcecioglu G, Hasirci N, Bilgen B, Hasirci V. A 3D printed PCL/hydrogel construct with zone-specific biochemical composition mimicking that of the meniscus. Biofabrication. 2019;11:025002.

[35] Goncalves EM, Oliveira FJ, Silva RF, Neto MA, Fernandes MH, Amaral M, et al. Three-dimensional printed PCL-hydroxyapatite scaffolds filled with CNTs for bone cell growth stimulation. J Biomed Mater Res B Appl Biomater. 2016;104:1210-9.

[36] Ulery BD, Nair LS, Laurencin CT. Biomedical Applications of Biodegradable Polymers. J Polym Sci B Polym Phys. 2011;49:832-64.

[37] Williams JM, Adewunmi A, Schek RM, Flanagan CL, Krebsbach PH, Feinberg SE, et al. Bone tissue engineering using polycaprolactone scaffolds fabricated via selective laser sintering. Biomaterials. 2005;26:4817-27.

[38] Yohe ST, Freedman JD, Falde EJ, Colson YL, Grinstaff MW. A mechanistic study of wetting superhydrophobic porous 3D meshes. Advanced functional materials. 2013;23:3628-37.

[39] Yoo HS, Kim TG, Park TG. Surface-functionalized electrospun nanofibers for tissue engineering and drug delivery. Advanced drug delivery reviews. 2009;61:1033-42.

[40] Bosworth LA, Hu W, Shi Y, Cartmell SH. Enhancing Biocompatibility without Compromising Material Properties: An Optimised NaOH Treatment for Electrospun Polycaprolactone Fibres. Journal of Nanomaterials. 2019;2019:4605092.

[41] Park JS, Kim J-M, Lee SJ, Lee SG, Jeong Y-K, Kim SE, et al. Surface hydrolysis of fibrous poly(ε-caprolactone) scaffolds for enhanced osteoblast adhesion and proliferation. Macromolecular Research. 2007;15:424-9.

[42] Ahmed EM. Hydrogel: Preparation, characterization, and applications: A review. Journal of advanced research. 2015;6:105-21.

[43] Zhu J, Marchant RE. Design properties of hydrogel tissue-engineering scaffolds. Expert review of medical devices. 2011;8:607-26.

[44] Baer AE, Wang JY, Kraus VB, Setton LA. Collagen gene expression and mechanical properties of intervertebral disc cell-alginate cultures. J Orthop Res. 2001;19:2-10.

[45] Chou AI, Akintoye SO, Nicoll SB. Photo-crosslinked alginate hydrogels support enhanced matrix accumulation by nucleus pulposus cells in vivo. Osteoarthritis Cartilage. 2009;17:1377-84.

[46] Alakpa Enateri V, Jayawarna V, Lampel A, Burgess Karl V, West Christopher C, Bakker Sanne CJ, et al. Tunable Supramolecular Hydrogels for Selection of Lineage-Guiding Metabolites in Stem Cell Cultures. Chem.1:298-319.

[47] Kim YB, Kim GH. PCL/alginate composite scaffolds for hard tissue engineering: fabrication, characterization, and cellular activities. ACS combinatorial science. 2015;17:87-99.

[48] Kang H-W, Lee SJ, Ko IK, Kengla C, Yoo JJ, Atala A. A 3D bioprinting system to produce human-scale tissue constructs with structural integrity. Nat Biotech. 2016;34:312-9.

[49] Kim MS, Kim G. Three-dimensional electrospun polycaprolactone (PCL)/alginate hybrid composite scaffolds. Carbohydr Polym. 2014;114:213-21.

[50] Haider A, Haider S, Kang I-K. A comprehensive review summarizing the effect of electrospinning parameters and potential applications of nanofibers in biomedical and biotechnology. Arabian Journal of Chemistry. 2018;11:1165-88.

[51] Murphy SV, Atala A. 3D bioprinting of tissues and organs. Nat Biotechnol. 2014;32:773-85.

[52] Hospodiuk M, Dey M, Sosnoski D, Ozbolat IT. The bioink: A comprehensive review on bioprintable materials. Biotechnology Advances. 2017;35:217-39.

[53] Ozbolat IT, Hospodiuk M. Current advances and future perspectives in extrusion-based bioprinting. Biomaterials. 2016;76:321-43.

[54] Shafiee A, Atala A. Printing Technologies for Medical Applications. Trends Mol Med. 2016;22:254-65.

[55] Yu Y, Moncal KK, Li J, Peng W, Rivero I, Martin JA, et al. Three-dimensional bioprinting using self-assembling scalable scaffold-free "tissue strands" as a new bioink. Scientific Reports. 2016;6:28714.

[56] Hinton TJ, Jallerat Q, Palchesko RN, Park JH, Grodzicki MS, Shue H-J, et al. Three-dimensional printing of complex biological structures by freeform reversible embedding of suspended hydrogels. Science Advances. 2015;1.

[57] Lee KY, Mooney DJ. Alginate: properties and biomedical applications. Prog Polym Sci. 2012;37:106-26.

[58] Morch YA, Donati I, Strand BL, Skjak-Braek G. Effect of Ca2+, Ba2+, and Sr2+ on alginate microbeads. Biomacromolecules. 2006;7:1471-80.

[59] Moshaverinia A, Chen C, Akiyama K, Ansari S, Xu X, Chee WW, et al. Alginate hydrogel as a promising scaffold for dental-derived stem cells: an in vitro study. Journal of materials science Materials in medicine. 2012;23:3041-51.

[60] Alsberg E, Anderson KW, Albeiruti A, Franceschi RT, Mooney DJ. Cell-interactive alginate hydrogels for bone tissue engineering. Journal of dental research. 2001;80:2025-9.

[61] Lee KY, Mooney DJ. Alginate: properties and biomedical applications. Prog Polym Sci. 2012;37:106-26.

[62] LeRoux MA, Guilak F, Setton LA. Compressive and shear properties of alginate gel: effects of sodium ions and alginate concentration. Journal of biomedical materials research. 1999;47:46-53.

[63] Skjåk-Bræk G, Grasdalen H, Smidsrød O. Inhomogeneous polysaccharide ionic gels. Carbohydrate Polymers. 1989;10:31-54.

[64] Ghanizadeh Tabriz A, Mills CG, Mullins JJ, Davies JA, Shu W. Rapid Fabrication of Cell-Laden Alginate Hydrogel 3D Structures by Micro Dip-Coating. Frontiers in Bioengineering and Biotechnology. 2017;5:13.

[65] Hong SH, Shin M, Lee J, Ryu JH, Lee S, Yang JW, et al. STAPLE: stable alginate gel prepared by linkage exchange from ionic to covalent bonds. Advanced healthcare materials. 2016;5:75-9.

[66] Fenn SL, Miao T, Scherrer RM, Oldinski RA. Dual-Cross-Linked Methacrylated Alginate Sub-Microspheres for Intracellular Chemotherapeutic Delivery. ACS applied materials & interfaces. 2016;8:17775-83.

[67] Foster S, Choudhury H, Colman J, Ingerman L, Robbins P. Toxicological review of barium and compounds. Environmental Protection Agency, Washington DC. 1998.

[68] Mørch YA, Qi M, Gundersen POM, Formo K, Lacik I, Skjåk-Braek G, et al. Binding and leakage of barium in alginate microbeads. J Biomed Mater Res A. 2012;100:2939-47.

[69] Samorezov JE, Morlock CM, Alsberg E. Dual Ionic and Photo-Crosslinked Alginate Hydrogels for Micropatterned Spatial Control of Material Properties and Cell Behavior. Bioconjug Chem. 2015;26:1339-47.

[70] Alan F-J, Catherine F, Dirk-Jan C, John G, Jason K, Aidan C, et al. Bioprinting of human pluripotent stem cells and their directed differentiation into hepatocyte-like cells for the generation of mini-livers in 3D. Biofabrication. 2015;7:044102.

[71] Fleming S, Debnath S, Frederix PWJM, Hunt NT, Ulijn RV. Insights into the Coassembly of Hydrogelators and Surfactants Based on Aromatic Peptide Amphiphiles. Biomacromolecules. 2014;15:1171-84.

[72] Shi J, Gao Y, Zhang Y, Pan Y, Xu B. Calcium ions to cross-link supramolecular nanofibers to tune the elasticity of hydrogels over orders of magnitude. Langmuir. 2011;27:14425-31.

[73] Lee H, Choi BG, Moon HJ, Choi J, Park K, Jeong B, et al. Chondrocyte 3D-culture in RGD-modified crosslinked hydrogel with temperature-controllable modulus. Macromolecular Research. 2012;20:106-11.

[74] Burdick JA, Anseth KS. Photoencapsulation of osteoblasts in injectable RGD-modified PEG hydrogels for bone tissue engineering. Biomaterials. 2002;23:4315-23.

9.5 **Chapter 5**

[1] Liliang O, Rui Y, Yu Z, Wei S. Effect of bioink properties on printability and cell viability for 3D bioplotting of embryonic stem cells. Biofabrication. 2016;8:035020.

[2] Ouyang L, Highley CB, Sun W, Burdick JA. A Generalizable Strategy for the 3D Bioprinting of Hydrogels from Nonviscous Photo-crosslinkable Inks. Advanced Materials. 2017;29:1604983.

[3] Groll J, Burdick JA, Cho DW, Derby B, Gelinsky M, Heilshorn SC, et al. A definition of bioinks and their distinction from biomaterial inks. Biofabrication. 2019;11:013001.

[4] Kim YB, Kim GH. PCL/alginate composite scaffolds for hard tissue engineering: fabrication, characterization, and cellular activities. ACS combinatorial science. 2015;17:87-99.

[5] Kang H-W, Lee SJ, Ko IK, Kengla C, Yoo JJ, Atala A. A 3D bioprinting system to produce human-scale tissue constructs with structural integrity. Nat Biotech. 2016;34:312-9.

[6] Hiraoka Y, Kimura Y, Ueda H, Tabata Y. Fabrication and biocompatibility of collagen sponge reinforced with poly(glycolic acid) fiber. Tissue Eng. 2003;9:1101-12.

[7] Sophia Fox AJ, Bedi A, Rodeo SA. The basic science of articular cartilage: structure, composition, and function. Sports Health. 2009;1:461-8.

[8] Bernhardt A, Paul B, Gelinsky M. Biphasic Scaffolds from Marine Collagens for Regeneration of Osteochondral Defects. Marine Drugs. 2018;16:91.

[9] Yang X, Lu Z, Wu H, Li W, Zheng L, Zhao J. Collagen-alginate as bioink for three-dimensional (3D) cell printing based cartilage tissue engineering. Mater Sci Eng C Mater Biol Appl. 2018;83:195-201.

[10] Aldana AA, Valente F, Dilley R, Doyle B. Development of 3D bioprinted GelMA-alginate hydrogels with tunable mechanical properties. Bioprinting. 2021;21:e00105.

[11] Yin J, Yan M, Wang Y, Fu J, Suo H. 3D bioprinting of low-concentration cell-laden gelatin methacrylate (GelMA) bioinks with a two-step cross-linking strategy. ACS applied materials & interfaces. 2018;10:6849-57.

[12] Ying G, Jiang N, Yu C, Zhang YS. Three-dimensional bioprinting of gelatin methacryloyl (GelMA). Bio-design and Manufacturing. 2018;1:215-24.

[13] Davies RL, Kuiper NJ. Regenerative Medicine: A Review of the Evolution of Autologous Chondrocyte Implantation (ACI) Therapy. Bioengineering (Basel). 2019;6.

[14] Schuurman W, Levett PA, Pot MW, van Weeren PR, Dhert WJ, Hutmacher DW, et al. Gelatin-methacrylamide hydrogels as potential biomaterials for fabrication of tissue-engineered cartilage constructs. Macromol Biosci. 2013;13:551-61.

[15] Kolesky DB, Homan KA, Skylar-Scott MA, Lewis JA. Three-dimensional bioprinting of thick vascularized tissues. Proceedings of the National Academy of Sciences. 2016;113:3179-84.

[16] Bahcecioglu G, Hasirci N, Bilgen B, Hasirci V. A 3D printed PCL/hydrogel construct with zone-specific biochemical composition mimicking that of the meniscus. Biofabrication. 2019;11:025002.

[17] Byambaa B, Annabi N, Yue K, Trujillo-de Santiago G, Alvarez MM, Jia W, et al. Bioprinted Osteogenic and Vasculogenic Patterns for Engineering 3D Bone Tissue. Adv Healthc Mater. 2017.

[18] Costantini M, Idaszek J, Szöke K, Jaroszewicz J, Dentini M, Barbetta A, et al. 3D bioprinting of BM-MSCs-loaded ECM biomimetic hydrogels forin vitroneocartilage formation. Biofabrication. 2016;8:035002.

[19] Daly AC, Critchley SE, Rencsok EM, Kelly DJ. A comparison of different bioinks for 3D bioprinting of fibrocartilage and hyaline cartilage. Biofabrication. 2016;8:045002.

[20] Zongjie W, Zhenlin T, Fredric M, Keekyoung K. Comparative study of gelatin methacrylate hydrogels from different sources for biofabrication applications. Biofabrication. 2017;9:044101.

[21] Gao T, Gillispie GJ, Copus JS, Pr AK, Seol Y-J, Atala A, et al. Optimization of gelatin–alginate composite bioink printability using rheological parameters: a systematic approach. Biofabrication. 2018;10:034106.

[22] Fennema E, Rivron N, Rouwkema J, van Blitterswijk C, de Boer J. Spheroid culture as a tool for creating 3D complex tissues. Trends Biotechnol. 2013;31:108-15.

[23] Mironov V, Visconti RP, Kasyanov V, Forgacs G, Drake CJ, Markwald RR. Organ printing: tissue spheroids as building blocks. Biomaterials. 2009;30:2164-74.

[24] Zhang K, Yan S, Cui L, Yin J. ASC spheroids formed in poly(L-glutamic acid)/chitosan scaffold to enhance hyaline-like cartilage regeneration. Frontiers in Bioengineering and Biotechnology.

[25] Zhuang P, Sun AX, An J, Chua CK, Chew SY. 3D neural tissue models: From spheroids to bioprinting. Biomaterials. 2018;154:113-33.

[26] Yu Y, Moncal KK, Li J, Peng W, Rivero I, Martin JA, et al. Three-dimensional bioprinting using self-assembling scalable scaffold-free "tissue strands" as a new bioink. Scientific Reports. 2016;6:28714.

[27] Fleming PA, Argraves WS, Gentile C, Neagu A, Forgacs G, Drake CJ. Fusion of uniluminal vascular spheroids: A model for assembly of blood vessels. Developmental Dynamics. 2010;239:spcone-spcone.

[28] Dahlmann J, Kensah G, Kempf H, Skvorc D, Gawol A, Elliott DA, et al. The use of agarose microwells for scalable embryoid body formation and cardiac differentiation of human and murine pluripotent stem cells. Biomaterials. 2013;34:2463-71.

[29] Yang X, Lu Z, Wu H, Li W, Zheng L, Zhao J. Collagen-alginate as bioink for three-dimensional (3D) cell printing based cartilage tissue engineering. Materials Science and Engineering: C. 2018;83:195-201.

[30] Yamaoka H, Asato H, Ogasawara T, Nishizawa S, Takahashi T, Nakatsuka T, et al. Cartilage tissue engineering using human auricular chondrocytes embedded in different hydrogel materials. Journal of Biomedical Materials Research Part A. 2006;78A:1-11.

[31] Heo J, Koh RH, Shim W, Kim HD, Yim H-G, Hwang NS. Riboflavin-induced photo-crosslinking of collagen hydrogel and its application in meniscus tissue engineering. Drug Delivery and Translational Research. 2016;6:148-58.

[32] Zeeman R, Dijkstra PJ, van Wachem PB, van Luyn MJ, Hendriks M, Cahalan PT, et al. Successive epoxy and carbodiimide cross-linking of dermal sheep collagen. Biomaterials. 1999;20:921-31.

[33] Weadock KS, Miller EJ, Bellincampi LD, Zawadsky JP, Dunn MG. Physical crosslinking of collagen fibers: comparison of ultraviolet irradiation and dehydrothermal treatment. Journal of biomedical materials research. 1995;29:1373-9.

[34] Ansari S, Pouraghaei Sevari S, Chen C, Sarrion P, Moshaverinia A. RGD-Modified Alginate–GelMA Hydrogel Sheet Containing Gingival Mesenchymal Stem Cells: A Unique Platform for Wound Healing and Soft Tissue Regeneration. ACS Biomaterials Science & Engineering. 2021.

[35] Seyedmahmoud R, Çelebi-Saltik B, Barros N, Nasiri R, Banton E, Shamloo A, et al. Three-Dimensional Bioprinting of Functional Skeletal Muscle Tissue Using GelatinMethacryloyl-Alginate Bioinks. Micromachines. 2019;10.

[36] Li X, Chen S, Li J, Wang X, Zhang J, Kawazoe N, et al. 3D Culture of Chondrocytes in Gelatin Hydrogels with Different Stiffness. Polymers (Basel). 2016;8:269.

[37] Anderson JM, Rodriguez A, Chang DT. Foreign body reaction to biomaterials. Semin Immunol. 2008;20:86-100.

[38] Park H, Lee KY. Cartilage regeneration using biodegradable oxidized alginate/hyaluronate hydrogels. Journal of Biomedical Materials Research Part A. 2014;102:4519-25.

[39] Reakasame S, Boccaccini AR. Oxidized alginate-based hydrogels for tissue engineering applications: a review. Biomacromolecules. 2018;19:3-21.

[40] Kadri R, Ben Messaoud G, Tamayol A, Aliakbarian B, Zhang HY, Hasan M, et al. Preparation and characterization of nanofunctionalized alginate/methacrylated gelatin hybrid hydrogels. RSC Advances. 2016;6:27879-84.

[41] Jin R, Teixeira LM, Dijkstra PJ, Karperien M, Van Blitterswijk C, Zhong Z, et al. Injectable chitosan-based hydrogels for cartilage tissue engineering. Biomaterials. 2009;30:2544-51.

[42] Wei Y, Hu Y, Hao W, Han Y, Meng G, Zhang D, et al. A novel injectable scaffold for cartilage tissue engineering using adipose-derived adult stem cells. Journal of Orthopaedic Research. 2008;26:27-33.

[43] Choi B, Kim S, Lin B, Wu BM, Lee M. Cartilaginous extracellular matrix-modified chitosan hydrogels for cartilage tissue engineering. ACS applied materials & interfaces. 2014;6:20110-21.

[44] Lee H, Choi BG, Moon HJ, Choi J, Park K, Jeong B, et al. Chondrocyte 3D-culture in RGD-modified crosslinked hydrogel with temperature-controllable modulus. Macromolecular Research. 2012;20:106-11.

[45] Guo Y, Yuan T, Xiao Z, Tang P, Xiao Y, Fan Y, et al. Hydrogels of collagen/chondroitin sulfate/hyaluronan interpenetrating polymer network for cartilage tissue engineering. Journal of Materials Science: Materials in Medicine. 2012;23:2267-79.

[46] Yu F, Cao X, Li Y, Zeng L, Yuan B, Chen X. An injectable hyaluronic acid/PEG hydrogel for cartilage tissue engineering formed by integrating enzymatic crosslinking and Diels–Alder "click chemistry". Polymer Chemistry. 2013;5:1082-90.

[47] Ahn S, Lee H, Puetzer J, Bonassar LJ, Kim G. Fabrication of cell-laden three-dimensional alginate-scaffolds with an aerosol cross-linking process. Journal of Materials Chemistry. 2012;22:18735-40.

[48] Jin R, Teixeira LM, Krouwels A, Dijkstra PJ, Van Blitterswijk C, Karperien M, et al. Synthesis and characterization of hyaluronic acid–poly (ethylene glycol) hydrogels via Michael addition: An injectable biomaterial for cartilage repair. Acta biomaterialia. 2010;6:1968-77.

[49] Burdick JA, Anseth KS. Photoencapsulation of osteoblasts in injectable RGD-modified PEG hydrogels for bone tissue engineering. Biomaterials. 2002;23:4315-23.

[50] Han Y, Zeng Q, Li H, Chang J. The calcium silicate/alginate composite: preparation and evaluation of its behavior as bioactive injectable hydrogels. Acta Biomater. 2013;9:9107-17.

[51] Lee J-C, Lee SY, Min HJ, Han SA, Jang J, Lee S, et al. Synovium-derived mesenchymal stem cells encapsulated in a novel injectable gel can repair osteochondral defects in a rabbit model. Tissue Engineering Part A. 2012;18:2173-86.

[52] Papadopoulos A, Bichara DA, Zhao X, Ibusuki S, Randolph MA, Anseth KS, et al. Injectable and photopolymerizable tissue-engineered auricular cartilage using poly (ethylene glycol) dimethacrylate copolymer hydrogels. Tissue Engineering Part A. 2011;17:161-9.

[53] Yunoki S, Ohyabu Y, Hatayama H. Temperature-Responsive Gelation of Type I Collagen Solutions Involving Fibril Formation and Genipin Crosslinking as a Potential Injectable Hydrogel. International Journal of Biomaterials. 2013;2013:620765.

[54] Somoza RA, Welter JF, Correa D, Caplan AI. Chondrogenic differentiation of mesenchymal stem cells: challenges and unfulfilled expectations. Tissue Eng Part B Rev. 2014;20:596-608.

[55] Turnbull G, Clarke J, Picard F, Riches P, Jia L, Han F, et al. 3D bioactive composite scaffolds for bone tissue engineering. Bioactive Materials. 2017.

[56] Levengood SL, Zhang M. Chitosan-based scaffolds for bone tissue engineering. Journal of materials chemistry B, Materials for biology and medicine. 2014;2:3161-84.

[57] Li Q, Lin H, Du Q, Liu K, Wang O, Evans C, et al. Scalable and physiologically relevant microenvironments for human pluripotent stem cell expansion and differentiation. Biofabrication. 2018;10:025006.

[58] Shi S, Cheng X, Wang J, Zhang W, Peng L, Zhang Y. RhBMP-2 microspheres-loaded chitosan/collagen scaffold enhanced osseointegration: an experiment in dog. J Biomater Appl. 2009;23:331-46.

[59] Zhang R, Ma J, Han J, Zhang W, Ma J. Mesenchymal stem cell related therapies for cartilage lesions and osteoarthritis. Am J Transl Res. 2019;11:6275-89.

[60] Zhang Y, Khan D, Delling J, Tobiasch E. Mechanisms Underlying the Osteo- and Adipo-Differentiation of Human Mesenchymal Stem Cells. The Scientific World Journal. 2012;2012:793823.

[61] Yu Y, Moncal KK, Li J, Peng W, Rivero I, Martin JA, et al. Three-dimensional bioprinting using self-assembling scalable scaffold-free "tissue strands" as a new bioink. Scientific reports. 2016;6:28714.

[62] Datta P, Wu Y, Yu Y, Moncal KK, Ozbolat IT. A Scaffold Free 3D Bioprinted Cartilage Model for In Vitro Toxicology. Methods in molecular biology (Clifton, NJ). 2021;2147:175-83.

[63] Parfenov VA, Koudan EV, Bulanova EA, Karalkin PA, Pereira FD, Norkin NE, et al. Scaffold-free, label-free and nozzle-free biofabrication technology using magnetic levitational assembly. Biofabrication. 2018;10:034104.

[64] Yang YH, Lee AJ, Barabino GA. Coculture-driven mesenchymal stem cell-differentiated articular chondrocyte-like cells support neocartilage development. Stem cells translational medicine. 2012;1:843-54.

[65] Dahlin RL, Kinard LA, Lam J, Needham CJ, Lu S, Kasper FK, et al. Articular chondrocytes and mesenchymal stem cells seeded on biodegradable scaffolds for the repair of cartilage in a rat osteochondral defect model. Biomaterials. 2014;35:7460-9.

[66] Liu Y, Zhou G, Cao Y. Recent progress in cartilage tissue engineering—our experience and future directions. Engineering. 2017;3:28-35.

[67] Samorezov JE, Morlock CM, Alsberg E. Dual Ionic and Photo-Crosslinked Alginate Hydrogels for Micropatterned Spatial Control of Material Properties and Cell Behavior. Bioconjug Chem. 2015;26:1339-47.

[68] Zuo Q, Cui W, Liu F, Wang Q, Chen Z, Fan W. Co-cultivated mesenchymal stem cells support chondrocytic differentiation of articular chondrocytes. International orthopaedics. 2013;37:747-52.

[69] Schuh E, Kramer J, Rohwedel J, Notbohm H, Müller R, Gutsmann T, et al. Effect of matrix elasticity on the maintenance of the chondrogenic phenotype. Tissue engineering Part A. 2010;16:1281-90.

9.6 **Chapter 6**

[1] Moroni L, Boland T, Burdick JA, De Maria C, Derby B, Forgacs G, et al. Biofabrication: A Guide to Technology and Terminology. Trends Biotechnol. 2018;36:384-402.

[2] Turnbull G, Clarke J, Picard F, Riches P, Jia L, Han F, et al. 3D bioactive composite scaffolds for bone tissue engineering. Bioactive Materials. 2017.

[3] Anthony MH, Alex C, Brian D, Lorna E, Andrew S, Wenmiao S. Rising to the challenge: applying biofabrication approaches for better drug and chemical product development. Biofabrication. 2017;9:033001.

[4] Mironov V, Kasyanov V, Markwald RR. Organ printing: from bioprinter to organ biofabrication line. Curr Opin Biotechnol. 2011;22:667-73.

[5] Schaffner M, Rühs PA, Coulter F, Kilcher S, Studart AR. 3D printing of bacteria into functional complex materials. Science Advances. 2017;3.

[6] Lehner BAE, Schmieden DT, Meyer AS. A Straightforward Approach for 3D Bacterial Printing. ACS Synth Biol. 2017;6:1124-30.

[7] Huang Y, Xia A, Yang G, Jin F. Bioprinting Living Biofilms through Optogenetic Manipulation. ACS Synthetic Biology. 2018;7:1195-200.

[8] Schmieden DT, Basalo Vázquez SJ, Sangüesa H, van der Does M, Idema T, Meyer AS. Printing of Patterned, Engineered E. coli Biofilms with a Low-Cost 3D Printer. ACS synthetic biology. 2018;7:1328-37.

[9] Connell JL, Ritschdorff ET, Whiteley M, Shear JB. 3D printing of microscopic bacterial communities. Proceedings of the National Academy of Sciences of the United States of America. 2013;110:18380-5.

[10] Willyard C. The drug-resistant bacteria that pose the greatest health threats. Nature. 2017;543:15.

[11] Bjarnsholt T. The role of bacterial biofilms in chronic infections. APMIS Supplementum. 2013:1-51.

[12] Jamal M, Ahmad W, Andleeb S, Jalil F, Imran M, Nawaz MA, et al. Bacterial biofilm and associated infections. Journal of the Chinese Medical Association. 2018;81:7-11.

[13] Hoiby N, Ciofu O, Bjarnsholt T. Pseudomonas aeruginosa biofilms in cystic fibrosis. Future microbiology. 2010;5:1663-74.

[14] Hengzhuang W, Wu H, Ciofu O, Song Z, Hoiby N. Pharmacokinetics/pharmacodynamics of colistin and imipenem on mucoid and nonmucoid Pseudomonas aeruginosa biofilms. Antimicrobial agents and chemotherapy. 2011;55:4469-74.

[15] Wu H, Moser C, Wang H-Z, Høiby N, Song Z-J. Strategies for combating bacterial biofilm infections. International Journal Of Oral Science. 2014;7:1.

[16] Garrett TR, Bhakoo M, Zhang Z. Bacterial adhesion and biofilms on surfaces. Progress in Natural Science. 2008;18:1049-56.

[17] Wolcott RD, Rhoads DD, Bennett ME, Wolcott BM, Gogokhia L, Costerton JW, et al. Chronic wounds and the medical biofilm paradigm. Journal of Wound Care. 2010;19:45-53.

[18] Parsek MR, Singh PK. Bacterial biofilms: an emerging link to disease pathogenesis. Annual review of microbiology. 2003;57:677-701.

[19] Bodelon G, Montes-Garcia V, Lopez-Puente V, Hill EH, Hamon C, Sanz-Ortiz MN, et al. Detection and imaging of quorum sensing in Pseudomonas aeruginosa biofilm

communities by surface-enhanced resonance Raman scattering. Nature materials. 2016;15:1203-11.

[20] Rutherford ST, Bassler BL. Bacterial Quorum Sensing: Its Role in Virulence and Possibilities for Its Control. Cold Spring Harbor Perspectives in Medicine. 2012;2:a012427.

[21] Baselga R, Albizu I, Amorena B. Staphylococcus aureus capsule and slime as virulence factors in ruminant mastitis. A review. Veterinary Microbiology. 1994;39:195-204.

[22] Bjarnsholt T, Alhede M, Alhede M, Eickhardt-Sorensen SR, Moser C, Kuhl M, et al. The in vivo biofilm. Trends Microbiol. 2013;21:466-74.

[23] Goeres DM, Hamilton MA, Beck NA, Buckingham-Meyer K, Hilyard JD, Loetterle LR, et al. A method for growing a biofilm under low shear at the air-liquid interface using the drip flow biofilm reactor. Nature Protocols. 2009;4:783-8.

[24] Hentzer M, Teitzel GM, Balzer GJ, Heydorn A, Molin S, Givskov M, et al. Alginate overproduction affects Pseudomonas aeruginosa biofilm structure and function. Journal of Bacteriology. 2001;183:5395-401.

[25] Lee JH, Kaplan JB, Lee WY. Microfluidic devices for studying growth and detachment of Staphylococcus epidermidis biofilms. Biomedical Microdevices. 2008;10:489-98.

[26] Pamp SJ, Sternberg C, Tolker-Nielsen T. Insight into the Microbial Multicellular Lifestyle via Flow-Cell Technology and Confocal Microscopy. Cytometry Part A. 2009;75A:90-103.

[27] Coenye T, Nelis HJ. In vitro and in vivo model systems to study microbial biofilm formation. Journal of Microbiological Methods. 2010;83:89-105.

[28] Bjarnsholt T, Alhede M, Alhede M, Eickhardt-Sorensen SR, Moser C, Kuhl M, et al. The in vivo biofilm. Trends in Microbiology. 2013;21:466-74.

[29] Roberts AEL, Kragh KN, Bjarnsholt T, Diggle SP. The Limitations of In Vitro Experimentation in Understanding Biofilms and Chronic Infection. Journal of Molecular Biology. 2015;427:3646-61.

[30] Bjarnsholt T. The role of bacterial biofilms in chronic infections. Apmis. 2013;121:1-58.

[31] Moroni L, Boland T, Burdick JA, De Maria C, Derby B, Forgacs G, et al. Biofabrication: A Guide to Technology and Terminology. Trends in Biotechnology. 2018;36:384-402.

[32] Luber P, Bartelt E, Genschow E, Wagner J, Hahn H. Comparison of broth microdilution, E test, and agar dilution methods for antibiotic susceptibility testing of Campylobacter jejuni and Campylobacter coli. Journal of Clinical Microbiology. 2003;41:1062-8.

[33] Jorgensen JH, Ferraro MJ. Antimicrobial Susceptibility Testing: A Review of General Principles and Contemporary Practices. Clinical Infectious Diseases. 2009;49:1749-55.

[34] McBain AJ. Chapter 4: In vitro biofilm models: an overview. Advances in applied microbiology. 2009;69:99-132.

[35] Hoiby N, Bjarnsholt T, Givskov M, Molin S, Ciofu O. Antibiotic resistance of bacterial biofilms. International Journal of Antimicrobial Agents. 2010;35:322-32.

[36] Macia MD, Rojo-Molinero E, Oliver A. Antimicrobial susceptibility testing in biofilm-growing bacteria. Clinical Microbiology and Infection. 2014;20:981-90.

[37] Tam VH, Chang KT, Abdelraouf K, Brioso CG, Ameka M, McCaskey LA, et al. Prevalence, Resistance Mechanisms, and Susceptibility of Multidrug-Resistant Bloodstream Isolates of Pseudomonas aeruginosa. Antimicrobial Agents and Chemotherapy. 2010;54:1160-4.

[38] Rolain JM, Abat C, Jimeno MT, Fournier PE, Raoult D. Do we need new antibiotics? Clinical Microbiology and Infection. 2016;22:408-15.

[39] Turnbull G, Clarke J, Picard F, Riches P, Jia L, Han F, et al. 3D bioactive composite scaffolds for bone tissue engineering. Bioactive Materials. 2018;3:278-314.

[40] Faulkner-Jones A, Fyfe C, Cornelissen DJ, Gardner J, King J, Courtney A, et al. Bioprinting of human pluripotent stem cells and their directed differentiation into hepatocyte-like cells for the generation of mini-livers in 3D. Biofabrication. 2015;7.

[41] Groll J, Boland T, Blunk T, Burdick JA, Cho DW, Dalton PD, et al. Biofabrication: reappraising the definition of an evolving field. Biofabrication. 2016;8.

[42] Holmes AM, Charlton A, Derby B, Ewart L, Scott A, Shu WM. Rising to the challenge: applying biofabrication approaches for better drug and chemical product development. Biofabrication. 2017;9.

[43] Schaffner M, Ruhs PA, Coulter F, Kilcher S, Studart AR. 3D printing of bacteria into functional complex materials. Science Advances. 2017;3.

[44] Lehner BAE, Schmieden DT, Meyer AS. A Straightforward Approach for 3D Bacterial Printing. Acs Synthetic Biology. 2017;6:1124-30.

[45] Huang YJ, Xia AG, Yang G, Jin F. Bioprinting Living Biofilms through Optogenetic Manipulation. Acs Synthetic Biology. 2018;7:1195-200.

[46] Schmieden DT, Vazquez SJB, Sanguesa H, van der Does M, Idema T, Meyer AS. Printing of Patterned, Engineered E. coil Biofilms with a Low-Cost 3D Printer. Acs Synthetic Biology. 2018;7:1328-37.

[47] Wu H, Moser C, Wang H-Z, Hoiby N, Song Z-J. Strategies for combating bacterial biofilm infections. International Journal of Oral Science. 2015;7:1-7.

[48] Kyle S. 3D Printing of Bacteria: The Next Frontier in Biofabrication. Trends in Biotechnology. 2018;36:340-1.

[49] Boyle KE, Heilmann S, van Ditmarsch D, Xavier JB. Exploiting social evolution in biofilms. Current Opinion in Microbiology. 2013;16:207-12.

[50] Logan BE, Hamelers B, Rozendal RA, Schrorder U, Keller J, Freguia S, et al. Microbial fuel cells: Methodology and technology. Environmental Science & Technology. 2006;40:5181-92.

[51] Dolatabadi S, Manjulakumari D. Microbial Biosensors and Bioelectronics. Research Journal of Biotechnology. 2012;7:102-8.

[52] Cassidy MB, Lee H, Trevors JT. Environmental applications of immobilized microbial cells: A review. Journal of Industrial Microbiology. 1996;16:79-101.

[53] Faulkner-Jones A, Greenhough S, King JA, Gardner J, Courtney A, Shu WM. Development of a valve-based cell printer for the formation of human embryonic stem cell spheroid aggregates. Biofabrication. 2013;5.

[54] Logan BE, Hamelers B, Rozendal R, Schröder U, Keller J, Freguia S, et al. Microbial Fuel Cells: Methodology and Technology. Environmental Science & Technology. 2006;40:5181-92.

[55] Su L, Jia W, Hou C, Lei Y. Microbial biosensors: a review. Biosensors & bioelectronics. 2011;26:1788-99.

[56] Bidarra SJ, Barrias CC, Granja PL. Injectable alginate hydrogels for cell delivery in tissue engineering. Acta Biomaterialia. 2014;10:1646-62.

[57] Tabriz AG, Hermida MA, Leslie NR, Shu W. Three-dimensional bioprinting of complex cell laden alginate hydrogel structures. Biofabrication. 2015;7.

[58] Zimmerli W, Sendi P. Orthopaedic biofilm infections. Apmis. 2017;125:353-64.

[59] Azeredo J, Azevedo NF, Briandet R, Cerca N, Coenye T, Costa AR, et al. Critical review on biofilm methods. Critical Reviews in Microbiology. 2017;43:313-51.

[60] Morch YA, Donati I, Strand BL, Skjak-Braek G. Effect of Ca2+, Ba2+, and Sr2+ on alginate microbeads. Biomacromolecules. 2006;7:1471-80.

[61] Garnett JA, Matthews S. Interactions in Bacterial Biofilm Development: A Structural Perspective. Current Protein & Peptide Science. 2012;13:739-55.

[62] Magana M, Sereti C, Ioannidis A, Mitchell CA, Ball AR, Magiorkinis E, et al. Options and Limitations in Clinical Investigation of Bacterial Biofilms. Clinical Microbiology Reviews. 2018;31.

[63] Wagner VE, Iglewski BH. P. aeruginosa Biofilms in CF Infection. Clinical Reviews in Allergy & Immunology. 2008;35:124-34.

[64] Serra R, Grande R, Butrico L, Rossi A, Settimio UF, Caroleo B, et al. Chronic wound infections: the role of Pseudomonas aeruginosa and Staphylococcus aureus. Expert Rev Anti Infect Ther. 2015;13:605-13.

[65] Bryers JD. Medical biofilms. Biotechnology and bioengineering. 2008;100:1-18.

[66] Patrie SM, Mrksich M. Self-assembled monolayers for MALDI-TOF mass Spectrometry for Immunoassays of human protein antigens. Analytical Chemistry. 2007;79:5878-87.

[67] Jamar W, Al Hashem G, Rotimi VO. Antimicrobial resistance among anaerobes isolated from clinical specimens in Kuwait hospitals: Comparative analysis of 11-year data. Anaerobe. 2015;31:25-30.

[68] McBain AJ. Chapter 4: In vitro biofilm models: an overview. Advances in applied microbiology. 2009;69:99-132.

[69] Anderl JN, Franklin MJ, Stewart PS. Role of antibiotic penetration limitation in Klebsiella pneumoniae biofilm resistance to ampicillin and ciprofloxacin. Antimicrobial agents and chemotherapy. 2000;44:1818-24.

[70] Bodelón G, Montes-García V, López-Puente V, Hill EH, Hamon C, Sanz-Ortiz MN, et al. Detection and imaging of quorum sensing in Pseudomonas aeruginosa biofilm communities by surface-enhanced resonance Raman scattering. Nature Materials. 2016;15:1203.

[71] Coenye T, Nelis HJ. In vitro and in vivo model systems to study microbial biofilm formation. J Microbiol Methods. 2010;83:89-105.

[72] Donlan RM. Biofilm Formation: A Clinically Relevant Microbiological Process. Clinical Infectious Diseases. 2001;33:1387-92.

[73] Hoiby N, Bjarnsholt T, Givskov M, Molin S, Ciofu O. Antibiotic resistance of bacterial biofilms. Int J Antimicrob Agents. 2010;35:322-32.

[74] Andrews JM. Determination of minimum inhibitory concentrations. J Antimicrob Chemother. 2001;48 Suppl 1:5-16.

[75] Baselga R, Albizu I, Amorena B. STAPHYLOCOCCUS-AUREUS CAPSULE AND SLIME AS VIRULENCE FACTORS IN RUMINANT MASTITIS - A REVIEW. Veterinary Microbiology. 1994;39:195-204.

[76] Connell JL, Kim J, Shear JB, Bard AJ, Whiteley M. Real-time monitoring of quorum sensing in 3D-printed bacterial aggregates using scanning electrochemical microscopy. Proceedings of the National Academy of Sciences of the United States of America. 2014;111:18255-60.

[77] Hentzer M, Teitzel GM, Balzer GJ, Heydorn A, Molin S, Givskov M, et al. Alginate Overproduction Affects Pseudomonas aeruginosa Biofilm Structure and Function. Journal of Bacteriology. 2001;183:5395-401.

[78] van Gennip M, Christensen LD, Alhede M, Qvortrup K, Jensen PØ, Høiby N, et al. Interactions between polymorphonuclear leukocytes and Pseudomonas aeruginosa biofilms on silicone implants in vivo. Infection and immunity. 2012;80:2601-7.

[79] Rasmussen RV, Fowler VG, Skov R, Bruun NE. Future challenges and treatment of Staphylococcus aureus bacteremia with emphasis on MRSA (vol 6, pg 43, 2011). Future microbiology. 2011;6:250-.

[80] Cosgrove SE, Sakoulas G, Perencevich EN, Schwaber MJ, Karchmer AW, Carmeli Y. Comparison of mortality associated with methicillin-resistant and methicillin-susceptible

Staphylococcus aureus bacteremia: A meta-analysis. Clinical Infectious Diseases. 2003;36:53-9.

[81] Huang Y, Xia A, Yang G, Jin F. Bioprinting Living Biofilms through Optogenetic Manipulation. ACS Synth Biol. 2018;7:1195-200.

[82] Lee KY, Mooney DJ. Alginate: properties and biomedical applications. Prog Polym Sci. 2012;37:106-26.

[83] Lee KY, Mooney DJ. Alginate: properties and biomedical applications. Prog Polym Sci. 2012;37:106-26.

[84] Caldwell DE, Korber DR, Lawrence JR. IMAGING OF BACTERIAL-CELLS BY FLUORESCENCE EXCLUSION USING SCANNING CONFOCAL LASER MICROSCOPY. Journal of Microbiological Methods. 1992;15:249-61.

[85] Schlafer S, Meyer RL. Confocal microscopy imaging of the biofilm matrix. Journal of Microbiological Methods. 2017;138:50-9.

[86] Vyas N, Sammons RL, Addison O, Dehghani H, Walmsley AD. A quantitative method to measure biofilm removal efficiency from complex biomaterial surfaces using SEM and image analysis. Scientific Reports. 2016;6:32694.

[87] Vickery K, Pajkos A, Cossart Y. Removal of biofilm from endoscopes: evaluation of detergent efficiency. Am J Infect Control. 2004;32:170-6.

[88] Caldwell DE, Korber DR, Lawrence JR. Imaging of bacterial cells by fluorescence exclusion using scanning confocal laser microscopy. Journal of Microbiological Methods. 1992;15:249-61.

9.7 Chapter 7

[1] Charnley J. ARTHROPLASTY OF THE HIP: A New Operation. The Lancet. 1961;277:1129-32.

[2] Jackson J. Father of the modern hip replacement: Professor Sir John Charnley (1911-82). Journal of medical biography. 2011;19:151-6.

[3] Turnbull GS, Scott CEH, MacDonald DJ, Breusch SJ. Gender and Preoperative Function Predict Physical Activity Levels After Revision Total Knee Arthroplasty. J Arthroplasty. 2019;34:939-46.

[4] Turnbull GS, Scott CEH, MacDonald DJ, Breusch SJ. Return to activity following revision total hip arthroplasty. Arch Orthop Trauma Surg. 2019;139:411-21.

[5] Turnbull GS, Scott CEH, MacDonald DJ, Breusch SJ. Return to activity following revision total hip arthroplasty. Archives of Orthopaedic and Trauma Surgery. 2018.

[6] Delanois RE, Mistry JB, Gwam CU, Mohamed NS, Choksi US, Mont MA. Current Epidemiology of Revision Total Knee Arthroplasty in the United States. The Journal of Arthroplasty. 2017;32:2663-8.

[7] Welsink CL, Lambers KTA, van Deurzen DFP, Eygendaal D, van den Bekerom MPJ. Total Elbow Arthroplasty: A Systematic Review. JBJS reviews. 2017;5:e4.

[8] Adkinson JM, Chung KC. Advances in small joint arthroplasty of the hand. Plastic and reconstructive surgery. 2014;134:1260-8.

[9] Cowie JG, Turnbull GS, Ker AM, Breusch SJ. Return to work and sports after total hip replacement. Arch Orthop Trauma Surg. 2013;133:695-700.

[10] Kurtz S, Ong K, Lau E, Mowat F, Halpern M. Projections of primary and revision hip and knee arthroplasty in the United States from 2005 to 2030. The Journal of bone and joint surgery American volume. 2007;89:780-5.

[11] Kurtz S, Mowat F, Ong K, Chan N, Lau E, Halpern M. Prevalence of primary and revision total hip and knee arthroplasty in the United States from 1990 through 2002. The Journal of bone and joint surgery American volume. 2005;87.

[12] Shahi N, Arosemena M, Kwon J, DiMuzio P, Abai B, Salvatore DM. A rare case of Clostridium septicum aortitis with colon adenocarcinoma. J Vasc Surg Cases Innov Tech. 2018;4:87-90.

[13] Aggarwal VK, Rasouli MR, Parvizi J. Periprosthetic joint infection: Current concept. Indian journal of orthopaedics. 2013;47:10-7.

[14] Zmistowski B, Karam JA, Durinka JB, Casper DS, Parvizi J. Periprosthetic joint infection increases the risk of one-year mortality. The Journal of bone and joint surgery American volume. 2013;95:2177-84.

[15] Peel TN, Dowsey MM, Buising KL, Liew D, Choong PF. Cost analysis of debridement and retention for management of prosthetic joint infection. Clinical microbiology and infection : the official publication of the European Society of Clinical Microbiology and Infectious Diseases. 2013;19:181-6.

[16] Klouche S, Sariali E, Mamoudy P. Total hip arthroplasty revision due to infection: a cost analysis approach. Orthopaedics & traumatology, surgery & research : OTSR. 2010;96.

[17] Bjarnsholt T. The role of bacterial biofilms in chronic infections. APMIS Supplementum. 2013:1-51.

[18] Hengzhuang W, Wu H, Ciofu O, Song Z, Hoiby N. Pharmacokinetics/pharmacodynamics of colistin and imipenem on mucoid and nonmucoid Pseudomonas aeruginosa biofilms. Antimicrobial agents and chemotherapy. 2011;55:4469-74.

[19] Wu H, Moser C, Wang H-Z, Høiby N, Song Z-J. Strategies for combating bacterial biofilm infections. International Journal Of Oral Science. 2014;7:1.

[20] Garrett TR, Bhakoo M, Zhang Z. Bacterial adhesion and biofilms on surfaces. Progress in Natural Science. 2008;18:1049-56.

[21] Izakovicova P, Borens O, Trampuz A. Periprosthetic joint infection: current concepts and outlook. EFORT Open Reviews. 2019;4:482-94.

[22] Abad CL, Haleem A. Prosthetic Joint Infections: an Update. Current Infectious Disease Reports. 2018;20:15.

[23] Li C, Renz N, Trampuz A. Management of Periprosthetic Joint Infection. Hip & pelvis. 2018;30:138-46.

[24] Olsen I. Biofilm-specific antibiotic tolerance and resistance. European Journal of Clinical Microbiology & Infectious Diseases. 2015;34:877-86.

[25] Jamal M, Ahmad W, Andleeb S, Jalil F, Imran M, Nawaz MA, et al. Bacterial biofilm and associated infections. Journal of the Chinese Medical Association. 2018;81:7-11.

[26] Berbari E, Mabry T, Tsaras G, Spangehl M, Erwin PJ, Murad MH, et al. Inflammatory blood laboratory levels as markers of prosthetic joint infection: a systematic review and meta-analysis. The Journal of bone and joint surgery American volume. 2010;92:2102-9.

[27] Shahi A, Tan TL, Kheir MM, Tan DD, Parvizi J. Diagnosing Periprosthetic Joint Infection: And the Winner Is? J Arthroplasty. 2017;32:S232-s5.

[28] Trampuz A, Hanssen AD, Osmon DR, Mandrekar J, Steckelberg JM, Patel R. Synovial fluid leukocyte count and differential for the diagnosis of prosthetic knee infection. The American journal of medicine. 2004;117:556-62.

[29] Reid G. Biofilms in infectious disease and on medical devices. International journal of antimicrobial agents. 1999;11:223-6.

[30] Springer BD. The Diagnosis of Periprosthetic Joint Infection. Journal of Arthroplasty. 2015;30:908-11.

[31] Portillo ME, Salvado M, Trampuz A, Siverio A, Alier A, Sorli L, et al. Improved diagnosis of orthopedic implant-associated infection by inoculation of sonication fluid into blood culture bottles. Journal of clinical microbiology. 2015;53:1622-7.

[32] Trampuz A, Piper KE, Jacobson MJ, Hanssen AD, Unni KK, Osmon DR, et al. Sonication of removed hip and knee prostheses for diagnosis of infection. The New England journal of medicine. 2007;357:654-63.

[33] Morgenstern C, Cabric S, Perka C, Trampuz A, Renz N. Synovial fluid multiplex PCR is superior to culture for detection of low-virulent pathogens causing periprosthetic joint infection. Diagnostic microbiology and infectious disease. 2018;90:115-9.

[34] Springer BD, Cahue S, Etkin CD, Lewallen DG, McGrory BJ. Infection burden in total hip and knee arthroplasties: an international registry-based perspective. Arthroplasty Today. 2017;3:137-40.

[35] Olubiyi OI, Lu F-K, Calligaris D, Jolesz FA, Agar NY. Chapter 17 - Advances in Molecular Imaging for Surgery. In: Golby AJ, editor. Image-Guided Neurosurgery. Boston: Academic Press; 2015. p. 407-39.

[36] Moody AS, Baghernejad PC, Webb KR, Sharma B. Surface Enhanced Spatially Offset Raman Spectroscopy Detection of Neurochemicals Through the Skull. Analytical Chemistry. 2017;89:5689-93.

[37] Huang Z, McWilliams A, Lui H, McLean DI, Lam S, Zeng H. Near-infrared Raman spectroscopy for optical diagnosis of lung cancer. International journal of cancer. 2003;107:1047-52.

[38] McMahon JM, Henry AI, Wustholz KL, Natan MJ, Freeman RG, Van Duyne RP, et al. Gold nanoparticle dimer plasmonics: finite element method calculations of the electromagnetic enhancement to surface-enhanced Raman spectroscopy. Analytical and Bioanalytical Chemistry. 2009;394:1819-25.

[39] Ivleva NP, Wagner M, Horn H, Niessner R, Haisch C. In Situ Surface-Enhanced Raman Scattering Analysis of Biofilm. Analytical Chemistry. 2008;80:8538-44.

[40] Nicolson F, Kircher MF, Stone N, Matousek P. Spatially offset Raman spectroscopy for biomedical applications. Chemical Society Reviews. 2021;50:556-68.

[41] Nicolson F, Jamieson LE, Mabbott S, Plakas K, Shand NC, Detty MR, et al. Through tissue imaging of a live breast cancer tumour model using handheld surface enhanced spatially offset resonance Raman spectroscopy (SESORRS). Chemical Science. 2018;9:3788-92.

[42] Stone N, Kerssens M, Lloyd GR, Faulds K, Graham D, Matousek P. Surface enhanced spatially offset Raman spectroscopic (SESORS) imaging - the next dimension. Chemical Science. 2011;2:776-80.

[43] Schulmerich MV, Dooley KA, Morris MD, Vanasse TM, Goldstein SA. Transcutaneous fiber optic Raman spectroscopy of bone using annular illumination and a circular array of collection fibers. Journal of Biomedical Optics. 2006;11.

[44] Mandair GS, Esmonde-White FWL, Akhter MP, Swift AM, Kreider J, Goldstein SA, et al. Potential of Raman Spectroscopy for Evaluation of Bone Quality in Osteoporosis Patients. Results of a Prospective Study. Conference on Photonic Therapeutics and Diagnostics VI. San Francisco, CA: Spie-Int Soc Optical Engineering; 2010.

[45] Sharma B, Ma K, Glucksberg MR, Van Duyne RP. Seeing through Bone with Surface-Enhanced Spatially Offset Raman Spectroscopy. Journal of the American Chemical Society. 2013;135:17290-3.

[46] Nicolson F, Jamieson LE, Mabbott S, Plakas K, Shand NC, Detty MR, et al. Multiplex imaging of live breast cancer tumour models through tissue using handheld surface enhanced spatially offset resonance Raman spectroscopy (SESORRS). Chemical Communications. 2018;54:8530-3.

[47] Nicolson F, Jamieson LE, Mabbott S, Plakas K, Shand NC, Detty MR, et al. Towards establishing a minimal nanoparticle concentration for applications involving surface enhanced spatially offset resonance Raman spectroscopy (SESORR) in vivo. Analyst. 2018;143:5358-63.

[48] McConoughey SJ, Howlin R, Granger JF, Manring MM, Calhoun JH, Shirtliff M, et al. Biofilms in periprosthetic orthopedic infections. Future Microbiology. 2014;9:987-1007.

[49] Willyard C. The drug-resistant bacteria that pose the greatest health threats. Nature. 2017;543:15.

[50] Viswanath BG, Lakshmi GJ, Nagamani K, Reddy NVN, Rao GP, Srinivas SSS, et al. Emergence of Antimicrobial Resistance among Anaerobic Bacteria. American Journal of Infectious Diseases and Microbiology. 2017;5:87-93.

[51] Rolain JM, Abat C, Jimeno MT, Fournier PE, Raoult D. Do we need new antibiotics? Clinical Microbiology and Infection. 2016;22:408-15.

[52] Olsen I. Biofilm-specific antibiotic tolerance and resistance. European journal of clinical microbiology & infectious diseases : official publication of the European Society of Clinical Microbiology. 2015;34:877-86.

[53] Wu H, Moser C, Wang H-Z, Hoiby N, Song Z-J. Strategies for combating bacterial biofilm infections. International Journal of Oral Science. 2015;7:1-7.

[54] Kyle S. 3D Printing of Bacteria: The Next Frontier in Biofabrication. Trends in Biotechnology. 2018;36:340-1.

[55] Su C, Huang K, Li H-H, Lu Y-G, Zheng D-L. Antibacterial Properties of Functionalized Gold Nanoparticles and Their Application in Oral Biology. Journal of Nanomaterials. 2020;2020:5616379.

[56] NHS. Statistics on Obesity, Physical Activity and Diet - England, 2017. In: Digital N, editor. NHS Digital 2017.

[57] Nicolson F, Jamieson LE, Mabbott S, Shand NC, Graham D, Faulds K. Through barrier detection of ethanol using handheld Raman spectroscopy—Conventional Raman versus spatially offset Raman spectroscopy (SORS). Journal of Raman Spectroscopy. 2017;48:1828-

9.8 **Chapter 8**

[1] Aldana AA, Valente F, Dilley R, Doyle B. Development of 3D bioprinted GelMA-alginate hydrogels with tunable mechanical properties. Bioprinting. 2021;21:e00105.

[2] Ansari S, Pouraghaei Sevari S, Chen C, Sarrion P, Moshaverinia A. RGD-Modified Alginate–GelMA Hydrogel Sheet Containing Gingival Mesenchymal Stem Cells: A Unique Platform for Wound Healing and Soft Tissue Regeneration. ACS Biomaterials Science & Engineering. 2021.

[3] Byambaa B, Annabi N, Yue K, Trujillo-de Santiago G, Alvarez MM, Jia W, et al. Bioprinted Osteogenic and Vasculogenic Patterns for Engineering 3D Bone Tissue. Adv Healthc Mater. 2017.

[4] Seyedmahmoud R, Çelebi-Saltik B, Barros N, Nasiri R, Banton E, Shamloo A, et al. Three-Dimensional Bioprinting of Functional Skeletal Muscle Tissue Using GelatinMethacryloyl-Alginate Bioinks. Micromachines (Basel). 2019;10.

[5] Yin J, Yan M, Wang Y, Fu J, Suo H. 3D bioprinting of low-concentration cell-laden gelatin methacrylate (GelMA) bioinks with a two-step cross-linking strategy. ACS applied materials & interfaces. 2018;10:6849-57.

[6] Ying G, Jiang N, Yu C, Zhang YS. Three-dimensional bioprinting of gelatin methacryloyl (GelMA). Bio-design and Manufacturing. 2018;1:215-24.

[7] Yue K, Trujillo-de Santiago G, Alvarez MM, Tamayol A, Annabi N, Khademhosseini A. Synthesis, properties, and biomedical applications of gelatin methacryloyl (GelMA) hydrogels. Biomaterials. 2015;73:254-71.

[8] Zongjie W, Zhenlin T, Fredric M, Keekyoung K. Comparative study of gelatin methacrylate hydrogels from different sources for biofabrication applications. Biofabrication. 2017;9:044101.

[9] Li X, Chen S, Li J, Wang X, Zhang J, Kawazoe N, et al. 3D Culture of Chondrocytes in Gelatin Hydrogels with Different Stiffness. Polymers (Basel). 2016;8:269.

[10] Mironov V, Kasyanov V, Markwald RR. Organ printing: from bioprinter to organ biofabrication line. Curr Opin Biotechnol. 2011;22:667-73.

[11] Drummond J, Tran P, Fary C. Metal-on-Metal Hip Arthroplasty: A Review of Adverse Reactions and Patient Management. Journal of functional biomaterials. 2015;6:486-99.

[12] Lou YR, Kanninen L, Kuisma T, Niklander J, Noon LA, Burks D, et al. The use of nanofibrillar cellulose hydrogel as a flexible three-dimensional model to culture human pluripotent stem cells. Stem Cells Dev. 2014;23:380-92.

[13] Adkinson JM, Chung KC. Advances in small joint arthroplasty of the hand. Plastic and reconstructive surgery. 2014;134:1260-8.

[14] Groll J, Boland T, Blunk T, Burdick JA, Cho DW, Dalton PD, et al. Biofabrication: reappraising the definition of an evolving field. Biofabrication. 2016;8.

[15] Holmes AM, Charlton A, Derby B, Ewart L, Scott A, Shu W. Rising to the challenge: applying biofabrication approaches for better drug and chemical product development. Biofabrication. 2017;9:033001.

[16] Huang Y, Xia A, Yang G, Jin F. Bioprinting Living Biofilms through Optogenetic Manipulation. ACS Synth Biol. 2018;7:1195-200.

[17] Connell JL, Ritschdorff ET, Whiteley M, Shear JB. 3D printing of microscopic bacterial communities. Proceedings of the National Academy of Sciences of the United States of America. 2013;110:18380-5.

[18] Kyle S. 3D Printing of Bacteria: The Next Frontier in Biofabrication. Trends in Biotechnology. 2018;36:340-1.

[19] Lehner BAE, Schmieden DT, Meyer AS. A Straightforward Approach for 3D Bacterial Printing. ACS Synth Biol. 2017;6:1124-30.